697-214

A MILLIMETER WAVELENGTH INTERFEROMETRIC STUDY OF ORGANIC MOLECULES IN COMET HALE-BOPP (C/1995 O1)

BY

JEFFREY MATTHEW VEAL

B. S., San Diego State University, 1994

THESIS

Submitted in partial fullfilment of the requirements
for the degree of Doctor of Philosophy in Astronomy
in the Graduate College of the
University of Illinois at Urbana-Champaign, 2000

Urbana, Illinois

UNIVERSITY OF ILLINOIS AT URBANA-CHAMPAIGN

THE GRADUATE COLLEGE

WE HEREBY RECOMMEND THAT THE THESIS BY

Jeffrey Matthew Veal

ENTITLED A MILLIMETER WAVELENGTH INTERFEROMETRIC STUDY OF ORGANIC

MOLECULES IN COMET HALE-BOPP (C/1995 O1)

BE ACCEPTED IN PARTIAL FULFILLMENT OF THE REQUIREMENTS FOR

THE DEGREE OF DOCTOR OF PHILOSOPHY

Director of Thesis Research

Head of Department

Committee on Final Examination†

Chairperson

† Required for doctor's degree but not for master's.

O-517

Physics

UNIVERSITY OF ILLINOIS AT URBANA-CHAMPAIGN

THE GRADUATE COLLEGE

July 29, 1998

WE HEREBY RECOMMEND THAT THE THESIS BY

Jeffrey Matthew Veal

ENTITLED A MILLIMETER WAVELENGTH INTERFEROMETRIC STUDY OF ORGANIC MOLECULES IN COMET HALE-BOPP (C/1995 01)

BE ACCEPTED IN PARTIAL FULFILLMENT OF THE REQUIREMENTS FOR

THE DEGREE OF DOCTOR OF PHILOSOPHY

Lewis E. Snyder
Director of Thesis Research

RMCrutcher
Head of Department

Committee on Final Examination†

Lewis E. Snyder
Chairperson

RMCrutcher

Kenneth M. Yoss

Edward C Sutton

Patrick Palmer

† Required for doctor's degree but not for master's.

O-517

UNIVERSITY OF ILLINOIS AT URBANA-CHAMPAIGN

GRADUATE COLLEGE DEPARTMENTAL FORMAT APPROVAL

THIS IS TO CERTIFY THAT THE FORMAT AND QUALITY OF PRESENTATION OF THE THESIS

SUBMITTED BY JEFFREY MATTHEW VEAL AS ONE OF THE

REQUIREMENTS FOR THE DEGREE OF DOCTOR OF PHILOSOPHY

IS ACCEPTABLE TO THE DEPARTMENT OF ASTRONOMY.

Full Name of Department, Division or Unit

March 21, 2000

Date of Approval

Carol Stickrod

Departmental Representative

A MILLIMETER WAVELENGTH INTERFEROMETRIC STUDY OF ORGANIC MOLECULES IN COMET HALE-BOPP (C/1995 O1)

Jeffrey Matthew Veal, Ph.D.
Department of Astronomy
University of Illinois at Urbana-Champaign, 2000
Lewis E. Snyder, Advisor

Observations of comet Hale-Bopp with the BIMA Array were conducted in interferometric and autocorrelation modes in the late winter and early spring of 1997. The following points summarize the highlights of this research project.

- The capability of the BIMA Array to detect new cometary molecules has been established, with the discovery of HCO^+ in comet Hale-Bopp.

- Millimeter wavelength interferometric maps of comet spectral line emission have been made for the first time, proving the concept that comets can be successfully observed with the BIMA Array.

- A new technique, the "difference map", has been developed for analyzing high resolution images. This technique provides direct evidence of deviations from spherical outflow.

- The full utility of dedicated data transfer links and high speed computers has been exploited, revealing the plausibility of yielding arcsecond level ephemeris corrections on a daily basis.

- A three dimensional, non-spherically symmetric Monte Carlo code has been written to calculate production rates, the results of which, when combined with analysis of the high resolution observations and difference maps, have yielded more accurate production rates than those of the standard model.

Dedicated to

two of the ingredients in a Life of Happiness:

Freedom To and Growth.

Acknowledgments

I acknowledge the fruitful interaction with my scientific collaborators, to whom I will always be grateful, for I could not have done this without their help: Dr. L. E. Snyder as my thesis advisor; Dr. L. E. Snyder, Dr. E. C. Sutton, Dr. P. Palmer, Dr. R. M. Crutcher, & Dr. K. M. Yoss agreed to be on the thesis committee, read my thesis and preliminary exam paper, and offered instructive comments; Dr. L. E. Snyder, Dr. M. C. H. Wright, L. M. Woodney, Dr. P. Palmer, Dr. J. R. Forster, Dr. I. de Pater, Dr. M. F. A'Hearn, & Dr. Yi-Jehng Kuan not only took part in this project and helped make it happen, but were tremendously helpful in getting the results published. Dr. D. K. Yeomans assisted with ephemerides. This work was partially supported by: NASA grant NAG5-4292 and NSF grant AST 96-139997; and by the University of Illinois.

I deeply and truly thank all of the people who have been a source of happiness during my graduate school years. Here are a few, in an order determined by a 48-bit random number generator with the linear congruential formula $X_{n+1} = (aX_n+c)_{\mathrm{mod}\ m}$, where $n \geq 0$, $m = 2^{48}$, $a = \mathrm{5DEECE66D}_{16} = 273673163155_8$, and $c = \mathrm{B}_{16} = 13_8$. This list is, in effect, a set of links to a myriad of good memories. I will enjoy looking back and recalling them over the years to come.

Yen-Hong Wang, Jeanie Kincer, Gerard & Jennifer Broeker, Saied Tabandeh, Bev & Al Krueger, Kathy & Jim Smith, Heather Foran, Nikki, Ray & Mary Plante, Liz Ott, Gordon & Marge Veal, Dimitri Mihalas, Rich & Connie Blazier, Tom Abel, Vicky Kalogera, Ed

Sutton, Lorraine Janeczko, Dave Sawyer, Deidra, Yosadara Ruiz, Ram Rao, Kim Gramlich, Anne Kohlhagen, Ross Beyer, Shawn Maskel, Laura Woodney, Yi-Jehng Kuan, John & Jeanne Conway, Yanti Miao, Jackie Burns, Icko Iben Jr., Chris Howk, Draza, Terrance Hill, Guillermo Garcia-Segura, Steve Hinkle, Chester Eng, Joyce & Bill Pitchford, Deana Pettigrew, Pam Starkey, Jean Hadfield, April Collier, Toshi Ueta, Gretchen Leuszler, Scott Teare, Rob Klinger, Ranjani Srinivasan, Sheng-Yuan Liu, Drew Gully, Dave Linton, Kate Grube, Brett Price, Brian Towey, Dave Fong, Steve Desch, Ron Webbink, Karen Davidson, Alan Calder, Vanessa Pence, Chris Daigneault, So Young Kim, Anna Maratos, Nancy Makri, Pam Lowrey, Patrick Hentges, Brad Carlson, Nina, Mandi Harvey, Stephanie & Brad Richmond, Tony Remijan, Cindy Sangerman, Silvia Zane, Cheryl Leal, Dave "Mooch" Lawless, Bryan Dunne, Sean Points, Karen Parks, Gail Conway, Lew & Doris Snyder, Tim Contreras, Margaret Meixner, Sara Vest, Dave Mehringer, Laird Thompson, Gary MacMullen, Randy Smith, Ashley Lane, Becca Lake, Sherry & Dave White, Fred Fleener, Chris & Jenny Presley, Sean Waddhams, Carol & Ainar Ayala, Bernie & Peggy Cohen, Patti McCauley, Gordon Buchanan, Mike Campbell, Doug Swesty, Mark & Theresa Sincell, Monika Ray, Eva Grebel, Joanna Woodson, Grey Tumiati, Rosie Chen, Kathy Ehrenfried, Rachel Konda, Bryan Davidson, Sandie Osterbur, Greg Veal, Jamie Barnes, Dan Thayer, Jim Kaler, Tracy DuFour, Rick James, Ken & Laura Hall, Jennifer, Steve England, Carol Diss, Robert Gruendl, Art Young, Daniel & Laurie Goscha, Mathilda Harvey, Adam Weems, Dick Plambeck, Terry Graves, Hope Veal, Grant Miller, MaryJean Bargren, Peter McCullough, Chip & Debra Manchester, Carol Stickrod, Hui-Chun Huan, Dan Briggs, Willa Hollis, Doug Roberts, Pat Palmer, Heidi Leuszler, Dimitrios Psaltis, Rich & Georgina Frazin, Les & Diane Ferguson, Ian Barton, Ken Hamer, Kevin Davidson, Kelly Pioletti, Fay Rouseff-Baker, Vicky & Norm Pence, Clara Veal, Aubrey Leffel, Leonidas Tsetseris, Gwen & Don MacMullen, Bob Lucas, Lyle Suess, Aaron Sparks, Tom Loew, Khrystian Richmond, Mark & Sandy Lane, John & Lanie Dickel, Ted Daub, Joe & Brandi Chesnut, Tony Beurskens, Paschalis & Laila Paschos, Andrea Hamilton, John Cwaygel, Trina Ray, Lance Contreras, Sam Smith, Jie

Zou, Ken & Norma Yoss, Vengu Lakshminarayanan, Shih-Ping Lai, Andrew Meyertholen, Michelle Edgcomb, Dave Leake

Preface

The Role of Comets in the Universe: A Puzzle

There are very few human endeavors that stand alone. Most, to some extent, stand on the shoulders of those that have come before. This thesis is no exception; it is a small piece in a very large puzzle. Even so, like a puzzle, all pieces are necessary to complete the picture. Here we have high angular resolution observations of comet Hale-Bopp's emission of radiation at wavelengths near three millimeters giving us a wealth of information through spectroscopy, interferometric images, and quality thinking. As our conclusions are drawn and compared to those from similar studies elsewhere around the world, several pieces of the puzzle begin to fit together: a recipe for the relative abundances and chemical composition of this wonderful comet will be discovered and a small section of the puzzle will be completed.

As comets come and go, astrophysicists and astronomers will assemble more small sections, study the ensemble as a whole, and prepare to complete a relatively large part of the puzzle: the underlying theme of the makeup of comets. From here, I expect the mysteries will unravel and the overall pattern to the puzzle will become clear. Answers will become available to our questions... Where do comets come from? How are they formed? How does cometary chemistry relate to interstellar chemistry? How are comets related to the star formation process? How are comets related to the origin of life on Earth? An avalanche of pieces and sections of the puzzle will come together in harmony. A long human endeavor, a collage of scientific effort and teamwork, will reach its finish. And somewhere, deep down in the project history, will reside a few unique and necessary minor steps like the discovery of cometary HCO^+, the exploration of non-spherical cometary structure with difference maps, and maybe even some other ideas to be found in the pages of this thesis. The work here will then have fulfilled its main purpose.

I must admit my slight dissatisfaction with the nature of this project; its utility is a function of the thesis topic and the era in which it has been written, and the combination of these two result in a piece of work that not only does not move or shake the world, but is indeed destined to be one small piece in a very large puzzle. We may have rocked the comet community a tiny bit, but we have not influenced huge masses of people at large. Moreover, it seems likely that I will not even live to see or experience any benefits to society that may arise as a direct consequence of my thesis. Such is the nature of pure research – rarely is one still alive to witness the full fruition of one's work.

In the end, this nature to have elusive immediate rewards is not a problem. Short term benefits are simply not the goal of research. Those who conduct pure research, scientists for example, understand and accept this. We are confident in the fact that our endeavors extend the bounding limits of knowledge and that our operations are necessary for the continuing growth of the human race. If pure research fails (perhaps funding is cut), then it will only be a short time before technology catches up to the edge of our body of knowledge and can go no further. Moreover, we know that it is impossible to fairly judge any current research as useless. For example, consider the development of quantum mechanics in its infancy. These studies gave birth to solid state physics, which in turn led to the development of the transistor and high speed computers. Now computers are helping us build better transportation and even new hybrids of vegetables, the combination of which can feed more people. In the beginning, one might have said that the project was a waste of time and resources, but we see in retrospect that it wasn't. Another poignant example comes from the branch of mathematics known as knot theory. After existing for a century totally absent of practical application, it is now being juxtaposed with viral studies and successfully promoting our knowledge of the ways in which viruses form and attack. There is no lack of examples that exhibit the unpredictability of the benefits of science, the point is clear, and the folly of premature judgment in the matter was succinctly expressed by Benjamin Franklin when he was asked, "What is the use of scientific research?" He replied, "What is the use of a newborn baby?"

When I attempt to consider this thesis in the absolute sense, I don't really believe that my contributed piece of the puzzle will result in anything so grand and ubiquitous as the sum of wonders that the human race has accomplished with the help of modern technology. But there's no suffering in this, because we may be comforted by the fact that there is at least one thing we can all rely on to be true beyond our wildest dreams whether it applies to the big picture, or one's life, or the impact of this thesis... Anything is possible.

Urbana, Illinois *Jeffrey M. Veal*
April, 1998

Contents

Chapter

Appendix

Chapter 1

Introduction

1.1 Why Study Comets?

Comets are one of the most spectacular displays of the nighttime sky. They have been fascinating observers for thousands of years and over this time have been the cause of much wonder and a fair amount of superstition. Comets also constitute the most numerous family of macroscopic objects in the Solar System, possibly numbering around 10^{11}. This may also imply that the number of comets far surpasses that of any other macroscopic entity in the universe. For these reasons, comets warrant study in and of themselves. Since cometary science is relatively young and individual comets have proven to be sometimes vastly different from one another, it presently pays to study each and every comet in the most detail possible. That is, we need to study a large ensemble of comets in order to begin to understand them.

Consider another reason to research comets. Currently, observations of comets are conducted around the world and in several different frequency bands of the electromagnetic spectrum. Each observation gleans a unique piece of information from a comet. For example, spectral line observations at different wavelengths can lead to production rates for different molecules. Together, many observations of this kind will lead to an estimate of the chemical composition of a particular comet. Over time, as several comets are observed in this manner, a general recipe for the chemical composition of comets is achieved. Information of this nature is requisite for understanding the formation of our Solar System and, furthermore, will help us to understand the star formation process at large. (See Greenberg (1982) for coverage of how comets may be related to interstellar dust.) Perhaps the most grand and profound of reasons for studying comets is their possible relation to the origin of life. As with any large payoff, the odds of any one contribution solving this mystery are extremely remote, and the relation is not yet based on any direct observational or experimental proof. In this area, we must proceed cautiously. But this notion can not be dismissed so easily, and seems to gain strength, rather than fade away, as time goes on and the science progresses. There is even a recently published book entitled *Comets and the Origin and Evolution of Life.*

As we search for a thorough understanding of cometary chemical composition and how and why it varies from comet to comet, we will no doubt advance far toward understanding the ways in which the less well understood cometary chemistry and the better understood interstellar chemistry are alike and the ways in which they are distinct.[1] An understanding of the connection between the chemistry of these two fields is likely to be beneficial for both fields, as it will facilitate the application of discoveries in one to the growth of knowledge in the other. This is especially important regarding the formation of organic molecules, as the existence of these in both comets and the interstellar medium is the first pointer toward the link between astrochemistry and the origin of life.

1.2 Single Element Radio Telescopes

Most of the early scientific discoveries related to comets were accomplished with observations of the visible and ultraviolet wavelengths, but the application of radio astronomy to cometary studies has resulted in several new and important discoveries, such as numerous new species that do not radiate efficiently in the visible and ultraviolet. Many of these new species are thought to be parent molecules rather than products of photodissociation or gas phase

---

[1] For a comparison of isotopic ratios between the two, see Jewitt et al. (1997).

chemistry. The abundances of these parent molecules have a closer connection to the chemical composition of the nucleus than the daughter molecules have because the need to thoroughly understand certain complicated physical processes, such as cometary gas phase chemistry, is much less critical. Two prominent examples of new parent molecules discovered are those of cometary hydrogen cyanide (HCN) (Huebner, Snyder, & Buhl 1974) in comet Kohoutek (C/1973 E1) and cometary methanol (CH_3OH) (Bockelée-Morvan et al. 1991) in comet Austin (C/1989 X1). These are important not only as new detections, but also as prompts for useful new models. For example, work by Bockelée-Morvan et al. (1984) discusses the vibrational excitation population and that HCN fluorescence equilibrium may dominate over collisions outside a certain distance from the nucleus.

Perhaps the most fruitful cometary radio observations in the past have been directed at the hydroxyl radical (OH), which is the primary dissociation product of water (H_2O). Since H_2O is probably by far the most abundant constituent of the nucleus and coma but is for the most part unobservable with ground based telescopes at ultraviolet, infrared, and radio wavelengths, OH becomes one of the best tracers of the coma's most abundant gas. Cometary OH was first observed at radio wavelengths by Turner (1974), and Biraud et al. (1974) in comet Kohoutek. Based on his observations, Turner stated several interesting facts: collisional excitation of the OH ground state Λ-doublet happens less than once per lifetime of the radical, each radical undergoes ~2500 ultraviolet excitations followed by fluorescence, and ground state Λ-doublet transitions induced by a 5 K background at 18 cm are negligible. Based on these facts, Turner verified the conclusion that the Λ-doublet transitions are a result of pumping by solar ultraviolet radiation.[2] Mies (1974) and Biraud et al. went a step further

---

[2] The ultraviolet OH pump refers to excitation of the OH radical from the $X^2\Pi$ electronic state to the $A^2\Sigma^+$ electronic state. From here, there are two possibilities, depending upon exactly which energy level of the $A^2\Sigma^+$ state the radical is excited to. In one case, the selection rules of the fluorescence cascade bring the radical into the $X^2\Pi_{3/2}$ J=3/2 Λ_+ state, causing a population inversion. Since spontaneous emission from this state is very slow, the inversion can then lead to a maser of cosmic or galactic background radiation. In the other case, the selection rules of the fluorescence cascade bring the radical into the $X^2\Pi_{3/2}$ J=3/2 Λ_- state, causing anti-inversion. This can lead to enhanced absorption of cosmic or galactic background radiation.

and explained the temporal variations in the brightness temperature of OH by way of the Swings effect.[3] Soon after, the Swings effect on the ultraviolet pump was verified in comet West (C/1975 V1-A) (Snyder et al. 1976). When radio OH was observed for the first time in a short period comet, comet d'Arrest (6P/1976) (Webber & Snyder 1977), it was proposed that the hyperfine splitting of the Λ-doublet should be considered in order to explain deviations of the observations from the standard ultraviolet OH pump. Elitzur (1981) calculated these effects and found they should be noticeable when the level populations change from inversion to anti-inversion, or vice versa. These peculiarities of the OH pump and Swings effect are important if the data are to be properly manipulated in calculations of the OH production rate. Another effect, important for the same reason, is the collisional quenching of the population inversion in the inner coma, which helps to explain why the OH production rates determined from radio observations were consistently less than those determined from ultraviolet observations. This brings to light the advantages of cometary studies in the radio regime, where those in the optical and ultraviolet are lacking: the coma is optically thin, spectral lines are resolved (revealing gas kinematics and outgassing asymmetries), and exploration of the size of the collision zone via quenching effects is possible.

In 1990, another approach to OH studies at radio wavelengths came about: a method with which to retrieve H_2O expansion velocities from the OH line profiles[4] (Bockelée-Morvan, Crovisier, & Gérard 1990). If the source size cannot be estimated, which is usually the case for observations from single-element telescopes, this knowledge of the parent expansion velocity is the necessary basis for modeling the coma and converting antenna temperatures to

---

[3] The Swings effect causes a moderation of the ultraviolet OH pump with time. As the comet orbits the Sun, its radial velocity with respect to the Sun changes. In consequence, the magnitude of the Doppler shift that the comet "sees" in the Sun's Fraunhofer absorption spectrum varies with time. So, as the Fraunhofer lines pass by the OH electronic excitation frequencies, the population inversions and anti-inversions will fade away and reappear.

[4] More precisely, the H_2O expansion velocities at the time of photodissociation are found. The method is as follows. Fit a trapezium to the OH line profile and assume the width of the base equals $2(v_p + v_d)$, where v_p is the H_2O expansion velocity and v_d is the relative OH ejection velocity. With a statistical base of nine comets, v_d is found to be $\sim$0.9 km/s. Then v_p can be immediately calculated for any comet with a measured OH line profile.

molecular abundances. Bockelée-Morvan, Crovisier, & Gérard (1990) also claim that at large Sun-comet distances (>1 AU), where the parent velocity doesn't depend on the production rate, previous estimates of the OH dissociation scale length were too large. Using their new method, they cleared up the remaining discrepancies between OH production rates derived from observations at ultraviolet wavelengths and those derived from observations at radio wavelengths. So we see that single-element radio telescopes have proven to be very useful in cometary research. Unfortunately, the OH line profile method spatially averages over many gas anisotropies, giving rise to ambiguities. The solution to this problem is to observe comets in such a way that a good estimation of the source size and distribution can be made. This requires observations with significantly higher angular resolution. The answer is radio interferometry.

1.3 Radio Interferometric Arrays

A radio interferometric array acts as a filter because it is not sensitive to structures larger than an angular size approximately determined by the minimum spacing of its elements. This means that the fraction of the flux measured by an array immediately shows how much flux is contained in structures smaller than this angular size. So an array observation can give information about the scale size of an emitting region even before the actual distribution of emission in an image is known. This fundamental property of arrays is not available with single-element telescopes. Consequently, arrays can be used to explore objects such as comets for the important small scale structures that may be masked by more obvious large scale structures. Furthermore, this means arrays can have vastly better angular resolution than that of single-element telescopes, allowing astronomers to finally make direct comparisons of radio and microwave observations with their counterparts at optical, ultraviolet, and infrared wavelengths.

With the rise of interferometry come more sophisticated observing strategies and, subsequently, more pitfalls. Comets, in particular, bring about certain problems that must be addressed before conducting a successful observing program. An ephemeris must be calculated for each comet so that telescopes can locate and track comets in the sky. Unfortunately, these ephemerides are prone to errors for several reasons. First, the orbit is calculated from positions reported by telescope observations, and, like any astronomical observation, there are inherent positional uncertainties. Second, with only a finite number of positions reported, the calculation of the orbit cannot be exact and carries formal errors. Third, as the comet approaches the Sun, nongravitational forces on the nucleus due to jetting activity are important enough to modify the comet's velocity through space, rendering a totally up-to-date ephemeris impossible. These effects can all add up to give a positional error of up to several arcseconds, which is on the order of the synthesized beam size. In addition to positional errors, those in radial velocity are inevitable for the same reasons. These can complicate the tracking of cometary spectral lines in velocity space. Luckily, ephemerides are updated every few weeks, which is enough to allow for the possibility of avoiding major problems. Another pitfall, the faint nature of comets, has always been a major obstacle, limiting us mainly to unusually bright comets, e. g., comets with large nuclei or nuclei with comet frost – the type of comet that comes by only once or twice in a century. The glorious opportunity brought to us by comet Hale-Bopp is just such an occurrence. One final problem that may arise, depending upon the comet and the observatory, is that of near-field optics. If the comet were close enough and the array baselines were long enough, the parallel plane wave approximation would no longer be valid for the incoming radiation. This situation did not apply to comet Hale-Bopp.

The first interferometric observation of a comet was in 1985 when comet Halley (1P/1982 U1) was observed with the Very Large Array (VLA) (de Pater, Palmer, & Snyder 1986). Right from the beginning, interferometric observations proved to be superior as the OH spatial distribution was resolved into clumps with non-nuclear maxima. With this kind of knowledge of the source size, production rates can be estimated with a new level of accuracy. An exemplary investigation into how much physical information about the gas can be derived from cometary array observations of OH was made with VLA observations of comet Shoemaker-Levy (C/1991 T2) (Palmer, de Pater, & Snyder 1999) in which interferometric maps and spectra and autocorrelation spectra are all used to determine the three dimensional distribution of the gas. Further advantage of cometary array observations, due to the high angular resolution, is the lack of primary beam dilution for relatively compact sources. The sensitivity is thereby increased. This is precisely what led to the first detection of cometary formaldehyde (H_2CO), made in 1986 with VLA observations of comet Halley (Snyder, Palmer, & de Pater 1989). Hence, it is apparent that interferometric arrays have proven to be quite useful in cometary research.

1.4 Two Recent Comets

Comets Hyakutake (C/1996 B2) and Hale-Bopp made very bright appearances within the past two and a half years. Comet Hyakutake was widely studied and allowed for a large number of publications. Even so, it was Hale-Bopp that was the first comet to be imaged at millimeter wavelengths (for example, see the Hyakutake continuum upper limit by de Pater et al. (1997) given in Appendix A). This is not to say that the observations of comet Hyakutake were not fruitful. Indeed, quite the opposite is true. Comet Hyakutake heralded the discoveries of cometary hydrogen isocyanide (HNC) (Irvine et al. 1996), ethane (C_2H_6) and methane (CH_4) (Mumma et al. 1996), $H^{13}CN$ and isocyanic acid (HNCO) (Lis et al. 1997), and x-ray emission (Lisse et al. 1996). Even more impressive, comet Hale-Bopp brought about the discoveries of a third type of tail (Cremonese et al. 1997) and several new cometary species; some examples are the formyl ion (HCO^+) (Veal et al. 1997), sulphur monoxide (SO) and formamide (NH_2CHO) (Lis et al. 1998), sulphur dioxide (SO_2) (Wink et al. 1997), deuterated hydrogen cyanide (DCN) (Meier et al. 1998), formic acid (HCOOH) (Wink et al. 1997), and methyl formate ($HCOOCH_3$) (Colom et al. 1997). Further discoveries via comet Hale-Bopp include direct evidence for cometary gas-phase reactions (Irvine et al. 1998) (through analyses of HNC and HCO^+) and the long awaited parents of C_2 and C_3: C_2H_2 and/or C_2H_6 (Crovisier 1998).

Despite the current number of publications on comet Hale-Bopp, no millimeter wavelength array image of a comet was published as of June 1998. This work contains numerous high-resolution millimeter-wavelength images of comet Hale-Bopp.

Chapter 2

Observations

Observations of comet Hale-Bopp were conducted with the BIMA Array[5] (Welch et al. 1996). The data were calibrated, edited and imaged in the usual way, using MIRIAD (Multichannel Image Reconstruction, Image Analysis, and Display) (Sault, Teuben, & Wright 1995). Absolute flux calibration, based on planet observations, is accurate to within 20% for autocorrelation and interferometric observations. The spectral line observations in autocorrelation mode were carried out in Mode 4, which has 4 spectral windows each simultaneously observing the upper and lower sidebands and 25 MHz bandwidth over 512 channels for each window. The spectral line observations in interferometric mode were mostly carried out in Mode 4, which has 8 spectral windows (4 observing each sideband) and 25 MHz bandwidth over 256 channels for each window; the exceptions in this mode were simultaneous observations of line and continuum and are described in Section 2.4 of this chapter.

2.1 Autocorrelation Data

Observations in autocorrelation mode are listed in Table 2.1, which gives the dates and times for each passband observed. The molecular transitions searched for in each passband are given in Appendix B.1 as Tables B.1 through B.8. Antennas 2, 4, 5, 6, 7, 8, and 9 of the array were equipped for autocorrelation observations. These antennas have a diameter of 6.1

---

[5] The BIMA Array is operated by the Berkeley-Illinois-Maryland Association under funding from the National Science Foundation.

TABLE 2.1: Observations in Autocorrelation Mode

Passband	UT Date	UT Start	Duration (hours)
85 GHz	04 Apr 1997	2200	6.8
87 GHz	04 Apr 1997	1420	7.0
89 GHz	05 Feb 1997[a]	2030	1.5
	12 Feb 1997[a]	1900	1.7
	19 Feb 1997[a]	1830	4.8
	22 Feb 1997[a]	1640	3.7
	25 Feb 1997[a]	0000	1.0
	26 Feb 1997[a]	0140	0.3
	27 Feb 1997[a]	1620	0.6
	27 Feb 1997[b]	2130	1.0
	28 Feb 1997[b]	1530	4.3
	02 Mar 1997[a]	1350	2.6
	05 Mar 1997[a]	2140	2.0
	09 Mar 1997[a]	2100	1.2
	12 Mar 1997[a]	2130	1.9
	03 Apr 1997[a]	0040	0.8
	17 Apr 1997[a]	1530	1.9
	20 Apr 1997[a]	1520	1.6
	21 Apr 1997[a]	1650	1.2
98 GHz	25 Feb 1997[c]	2100	2.5
	28 Feb 1997[c]	1950	1.6
	02 Mar 1997[c]	2130	4.0
	02 Apr 1997[d]	2345	1.0
	03 Apr 1997[d]	0140	0.5
	17 Apr 1997[d]	1730	1.8
	20 Apr 1997[d]	1650	1.3
101 GHz	06 Apr 1997	2120	8.0
110 GHz	06 Apr 1997	1500	6.3

[a] see Table B.1, [b] see Table B.2, [c] see Table B.3, [d] see Table B.4

meters with a consequent angular resolution of $2.3'$ for all autocorrelation observations. These seven antennas give the equivalent collecting area of a 16 meter single-element telescope.

After first deciding to conduct autocorrelation observations, we took several steps to arrive at a quality spectrum. This process involves creating a correlator setup, writing an observe command file, and carefully reducing the data. One example each of an observe command file, a data reduction script, and a correlator setup for autocorrelation observations can be found in Appendices B.2 through B.4, respectively.

2.1.1 HCO^+

Until BIMA Array autocorrelation observations of comet Hale-Bopp were conducted, HCO^+ was not known to exist in comets. The IAU Circular No. 6575 (Veal et al. 1997) describes the first detection of this ion in a comet. A copy of this circular is given in Appendix C.1 with ephemeris data for the comet in Appendix C.2. Confirmation of the existence of cometary HCO^+ immediately followed at several telescopes, including the Kitt Peak 12-m (Apponi et al. 1997), the FCRAO 14-m (Lovell et al. 1997), and the 10-m Heinrich Hertz Telescope (Narayanan et al. 1997). BIMA autocorrelation observations of HCO^+ were carried out on the dates indicated in Table 2.1 for the 89 GHz passband. Other molecular transitions aside from HCO^+ that are included in this passband can be found in Tables B.1 and B.2 and will be discussed below. For these tables and the others, the source of the rest frequencies is the standard Lovas line list (www.nist.gov, search "molecular lines").

The two best spectra described in the IAU Circular in Appendix C.1 and other spectra of equally high quality are shown in Figure 2.1. The abscissa measures the radial velocity

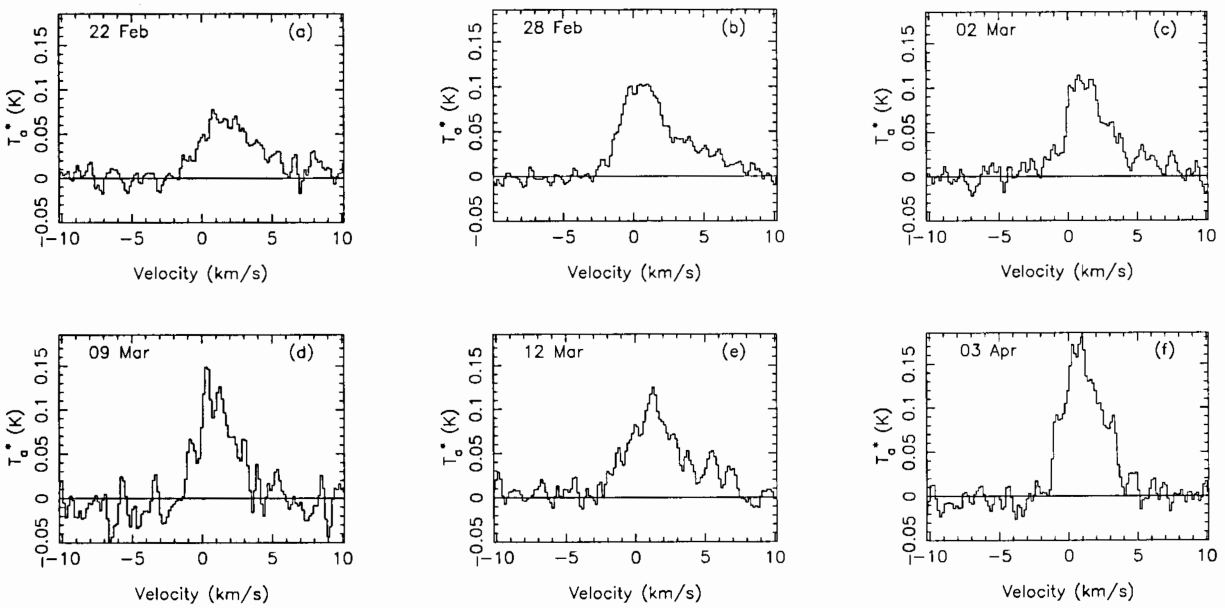

FIGURE 2.1: HCO^+ $J=1\rightarrow0$ in comet Hale-Bopp observed with the BIMA Array in autocorrelation mode. The velocity resolution is ~0.17 km/s per channel. The rms values in the 6 spectra are, in units of mK: (a) 9, (b) 6, (c) 11, (d) 18, (e) 11, and (f) 14.

in units of km/s; the velocity scale is zeroed on the radial velocity of the comet's nucleus with respect to the array, insofar as the comet velocity predicted by the ephemeris is correct. The velocity resolution is ~0.165 km/s. The ordinate scale, in units of Kelvins, is the source antenna temperature corrected for atmospheric and ohmic losses and rearward spill-over, ${T_a}^*$. The spectra in Figure 2.1 were observed on UT dates 22 Feb, 28 Feb, 02 Mar, 09 Mar, 12 Mar, and 03 Apr 1997, as shown in the upper left corner of each panel. There are a few interesting points to note here, such as the fact that the interferometric observations did not produce a map. This will be discussed further in Section 2.2 of this chapter. Also of note is the steady increase in peak ${T_a}^*$ over the course of the observations. This increase correlates well with the fact that perihelion was on 01 Apr 1997 UT. The comet should be expected to heat up as it approaches the Sun. Figure 2.2 shows how the peak ${T_a}^*$ (normalized to 1 AU) varies with R, the distance between the comet and the Sun. The diamonds and their error bars represent the peak ${T_a}^*$ values (normalized to 1 AU) and the rms values for the six spectra in Figure 2.1. The dotted curve is $f(R) = 0.32\ R^{-2.1}$ with probable uncertainties for the coefficient and exponent of 0.01 and 0.2, respectively. The curve has a goodness-of-fit probability of 1×10^{-5}, implying that the fit is unreliable – generally, 0.001 is the lower limit to reliability. However, notice how closely the HCO^+ variation matches the predicted $1/R^2$ law. The curves were fit to the data with the usual method of substituting logarithms into a linear least squares routine.[6] The last point to note is the redward wing seen in most of the spectra in Figure 2.1. The most probable explanation for this, as well as the redward offset of the line center from 0 km/s, is the interaction of the solar wind with this positively charged ion, accelerating the HCO^+ away from us. Lovell et al. (1998) agree.

The issue of converting the autocorrelation data from ${T_a}^*$ into other representations is

---

[6] More specifically, when one wants to fit a curve of the form $f(R) = cR^d$ to a set of data points, where c and d are constants, an easy way to go about this is to take a logarithm of this equation. This results in $\ln f(R) = \ln c + d \ln R$, which has the same form as the usual $y = a + bx$ of a linear least squares fit. Moreover, when each data point, (x_i, y_i), has a unique standard deviation, σ_{y_i}, associated with it, chi-square fitting is also used. Here, the best fit is obtained by minimizing the chi-square, $\chi^2 = \sum_i [(y_i - y)/\sigma_{y_i}]^2$. In this case, where logarithms are being used, σ_{y_i} is related to σ_{f_i} (where σ_{f_i} is the standard deviation associated with each data point *before* the logarithm has been taken) by $\sigma_{y_i}^2 = \sigma_{f_i}^2 (\partial y/\partial f)^2$, resulting in $\sigma_{y_i} = \sigma_{f_i}/f$.

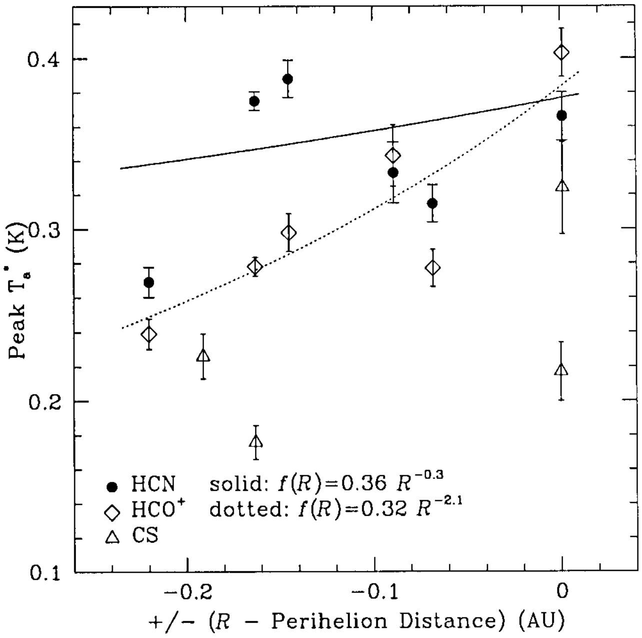

FIGURE 2.2: BIMA Array autocorrelation observations. Peak ${T_a}^*$ values (normalized to 1 AU) of HCN, HCO$^+$, and CS are shown as a function of R, the distance between the comet and the Sun, as well as fits to the HCN and HCO$^+$ data sets. The abscissa is shifted so that perihelion (0.914 AU) is at 0.

an interesting one. One possible conversion is from ${T_a}^*$ to a flux density, S_ν, in Janskys (1 Jy = 10^{-23} erg s^{-1} cm^{-2} Hz^{-1}). The method for doing this for a source with an angular diameter that is small relative to the primary beam pattern is as follows. The signal received by the telescope is $k{T_a}^* = S_\nu A_e/2$. Here k is Boltzmann's constant, and A_e is the effective aperture of the telescope dish. The factor of 2 in the formula accounts for the fact that the receiver measures only a single polarization of the incoming unpolarized radiation. If we then define the sensitivity of the telescope as $\Gamma \equiv \pi \eta_a D^2/8k$, where $\eta_a = A_g/A_e$ (ratio of geometric to effective apertures), then the conversion is simply $S_\nu = {T_a}^*/\Gamma$. The average value of Γ^{-1} for the observations described in this section is 134 (± 10%) Jy/K. Another desirable conversion is from ${T_a}^*$ to a main beam brightness temperature, T_{mb}. This does not account for primary beam dilution, but is directly convertible from ${T_a}^*$ via $T_{mb} = {T_a}^*/\eta_m$, where η_m is the main beam efficiency and is equal to 0.83 for the BIMA Array (Pound & Helfer 1997). This number has been calculated from observations of extended sources and is therefore not applicable to our autocorrelation observations of HCN and CS. However, as the HCO^+ is thought to be spatially extended, the $T_a{}^*$ values for this ion may be accurately converted to T_{mb}. The third possible conversion is to the brightness temperature, T_B, which is the Rayleigh-Jeans temperature of an equivalent black body radiating with the same flux density per beam. This requires knowledge of the source size and distribution, as the primary beam dilution factor must be known. This process is fairly complicated and will be addressed again only briefly in Section 2 of Chapter 3.

2.1.2 HCN

HCN was originally the target molecule of the 89 GHz passband. BIMA autocorrelation observations of HCN in the J=1→0 transition were carried out on the dates indicated in Table 2.1 for the 89 GHz passband. Other molecules that were included with HCN in the 89 GHz correlator setup can be found in Tables B.1 and B.2. The highest quality autocorrelation spectra of HCN, shown in Figure 2.3, were observed on UT dates 22 Feb, 28 Feb, 02 Mar, 09 Mar, 12 Mar, and 03 Apr 1997. These dates are given in the upper left corner of each panel. For explanation of the axes, refer to Section 1.1 of this chapter. In most of the spectra, all three hyperfine components (electric quadrupole splitting) of the line are visible: F=0→1, F=2→1, and F=1→1. The cases where the weakest component is not seen are simply due to a low signal to noise ratio. The relative strengths of the components are seen to be roughly equal to the expected local thermodynamic equilibrium (LTE) ratio of 1:5:3, which is just the ratio of the values of $2F_{upper}+1$ for the three transitions. Most of the lines also display two peaks, likely due to spherical expansion if the emitting region is resolved, along with some asymmetry arising from anisotropic outgassing. Also notable in Figure 2.3, though not as drastic as for the HCO^+, is an increase in peak $T_a{}^*$ with time as the comet heats up. Figure 2.2 shows how the peak $T_a{}^*$ varies with R. The dots and their error bars represent the peak $T_a{}^*$ values (normalized to 1 AU) and the rms values for the six spectra in Figure 2.3. The solid curve is $f(R) = 0.36\ R^{-0.3}$ with probable uncertainties in the coefficient

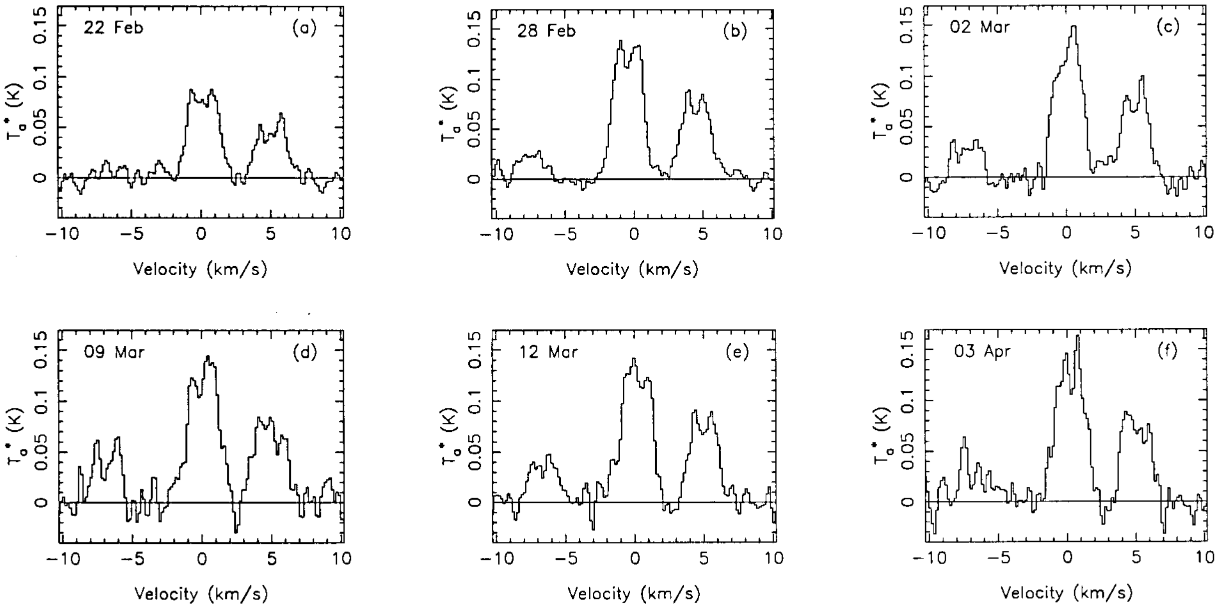

FIGURE 2.3: HCN J=1→0 in comet Hale-Bopp observed with the BIMA Array in autocorrelation mode. The three hyperfine components, from left to right, are F=0→1, F=2→1, and F=1→1, respectively. The velocity resolution is ~0.17 km/s per channel. The rms values in the 6 spectra are, in units of mK: (a) 9, (b) 6, (c) 11, (d) 18, (e) 11, and (f) 14.

and exponent of 0.01 and 0.2, respectively. The curve has a goodness-of-fit probability of 3×10^{-22}, implying that the fit is unreliable.

2.1.3 CS

BIMA autocorrelation observations of carbon monosulfide (CS) in the J=2→1 transition were carried out on the dates indicated in Table 2.1 for the 98 GHz passband. Other molecules that were included with CS in the 98 GHz correlator setup can be found in Tables B.3 and B.4. The highest quality autocorrelation spectra of CS, shown in Figure 2.4, were observed on UT dates 25 Feb, 28 Feb, 02 Apr, and 03 Apr 1997. For explanation of the axes, refer to Section 1.1 of this chapter. Of obvious note in Figure 2.4 is the overall increase in peak $T_a{}^*$ of CS emission with time, as was seen for HCN and HCO^+.

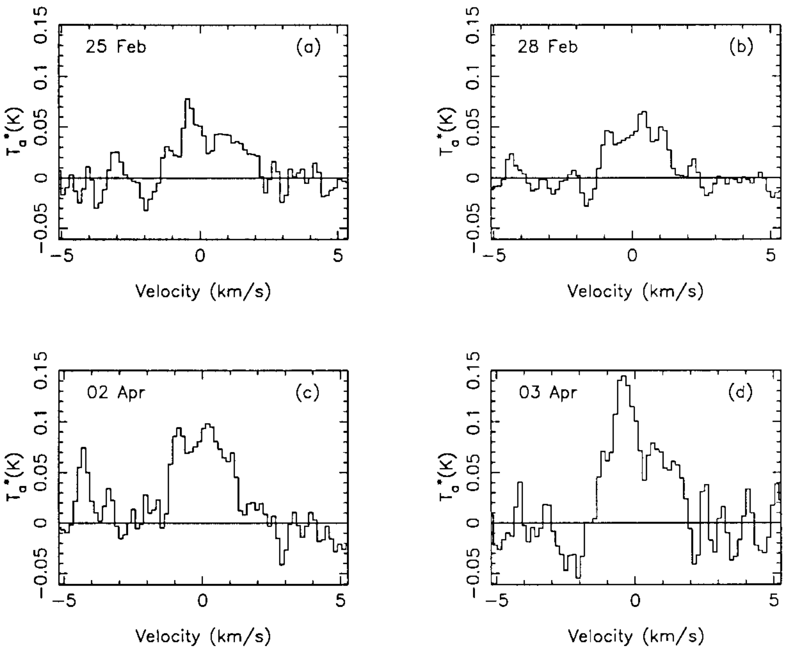

FIGURE 2.4: CS J=2→1 in comet Hale-Bopp observed with the BIMA Array in autocorrelation mode. The velocity resolution is ~0.15 km/s per channel. The rms values in the 4 spectra are, in units of mK: (a) 13, (b) 10, (c) 17, and (d) 27.

2.1.4 Other Molecular Transitions

While at the observing site, each day's data were quickly inspected to see which, if any, obvious detections were made. The rest of the transitions in Tables B.1 through B.8 that were not obviously detected will be analyzed more closely. New detections will be published and nondetections will be be used for upper limits on column densities and production rates.

2.2 Interferometric Data

Observations in interferometric mode are listed in Table 2.2, which gives the dates and times for each passband observed. The molecular transitions searched for in each passband are given in Appendix D.1 as Tables D.1 through D.12. All nine antennas of the array were used for the interferometric observations. The array was in the "soft" C configuration, as shown in Figure 2.5. The antennas are numbered as they are at the site. The italic numbers give the antenna positions in nanoseconds relative to the point of intersection of the north-south and east-west baselines. Also shown in Figure 2.5 is the *uv*-coverage this configuration gives

TABLE 2.2: Observations in Interferometric Mode

Passband	UT Date	UT Start	Duration (hours)
73 GHz	25 Mar 1997	2000	8.0
87 GHz	28 Mar 1997	1330	6.3
89 GHz	08 Mar 1997[b]	1740	3.3
	10 Mar 1997[b]	2000	2.5
	12 Mar 1997[b]	1250	3.6
	13 Mar 1997[b]	1220	14.3
	14 Mar 1997[b]	1750	2.0
	17 Mar 1997[b]	1730	2.3
	18 Mar 1997[a]	1230	13.0
	22 Mar 1997[d]	2200	0.5
	23 Mar 1997[d]	2200	6.0
	25 Mar 1997[c]	1320	2.0
	27 Mar 1997[c]	0120	2.6
	28 Mar 1997[c]	2000	8.3
	29 Mar 1997[c]	1320	15.2
	01 Apr 1997[c]	2200	6.0
	04 Apr 1997[d]	1400	10.5
	15 Apr 1997[c]	1900	3.0
	16 Apr 1997[c]	0140	2.6
	24 Apr 1997[a]	1800	10.0
	06 May 1997[d]	1620	8.3
91 GHz	27 Mar 1997	2100	7.3
97 GHz	27 Mar 1997	1330	7.0
	31 Mar 1997	1400	14.5
	08 Apr 1997	1500	6.3
98 GHz	25 Mar 1997	1520	12.5
	01 Apr 1997	1400	7.0
	05 Apr 1997	1440	14.0
	15 Apr 1997	1600	3.0
	15 Apr 1997	2240	2.8
	22 Apr 1997	1700	1.0
104 GHz	26 Mar 1997	1320	2.5
	02 Apr 1997	1400	6.0
	03 Apr 1997	0220	2.0
109 GHz	07 Apr 1997	1440	6.6
112 GHz	30 Mar 1997	1300	7.6
115 GHz	30 Mar 1997	2200	4.0
	07 Apr 1997	2220	6.6

[a] see Table D.1, [b] see Table D.2, [c] see Table D.3,
[d] mosaiced data, see Table D.1

for a full day[7] of comet observing. The typical resulting full width half power synthesized beam size is approximately 8″ by 10″.

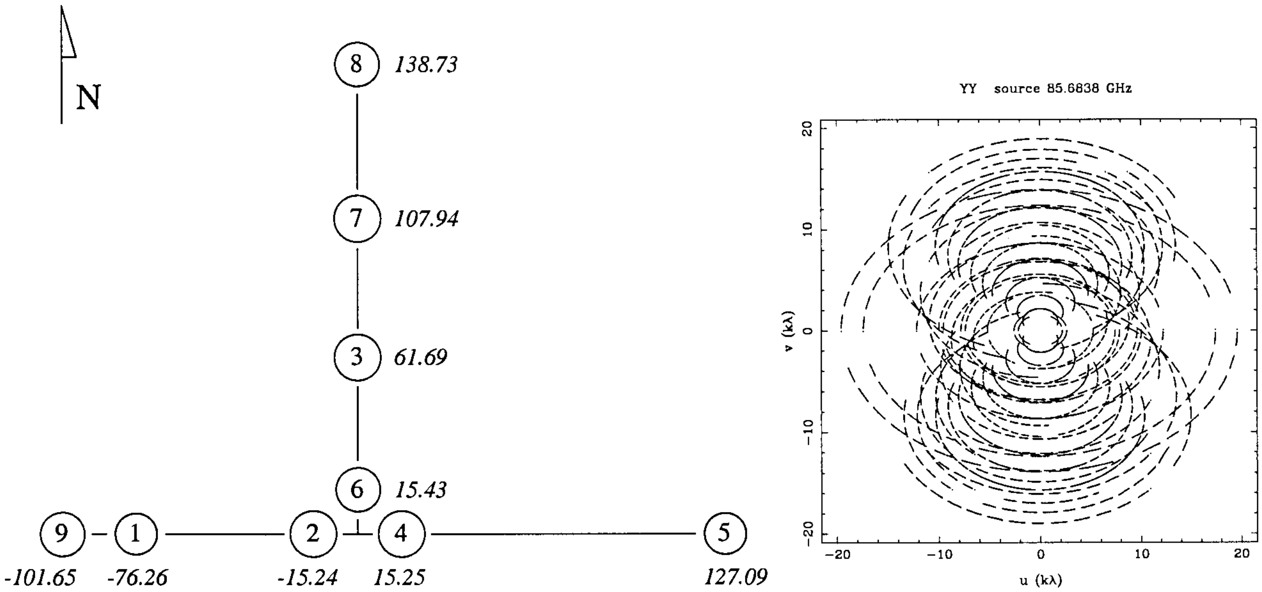

FIGURE 2.5: The BIMA Array "soft" C configuration used for interferometric observations of comet Hale-Bopp and the corresponding *uv*-coverage for a 15 hour comet track.

The process running from the first conception of acquiring interferometric data to the final output of a quality map and spectrum involves creating a correlator setup, writing an observe command file, and carefully reducing the data. One example each of an observe command file, a data reduction script, and a correlator setup for interferometric observations can be found in Appendices D.2 through D.4, respectively. The data were first all corrected to the JPL ephemeris reference orbit 77, and the zeros are centered on this location. More recently, the data have been corrected to reference orbit 106. Hence, the crosses are centered on this position, and the comet-Sun lines are anchored at this position as well. During the observing run, one important practical point in particular demanded our attention; we wanted a small interval of time between acquisition of the data and the dissemination of preliminary results. Comets are variable on time scales as short as hours. As a result, the observing run was

---

[7] A full day consists of tracking the comet from 15° above the northeast horizon to a few degrees east of zenith, pausing for a short period while the comet transits through zenith where the altitude-azimuth mounts of the telescopes don't track very well, and then resuming tracking of the comet a few degrees west of zenith down to 15° above the northwest horizon: a total of about 15 hours of observing.

best planned on a daily basis. With access to a dedicated high speed data transfer link and high speed NCSA computing facilities and with a little diligence, we were able to decide what to observe the next day based on the success, or lack thereof, of the current day's observations. Furthermore, comet observations at the Owens Valley Radio Observatory (Caltech), the Five College Radio Astronomy Observatory (U. of Massachusetts), and the 12-meter radio telescope at Kitt Peak were all able to benefit from timely discussions in which we conveyed our remarkably up-to-date results. This indicates the possibility of improving the observations of the entire comet community. If this fast data reduction can be used to find the true location of the comet's nucleus, this information can be made available for fast ephemeris calculations. In the future, comet observers around the world could have access to a new ephemeris immediately before their observing begins.

2.2.1 HCN

BIMA Array interferometric observations of HCN in the J=1→0 transition in comet Hale-Bopp were a tremendous success. The dates and times of these 89 GHz passband observations are given in Table 2.2. The other transitions included in this passband can be found in Tables D.1, D.2, and D.3. Figure 2.6 shows 12 days of HCN observations. The coordinates are in pixels offset relative to the position of the nucleus given by the ephemeris 77 with update to ephemeris 106 indicated by the start of the comet-Sun line, as explained above. In all maps, there is one arcsecond per pixel. The conversion from arcseconds to physical size at the nucleus varies from day to day, ranging from 1013.9 km/arcsec on 08 Mar UT to 953.7 km/arcsec on 22 Mar UT (perigee) to 1106.1 km/arcsec on 16 Apr UT. (See Appendix C.2 and Table K.2 for more complete ephemeris information.)

The maps in Figure 2.6 show the brightness distribution of HCN in the F=2→1 and F=1→1 hyperfine components of the J=1→0 transition for 12 days. Each of these two hyperfine transitions was approximately 7 channels (2.33 km/s) wide. These 7 channels were averaged for each line, and then the two lines were added together. The resulting

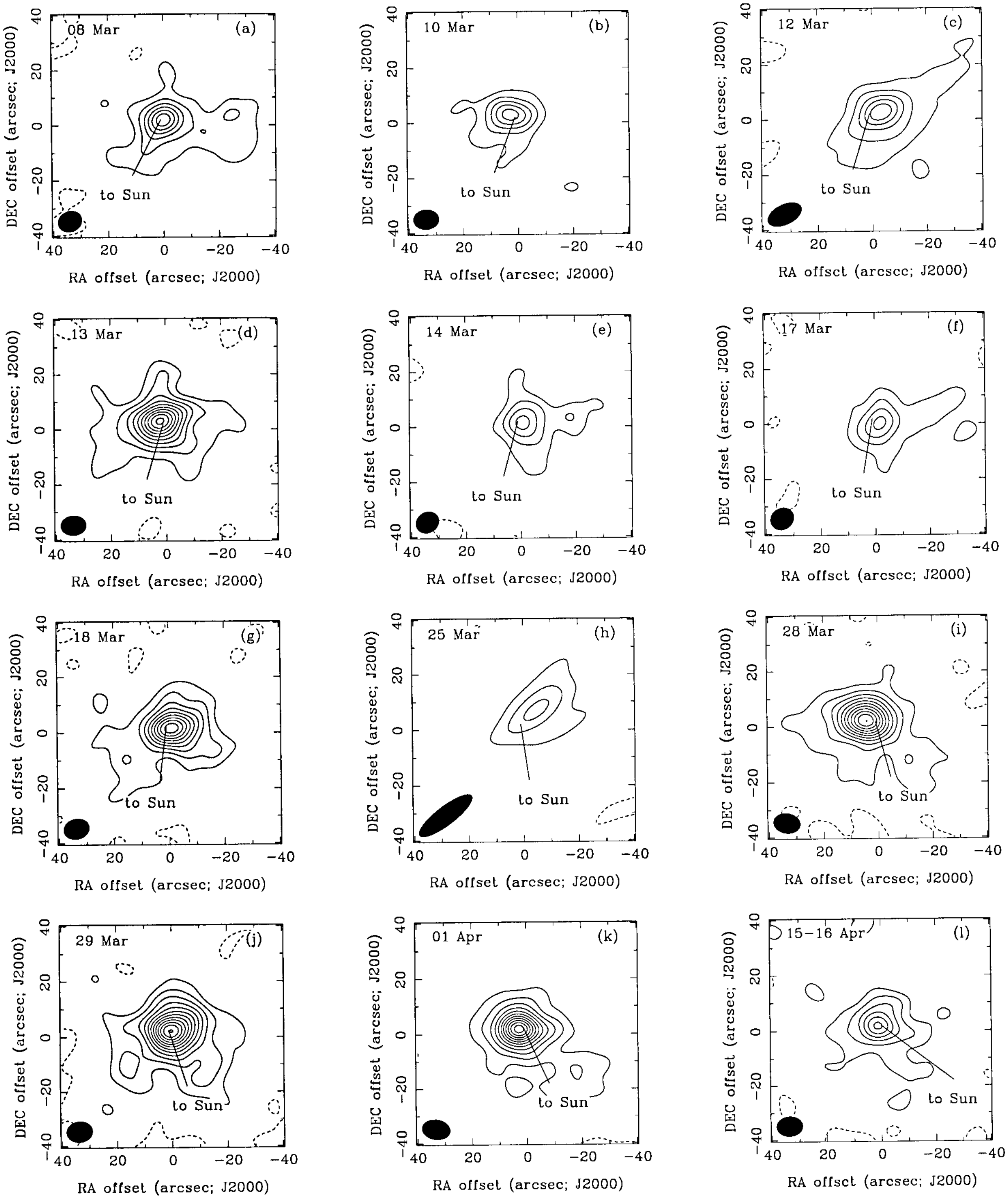

FIGURE 2.6: HCN J=1→0 in comet Hale-Bopp observed with the BIMA Array. For each date, a sum map of the F=2→1 and F=1→1 hyperfine transitions is shown. The contours are sucessive multiples of 3σ, with dashed contours being negative. The peak flux densities per beam and 1σ values are, in Jy/bm: (a) 1.98 and 0.10, (b) 1.70 and 0.10, (c) 2.11 and 0.12, (d) 1.95 and 0.06, (e) 1.67 and 0.13, (f) 1.64 and 0.13, (g) 1.80 and 0.06, (h) 2.51 and 0.25, (i) 2.11 and 0.06, (j) 2.11 and 0.06, (k) 2.61 and 0.08, and (l) 1.82 and 0.10.

single channel map is shown. The date of observation is in the upper left of each panel. The contours for each map are multiples of 3σ in the map. The rms in the map is equal to the rms in the data cube multiplied by $\sqrt{2}/\sqrt{7}$ to account for the averaging process. (The rms was calculated from a subsection of the data cube containing no emission.) By far, the most prominent cause of the changing number of contours from map to map is the different number of hours of each comet observation, resulting in a different signal to noise ratio from one image to the next. In the lower left corner of each map is given the size of the synthesized beam at full width half power. The line segment in each map serves to show the direction on the sky toward the Sun relative to the comet. The top end of the line segment is always anchored at the predicted position of the comet nucleus. The offset in the HCN emission relative to the predicted position is thought to be a real effect due to errors in the ephemeris averaged over the integration time. The peak flux densities per beam, in Jy/beam, can be found in the figure caption. While the change in flux density per beam does not vary smoothly with time, the general trend is to increase and then decrease. Figure 2.7 shows this trend in a fashion analogous to Figure 2.2, but for the values quoted in the caption of Figure 2.6. The solid curve is $f(R) = 1.8\ R^{-2.3}$ with probable uncertainties in the coefficient and exponent of 0.04 and 0.4, respectively. The curve has a goodness-of-fit probability of 8×10^{-12}, implying that the fit is unreliable. Figure 2.8 shows 12 days of HCN spectra. Each spectrum comes from a column, one pixel on a side, passing through the data cube at the coordinates of the pixel containing the peak in the corresponding map in Figure 2.6. The velocity resolution is equal to 0.33 km/s per channel. The flux density per beam is in units of Jy/beam. For most of the interferometric observations, the signal to noise ratio is not quite high enough for the weakest hyperfine component to show up conclusively. However, even in these cases, the ratio of integrated flux densities per beam for the two stronger components is seen from the figures to be roughly 5:3, the LTE ratio. In the cases of high signal to noise (13, 18, 28, 29 Mar and 01 Apr), all three hyperfine components are visible in the spectra. Again, the ratios of integrated flux densities per beam do not appear to deviate significantly

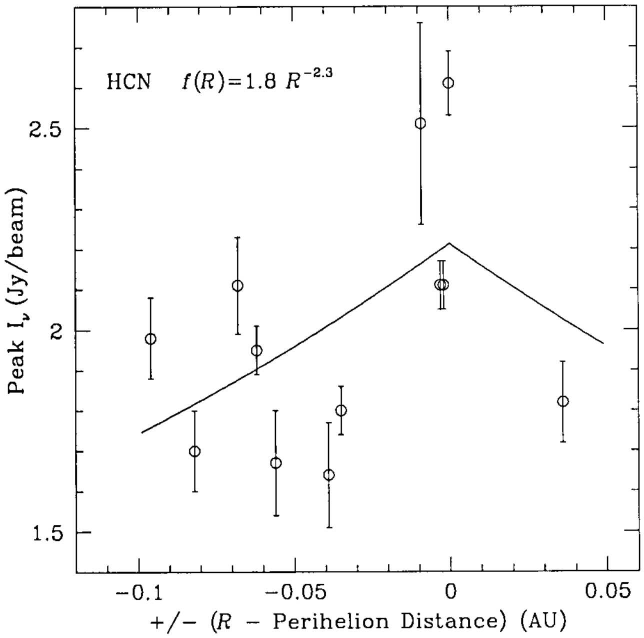

FIGURE 2.7: BIMA Array interferometric observations. Peak flux densities per beam of HCN are shown as a function of R, the distance between the comet and the Sun, as well as a fit to the HCN data set. The abscissa is shifted so that perihelion (0.914 AU) is at 0.

from the LTE ratio of 1:5:3. The variation in flux density per beam from day to day is clearly seen in the spectra, more so than in the maps. Also of note are the line profiles. The variation from day to day is not obviously significant. Of more interest is the blueward peak. With the use of Aipsview, the data can be quickly inspected for profile variation with respect to map position; the blueward peak remains prominent. The strength, of course, varies with distance from the peak in the map, but the profiles themselves are relatively constant over the emission region. In addition to MIRIAD and Aipsview, Dataview, the 3-D data visualization tool on the console of the SGI Onyx (Monet) has also been used to inspect the comet data. This tool is particularly helpful in allowing the researcher to understand the extent to which the emission differs from that expected with the standard Haser model for comets. The HCN data set on 29 Mar, for instance, has two extra "blobs" of significant strength, at slightly different velocities. Unfortunately, these types of features are not duplicated from day to day. Therefore, we did not take full advantage of the ease

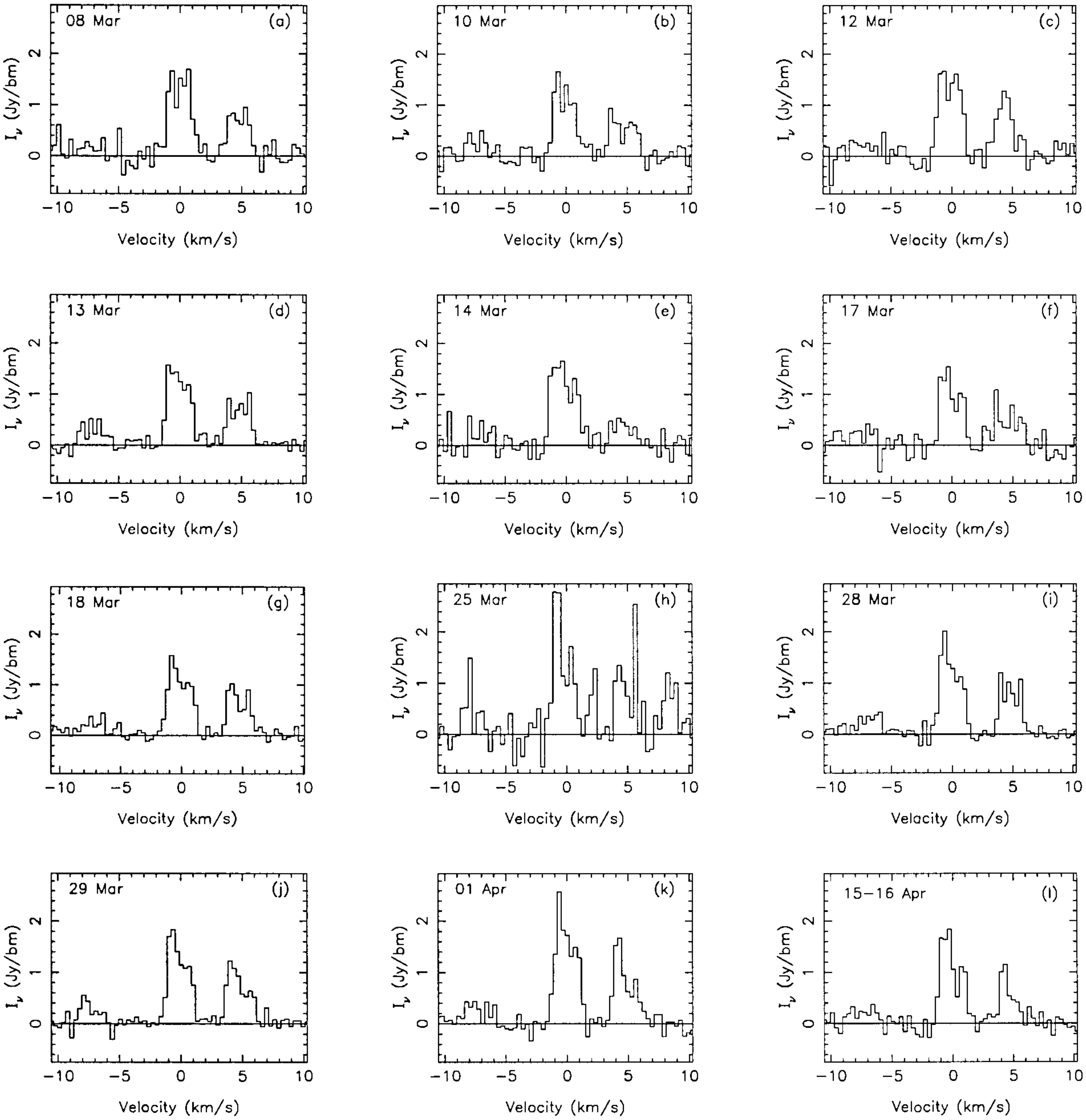

FIGURE 2.8: HCN J=1→0 in comet Hale-Bopp observed with the BIMA Array in interferometric mode. The three hyperfine components, from left to right, are F=0→1, F=2→1, and F=1→1, respectively. The velocity resolution is ~0.33 km/s per channel. The 1σ values in the data cube for each date are, in Jy/bm: (a) 0.19, (b) 0.19, (c) 0.22, (d) 0.11, (e) 0.24, (f) 0.24, (g) 0.11, (h) 0.47, (i) 0.12, (j) 0.11, (k) 0.15, and (l) 0.19. Each spectrum is extracted through the pixel of the maximum in the corresponding map in Figure 2.6.

with which such patterns may be recognized with this software.

It is interesting to note the overall difference in HCN spectral line profiles between the interferometric data set and the autocorrelation data set. It is easily seen that the first displays profiles that have, for the most part, a blue peak, while the second displays profiles that have, for the most part, both red and blue peaks. We believe this to be due to the different angular resolutions of the two data sets. The interferometric data concentrate on the region relatively close to the nucleus, where any anisoptropic outgassing would result in a strong Doppler shift signature in the line profile. In contrast, the autocorrelation data concentrate on a much larger region, which is essentially an older sample of molecules. That is, the average HCN molecule within primary beam has been in the gas phase on the order of 3/4 of a day, much longer than that in the synthesized beam, which is on the order of one hour. Hence, any anisotropies have had more time to dissipate and/or become less collimated during free expansion, resulting in a relatively weaker Doppler shift signature in the line profile. In order to inspect this hypothesis, we have investigated a few of the interferometric HCN data sets by averaging spectra over larger angular regions and by making new maps with very small *uv*-distance limits on the data. Neither approach significantly changed the profiles in the data. However, this does not nullify our conclusion in this matter, as the average "*uv*-distance" for the autocorrelation observations is only about one half of a dish diameter, resulting in a sensitivity to size scales differing by a factor of 2 from the autocorrelation to interferometric modes.

Time variability is not restricted to daily changes. Figure 2.9 shows hourly variation. Each of the four maps in the left column represents roughly two hours of data. As before, the maps are sums of averaged F=2→1 and F=1→1 components. The time in the upper left corner of each panel is the approximate center of the time interval over which the data for each map were collected. The contours in Figure 2.9 are slightly different than for Figure 2.6. Here, they are all successive multiples of 0.23 Jy/beam, which is approximately equal to 2σ in each of the maps. The peak flux densities per beam for the left column, in Jy/beam

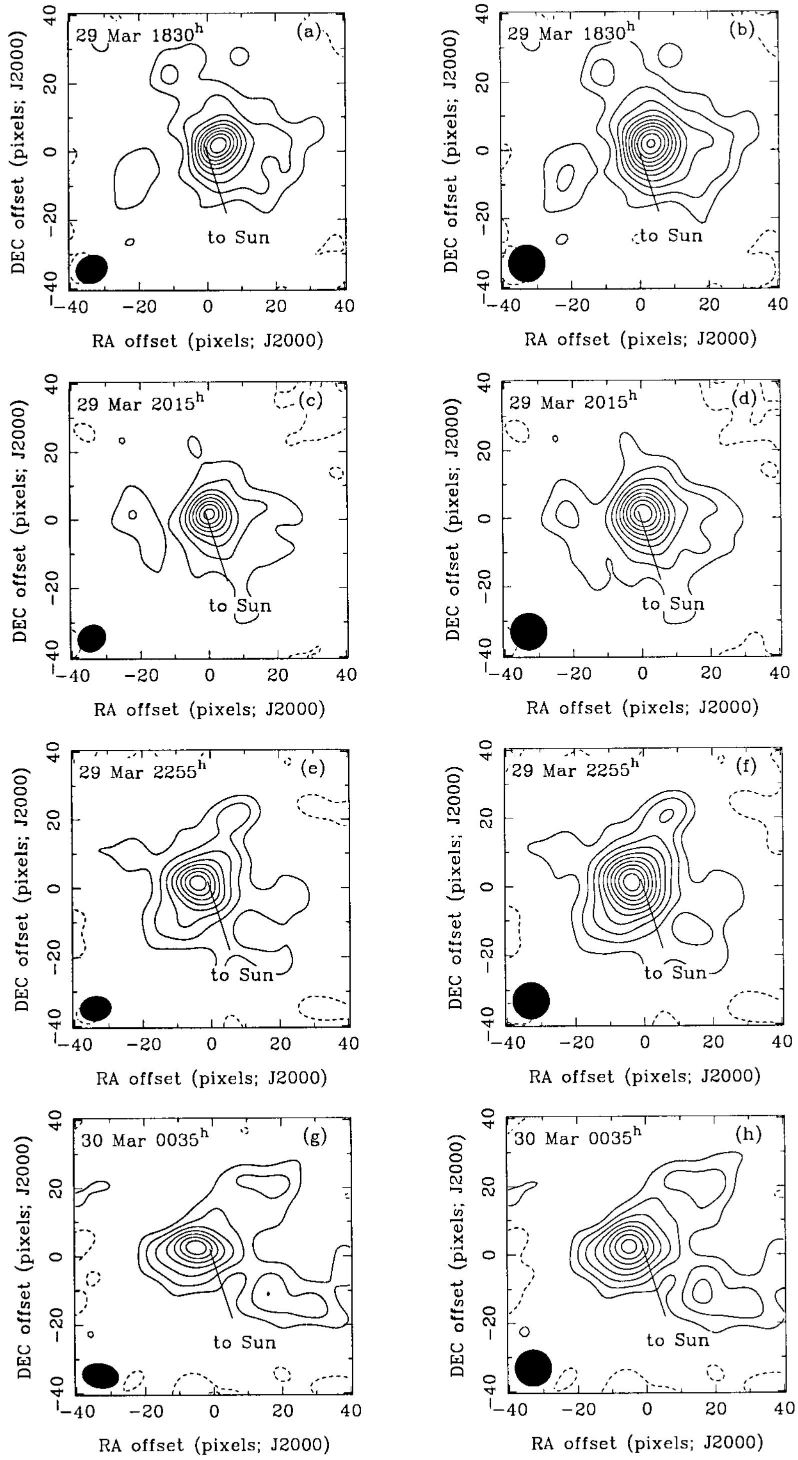

FIGURE 2.9: HCN J=1→0 in comet Hale-Bopp observed with the BIMA Array. The right column differs from the left in its synthesized beam; all 4 maps in the right column have been restored with a circular Gaussian synthesized beam of dimension equal to the largest beam dimension in the left column, 10.85″. For each time a sum map of the F=2→1 and F=1→1 transitions is shown. The contours are successive multiples of 0.23 Jy/beam, which is approximately equal to 2σ in each of the maps. Dashed contours are negative.

and in chronological order, are 2.29, 1.96, 2.02, and 1.81. This is a variation of larger than 4σ, implying a confidence interval that the change is real by better than 99.99%. This is not surprising considering the results of Blake, Qi, & Muhleman (1998), in which strong variations in carbonyl sulphide (OCS) were observed on time scales as short as 2 hours.

Figure 2.9 also shows that the outer structure (farther from the nucleus) does not depend significantly on whether the data are restored with a regular Gaussian synthesized beam or a circular Gaussian synthesized beam; the general features remain the same. We also note that while the left column may show emission distributions that are artificially elongated along the beam axes, the right column may show emission distributions that have lower resolution. For these two reasons, we have limited this type of restoration process with a circular Gaussian synthesized beam to Figure 2.9.

2.2.2 HCO^+

After the discovery of HCO^+, we made several attempts to map the J=1→0 transition, including a setup with a hex 7 mosaic pattern. The hex 7 mosaic is a pattern in which the observations are split equally among 7 pointing positions. Six of the pointing positions are on the vertices of a hexagon with the seventh at the center. The size of the hexagon is such that the length of one side is equal to the distance from the center of the primary beam out to the half power point. The dates and times of these events are given in Table 2.2 under the 89 GHz passband marked with a superscript "d". Most attempts were without result. This implies an extremely smooth brightness distribution over the field of view. However, with much effort, a minimal detection was made with the mosaic technique (Wright et al. 1998, given in Appendix E).

2.2.3 Other Detected Molecules: CS, CH_3OH, and CO

Interferometric observations of comet Hale-Bopp with the BIMA Array led to the detection of three other molecules: CS, CH_3OH, and CO. The dates and times of the CS observations can be found in Table 2.2 under the passband 98 GHz. Other transitions included in this passband are given in Table D.4. Figure 2.10 shows a representative map and spectrum of the high quality CS data. The map is emission from the J=2→1 transition, averaged over 7 channels (~2 km/s). The contours are multiples of 3σ, calculated the same as for HCN, but multiplied by $1/\sqrt{7}$ instead. The coordinates, sunward direction, and synthesized beam are the same as described for HCN. The peak flux density per beam in the map is 1.84 Jy/beam. The spectrum is derived from the map in the same fashion as the HCN spectra. The spectral line shows an asymmetric profile with a blueward peak. This feature, similar to the HCN spectral line, is not a function of position in the map.

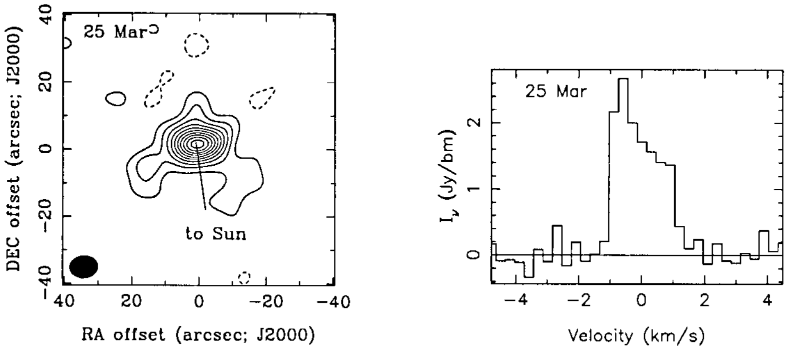

FIGURE 2.10: CS J=2→1 in comet Hale-Bopp observed with the BIMA Array. A map of the transition is shown as well as a spectrum through the data cube at the pixel of peak value in the map. The contours are successive multiples of 3σ, with dashed contours being negative. The 1σ value in the data cube is ~0.15 Jy/bm; in the map it is ~0.06 Jy/bm. The velocity resolution is ~0.30 km/s per channel

The dates and times of the CH_3OH observations can be found in Table 2.2 under the passband 97 GHz. Other transitions included in this passband are given in Table D.5. Figure 2.11 shows a map and spectrum of the CH_3OH emission. The map shows the brightness distribution of CH_3OH in the $J_K = 2_{-1} \rightarrow 1_{-1}$ E, $J_K = 2_0 \rightarrow 1_0$ A^+, $J_K = 2_0 \rightarrow 1_0$ E, and $J_K = 2_1 \rightarrow 1_1$ E transitions. Each of these lines is approximately 7 channels (~2 km/s) wide. The 7 channels were averaged over for each line, and then the four lines were added together. The resulting single channel map is shown. The contours are multiples of 2σ, calculated the same as for HCN, but multiplied by $2/\sqrt{7}$, instead. The coordinates, sunward direction, and synthesized beam are the same as described for HCN. The peak flux density per beam in the map is 1.45 Jy/beam. The spectrum is derived from the map the same way as the spectra for HCN. The spectral lines are not as prominent as the HCN or CS lines; the signal to noise ratio is much lower. The spectrum has been Hanning smoothed with a width of 3 channels and the resulting four lines are located at approximate velocities of -43, -10, 0, and 7 km/s. The apparent intensity enhancement in some lines relative to others may be due to a weak maser in these lines. It is also possible that the stronger lines have only thermal intensity but the intensities of the weaker lines are actually too low due to self-absorption in cooler intervening gas. However, we refrain from any formal interpretation in light of the low signal-to-noise ratio of the data.

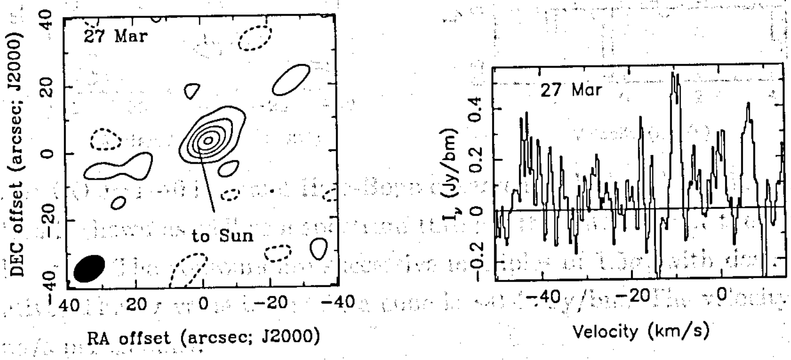

FIGURE 2.11: CH_3OH in comet Hale-Bopp observed with the BIMA Array. A sum map of the $J_K = 2_{-1} \rightarrow 1_{-1}$ E, $J_K = 2_0 \rightarrow 1_0$ A^+, $J_K = 2_0 \rightarrow 1_0$ E, and $J_K = 2_1 \rightarrow 1_1$ E transitions is shown as well as a spectrum through the data cube at the pixel of peak value in the map. The contours are successive multiples of 2σ, with dashed contours being negative. The 1σ value in the data cube is ~0.19 Jy/bm, in the map it is ~0.14. The velocity resolution is ~0.30 km/s per channel. The four lines can be seen in the spectrum at approximate velocities of -43, -10, 0, and 7 km/s. Snyder et al (1999) show a similar spectrum that is averaged over several days; see Appendix F.

The dates and times of the CO observations can be found in Table 2.2 under the passband 115 GHz. CO was observed only in interferometric mode. Other transitions included in this passband are given in Table D.6. Figure 2.12 shows a map and spectrum of CO. The map is emission from the J=1→0 transition. The contours are multiples of 1.5σ, calculated the same as for HCN. The coordinates, sunward direction, and synthesized beam are the same as described for HCN. The peak flux density per beam in the map is 2.02 Jy/beam. The spectrum is derived from the map the same way as the spectra for HCN, but has also been Hanning smoothed with a width of 3 channels. We emphasize the low signal to noise ratio of the CO data.

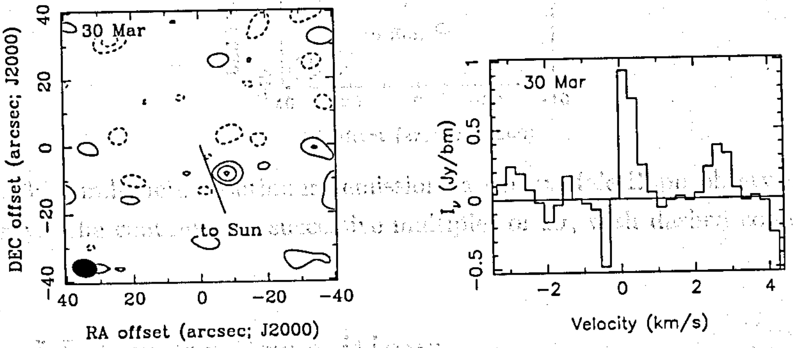

FIGURE 2.12: CO J=1→0 in comet Hale-Bopp observed with the BIMA Array. A map of the transition is shown as well as a spectrum through the data cube at the pixel of peak value in the map. The contours are successive multiples of 1.5σ, with dashed contours being negative. The 1σ value in the data cube is ~0.43 Jy/bm. The velocity resolution is ~0.25 km/s per channel.

2.2.4 Continuum

Observations of 3-millimeter wavelength continuum of comet Hale-Bopp were also carried out with the BIMA Array. The passbands with correlator setups containing windows adapted for continuum observations (see Welch et al. (1996), for a thorough explanation) are 89 GHz, 104 GHz, 109 GHz, 112 GHz, and 115 GHz. The other transitions within these passbands are to be found in Tables D.1, D.7, D.8, D.9, and D.6, respectively. The continuum measurement comes from 8 100 MHz windows of 32 channels each (4 windows in each sideband) for a total of 800 MHz. Figure 2.13 shows continuum emission from comet Hale-Bopp observed with the BIMA Array with a bandwidth of 800 MHz centered at approximately 88.6 GHz. The observation took place on March 18 (see Table 2.2). The contours are successive multiples of 2σ, calculated in the same way as for the HCN maps, except for multiplication by an averaging factor. The coordinates, sunward direction, and synthesized beam are the same as described for HCN. The peak flux density per beam in the map is 0.0115 Jy/beam, with a 1σ value of 0.0015 Jy/beam.

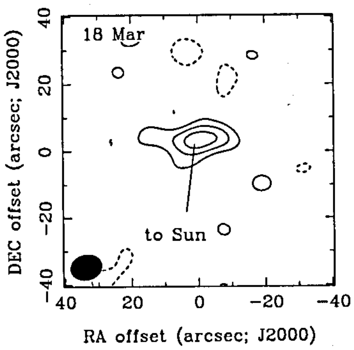

FIGURE 2.13: 3-millimeter continuum emission in comet Hale-Bopp observed with the BIMA Array. The contours are successive multiples of 2σ, with dashed contours being negative.

2.2.5 Other Molecular Transitions

The rest of the transitions in Tables D.1 through D.12 will be analyzed more closely. New detections will be published and nondetections be used for upper limits on column densities and production rates.

Chapter 3

Analysis

3.1 Production Rates and Column Densities

When reporting cometary results, it is useful to present them in terms that are easily compared to results from other research programs. This machinery is already well in place for comets: gas production rates. This is a measure of how many molecules of a species are leaving the surface of the comet per second. The typical gas production rate (R=1 AU) for water is $Q \sim 10^{30}$ s^{-1}. In the very simplest model, a spherical comet nucleus is releasing molecules into the coma with a sublimation rate of s cm^{-2} s^{-1}. This leads to an average surface production rate of

$$Q = 4\pi {r_n}^2 s \tag{3.1}$$

where r_n is the radius of the nucleus. For a gas outflow velocity of v, the number of particles in a spherical shell of radius r and thickness d centered on the nucleus is Qd/v, and the volume of the shell is $4\pi r^2 d$, giving

$$n(r) = \frac{Q}{4\pi r^2 v} \tag{3.2}$$

for the number density. Equation 3.2 can be integrated along the line of sight to arrive at a formula for the brightness distribution of the coma as a function of projected distance from the nucleus. Figure 3.1 shows the relevant geometry, where z represents the line of sight as it passes through the coma, a is the impact parameter, and r is the distance from center

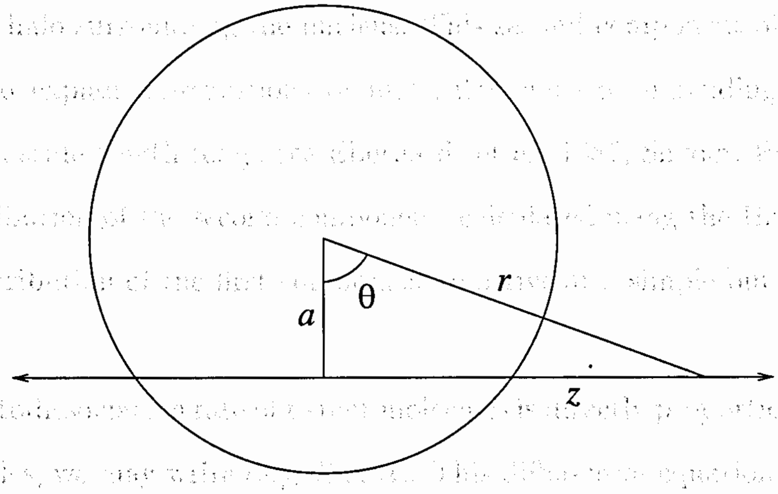

FIGURE 3.1: The geometry relevant to integrating Equation 3.2 along the line of sight.

of the comet nucleus. If a variable substitution from z to θ is incorporated, a very simple integral over θ is left, which leads to

$$N(a) = \frac{Q}{4av}, \tag{3.3}$$

where $N(a)$ is essentially a column density. (Incidentally, $N(r_n)$ is exactly a factor of π greater than the column density going from the nuclear surface radially outward.)

3.1.1 The Haser Method

The Haser model attempts to describe $n(r)$, the number density, and $N(a)$, the column density, while taking into account the fact that as the molecules flow out from the nucleus, they are exposed to solar ultraviolet radiation, resulting in dissociation (Haser 1957). This is the parent-daughter scheme of cometary chemistry, the daughter molecules being dissociation products of the parents. A model of this type is warranted because optically thick effects are thought to be important only within a distance of 100 km of the nucleus. As a result, nearly all of the coma gas is subject to photodissociation and photo-ionization.

There is another scenario in which the machinery of the Haser model is useful: that of the icy grain halo surrounding the nucleus. In this scenario, there are parent molecules sublimating from two different sources: the surface of the comet nucleus, and the surfaces of the grains in the halo surrounding the nucleus. This second component of parent molecules has been used to explain observations of molecular emission extending well beyond the photodissociation scale length (e. g., see Eberhardt et al. 1987, Snyder, Palmer, & de Pater 1989). The distribution of the second component, calculated using the Haser model, can be added to the distribution of the first component to arrive at a simple but more appropriate model.

Since the photodissociation rate of parent molecules is directly proportional to the number of parent molecules, we may write $dn_p/dt \propto n_p$. This differential equation leads us to define a typical lifetime of parent molecules, τ_p. (More specifically, τ_p is the amount of time it takes for 1/e of a sample of molecules to be dissociated by solar radiation.) The typical distance, or scale length, they travel from the surface of the nucleus is then just $\Lambda_p = v\tau_p$. The number density of parent molecules can then be written as

$$n_p(r) = \frac{Q}{4\pi r^2 v}\, e^{-(r-r_n)/\Lambda_p}. \tag{3.4}$$

Integration of $n_p(r)$ along the line of sight gives

$$N_p(a) = \frac{Q}{2\pi v}\, e^{r_n/\Lambda_p} \int_0^\infty \frac{e^{-\sqrt{a^2+z^2}/\Lambda_p}}{a^2+z^2}\, dz, \tag{3.5}$$

where the relation $r^2 = a^2 + z^2$ has been used. Equations 3.4 and 3.5 represent what is commonly called the Haser model for parent molecules. In practice, the latter can be taken one step further and then compared directly to observations. In order to accomplish this, the distribution given by Equation 3.5 must be averaged over the Gaussian synthesized beam centered on the nucleus of the comet. This average is expressed by

$$\langle N_p(a)\rangle = \frac{1}{B}\frac{Q}{2\pi v}\, e^{r_n/\Lambda_p} \int_0^{2\pi} \int_{r_n}^{r(\phi)} \int_0^\infty \frac{e^{-\sqrt{a^2+z^2}/\Lambda_p}}{a^2+z^2}\, dz\; a da\; d\phi. \tag{3.6}$$

Here, the area of the integrated sky region, B, is given by

$$B = \int_0^{2\pi} \int_{r_n}^{r(\phi)} a da\; d\phi \tag{3.7}$$

and the limit $r(\phi)$ is given by

$$r(\phi) = \frac{1}{2} \times \frac{1}{206264.8} \times \frac{{\theta_b}^2 \Delta}{\theta_a - ({\theta_a}^2 - {\theta_b}^2)^{1/2} \cos\phi}. \tag{3.8}$$

In Equation 3.8, Δ is the distance between the comet and the Earth. This equation is simply the representation of an ellipse in polar coordinates with three extra factors: a scale to allow for full-width beam dimensions instead of semi-major axes, a conversion from arcseconds to radians, and a conversion from radians to physical distance through Δ. In the case of a circular synthesized beam, Equation 3.8 reduces to $r = \theta_d \Delta/(2 \times 206264.8)$, where θ_d is the angular diameter in arcseconds of the synthesized beam at half power. The quantity $\langle N_p(a) \rangle$ can be set equal to the observed column density, N_{obs}, which is directly proportional to the area of the observed spectral line. Miao et al. (1996) find

$$N_{obs} = 2.04 \times 10^{20} \left(\frac{W}{\theta_a\ \theta_b}\right) \left[\frac{B(T_k)}{B(T_k) - I_b}\right] \frac{C_{pbr}\ Z\ e^{E_u/T_{rot}}}{g_I\ g_K\ S\ \mu^2\ \nu^3} \quad (\mathrm{cm}^{-2}), \tag{3.9}$$

where $W = \int I_\nu dv$ (Jy beam^{-1} km s^{-1}) is the integrated line intensity, θ_a and θ_b are the full-width half-maximum dimensions of the elliptical synthesized beam (arcsec), $B(T_k)$ is the Planck function, I_b is the total background continuum contribution (usually negligible), C_{pbr} is a scaling factor correcting for the primary beam response, Z is the partition function, E_u is the energy of the upper level of the transition (K), T_{rot} is the rotation temperature of the gas (K), g_I is the reduced nuclear spin weight, g_K is the K-level degeneracy, S is the line strength, μ is the dipole moment (Debye), and ν is the rest frequency (GHz). Finally if we define $\mathcal{N}_p \equiv \langle N_p(a) \rangle / Q$ and solve the equation $\langle N_p(a) \rangle = N_{obs}$ for Q, we arrive at the simple expression

$$Q = \frac{N_{obs}}{\mathcal{N}_p} \tag{3.10}$$

At the very least, the numerical value of $\mathcal{N}_p$ can be found by the usual Monte Carlo integration method.[8] This is not the most efficient method, but with the present state of

---

[8] That is, select a shape of known volume that encompasses the volume over which the function to be integrated is nonzero. Next, generate random numbers to serve as coordinates of points within the shape of the known volume. For each of the points that lie inside the volume to be integrated over, calculate the

computing, neither is it an abuse of processor time. The method is nicely suited to run on Sun workstations, as they have a built in 48-bit random number generator, allowing for a factor of 2^{16} *more* random samples than the usual random number generating routines. The value for Q then found can be compared to values from previous comets and to values found for comet Hale-Bopp from other observatories.

To derive the Haser model for daughter molecules, consider that the number of parent molecules per second crossing the surface of a sphere of radius x is

$$C(x) = Qe^{-(x-r_n)/\Lambda_p}, \tag{3.11}$$

and this number of parent molecules per second crossing the spherical surface decreases – due to photodestruction – as x gets larger. This decrease is simply expressed by $dC(x)/dx$. Consequently, the change in the number of daughter molecules per second crossing the spherical surface as x varies is

$$-\frac{dC(x)}{dx} = \frac{Q}{\Lambda_p}\, e^{-(x-r_n)/\Lambda_p}. \tag{3.12}$$

Note that the change in the number of daughter molecules per second crossing a surface is equal to the number created at that surface. Now, when the daughter molecules produced at a distance x from the nucleus reach a distance of r, their number has been reduced by a factor of $\exp\left[-(r-x)/\Lambda_d\right]$. As a result, the number of daughter molecules per second crossing a spherical surface of radius r that were created in a layer of thickness dx at a radius of x is

$$\frac{Q}{\Lambda_p}\, e^{-(x-r_n)/\Lambda_p}\, e^{-(r-x)/\Lambda_d}\, dx. \tag{3.13}$$

(See Figure 3.2.) Therefore, the number of daughter molecules per second crossing a spherical surface of radius r is

$$\frac{Q}{\Lambda_p}\, e^{r_n/\Lambda_p}\, e^{-r/\Lambda_d} \int_{r_n}^{r} e^{-x(\frac{1}{\Lambda_p}-\frac{1}{\Lambda_d})} dx. \tag{3.14}$$

---

value of the function to be integrated at those coordinates and sum over all the values calculated. This sum, divided by the total number of random points generated within the shape of known volume, is then just the ratio of the sought after value of the integral to the volume of the known shape.

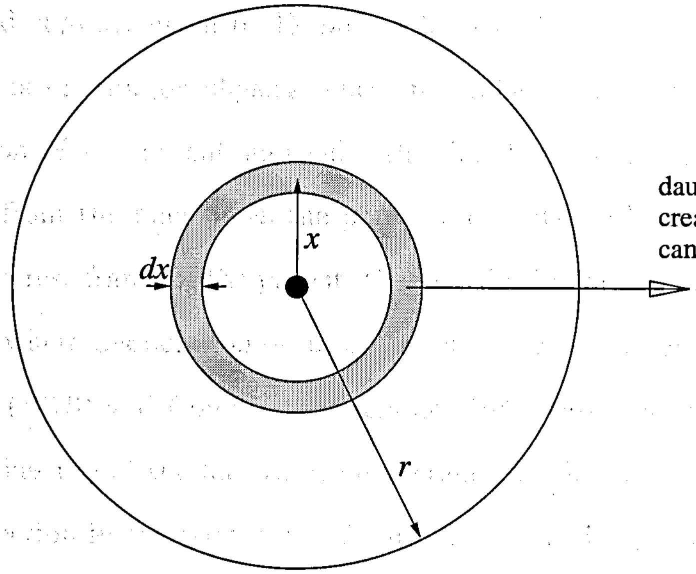

daughter molecules
created within dx
can cross a shell of radius r

FIGURE 3.2: The role of daughter molecules in the Haser model.

Finally, by integrating Equation 3.14 to get the daughter molecule production rate at radius r and by using reasoning similar to that given between Equations 3.1 and 3.2, the resulting number density of daughter molecules is

$$n_d(r) = \frac{Q}{4\pi r^2 v} \frac{\Lambda_d}{\Lambda_p - \Lambda_d} \left[e^{-(r-r_n)/\Lambda_p} - e^{-(r-r_n)/\Lambda_d} \right], \tag{3.15}$$

which can then be integrated along the line of sight to find

$$N_d(a) = \frac{Q}{2\pi v} \frac{\Lambda_d}{\Lambda_p - \Lambda_d} \int_0^\infty \left[e^{-(\sqrt{a^2+z^2}-r_n)/\Lambda_p} - e^{-(\sqrt{a^2+z^2}-r_n)/\Lambda_d} \right] \frac{dz}{a^2+z^2}. \tag{3.16}$$

These last two equations represent what is commonly called the Haser model for daughter molecules. Due to the very similar nature of Equations 3.5 and 3.16, we may write another expression for Q, analogous to Equation 3.10

$$Q = \frac{N_{obs}}{\mathcal{N}_d} \tag{3.17}$$

where N_{obs} is given by Equation 3.9, $\mathcal{N}_d$ is defined similarly to $\mathcal{N}_p$ as $\mathcal{N}_d \equiv \langle N_d(a) \rangle / Q$,

$$\langle N_d(a) \rangle = \frac{1}{B} \frac{Q}{2\pi v} \frac{\Lambda_d}{\Lambda_p - \Lambda_d} \int_0^{2\pi} \int_{r_n}^{r(\phi)} \int_0^\infty \left[e^{-(\sqrt{a^2+z^2}-r_n)/\Lambda_p} - e^{-(\sqrt{a^2+z^2}-r_n)/\Lambda_d} \right] \frac{dz \; a da \; d\phi}{a^2+z^2}, \tag{3.18}$$

and B and $r(\phi)$ are given by Equations 3.7 and 3.8.

There is one major physical effect not taken into account by the Haser model: upon dissociation of the parent molecule, the daughter molecule does not flow out in a radial direction from the nucleus as the parent did. First order models make the approximation that in the rest frame of the parent, the distribution of daughter velocities is isotropic about the point where dissociation occurs. One clever way to take this into account is the method of Festou (1978) and Combi & Delsemme (1980), also known as the vectorial model. This model makes use of the fact that, on average, the daughter velocity is perpendicular to the radial direction in the parent rest frame. This effectively slows down the rate at which the daughter molecules flow out from the nucleus, causing them to spend more time near the nucleus and to be dissociated closer to the nucleus than is predicted by the Haser model. As a result, the photodissociation scale lengths need only be rescaled by a trigonometric factor and then again inserted into the Haser model, which then produces much better agreement with observations. However, even the vectorial model can run into problems if the region of interest is small enough and close enough to the nucleus for the collision zone to become important. (The collision zone is the region near the nucleus where collisions between molecules are frequent enough to dominate the radiative processes). Section 4 of this chapter describes a type of model able to handle complicated scenarios such as this.

3.1.2 Results from the Haser Method

Column densities and production rates for HCN, CS, CO, and CH_3OH have been calculated. The results are given in Table 3.1. The column densities have been found with Equation 3.9, and the parameters used for each species are also shown in Table 3.1. The production rates in the table have been calculated using the Haser method. More specifically, Equation 3.10 has been used in conjunction with Equations 3.6, 3.7, 3.9, and the circular approximation to Equation 3.8.

TABLE 3.1: Production Rates with the Haser Method

	HCN	CS	CO	CH_3OH
W (Jy/bm km/s)	5.905	3.976	0.481	1.176
$\theta_a \times \theta_b$ ($''$)	9.52 × 7.74	8.47 × 6.72	7.44 × 5.39	10.19 × 6.97
C_{pbr}	1	1	1	1
Z	$\sum_{J=0}^{70}(2J+1)e^{-hB_0J(J+1)/kT}$	$\sum_{\text{same}}$	$\sum_{\text{same}}$	$2\left[\frac{\pi(kT)^3}{h^3ABC}\right]^{1/2}$
E_u (K)	4.25352	7.05329	5.53197	12.190
T_{rot} (K)	104	104	104	104
g_I	1	1	1	1
g_K	1	1	1	1
S	1	2	1	$\left[S\mu^2 = 1.617 \right.$
μ (Debye)	2.984594	1.958	0.112	
ν (GHz)	88.631847	97.981007	115.271204	96.74458
N_{obs} (cm^{-2})	1.35×10^{14}	1.88×10^{14}	5.09×10^{15}	3.51×10^{15}
Λ_p (cm)	9.2×10^{9}	1.2×10^{10}	1.6×10^{11}	1.0×10^{10}
Q (s^{-1})	1.46×10^{28}	1.72×10^{28}	3.90×10^{29}	3.79×10^{29}
Q (metric tons s^{-1})	0.7	1.3	18.2	20.3

3.2 Profiling the HCN data

One of the advantages of interferometric data sets is that they reveal something of the source structure even before an image is made. Figure 3.3 shows an amplitude vs. *uv*-distance for the 29 Mar data with error bars. Clearly, the source is resolved, as the points would form a horizontal line if it weren't. Figure 3.3 also shows the same plot for a model *uv* data set, based on what would be measured if the parent molecule distribution were obeying a Haser model (See Section 1.1 of this chapter for details on the model). We see by comparison that since the real *uv* data drop to nearly zero, while the model *uv* data don't, that the HCN emission must not be so narrowly peaked at the nucleus as the model.

Figure 3.4 shows the flux for the 29 Mar HCN data set. The values used to create this figure show the flux collected interferometrically is roughly 27.9 Jy on the 29th of Mar. This is only ~40% of the flux received in autocorrelation mode with the array (Snyder et al. 1999). It is clear from Figure 2.6 that much of the flux is within a region much smaller than the primary beam, yet most must be very smooth on large scales for the interferometer to not detect it. Sources with such odd spatial distribution produce difficulties when trying

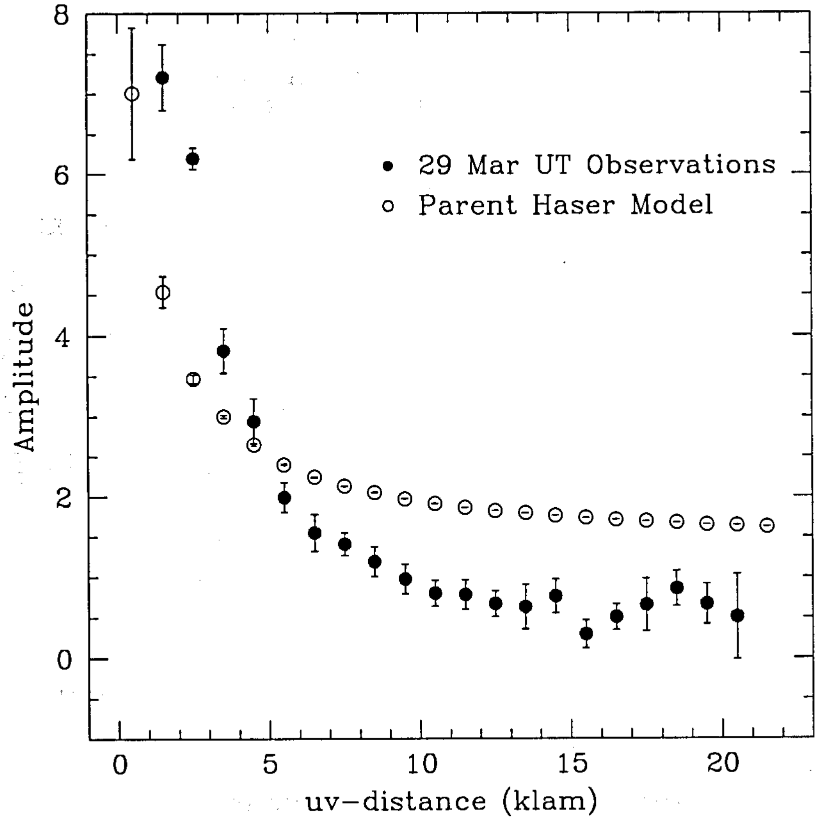

FIGURE 3.3: Comparison of real and model *uv* data sets.

to determine the primary beam dilution factor needed to find T_B. (Recall Section 1.1 of Chapter 2.)

3.3 Evidence of Deviations from Spherical Outflow

In order to explore the deviation of the detected emission from that expected for a spherically symmetric nuclear source, model images were subtracted from several HCN images (Figures 2.6d, 2.6g, 2.6i, 2.6j, and 2.6k) and one CS image (Figure 2.10). The model images were created under the guidelines that follow. According to the Haser model for a spherically symmetric ball of gas expanding at constant velocity in the presence of solar ultraviolet radiation, the column density is given by Equation 3.5 (Haser 1957). We assume the coma is optically thin and the flux density per beam is directly proportional to the column density.

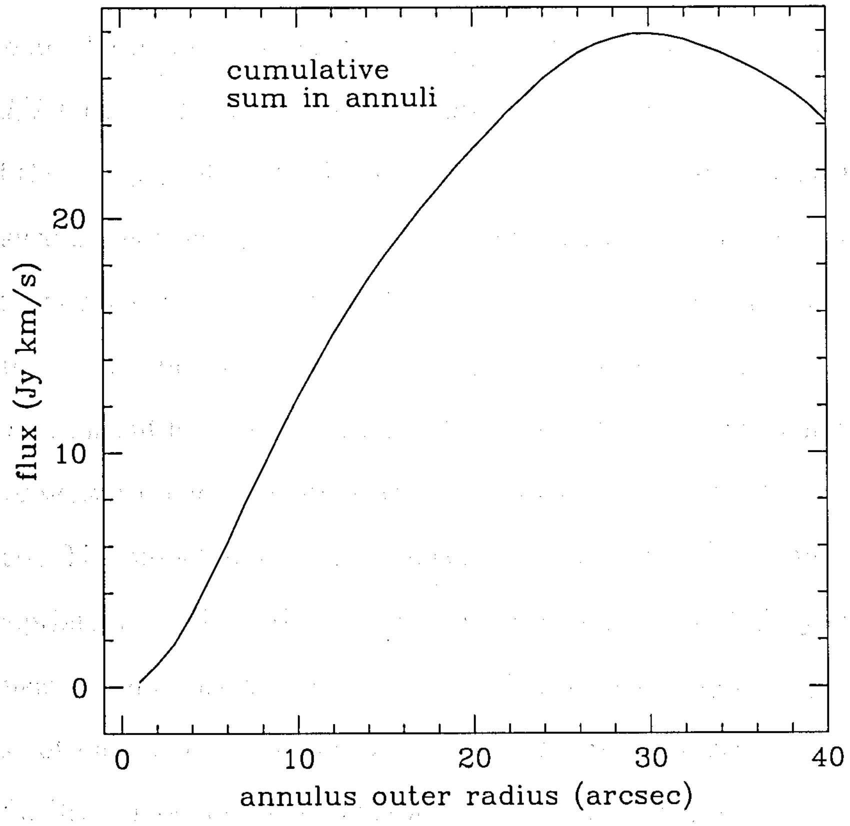

FIGURE 3.4: Measured flux for the 29 Mar HCN data set.

This may be stated as $I(a)/I(r_n) = N(a)/N(r_n)$, where a is the projected distance from the comet nucleus and r_n is the radius of the nucleus. (Also of note is the fact that $I(r_n) = I_{max}$ and $N(r_n) = N_{max}$.) With simple rearrangement of terms and substitution from Equation 3.5, the flux density per beam in the model image as a function of projected distance from the nucleus can be written as

$$I(a) = I_{max} \frac{\int\limits_0^\infty \frac{e^{-\sqrt{a^2+z^2}/\Lambda}}{a^2+z^2}\, dz}{\int\limits_0^\infty \frac{e^{-\sqrt{r_n^2+z^2}/\Lambda}}{r_n^2+z^2}\, dz}, \tag{3.19}$$

where I_{max} is the value of the peak flux density per beam in the map and z is the distance along the line of sight.

In practice, these integrals must be solved numerically. Equation 3.19 was solved for all values of a corresponding to the center of a pixel in the model image, with integration over z

from 0 to 0.1 AU (excepting $a = 0$, where $a = r_n$ was used). The program (given in Appendix G) used to create the model image sets $a = S\sqrt{(i - \Delta i)^2 + (j - \Delta j)^2}$ while looping over i and j from $-d/2 + 1$ to $d/2$, where S is the number of centimeters per pixel, $(\Delta i, \Delta j)$ are the coordinates of the image peak, and d is the number of pixels on one side of the square image. That is, a is successively set equal to the center of each pixel in the image. The values of physical constants ranged as r_n =10, 20, 30 km, $\Lambda_{\mathrm{HCN}} = 4.7 \times 10^9, 7.7 \times 10^9, 9.5 \times 10^9$ cm, and $\Lambda_{\mathrm{CS}} = 10.2 \times 10^9$ cm. These values of Λ_{HCN} correspond to a Sun-comet distance of R=0.916 AU and an outflow velocity range of v=0.8, 1.2, 1.6 km/s. The range in Λ could alternately represent a range in photodestruction rates of 2.0×10^{-5}, 1.3×10^{-5}, 1.0×10^{-5} s^{-1}, respectively. The model image was then convolved with the Gaussian synthesized beam from the appropriate day. The early attempts at this proved to be slightly inaccurate, due to the fact that near the nucleus, where the column density is changing very rapidly, the pixel resolution was not high enough for the convolved model image to accurately represent a true convolution of a Haser model with a Gaussian. To alleviate this problem, all relevant images were regridded with a new linear pixel size of 1/4 the original pixel size. That is, the scale was changed from 1 square arcsecond per pixel to 1/16 of a square arcsecond per pixel. I_{max} was adjusted until the value of the peak in the model image was equal to the peak in the observed image. This final model image was then subtracted from the regridded observed image. A sample MIRIAD script for creating these images may be found in Appendix H.

Figure 3.5 shows the resulting difference maps, where $r_n = 20$ km (after de Pater et al. (1998): given in Appendix I, Weaver (1998), and Fernandez et al. (1998)), $v = 1.2$ km/s (in accordance with our observed autocorrelation and interferometric spectral lines), $\Lambda_{\mathrm{HCN}} = 7.7 \times 10^9$ cm (after Huebner, Keady, & Lyon 1992), and $\Lambda_{\mathrm{CS}} = 10.2 \times 10^9$ cm (A'Hearn 1998). The axes, noise level, and synthesized beam are the same, by date, as for Figure 2.6 described above. The contours are multiples of 2σ. The cross at the middle denotes the location of the HCN peak of the corresponding map in Figure 2.6, and, consequently, the most probable location of the nucleus. The manner in which the distribution of the

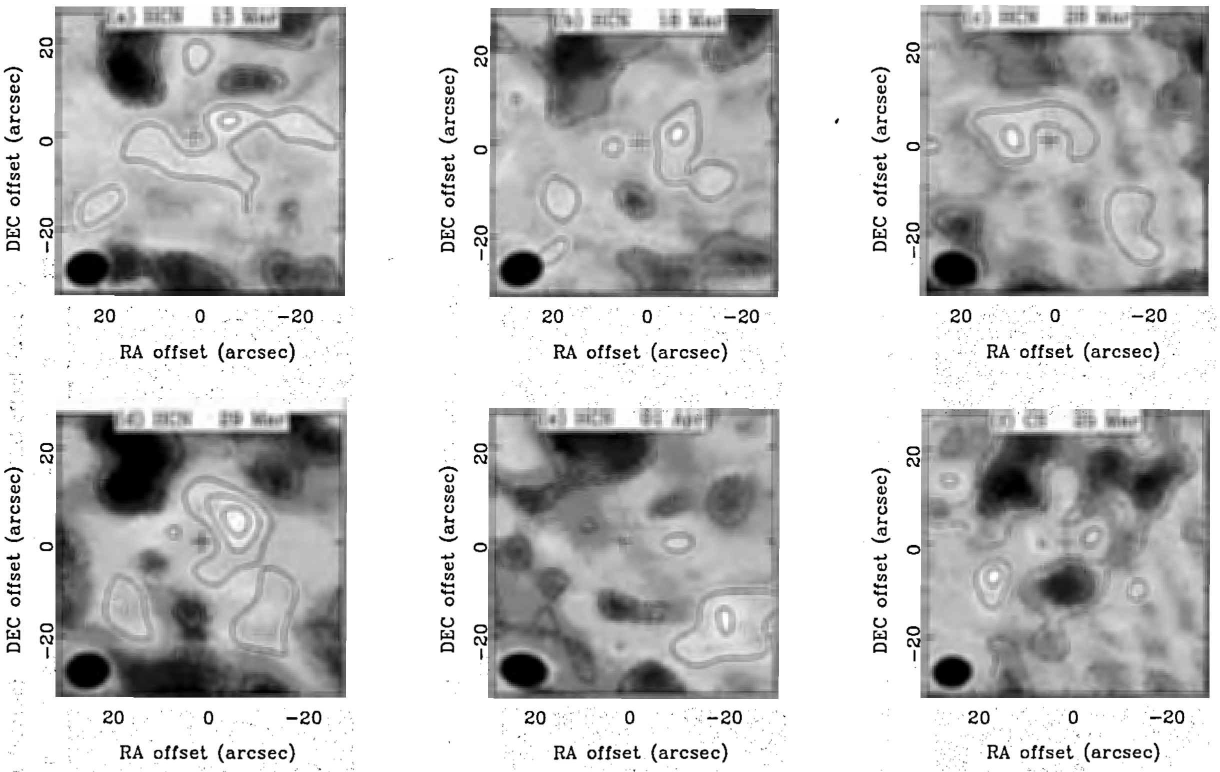

FIGURE 3.5: Difference maps of HCN J=1→0 and CS J=2→1 in C/1995 O1 observed with the BIMA Array. The percentage of flux in (d) due to the excess emission relative to the observed image is ~15%.

excess emission depends on parameters such as r_n, Λ, v, and $1/\tau$ is explored via Figure 3.6. The range over which the values of these parameters vary in the figure is described in the paragraph immediately above. We note that negative contours may be just as indicative of deviations from spherical symmetry as positive contours.

There are several physical scenarios that can be considered in order to investigate what the difference maps are representing. (1) Assume the coma gas is sublimating from the nucleus at a constant rate and in a spherically symmetric manner. In this case, the excess emission in a difference map like Figure 3.5d would be due to a different excitation temperature at the location of the maximum, and not due to a higher column density. To explore this hypothesis, the flux density per beam in Figure 2.6j was measured at two particular points. The first point coincides with the location of the maximum in Figure 3.5d, 7.5″ west and 4.5″ north of the nucleus. The second point in the image is opposite the nucleus from the first. These

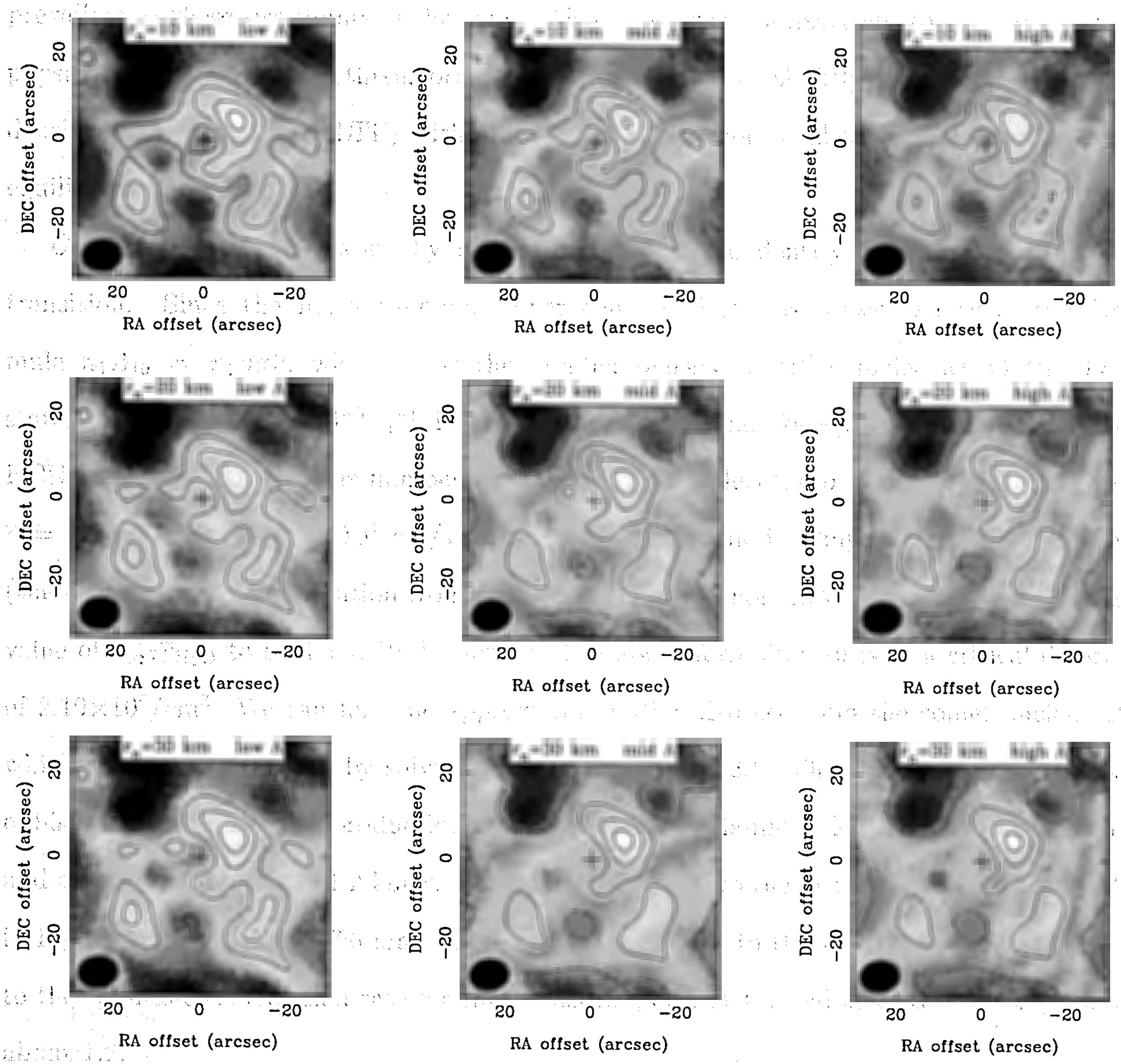

FIGURE 3.6: A set of HCN difference maps for 29 Mar showing variations due to ranging nucleus size and photodestruction scale length. See text for values of Λ and their interpretation. Contours are successive multiples of 2σ.

two points should have roughly the same number density and column density within the guidelines of this first scenario; they have flux densities per beam of 1.09 and 0.71 Jy/bm, respectively. What sort of temperature difference this implies depends upon the physics prevailing at these two points in the coma. There are several approaches to analyzing coma physics. We will consider three, progressing from simple to slightly complicated: critical density, detailed balance (LTE) without stimulated emission or absorption, and statistical equilibrium.

Critical Density. We start by calculating the critical density for the HCN J=1→0 transition. Since the most abundant inner coma molecule is water, we write the formula $n_1 A_{10} = n_1 n \sigma \overline{v}$, where n_1 is the number density of HCN molecules in the J=1 state, $A_{10} = 2.4062 \times 10^{-5}$ s^{-1} is the Einstein coefficient for spontaneous emission of HCN in this transition, n is number density of water molecules, $\sigma = \pi r^2 = 3.14$ Å^2, and $\overline{v} = \sqrt{8kT_k/\pi m} = 3.49 \times 10^4$ cm/s for water at a gas kinetic temperature, T_k, of 104 K (the temperature determination from Bird et al. (1997)). For these quantities, we find the value of $\sigma_{\pi r^2} \overline{v}_{\mathrm{H_2O}}$ to be 1.1×10^{-11} cm^3/s.[9] The above formula results in a critical density of 2.19×10^6/cm^3. We can find the approximate radial distance from the comet nucleus at which this density prevails by solving for r in Equation 3.2.[10] This yields a critical radius of 9530 km, using a water production rate of 3×10^{30}/s (Flammer, Mendis, & Houpis 1998) and an outflow velocity of 1.2 km/s. This is roughly equal to the distance to the excess peak in Figure 3.5d, which is 8750 km. Therefore, a lower limit to the ratio of the collision rate to the spontaneous emission rate for this transition, c/e, at the radius of the excess peak is about 1.2.

It should be noted that though we call this ratio a lower limit, it is a very unlikely lower

---

[9] This is within a factor of 2 of the rate constant of this transition for collisions with low energy He atoms, published by Green & Thaddeus (1974).

[10] The photodestruction exponential factor need not be considered in a first approximation as the total number density of all species mostly drops off due to spherical expansion. If we consider it regardless, the factor varies from 0.94 to 0.89 for r ranging from 5000 km to 10000 km (based on Huebner et al.'s (1992) photorate of 1.2×10^{-5}/s to get $\Lambda_{\mathrm{H_2O}} = 8.4 \times 10^9$ cm).

limit for several reasons. (a) The production rate estimate we used may be too low by a factor of 3, as Meier et al. (1998) estimate $Q_{\mathrm{H_2O}} = (1.0 \pm 0.2) \times 10^{31}$/s from measurements of OH. This would lead to $c/e = 3.9$. (b) The estimate for $\sigma_{\pi r^2}\overline{v}_{\mathrm{H_2O}}$ is probably too small. If we instead use the estimates from Green & Thaddeus (1974) for collisions between HCN molecules and neutral He atoms at T_k = 100 K for HCN transitions J=1 → J≤7, then $\sigma v = 1.184 \times 10^{-10}$ cm^3/s. This would lead to $c/e = 13$. (c) Even the Green & Thaddeus estimate of σv is probably too small. If we adopt the Meier et al. (1998) water collision cross section of $\sigma_{\mathrm{HDO-H_2O}} = 5 \times 10^{-14}$ cm^2, then $\sigma_{\mathrm{HDO-H_2O}}\overline{v}_{\mathrm{H_2O}} = 1.745 \times 10^{-9}$ cm^3/s. This would lead to $c/e = 190$. (d) Here, we combine (a) and (c) by compromising between the two values of $Q_{\mathrm{H_2O}}$ (we use 6.5×10^{30}) and using $\sigma_{\mathrm{HDO-H_2O}}\overline{v}_{\mathrm{H_2O}}$. This gives $c/e = 410$ at a distance of 8750 km from the nucleus in this scenario. (e) Finally, in addition to (d), HCN has a larger dipole moment than water (the dipole moments in Debye of HCN and H_2O are 2.98 and 1.94, respectively), and we would therefore expect $c/e > 410$. Therefore, insofar as the critical density analysis is accurate, collisions are the dominant physical process in the coma of scenario 1 at the locations of the excess emission in Figure 3.5.

Detailed Balance (LTE) without Stimulated Emission or Absorption. If collisions dominate, the stimulated emission rate of the J=1→0 transition can be ignored relative to the collisional de-excitation rate, barring significant optical depth effects from photon trapping. We now try approximating the situation with a detailed balance (LTE) equation for J=1→0 without stimulated emission or absorption.

$$n_0 n \sigma \overline{v} \frac{g_1}{g_0} e^{-h\nu/kT_k} = n_1 A_{10} + n_1 n \sigma \overline{v} \tag{3.20}$$

Here, in addition to the quantities defined for the critical density calculation above, n_0 is the number density of HCN molecules in the J=0 state, and g_1/g_0 is the ratio of statistical weights of the two rotational levels. In this case, since $h\nu \ll kT_k$, the temperature in the Maxwellian $\overline{v}$ dominates and any change in intensity in the map between two points at equal radii from the nucleus must be due to a $\sqrt{T_k}$ factor, since here we are saying the intensity is proportional to n_1. Consequently, in order to produce the intensity shift mentioned above of 0.71 to 1.09 Jy/bm, there must be a kinetic gas temperature shift of factor 2.3. If the typical coma temperature is 104 K (Bird et al. 1997), this may imply a temperature of 240 K at the excess emission peak. However, there are no reports in the literature to date confirming such conspicuous temperature enhancements in this region of the coma.

Before moving on, we illuminate one other aspect of Equation 3.20 by considering three versions of it, one for each of the three hyperfine components of HCN that were observed. If we then take the ratio of these equations, we can determine the relative number densities of the HCN molecules in the three hyperfine states. We find them to be directly proportional to their statistical weights: 1/5/3. This agrees very well with the optically thin approximation of the radio radiative transfer equation $T_B = (T_e - T_b)(1 - e^{-\tau})$, which is $T_B = \tau T_e$. Here T_B is the line brightness temperature, τ is the optical depth, T_e is the excitation temperature, and T_b is the brightness temperature of the background source. For the comet, $T_b \simeq 0$. For the optically thin case, the excitation temperature is the same for all three hyperfine states, and the optical depth is directly proportional to the column density of the states, giving 1/5/3.

Statistical Equilibrium. We now move to a more accurate approach: statistical equilibrium. We assume nothing but a relatively steady state. Consider a set of equations all similar to the following, one for each pair of rotational levels in the HCN molecule.

$$n_u n \sigma_{ul} \overline{v} + n_u A_{ul} + n_u \overline{B}_\nu B_{ul} = n_l n \sigma_{ul} \overline{v} \, \frac{g_u}{g_l} e^{-h\nu/kT_k} + n_l \overline{B}_\nu B_{lu} \qquad (3.21)$$

Here, in addition to the quantities defined for the critical density analysis and for Equation 3.20, $n_u n \sigma_{ul} \overline{v}$ is the collisional de-excitation rate from the upper state to the lower state for HCN-H_2O collisions, $n_u A_{ul}$ is the spontaneous emission rate, $n_u \overline{B}_\nu B_{ul}$ is the stimulated emission rate with $\overline{B}_\nu$ being the directionally averaged radiation field at the frequency of the transition, $n_l n \sigma \overline{v} \, \frac{g_u}{g_l} e^{-h\nu/kT_k}$ is the collisional excitation rate, and $n_l \overline{B}_\nu B_{lu}$ is the absorption rate. A set of these equations for all the possible transitions between states with values of

J≤7 has been evaluated with the help and code of thesis committee member E. C. Sutton. The code does not explicitly solve the set of equations, but rather runs through time steps for the set of equations (of form $dn_i/dt = ...$) and allows the initial guess populations to relax into the final populations ($dn_i/dt \rightarrow 0$). The code was run fifteen times with a line width of 1.2 km/s. The optical depths, τ, and antenna temperatures for the J=1→0 transition are shown in Table 3.2. T_R represents a Rayeigh-Jeans brightness temperature on the sky (no telescope beam characteristics enter). T_k is the gas kinetic temperature, n is the number density of water molecules, and N_{HCN} is the HCN column density. There are several interesting things to notice in Table 3.2. First, the J=1→0 line is in all cases optically thin and therefore must be so for all three of its hyperfine components (in agreement with Crovisier (1987) and Irvine et al. (1998)). Second, for fixed N_{HCN}, an increase in n or T_k results in a lower T_R. When n goes up, the collision rate goes up and the higher J states remain populated without there being enough time for most of the HCN molecules to cascade down to J=1 to allow for the photon of interest to be released. Likewise, when T_k goes up, the average collision has more energy and the higher states are again populated with the same effect. This implies that if scenario 1 demands no density anisotropies, then the excess emission must be due to a cooler region, while the depressions in Figure 3.5 may be produced by warmer regions. However, there is no available evidence in the literature to date to support such ideas of heating and cooling mechanisms necessary for the significant temperature fluctuations within a zone of constant density needed to result in Figure 3.5.

TABLE 3.2: Statistical Equilibrium Calculation Results

	$T_k = 100$ K $n = 2 \times 10^6$ cm^{-3}		$T_k = 100$ K $n = 5 \times 10^6$ cm^{-3}		$T_k = 170$ K $n = 5 \times 10^6$ cm^{-3}	
N_{HCN} (cm^{-2})	τ	T_R (K)	τ	T_R (K)	τ	T_R (K)
3×10^{12}	-0.04	0.9	-0.01	0.6	-0.01	0.5
1×10^{13}	-0.13	2.8	-0.03	1.9	-0.03	1.6
3×10^{13}	-0.27	7.4	-0.09	5.4	-0.10	4.6
1×10^{14}	-0.15	27	-0.16	15.5	-0.26	13.4
3×10^{14}	0.00	46	0.03	39.2	-0.35	34.4

Essentially, the statistical equilibrium analysis tells us that the HCN J=1→0 transition is optically thin, implying that scenario 1 implies that the intensity enhancements in Figure 3.5 are a result of extreme coma temperature fluctuations described in the detailed balance analysis – extreme enough to be unphysical.

In conclusion to scenario 1, we note that the approaches to this scenario have dealt with upper limits on densities; since the excess emission may not be in the plane of the sky, it could therefore be at a greater distance from the nucleus than the projected distance seen in the difference maps. However, we note that while this may be the case, given the likelihood of any point on a spherical shell being equal (and we are thinking of spherically symmetric geometry here), the further from the plane of the sky it is, the less likely it is to appear so close to the nucleus. Hence, we argue that our estimated densities are not severely wrong. Finally, we conclude that scenario 1 is highly improbable and we rule out the possibility that Figure 3.5 can be a result of gas temperature enhancements without any gas density enhancements. The excess emission in the difference maps must be due, in some way, to a gas density enhancement – most likely a combination of density and temperature enhancements.

We now proceed to the second scenario. (2) Assume that the difference maps are a result of some of the HCN being a daughter molecule. This implies that there would be a parent just as abundant near the nucleus as the daughters are further out, giving a very detectable column density. However, there doesn't seem to be any good candidate parent of HCN among the commonly observed cometary molecules. (3) Assume anisotropic outgassing has caused one or more jets, constant in intensity, to emanate from the rotating nucleus. This cannot produce the distribution in Figure 3.5, as there is clear time variability. (4) This scenario is the same as (3) except we assume the anisotropic outgassing is time variable. Again, any jet, while active, will produce a maximum in the flux density per beam in the nuclear region. However, there are two possibilities why this may not be observed. One is if the jet(s) are declining in intensity or inactive at the time the observation begins. Figure 3.5 could be explained by a jet remnant expanding outward at a certain angle with respect to the plane of the sky. If this is the case, one may expect the location of the maximum flux density per beam to move away from the nucleus and the value of the maximum to decrease with time. A slight digression must be made here in order to explore temporal variations.

Temporal variations on an hourly scale in the inner coma are quite common as a result of anisotropic outgassing and rapid rotation of an asymmetric nucleus. These phenomena lead one to ask if Figure 3.5 reflects a relatively static (hourly time scale) configuration of the extended source. Fortunately, the signal-to-noise ratio of the 29 Mar data set is large enough ($s/n \approx 35$) to create Figure 2.9, in which four HCN images, corresponding to successive two-hour time intervals (two just prior to transit and two just following transit) within the 29 Mar data set, are shown (see above text for details). There are many possibilities here, and we will discuss only the two extremes. The first is that the excess gas is moving away from the nucleus on the plane of the sky. In this case, the span of roughly six hours represented by Figure 2.9 combined with an outflow velocity of 1.2 km/s, gives a distance of about 2.6×10^4 km, or $\sim 27''$, from the nucleus. Clearly this would not average to the peak in Figure 3.5d, which is only about 8500 km, or $\sim 9''$, from the nucleus. The second possibility is that the excess gas is moving away from the nucleus nearly perpendicular to the plane of the sky. In this case, we must consider the flux density per beam as a function of time, which should decrease since time translates into free expansion of the anisotropy. The difference maps (not shown) corresponding to the images in Figure 2.9 are too noisy to preclude this possibility.

The second possibility, and the more likely explanation regarding the gas jet phenomenon is that they are the cause, but there is no peak at the nucleus because the model images have been scaled to the maximum in the observed images. Hence, our dataset contains no evidence to eliminate the possiblility of the gas jet explanation, and scenario 4 remains a valid consideration.

(5) Assume the nucleus is a static and spherically symmetric source of icy dust grains that become entrained with the coma gas flowing outward from the nucleus. As the grains absorb solar radiation, they heat up and act as an extended source for sublimation of HCN.

(For examples of work regarding grains in cometary comae, see Jewitt & Matthews (1997), Sarmecanic et al. (1997), de Pater et al. (1997), Williams et al. (1997).) (The idea that emission from grains could radiatively excite the HCN may be dismissed (Crovisier 1987).) The time it takes for the grains to heat up could explain a separation between the nuclear region and the maximum in a difference map, and this scenario should produce a ring like structure around the nuclear region. Or, perhaps if the grains are causing optical depth effects, part of the ring on the far side of the nucleus from the Sun may be wiped out, yet this missing region would be so small that it would probably not be noticeable. In either case, the structure should be symmetric about a comet-Sun line, but the evidence contradicts this. (6) Assume the nucleus is a static and anisotropic source of grains like those in scenario 5. In argument, the level of temporal variability displayed in Figure 3.5 from day to day would seem to conflict with the possibility of this.

(7) There is at least one remaining possibility. The nucleus could be a dynamic and anisotropic source of icy dust grains that are likely to be entrained with the gas in the coma, including jets, flowing out from the nucleus. Figure 3.5 cannot eliminate this scenario. Essentially, this implies that Figure 3.5 is showing maps of the distribution of HCN sublimating from an extended source as opposed to coming directly from the nucleus. It is interesting to note that Eberhardt et al. (1987) found the total amount of CO gas released in concentric shells about the nucleus of comet P/Halley to be a maximum between 8,000 and 10,000 km from the nucleus, and they subsequently propose that CO or a very short-lived parent is released in the coma from cometary dust grains. (We note here that this conclusion is by no means beyond question. See Greenberg & Li (1998).) However, even if the CO set of numbers actually does represent the same physical property of the extended source that we are measuring in our difference maps, any direct comparison would be risky given the history of large variation in characteristics from one comet to the next.

If the excess emission is the result of scenarios 4 or 7, then Figure 3.5d is indicative of a problem with past analyses of HCN production rates. More specifically, the primary beam dilution factor for single-element telescope observations may have been miscalculated due to error in the assumed source distribution. This would lead to column density and production rate estimates that were too large. The extent of this effect on column density and production rate is investigated with a Monte Carlo code in Section 4.2 of this chapter.

3.4 The Monte Carlo Method

As usual, the term "Monte Carlo" refers to nothing more specific than the use of large doses of random numbers in solving problems. This investigation uses a 48-bit random number generator with the linear congruential formula $X_{n+1} = (aX_n + c)_{\text{mod } m}$, where $n \geq 0$, $m = 2^{48}$, $a = 5\text{DEECE66D}_{16} = 273673163155_8$, and $c = \text{B}_{16} = 13_8$. The method of Monte Carlo was first used to calculate production rates in comets by Combi & Delsemme (1980), where they calculated individual trajectories for a large number of parent and daughter molecules and then tallied up numbers of particles in predefined volume elements in the coma in order to find number density and column density. Monte Carlo methods in cometary studies have grown in popularity. The reason for this is not surprising, for they are robust to the point of having no weaknesses, as any number of geometrical asymmetries and temporal variations in several dimensions can be handled effectively. Many studies of cometary comae have been made using the Monte Carlo method, but a new code has been derived and written as part of this thesis to specifically take into account the deviations from spherical symmetry for parent molecules displayed in Figure 3.5.

How does Monte Carlo work? In general, there is more than one method with which to utilize a set of random numbers. Here, we use three, which we will call natural, inverse, and rejection. The natural method is the most straightforward and involves a uniform use of the random samples. A very simple example of this would be to generate a random set of points on a unit circle. If the random number generator produces numbers, Ω, between 0 and 1, then each sample need only be multiplied by a factor of 2π in order to acquire the desired distribution of points. This example uses a probability distribution function with positive arguments only, but it has started us off on the right foot, for throughout the Monte Carlo study, we will only need to use positive probability distributions. In light of this, some of the following explanations have been simplified and are accurate for this scenario only.

The inverse method is more complicated and is based on the following line of reasoning. If we start with a probability distribution function, $f(x)$, then the cumulative normalized probability distribution is given by

$$F(x) = \int_0^x \frac{f(x)}{\int_0^\infty f(x)\,dx}\,dx, \tag{3.22}$$

and it must be true that $0 < F(x) < 1$. Now, if we let our random number be Ω, and say $y = F^{-1}(\Omega)$, then we may write the following explanation of the inverse method:

$$\mathcal{P}\{y < x\} = \mathcal{P}\{F^{-1}(\Omega) < x\} = \mathcal{P}\{\Omega < F(x)\} = F(x). \tag{3.23}$$

Here, we note that expression $\mathcal{P}\{y < x\}$ is read "the probability that y is less than x" and that the last equality is true because Ω is evenly distributed between 0 and 1. Simply put, Equation 3.23 is saying that if we operate with F^{-1} on a homogeneously distributed random number, Ω, to get a new pseudo-random number, then the probability that this new number is less than x is exactly $F(x)$. In other words, a set of these pseudo-random numbers will have a probability distribution function identical to $f(x)$. This means our recipe for generating a set of random numbers with some probability distribution, f, is to operate with F^{-1} on each of our random numbers generated between 0 and 1.

Unfortunately, not all functions are invertible, and the third method, rejection, takes over when this is the case. This method is graphical in nature and relies on the fact that a uniformly distributed set of random points in the area under a given probability distribution curve will have the property that the x values of those random points will have the desired probability distribution. Consider some normalized probability distribution function,[11] $f(x)$ and a second function, $g(x)$, such that $g(x) > f(x)\ \forall\ x$. $g(x)$ must have a finite area under

---

[11] Our use of the symbol "$f(x)$" here is not to be identified with that used above in the discussion of the inverse method.

its curve, though this should not be a problem given the fact that $\int_0^\infty f(x)\,dx = 1$. The next step is to uniformly generate random points in the area under $g(x)$. Each point that lies in the area under $g(x)$ and not in the area under $f(x)$ is rejected, while each point that lies in the area under both curves is accepted. The accepted points then have x values with the desired probability distribution. It is clear that the better $g(x)$ approximates $f(x)$, the more efficient the code is and the shorter its runtime, because the ratio of rejected to accepted points is smaller. So how does one choose an appropriate $g(x)$? As we have said, $f(x)$ need not be invertible. However, $g(x)$ must have an analytically solvable indefinite integral, which itself must be analytically invertible. This allows us to uniformly generate points in the area under $g(x)$. First generate Ω and multiply it by A_{tot}, where A_{tot} is the total area under $g(x)$. Then let $\Omega A_{tot} = A(x) = \int_0^x g(x)\,dx$ and solve for x. This value of $x_\Omega = A^{-1}(\Omega A_{tot})$ is then used as the x-coordinate of the point in the area under $g(x)$. The y-coordinate is then just a new random number multiplied by $g(x_\Omega)$. Hence, when these points are subject to rejection, the leftover x values will be usable.

3.4.1 The Model

The Monte Carlo Phase

The deviations from spherical outflow in the comet, as a result of gas jets or dust jets producing an extended source of gas such as icy grains, can be difficult to model because of the lack of symmetry in three dimensions. The code in this thesis is aimed at modeling these asymmetries – by injecting gas via excess sublimation at specific locations[12] in the space around the nucleus – and calculating $n_p(r)$, $N_p(a)$, and Q under these asymmetric conditions. The Monte Carlo portion of it can be conveniently outlined in a step-by-step fashion by addressing the following six questions. 1) When does the molecule appear? 2) When is the molecule destroyed? 3) Does the molecule sublimate from the nucleus or from

---

[12] The exact location and shape of the model asymmetries is somewhat random by nature of the Monte Carlo method and the random outflow velocity vectors of the sublimation from icy grains. However, the general locations and shapes are determined by model parameters as a result of these velocity vectors having small magnitude relative to the general outflow velocity of gas from the nuclues.

the extended source? 4) If the molecule sublimates from the nucleus, what is its subsequent trajectory? 5) If the molecule sublimates from the extended source, where in the halo does it appear? 6) If the molecule appears in the halo, what is its subsequent trajectory? Points 1, 2, and 4 are identical to the approach of Combi & Delsemme (1980), and a method similar to theirs of addressing these points is used. These six steps are explained in detail below.

Step 1. The time at which the molecule sublimates into the gas phase, t_s, will be between 0 and t_f, the time at which $n_p(r)$ and $N_p(a)$ are tabulated. t_f should be long enough so that a good approximation to a steady state situation is achieved. Using the natural method, we have

$$t_s = \Omega t_f, \tag{3.24}$$

where the symbol, Ω, is used to denote the random number between 0 and 1 that is produced by the generator and will be used so throughout the discussion. At this point, the code continues to the next step.

Step 2. The time, t_d, at which the molecule is destroyed by photodissociation due to solar ultraviolet radiation is generated using the inverse method. Here, $f(x)$ in Equation 3.22 becomes $f(t) \propto e^{-t/\tau_p}$, where τ_p is the photodissociation lifetime. A straightforward calculation[13] leads to $t = F^{-1}(\Omega) = -\tau_p \ln(1-\Omega)$, which becomes

$$t_d = t_s - \tau_p \ln \Omega, \tag{3.25}$$

since $1 - \Omega$ is essentially the same as Ω. If $t_d \geq t_f$, then the molecule in question will contribute to $n_p(r)$ and $N_p(a)$ and the code continues to the next step. If $t_d < t_f$, then the code returns to the first step.

Step 3. Whether the molecule sublimates from the nucleus or from the extended source is determined by the fraction of the total flux coming from the HCN that has sublimated from each source. We will use the ratio of flux in several positive locations in the difference map to the flux in the observed map and call it r_{do}. We then generate another random number. If

---

[13] Simply substitute $f(t) = e^{-t/\tau_p}$ for $f(x)$ in Equation 3.22. As before, we are interested in F^{-1} operating on Ω, or $F^{-1}(\Omega)$. That is, here $F(t) = \Omega$, which we solve for t.

$0 \leq \Omega \leq r_{do}$, then the molecule sublimates from the extended source and the code proceeds to the fifth step. If $r_{do} < \Omega \leq 1$, then the molecule sublimates from the nucleus and the code proceeds to the fourth step.

Step 4. The molecule's trajectory from the nucleus is assumed to be radial. Even though each point on the surface of the nucleus actually offers the molecule 2π steradians of directions from which to choose, this is a valid approximation because the nucleus is small compared to the sizes we are concerned with. For example, consider two trajectories, $\overline{AB}$ that runs radially out from the surface of the nucleus, and $\overline{CD}$ that runs parallel to $\overline{AB}$ but tangential to the surface of the nucleus. If B and D are at a distance of $r \sim 2000$ km, the angle $\angle BAD$ is only 0.57°, for a nucleus with $r_n = 20$ km. And the difference in length between $\overline{AD}$ and $\overline{CD}$ is only $\sim 1\%$. This geometry is approximated in Figure 3.7. Furthermore, we will assume that the radial trajectories are isotropically distributed over the 4π steradians surrounding the nucleus. Now we require two coordinates to uniquely determine a direction and therefore we need two random numbers. The first coordinate, ϕ, is determined with the natural method by

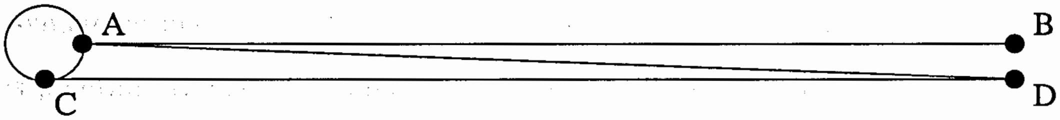

FIGURE 3.7: The geometry relevant to the approximation made in step 4 of the Monte Carlo code.

$$\phi = 2\pi\Omega. \tag{3.26}$$

ϕ may be thought of as measuring an angular coordinate from the x direction in the xy-plane. This would be a plane including the comet, Sun, and Earth, and with $\hat{\mathbf{x}}$ pointing from the comet toward the Sun. The second coordinate is determined by

$$\theta = \arccos(1 - 2\Omega) \tag{3.27}$$

because $\cos\theta$ is uniformly distributed between -1 and 1 for an isotropic distribution. θ may be thought of as measuring an angular coordinate from the z direction, perpendicular to ϕ.

We will define the comet frame as this xyz coordinate system. Given ϕ, θ, and the outflow velocity, v, the position, (x_f, y_f, z_f), of the molecule at t_f is readily determined:

$$\begin{aligned} x_f &= [v(t_f - t_s) + r_n] \sin\theta \cos\phi \\ y_f &= [v(t_f - t_s) + r_n] \sin\theta \sin\phi \\ z_f &= [v(t_f - t_s) + r_n] \cos\theta. \end{aligned} \tag{3.28}$$

Step 5. If the molecule sublimates from the extended source, its initial comet frame position in the halo is determined by three coordinates, (r_s, θ_s, ϕ_s), where, as with t_s, the s subscript stands for "sublimation". The final position in the halo is given, after much development, by Equation 3.43. We will be assuming cylindrical symmetry of each distinct extended source; the symmetry axis points toward the location of excess emission. The axis of this symmetry may be related to the direction toward which the afternoon side of the comet is pointing, though determination probably will best be decided empirically. Under this assumption it will be simplest to handle the situation by performing a coordinate transformation so that a new Z-axis is directed along the axis of symmetry. This transformation and others we will be performing are accomplished with the standard rotation matrices:

$$R_x(\gamma) = \begin{bmatrix} 1 & 0 & 0 \\ 0 & \cos\gamma & \sin\gamma \\ 0 & -\sin\gamma & \cos\gamma \end{bmatrix} \qquad R_y(\gamma) = \begin{bmatrix} \cos\gamma & 0 & -\sin\gamma \\ 0 & 1 & 0 \\ \sin\gamma & 0 & \cos\gamma \end{bmatrix}$$

$$R_z(\gamma) = \begin{bmatrix} \cos\gamma & \sin\gamma & 0 \\ -\sin\gamma & \cos\gamma & 0 \\ 0 & 0 & 1 \end{bmatrix}. \tag{3.29}$$

It should be noted that these standard matrices represent rotations of the coordinate system and that rotations of vectors within the coordinate system are the same except for the γ's being everywhere replaced by $-\gamma$. As a demonstration, Figure 3.8 shows a graphical view of the following equation relating the rotated vector to the original one.

$$\begin{bmatrix} x \\ y \\ z \end{bmatrix} = R_z(-\phi) R_y(-\theta) \begin{bmatrix} 0 \\ 0 \\ 1 \end{bmatrix} \tag{3.30}$$

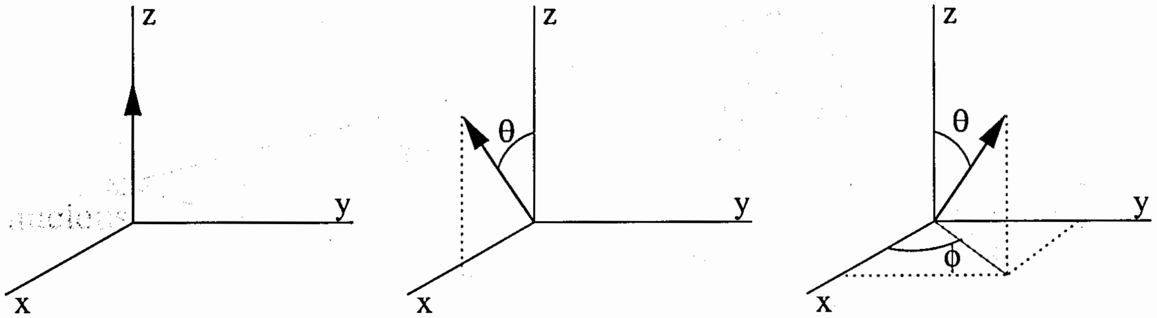

FIGURE 3.8: A graphical view of Equation 3.30. The origin is the comet nucleus. The xy-plane contains the comet, Sun, and Earth, with $\hat{\mathbf{x}}$ pointing from the comet toward the Sun.

Before we actually rotate our z-axis to the new Z-axis (the axis of symmetry), we will first generate the angles designating the symmetry frame position of the location in the halo at which the molecule sublimates into the gas phase, $(r_{sym}, \theta_{sym}, \phi_{sym})$. It is obviously appropriate to use the natural method for ϕ_{sym}:

$$\phi_{sym} = 2\pi\Omega. \tag{3.31}$$

The method by which θ_{sym} is generated depends on the function used to represent the probability distribution. It should be noted that there is no conclusive evidence leading us to pick an exact probability distribution, and it is hoped that future work of some kind may bring this to light. In this case, the probability distribution function has been chosen on a semi-empirical basis and is given, using the natural method, by

$$\theta_{sym} = m\Omega, \tag{3.32}$$

where m is the half angle of the cone. Figure 3.9 shows the resulting probability distribution function in ϕ_{sym} and θ_{sym}.

The next task is to determine how far from the nucleus the sublimation takes place, to find r_{sym}. We note that $r_{sym} = r_s$, since the transformations to determine sublimation location are strictly rotations, and involve no translations. As in choosing θ_{sym}, there is no conclusive evidence to support the specific choice of any one function, and it is again hoped that the future will tell us the answer. The semi-empirically determined, normalized

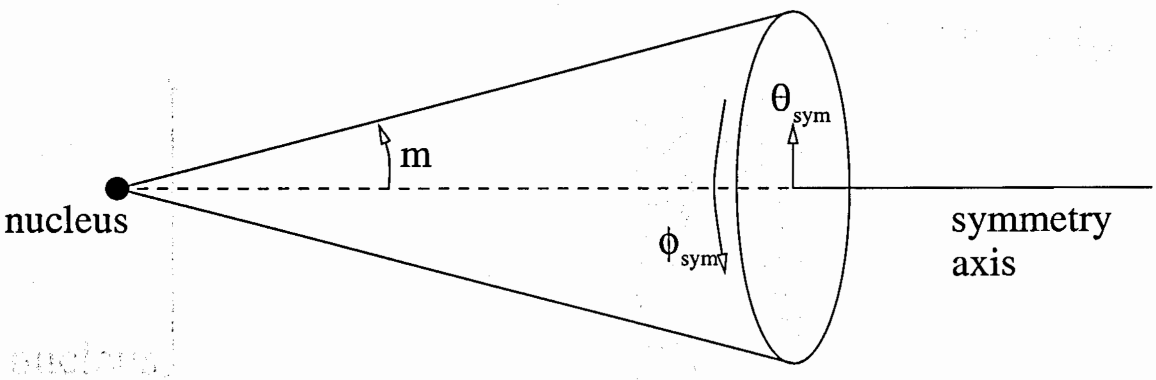

FIGURE 3.9: The ϕ_{sym} and θ_{sym} probability distribution function for the symmetry frame coma sublimation location. We have assumed cylindrical symmetry of each distinct extended source of sublimation; the symmetry axis points from the nucleus to the center of the excess emission.

probability distribution function, $f(r_s)$ and the second function $g(r_s)$, which will be used for the rejection method, are given by

$$f(r_s) = \begin{cases} \frac{r_r - |r_s - r_{max}|}{{r_r}^2}, & (r_{max} - r_r) < r_s < (r_{max} + r_r) \\ 0, & r_s \leq (r_{max} - r_r), (r_{max} + r_r) \leq r_s \end{cases} \quad \text{and} \quad g(r_s) = \frac{1}{r_r}, \tag{3.33}$$

where r_{max} is the distance from the nucleus at which the difference map peaks and r_r is ranging radial distance from r_{max} over which coma sublimation takes place. We note that the inverse method probably would have been feasible for this form, but we feel that one of the first items of business to follow up on this thesis would be to update this function – it is likely that any new function would not be appropriate for the inverse method; hence, we use rejection to make the model easier to build on in the future.

Before we actually apply the rejection method to this function, $f(r_s)$, it is useful to shift it so it is centered at the origin; that is, $r_s \to r_s - r_{max}$ (this places r_{max} at $r_s = 0$ in Fig. 3.10 and makes the computation easier). Then we apply the rejection method and shift back, adding the quantity r_{max} to each accepted value of r_s. The curves $f(r_s)$ and $g(r_s)$ are shown in Figure 3.10. The total area, A_{tot}, under $g(r_s)$ is equal to 2. This leads us, upon inversion of the indefinite integral[14] of $g(r_s)$, to find $r_s = 2r_r\Omega$, where $0 \leq \Omega \leq 1$. However, since we

---

[14] Recall from the above discussion of the rejection method and the indefinite integral of $g(x)$ that $\int_0^x g(x)\,dx = \Omega A_{tot}$.

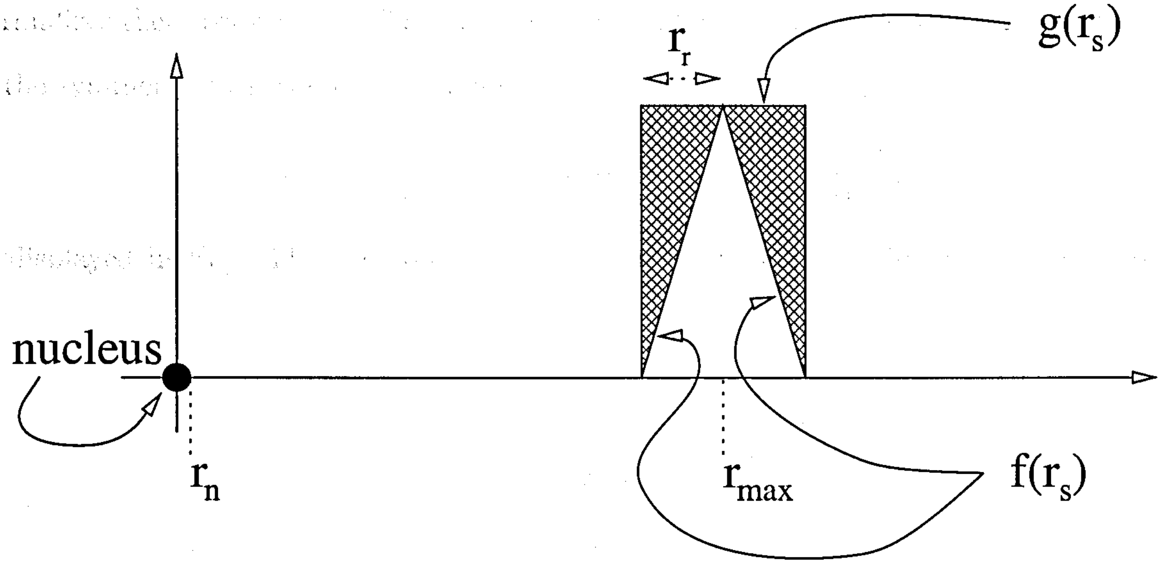

FIGURE 3.10: The rejection method is used for determining the r_s coordinate of the sublimation location in the halo. The shaded area represents the rejected points and the inner white area the accepted points. $f(r_s)$ shows the normalized probability distribution function. Ordinates: $f(r_s)$ and $g(r_s)$. Abscissa: r_s.

are applying rejection to the shifted functions, we have

$$r_s = (2\Omega - 1)r_r. \tag{3.34}$$

These values of r_s will be rejected if, upon generation of another random number, $\Omega g(r_s) > f(r_s)$. We then shift back with the formula

$$r_s \to r_s + r_{max}. \tag{3.35}$$

Now that we have $(r_{sym}(= r_s), \theta_{sym}, \phi_{sym})$, we can find the comet frame direction cosines of the sublimation location with the following relation:

$$\mathbf{\hat{r}_s} = \frac{1}{r_s}\begin{bmatrix} r_{s,x} \\ r_{s,y} \\ r_{s,z} \end{bmatrix} = R_z(-\mu)R_y(-c)R_z(-\phi_{sym})R_y(-\theta_{sym})\begin{bmatrix} 0 \\ 0 \\ 1 \end{bmatrix} = \begin{bmatrix} \cos d \\ \cos e \\ \cos f \end{bmatrix}, \tag{3.36}$$

where $\mathbf{\hat{r}_s}$ is the unit vector in the direction of the comet frame sublimation location, and $\cos d$, $\cos e$, and $\cos f$ are the comet frame direction cosines of the sublimation location. We note that while the direction cosines are normalized in the analytical sense, they are not necessarily normalized in the numerical sense, due to roundoff error. Therefore, the code normalizes them prior to use. The quantity μ is related to the comet frame direction cosines of the symmetry axis, $\cos a$, $\cos b$, and $\cos c$, by

$$\cos\mu = \frac{\cos a}{\sin c} \qquad \text{and} \qquad \sin\mu = \frac{\cos b}{\sin c}, \tag{3.37}$$

as displayed in Fig 3.11. This quantity (μ) is necessary because direction cosines are not linearly independent, but rotation matrices must be. Hence, $\cos a$ and $\cos b$ may be taken care of by $R_z(-\mu)$ as long as $\cos c$ is taken care of by $R_y(-c)$. The quantities c and μ are simply the spherical coordinates of the Z axis in the xyz-space. (Figure 3.12 demonstrates the effect of the $R_z(-\mu)R_y(-c)$ rotations in Equation 3.36 by continuing from Figure 3.8.) The resulting direction cosines are given by:

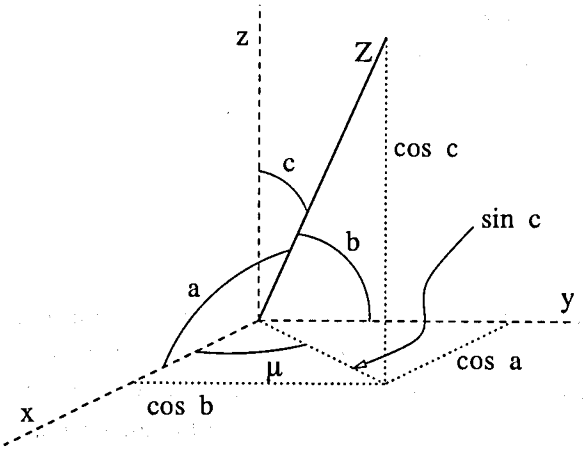

FIGURE 3.11: A graphical demonstration of Equation 3.37, and the comet frame direction cosines of the symmetry axis. The xyz frame is the comet frame with the comet at the origin; the xy-plane is the Sun-comet-Earth plane, with x pointing toward the Sun. Z points along the symmetry axis of the extended source of sublimation.

$$\begin{aligned}
\cos d &= \frac{\sin\theta_{sym}}{\sin c}(-\cos b\sin\phi_{sym} + \cos a\cos c\cos\phi_{sym}) + \cos a\cos\theta_{sym} \\
\cos e &= \frac{\sin\theta_{sym}}{\sin c}(\cos a\sin\phi_{sym} + \cos b\cos c\cos\phi_{sym}) + \cos b\cos\theta_{sym} \\
\cos f &= -\sin c\sin\theta_{sym}\cos\phi_{sym} + \cos c\cos\theta_{sym}.
\end{aligned} \tag{3.38}$$

Before these can be used to finally determine the comet frame sublimation location, they must be normalized for numerical accuracy. That is, each term on the left of the Equation Set 3.38 must be divided by $\sqrt{\cos^2 d + \cos^2 e + \cos^2 f}$ before being multiplied by r_s.

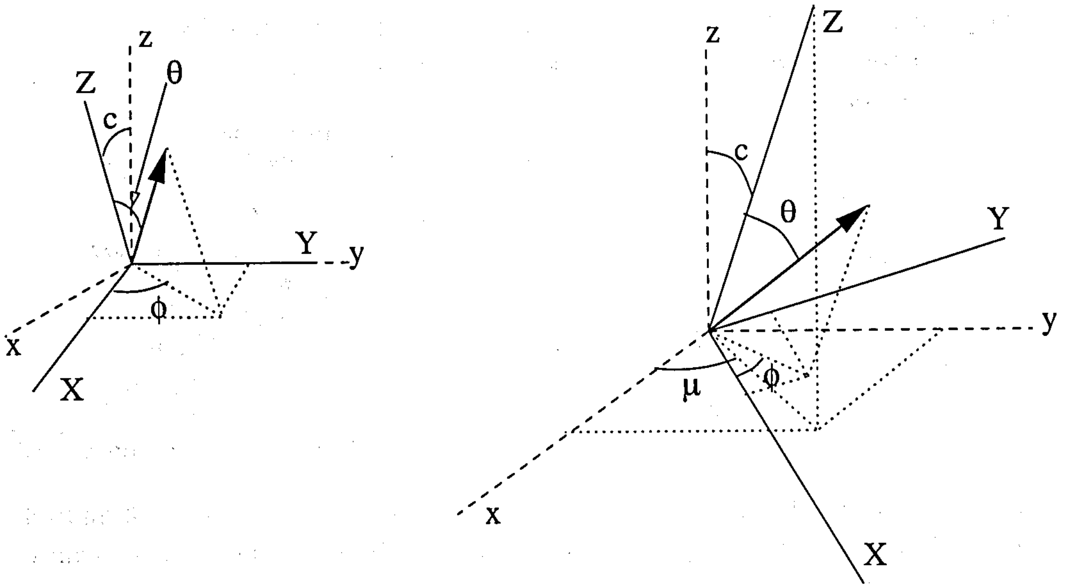

FIGURE 3.12: A graphical demonstration of $R_z(-\mu)R_y(-c)$ in Equation 3.36. The xyz frame is the comet frame with the comet at the origin; the xy-plane is the Sun-comet-Earth plane, with x pointing toward the Sun. The XYZ frame is the symmetry frame; Z points along the symmetry axis of the extended source of sublimation. Note the angles a and b, not shown here, are shown in Fig. 3.11.

Step 6. The direction of the trajectory of the molecule that sublimates from the extended source is determined with Equations 3.27 and 3.26, which we rewrite as

$$\zeta = \arccos(1-2\Omega) \qquad \text{and} \qquad \eta = 2\pi\Omega, \tag{3.39}$$

noting that (ζ,η) measures the same coordinates as (θ,ϕ) in step 4. We assume that the molecule sublimates from a particle moving away from the nucleus in a radial direction, such as a dust grain. The molecule's subsequent trajectory is then assumed to be isotropic in the moving frame of the dust grain, and the direction of the trajectory (which doesn't include the magnitude) is even isotropic in the comet frame. So, let us first find the comet frame direction cosines of the trajectory. This mathematical calculation is the same as in Equation 3.37, and is given here by

$$\begin{bmatrix} \cos g \\ \cos h \\ \cos i \end{bmatrix} = \begin{bmatrix} \sin\zeta\cos\eta \\ \sin\zeta\sin\eta \\ \cos\zeta \end{bmatrix}, \tag{3.40}$$

where $\cos g$, $\cos h$, and $\cos i$ are the comet frame direction cosines of the molecule trajectory, as shown in Fig. 3.13 (see figure caption). Next, we want to know the magnitude of the

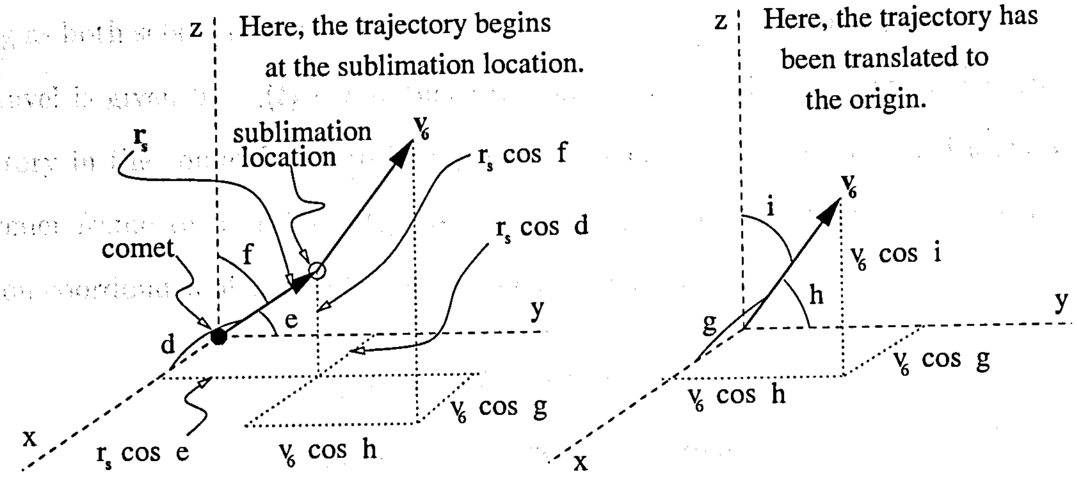

FIGURE 3.13: A graphical demonstration related to Equation 3.40, the only difference being that this display shows the actual vectors, while Equation 3.40 deals with the unit vectors, $\hat{\mathbf{r}}_\mathbf{s}$ and $\hat{\mathbf{v}}_\mathbf{6}$. The xyz frame is the comet frame with the comet at the origin; the xy-plane is the Sun-comet-Earth plane, with x pointing toward the Sun. Here, the vector $\mathbf{r}_\mathbf{s}$ indicates the comet frame sublimation location in the extended source, and the vector $\mathbf{v}_\mathbf{6}$ indicates the molecule's trajectory as it leaves the point at the tip of $\mathbf{r}_\mathbf{s}$.

velocity of this trajectory, v_6, where the 6 subscript stands for step 6. Clearly, v_6 will depend on the angle between the trajectory we have just determined, $\hat{\mathbf{v}}_\mathbf{6}$, and the direction of the vector from the nucleus to the sublimation location, $\hat{\mathbf{r}}_\mathbf{s}$, from Equations 3.36 and 3.38. For example, if $\hat{\mathbf{v}}_\mathbf{6} \parallel \hat{\mathbf{r}}_\mathbf{s}$, then $v_6 = v_e + v_{grain}$, and if $\hat{\mathbf{v}}_\mathbf{6} \parallel -\hat{\mathbf{r}}_\mathbf{s}$, then $v_6 = v_e - v_{grain}$. Here, we assume that the extended source is a halo of dust grains in the coma and each grain moves away from the nucleus at approximately $v/10$ (Grün & Jessberger 1990). v_e is the magnitude of the velocity of the HCN molecule with respect to the grain from which it sublimates and is approximately equal to 3.86×10^4 cm/s.[15] If we call the angle between these two directions ψ, then we may write

$$v_6 = v_e + v_{grain} \cos\psi, \tag{3.41}$$

where

$$\cos\psi = \hat{\mathbf{r}}_\mathbf{s} \cdot \hat{\mathbf{v}}_\mathbf{6} = \cos d \cos g + \cos e \cos h + \cos f \cos i, \tag{3.42}$$

---

[15] We assume that the vapor sublimating from the surface of the grain is in equilibrium with the surface and initially has the same temperature. We also assume the sublimation is controlled by H_2O, causing this temperature to be approximately 190 K (Houpis & Mendis 1981). We then set v_e equal to the average Maxwellian velocity of a gas at this temperature.

as long as both sets of direction cosines are normalized. Therefore, the distance the molecule will travel is given by $v_6(t_f - t_s)$. Since we know the initial xyz-point of the straight line trajectory in the comet frame to be $(r_s \cos d, r_s \cos e, r_s \cos f)$, and the trajectory vector in the comet frame to be $v_6(t_f - t_s)[\cos g\ \hat{\mathbf{x}} + \cos h\ \hat{\mathbf{y}} + \cos i\ \hat{\mathbf{z}}]$, then the xyz comet frame location coordinates of the molecule at time t_f are given by

$$\begin{aligned} x_f &= r_s \cos d + v_6(t_f - t_s) \cos g \\ y_f &= r_s \cos e + v_6(t_f - t_s) \cos h \\ z_f &= r_s \cos f + v_6(t_f - t_s) \cos i. \end{aligned} \tag{3.43}$$

It remains only to use this information to tabulate column densities and production rates.

Extracting Information from the Monte Carlo Phase

In order to calculate column densities, we will start by tallying up the numbers of molecules in each bin, where each bin corresponds to a pixel in one of the observed images. We need to rotate the comet frame coordinate system around $\hat{\mathbf{z}}$ by β (given in the ephemeris in Table K.2) so that $\hat{\mathbf{x}}$ points toward the Earth. This operation is expressed by

$$\begin{bmatrix} x_{new} \\ y_{new} \\ z_{new} \end{bmatrix} = R_z(\beta) \begin{bmatrix} x_f \\ y_f \\ z_f \end{bmatrix}, \tag{3.44}$$

and its purpose is to make the three dimensional distribution of molecules ready for 1) projection onto an image plane and 2) column density calculations. That is, we want to make the distribution look as it does from the Earth, not as it does from the Sun. Equation 3.44 is displayed in Fig 3.14. The image coordinates on the plane of the sky are then just $(x_i, y_i) = (y_{new}, z_{new})$, also shown in Fig 3.14. At this point, the distribution is in image form, but the image axes are based on comet and Sun locations, rather than the more useful right ascension and declination. Hence, these may then be rotated by an angle $-\omega$, where ω is just $\pi/2$+PsAng (from the ephemeris), to give right ascension, α, and declination, δ, in

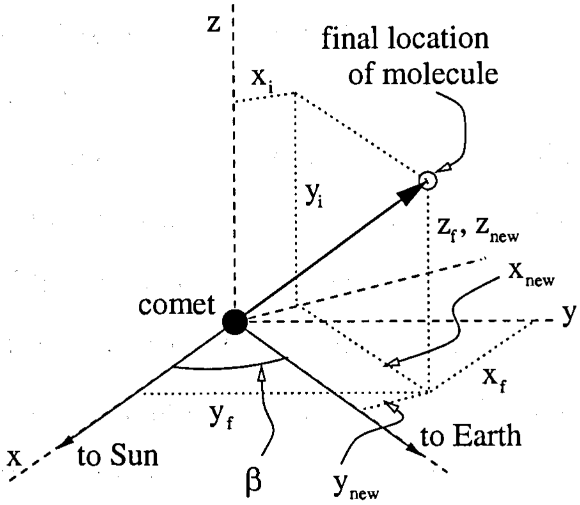

FIGURE 3.14: A graphical demonstration of Equation 3.44 and the preliminary image coordinates. $R_z(\beta)$ moves the x-axis from the comet-Sun direction to the comet-Earth direction. Note that $(x_i, y_i) = (y_{new}, z_{new})$.

the final image. This rotation operation in two dimensions is expressed by

$$\begin{bmatrix} \alpha \\ \delta \end{bmatrix} = \begin{bmatrix} \cos\omega & -\sin\omega \\ \sin\omega & \cos\omega \end{bmatrix} \begin{bmatrix} x_i \\ y_i \end{bmatrix}, \tag{3.45}$$

and is shown in Fig 3.15.

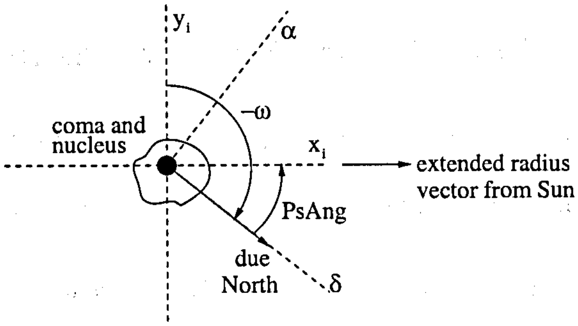

FIGURE 3.15: A graphical demonstration – in the plane of the sky – of Equation 3.45, which deals with the preliminary image coordinates, (x_i, y_i), in Fig. 3.14. PsAng is the phase of the comet (as given in the ephemeris in Appendix C.2). The comet-Earth direction is perpendicular to and out of the page.

If we are to store the image information in an array, we must discretize α and δ; each molecule's image coordinates will take on integer values of S, the number of km/pixel in the observed images. These coordinates, (α_i, δ_i), will then form the basis of an array. Each time a molecule's (α_i, δ_i) is found, the value of the corresponding array pixel will be increased by unity. In this manner, the array will fill up with numbers and arrive at a form appropriate for viewing with an image viewer.

The transition from the image to column densities and production rates is straightforward. First the model parameters must be adjusted so as to make the model image look like the observed image. These parameters and their corresponding equation numbers are t_f (3.24), v (3.28), m (3.32), r_{max} and r_r (3.33), c and μ (3.36), v_e and v_{grain} (3.41), β (3.44), and ω (3.45). Once this is accomplished, the image will be multiplied by a scale factor, F, so the column densities per beam will match the observed column densities per beam determined with Equation 3.9. From here, we find

$$Q = NF/t_f, \tag{3.46}$$

where N is the total number of molecules generated by the code. In summary, this model will use Monte Carlo methodology in creating a theoretical distribution of HCN molecules in the coma, which can then be modified until it fits the observations. This done, the production rate follows immediately. The code may be found in Appendix J.

3.4.2 Results from the Monte Carlo Method

Table 3.3 shows the constants used when running the code to match the HCN observations on 29 Mar. Table 3.4 shows the adjustable values used when running the code to match the HCN observations on 29 Mar. The model gives $Q_{\mathrm{HCN}} = 1.51 \times 10^{28}\ \mathrm{s}^{-1}$ for $r_{do} = 0$ and $N = 10^8$. This is analogous to the Haser model for parent distribution (no excess emission)

TABLE 3.3: Some Constants in the Monte Carlo Code.

$\tau_p = (1.3 \times 10^{-5})^{-1}$ s
$v = 1.2 \times 10^5$ cm/s
$r_n = 2.0 \times 10^6$ cm
$r_{do} = 0.147$
$v_e = \sqrt{8kT/\pi m_{HCN}} = 2.8 \times 10^4$ cm/s (T=190 K)
$v_{grain} = v/10$ cm/s
$N_{obs} = 1.35 \times 10^{14}\ \mathrm{cm}^{-2}$
$S = (1.332\ \mathrm{AU})(1.496\times10^{13}\ \mathrm{cm/AU}) \tan(0.25'')$ cm/pixel

TABLE 3.4: Some Adjustable Parameters in the Monte Carlo Code.

$t_f = 7\tau_p$ s
$\beta = 48.5°$
$\omega = 17.7°$

for excess peaked at $\Delta\alpha = -7.5'', \Delta\delta = 4.5''$:
$m = 60°$
$r_{max} = 8.346 \times 10^8$ cm
$r_r = r_{max}/8$ cm
$c = 160°$
$\mu = 90°$

for excess peaked at $\Delta\alpha = -13.0'', \Delta\delta = -17.0''$:
$m = 30°$
$r_{max} = 2.067 \times 10^9$ cm
$r_r = r_{max}/15$ cm
$c = 110°$
$\mu = -40°$

for excess peaked at $\Delta\alpha = 16.2'', \Delta\delta = -13.4''$:
$m = 5°$
$r_{max} = 2.031 \times 10^9$ cm
$r_r = r_{max}/15$ cm
$c = 30°$
$\mu = -30°$

and agrees well with its values of $Q_{\rm HCN} = 1.46 \times 10^{28}$ s^{-1}, as given in Table 3.1. We believe this agreement between vastly different methods is a mutual confirmation of models and is representative of the success, at a simple level, of both models. Furthermore, the strong similarities between Figures 3.5d and 3.17 indicate that the Monte Carlo model reproduces the observed distribution reasonably well. In light of this, we investigated the extent to which the HCN gas production rate changed when r_{do} was set equal to the ratio of the values of the fluxes in the maps 3.5d and 2.6j. We found $Q_{\rm HCN} = 1.63 \times 10^{28}$ s^{-1} for $r_{do} = 0.147$ and $N = 10^8$. Images are shown for this scenario. Figure 3.16 shows the distribution of particles produced by the Monte Carlo model on the left; contours, in percent of maximum, are .8, 2, 4, 6, 8, 10, 20, 30, 40, 50, 60, 70, 80, 90, and 99. On the right is the same distribution convolved with the Gaussian synthesized beam from the HCN observations on 29 Mar; contours are the same as for Figure 2.6j. Figure 3.17 shows the difference map resulting from a model image

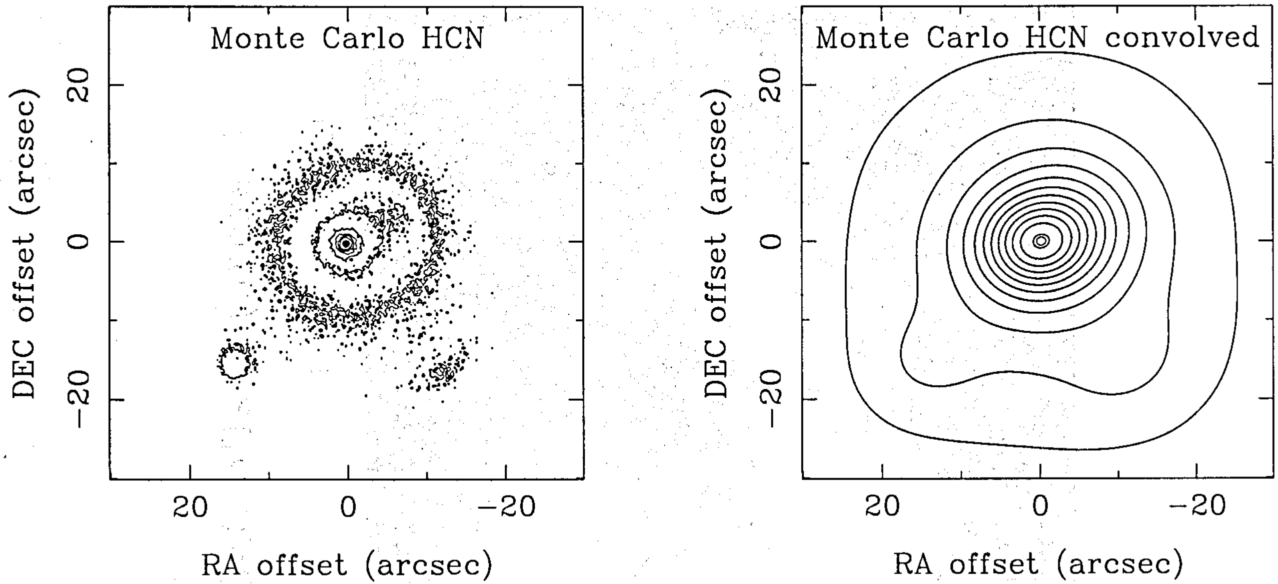

FIGURE 3.16: Model distribution of HCN molecules in comet Hale-Bopp.

being subtracted from the convolved map in Figure 3.16, a process analogous to that which created Figure 3.5d. Figures 3.5d and 3.17 show the same contour levels. This increase in calculated Q_{HCN} may indicate that gas production rate calculations that are based on interferometric observations and the Haser model are systematically to low by a factor on the order of 10% as a result of the excess emission of the type shown in the difference maps in Figure 3.5. This higher value is then closer to the production rate calculated from the autocorrelation data, 1.7×10^{28} s^{-1} (Snyder et al. 1999).

3.5 CN Versus HCN

The issue of whether or not HCN is the parent of CN is a long standing one. Comet Halley (1P/1982 U1) provided and opportunity to consider this question anew, but did not seem to provide any conclusive evidence. Observations of this comet led some researchers to conclude that HCN is not the main parent of CN (Despois et al. 1986), while others believed that HCN should not be ruled out as CN's main parent (Schloerb et al. 1986). A'Hearn et al. (1986) observed Comet Halley as well, and found spiral structures of CN emission. Yet these structures were further from the nucleus than the HCN scale length, implying yet again

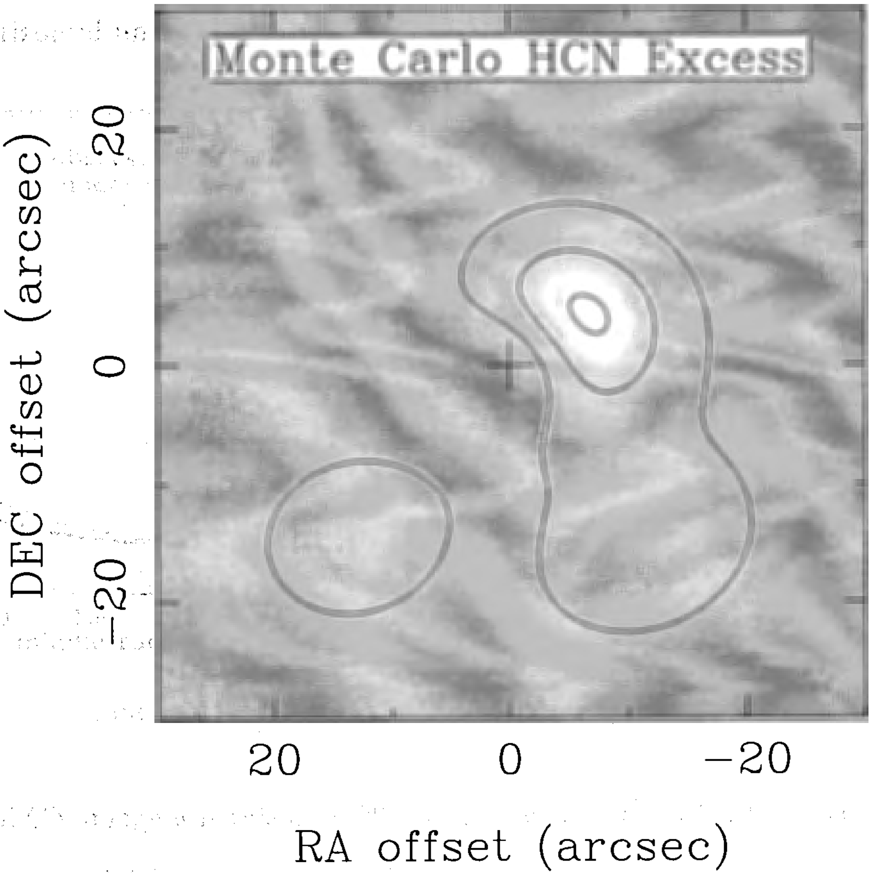

FIGURE 3.17: A Monte Carlo difference map representing the excess emission from the model distribution in Figure 3.16.

another source of CN: dust. We briefly explore the issue in this section.

Figure 3.18 shows the intensity as a function of projected distance from the nucleus for CN observed on 29 Mar in comet Hale-Bopp. Also shown is the same for a model CN distribution, based on the assumption that CN is the daughter of HCN and follows the Haser method. This model intensity distribution is given by

$$I(a) = I_{max}\frac{\int\limits_0^\infty [e^{-(\sqrt{a^2+z^2}-r_n)/\Lambda_p} - e^{-(\sqrt{a^2+z^2}-r_n)/\Lambda_d}]\frac{dz}{a^2+z^2}}{\int\limits_0^\infty [e^{-(\sqrt{{r_n}^2+z^2}-r_n)/\Lambda_p} - e^{-(\sqrt{{r_n}^2+z^2}-r_n)/\Lambda_d}]\frac{dz}{{r_n}^2+z^2}}, \tag{3.47}$$

where I_{max} is the value of the peak flux density per beam in the observed CN image, r_n=20 km, and Λ_p and Λ_d are the photodissociation scale lengths for HCN and CN, respectively. Figure 3.18 also shows $aI(a)$ vs. a for the observations and the model; clearly CN is not sublimating from the nucleus, or else the $aI(a)$ vs. a data points would much more closely resemble a horizontal line.

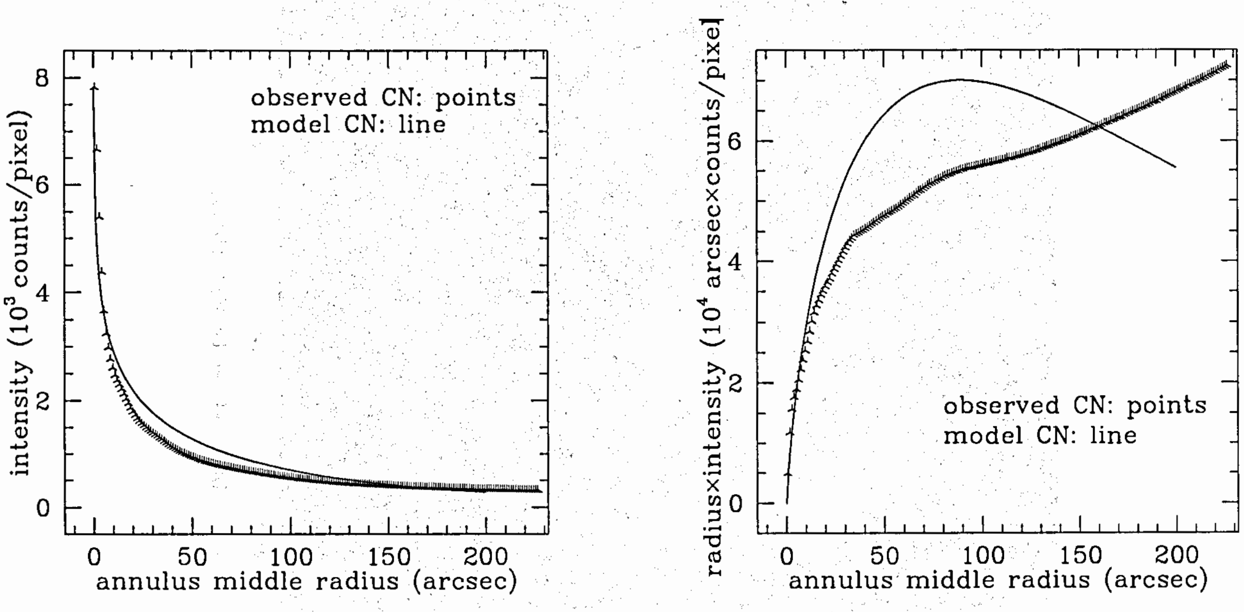

FIGURE 3.18: Intensity and scaled intensity profiles for CN.

An original CN image was taken on 29 Mar at 03:04:30 UT with the Lowell 2048 camera system on the Lowell Observatory 42-inch Hall telescope operating at f/8. The observers on this night were Tony Farnham and Bob Millis. The observing team for the entire run additionally included Laura Woodney, Dave Schleicher, Dennis Wellnitz, Mike A'Hearn, and Alison Sherwin. The plate scale is 1.136″ per pixel. The filter was a narrowband CN filter centered at 3870 Å, for observations of the $B^2\Sigma^+ - X^2\Sigma^+(0-0)R$-Branch. The CN optical image has been processed by subtracting a model image based on Equation 3.47 from the observed image. The resulting image is shown with a square root grey scale in Figure 3.19. The reason for this approach is to bring out the non-sphericity and jet structure of CN. These qualities are clearly seen in a direction to the southwest of the nucleus. The linear scale is 1.136″ per pixel. This leads to a minimum step size from nucleus to first spiral to second spiral of 13,000 km. Along with this, the nucleus had a rotation period near 12 hours, implying this same step size is at most 12 hours, assuming the two spiral sections have come from the same jet. This leads to a minimum outflow velocity of 1,100 km/hour, or 0.3 km/s. This is roughly 1/4 to 1/3 of the HCN outflow velocity based on our observation, implying

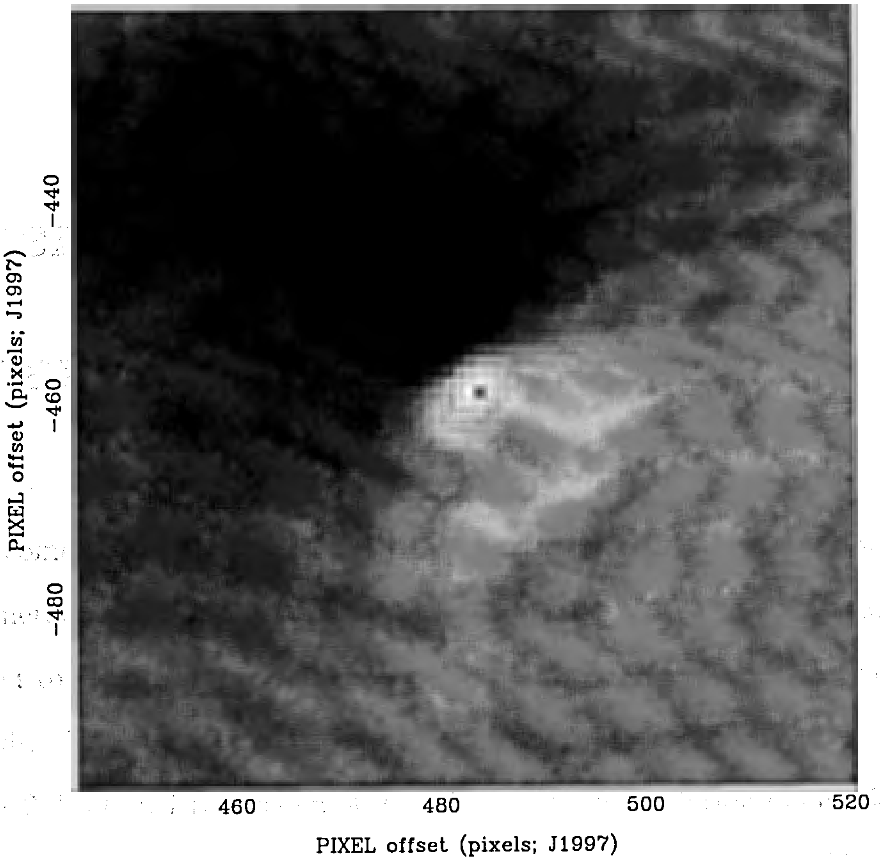

FIGURE 3.19: Processed CN image.

that the spiral structures are indeed CN, and not dust continuum, because the dust moves outward much more slowly. Comparison of the CN excess in Figure 3.19 to the HCN excess on the same day in Figure 3.5d, we see that the two distributions do not coincide at all, allowing us to conclude that our observations of HCN do not resolve the mystery of the parent of CN.

Chapter 4

Summary

We observed comet Hale-Bopp with the BIMA Array in the late winter and early spring of 1997. Numerous correlator setups, observe command files, and data reduction scripts were developed to facilitate successful research in both interferometric and autocorrelation observing modes. The run at Hat Creek was a tremendous success.

In Chapter 2, Section 1 reports on observations in autocorrelation mode. Several spectra of HCO^+ are present, including the signals constituting the discovery of this ion in comets. Several spectra of HCN are also present, showing the distinct double peaked profiles indicative of emission from a resolved, spherically expanding shell. CS was also detected. Time variation on a weekly scale is displayed for all three species, showing a general trend of increasing brightness as the comet approaches the Sun.

Section 2 of Chapter 2 reports on observations in interferometric mode. Twelve days worth of HCN maps and spectra are presented. The spectra tend to show blueward peaks, as a result of the high angular resolution focusing in on collimated anisotropic outgassing near the nucleus. The maps show changes in the emission distribution on a daily scale. Time variation in intensity is also displayed on a weekly scale, showing a general trend of increasing brightness as the comet approaches the Sun. Changes in intensity on an hourly scale are also explored, with strong evidence displayed. HCO^+ did not produce any strong image signals, and we infer that the spatial distribution is relatively smooth. CS, CH_3OH, and CO were also detected, and a sample image and spectrum of each is displayed along with a map of 3 mm continuum.

In Chapter 3, Section 1 reformulates the Haser model within the framework of the thesis and presents column densities and gas production rates for HCN, CS, CH_3OH, and CO through its use. These calculations give rise to abundances of HCN, CS, and CH_3OH relative to water of 0.2%, 0.5%, and 2%, respectively.

Section 3 of Chapter 3 reveals evidence of deviations from spherical outflow of HCN and lays out arguments justifying why an extended source of sublimation is the likely cause. The arguments are made on the bases of (1) statistical equilibrium calculations and (2) logical refutation of initially plausible scenarios that might produce the evidence in consideration. The evidence takes form with a new technique we have developed for analyzing high angular resolution images: the "difference map". Essentially, this results from the subtraction of a Haser model parent distribution from an observed image. The appearance of significant amounts of emission in these difference maps – as much as 15% of the observed interferometric flux – is the foundation of this section.

Section 4 of Chapter 3 responds to the weakness of the Haser model regarding the deviations from sphericity. We have developed a Monte Carlo code to model the anisotropic, three-dimensional distribution of the HCN molecules in comet Hale-Bopp on 1998 Mar 29 UT. The "Monte Carlo difference map" produced as a result agrees with the observed difference map, confirming the utility of this straightforward but powerful method. Production rates determined from the Monte Carlo model agree very well with those of the Haser model when the excess emission is left out of the calculation. With the excess emission included in the model, the production rate increases by $\sim$10%, revealing an inaccuracy in the Haser model of this order.

Finally, a more refined presentation of the interferometric HCN data is given in Appendix K, which contains the manuscript accepted for publication in the Astronomical Journal.

Appendix A

BIMA array observations of comet Hyakutake: upper limit to the 2.7 mm continuum emission

Pergamon

Planet. Space Sci., Vol. 45, No. 6, pp. 731–734, 1997

0032–0633/97 $17.00+0.00

PII: S0032–0633(97)00078–0

BIMA array observations of comet Hyakutake: upper limit to the 2.7 mm continuum emission

Imke de Pater,[1] Lewis E. Snyder,[2] David M. Mehringer,[3] Melvyn Wright,[1] Jeffrey M. Veal,[2] Yanga R. Fernández,[5] Patrick Palmer[4] and Michael F. A'Hearn[5]

[1]Astronomy Department, 601 Campbell Hall, University of California, Berkeley, CA 94720, U.S.A.
[2]Department of Astronomy, 103 Astronomy Bldg., 1002 W. Green St., University of Illinois, Urbana, IL 61801, U.S.A.
[3]Caltech, Downs Laboratory of Physics, MC 320-47, Pasadena, CA 91125, U.S.A.
[4]Department of Astronomy and Astrophysics, 5640 S. Ellis, University of Chicago, Chicago, IL 60637, U.S.A.
[5]Astronomy Department, University of Maryland, Baltimore, Maryland, U.S.A.

Received 16 December 1996; accepted 24 February 1997

Abstract. Comet Hyakutake (C/1996 B2) was observed with the BIMA array at a wavelength of 2.7 mm. An upper limit of 6.3 mJy per beam is reported, which, if all due to thermal emission from the nucleus of the comet itself, translates into an upper limit of 2.5 km for the comet's radius. The results are compared with detections at sub-mm wavelengths (Jewitt and Matthews, *Astron. J.* **113**, 1145–1151, 1997), and the likelihood of detecting comet Hale–Bopp at mm–cm wavelengths is commented on. © 1997 Elsevier Science Ltd

Introduction

All solid bodies at finite temperature emit thermal radiation. The flux density depends upon the temperature of the object, its size and emissivity. In addition, at radio wavelengths the temperature structure with depth, which depends upon the composition and compactness of the material, is important; as well as the precise radio opacity (loss tangent) of the material, which determines how deep one probes. One typically probes about ten wavelengths deep into a solid body's crust, and much deeper if the crust is made up of pure water-ice. Thus one samples layers in a comet's nucleus which are at least a few centimeters below the surface at millimeter wavelengths. If the object is surrounded by particles, these particles may contribute measurably to the radio brightness, even if the particles are too small to be opaque at radio wavelengths. What matters is the effective cross section and optical depth of the coma within a radio beam, which are determined by the composition, shape, and size spectrum of the particles.

In 1983 we utilized the VLA (Very Large Array) to search for thermal emission from comet IRAS–Araki–Alcock (de Pater *et al.*, 1985) at wavelengths of 2 and 6 cm. Despite the comet's close proximity to Earth (0.035 AU), we did not detect any emission. Altenhoff *et al.* (1983) reported a positive detection of this comet with the MPIfR 100 m telescope in Effelsberg, Germany at a wavelength of 1.3 cm. The two data sets combined suggested either the presence of a halo of relatively large particles (which was also suggested by the detection of radar echoes (Goldstein *et al.*, 1984)), or a steep temperature gradient in the comet's nucleus (de Pater *et al.*, 1985). All other attempts with the VLA to detect a comet's thermal emission at wavelengths of 2–6 cm have yielded negative results: comet Austin (Snyder *et al.*, 1983), comet Crommelin (Schenewerk *et al.*, 1986), and comet Halley (Hoban and Baum, 1987). In addition, upper limits of comet Halley and four other comets observed at Effelsberg at wavelengths of 1–3 cm were reported by Altenhoff *et al.* (1986), while the same authors report a positive detection of comet Halley at 86, 226 and 250 GHz with the 30 m IRAM telescope (Altenhoff *et al.*, 1989). They measured Halley's flux density to be 5.9 ± 1.4 mJy at 86 GHz, 52 ± 15 mJy at 226 GHz, and 51.6 ± 5.2 mJy at 250 GHz. Since the intensity is too high to be explained by thermal emission from the nucleus alone, while the flux densities do follow a ν^2 dependence as expected from macroscopic bodies emitting thermal radiation, the authors suggest the radiation to be caused by thermal emission from a halo of relatively large ($\gtrsim$cm-sized) particles surrounding the comet.

Several telescopes have been used to observe the continuum emission from comet Hyakutake. The comet was detected at sub-mm wavelengths (Jewitt and Matthews,

---

Correspondence to: I. de Pater

1997), while upper limits were reported at wavelengths of 0.2–3.6 cm (Jewitt and Matthews, 1997; Altenhoff *et al.*, 1996; Fernandez *et al.*, 1997; Minter and Langston, 1996). We note explicitly the low upper limits of 0.25 mJy and 23 μJy obtained with the VLA at 1.3 and 3.6 cm, respectively, reported by Altenhoff *et al.* (1996) and Fernandez *et al.* (1997). In this paper we report further limits to the radio emission of comet Hyakutake, obtained with the BIMA (Berkeley–Illinois–Maryland Association) array at a wavelength of 2.7 mm.

Observations

We observed comet Hyakutake (C/1996 B2) on March 24–26, 1996 (see Table 1) with the BIMA array, which consists of nine 6 m dishes and is located at the Hat Creek Radio Observatory in northern California. The instrument is described in detail by Welch *et al.* (1996). The comet's average geocentric distance during this time was 0.104 AU. The observations were carried out at frequencies of 107.5 (lower sideband) and 111.5 GHz (upper sideband) simultaneously, with a bandwidth of 625 MHz each. We combined the data, so the effective frequency is 109.5 GHz. The ephemeris used at the time of the observations (Yeomans' orbit solutions 16 and 18) was compared to the "a posteriori" ephemeris (Yeomans, 1996). The positional offset is typically less than 2″, while the smearing induced due to positional inaccuracies is $\lesssim 0.7''$ in RA and $\lesssim 1.5''$ in Dec. The smearing is less than our synthesized beam width of 5″ and would reduce the flux of a point source by $\lesssim 13\%$. However, because no signal was detected, we did not attempt to correct for these errors. Absolute calibration was performed using the radio sources 3C345, 3C273 and 1800+784, whose flux densities were determined from observations of planets at short baselines. The flux scale is accurate to 20%. After the data were edited and calibrated, we made a series of images of each sideband and day separately, which all yielded negative results. We made natural weighted images, where each point in *uv*-coordinates is weighted according to the number of *uv*-datapoints per gridcell. This weighting weighs the short spacings in the data most heavily, and is best for detection experiments. A natural weighted image in which all data were combined, shows an r.m.s. noise of 2.1 mJy per beam, which translates into a 3σ upper limit for the comet's flux density of 6.3 mJy. The beam width (HPFW) of 5″ corresponds to 375 km at the comet at its mean geocentric distance, which is far larger than the expected size of a comet's nucleus (typically a few km), but smaller than the size of an "icy grain" or large-particle halo (typically $\lesssim$ a few thousand km).

TABLE A.1: Observations

Date (UT)	α (J2000)	δ (J2000)	Δ (AU)	R (AU)
24 Mar 06^h start:	14^{h}42^m	41°	0.107	1.064
–24 Mar 11^h end:	14^{h}40^m	44°	0.106	1.060
25 Mar 04^h start:	14^{h}32^m	57°	0.102	1.045
–24 Mar 16^h end:	14^{h}22^m	66°	0.102	1.034
25 Mar 20^h start:	14^{h}17^m	69°	0.103	1.031
–26 Mar 04^h end:	14^{h}01^m	75°	0.106	1.024

Discussion

Nucleus

The equilibrium temperature, T_{eq}, for a rapidly rotating body at a heliocentric distance of 1 AU, Bond albedo $A_b = 0.04$ (i.e. Halley's albedo) and infrared emissivity of 0.9 is equal to 285 K ($T_{eq} = \mathscr{F}_{\odot}(1-A_b)/4\epsilon\sigma)^{1/4}$, with $\mathscr{F}_{\odot}$ the solar constant). This temperature is equal to the body's physical temperature below the diurnal solar heating wave. The surface temperature, T_s, at the subsolar point $T_s \approx 4^{1/4} T_{eq} \approx 400$ K. A clump of ice at this distance, however, is at the sublimation temperature of water-ice, which is 195 K (Delsemme, 1982). Since a comet consists of a mixture of water-ice and refractory materials, the average surface temperature is likely somewhere in between. Since we probe subsurface layers, we use a temperature $T = 195$ K in this paper. Using the Planck radiation law, our upper limit of 6.3 mJy yields an upper limit to the radius of the nucleus $R = 2.5$ km, assuming a radio emissivity of unity and $T = 195$ K (a higher temperature would translate into a smaller value for the radius; i.e. $T = 220$ K gives $R = 2.4$ km). This number is essentially equal to the upper limit derived from the 3.6 cm VLA data (Fernandez *et al.*, 1997), and is in good agreement with the radar measurement of 1 km for the comet's radius (Harmon *et al.*, 1996).

Halo

Jewitt and Matthews (1997) observed comet Hyakutake at sub-mm wavelengths with the JCMT, and detected emission at four wavelengths ranging from 350 μm up to 1.1 mm. At these wavelengths, one is sensitive to thermal emission from both the nucleus and relatively large ($\gtrsim$ several tens of μm, e.g. de Pater *et al.* (1985)) dust grains in a halo around the nucleus. To model their data, Jewitt and Matthews scaled the flux density to a common beam width of 16″ (i.e. 1200 km at the comet), which should include most, if not all, of the comet's halo. To compare our results with the sub-mm observations, we tapered our data to produce an image with a resolution of 16″. We note that the reduction in the flux density of a point source due to the positional smearing in this low-resolution image is $\lesssim 2\%$. The r.m.s. noise in this image is 6.5 mJy per beam, which results in a 3σ upper limit of 20 mJy. Note that the r.m.s. noise increases by a factor of three after tapering: this is a consequence of the array's relative lack of sensitivity to objects that are "too large" because of over-resolution.

Figure 1 shows a spectrum from 350 μm up to 3 mm wavelength, where the data points from Jewitt and Matthews (1997) are indicated by open symbols, and the BIMA upper limit by a filled circle. The four short wavelength JCMT data points were fitted with a power law $S \propto \nu^q$ (S is flux density, and ν the frequency), and it was found that $q = 2.8$ gave an excellent fit to the JCMT data.

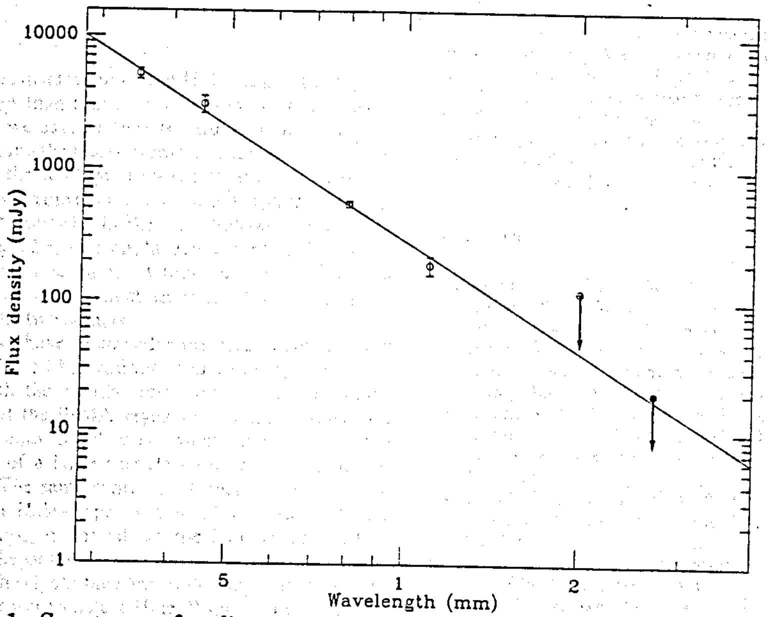

FIGURE A.1: Spectrum of radio emission from comet Hyakutake. The data points with open symbols are from the JCMT; the solid circle is the BIMA upper limit. The line is the best fit through the JCMT detections ($S \propto \nu^{2.8}$).

For thermal black body emission from a large object, q should be equal to 2 (Planck radiation law in the Rayleigh Jeans limit), while for Rayleigh scattering by small particles $q = 4$. Jewitt and Matthews (1997) wrote this same proportionality in a slightly different form: $S \propto B_\nu(T)\nu^\beta$, where β is referred to as the opacity index, and $B_\nu(T)$ is the brightness of a black body radiator. They obtained $\beta = 0.89 \pm 0.10$, a value in between that for a large black body radiator ($\beta = 0$) and Rayleigh scattering by small particles ($\beta = 2$), which led to their conclusion that the sub-mm emission originates from a distribution of relatively large ($\gtrsim$ sub-mm-sized) particles. We note that our 3σ upper limit of 20 mJy falls exactly along the JCMT curve. The VLA data points from Fernandez *et al.* (1997) should also be scaled to an angular size of 16″ to compare their data to this curve. This implies that the quoted 3σ upper limits of 0.25 mJy at 1.3 cm and 23 μJy at 3.6 cm should be increased, probably by a factor of $\gtrsim 5$ and $\gtrsim 2$, respectively. The flux densities predicted from the JCMT curve would be 0.2 mJy at 1.3 cm and 13 μJy at 3.6 cm, very close to the 3σ upper limits for the untapered VLA data. Hence, the VLA upper limits do not provide significant constraints for emission from the halo.

Whipple (1951) shows that there must be a maximum size for particles to be dragged off the surface with the subliming gas, which for a comet with a 1 km radius at Earth's orbit is ~20 cm (de Pater *et al.*, 1985). Observationally, the presence of such large grains in Hyakutake's halo is expected from the radar observations by Harmon *et al.* (1996). The latter authors detected the coma at a wavelength of 3.6 cm, with a radar cross section an order of magnitude higher than that of the nucleus. So there must be cm-sized material in the comet's coma. However, whether the size distribution of such grains follows the same power law as derived from observations at shorter wavelengths is not known. A comparison of the size distribution of the various sized particles (micron–submillimeter–centimeter) must contain information on the ejection mechanisms of such material. Unfortunately, our 2.7 mm upper limit of 20 mJy for comet Hyakutake is not sensitive enough to determine an upper limit to the size distribution of cometary grains; the VLA data are even less sensitive, as mentioned above.

Expectations for comet Hale–Bopp

Nucleus

Comet Hale–Bopp is expected to be "the comet of the century". Estimates of its size range up to over 100 km. Closest approach is on 1997 March 22, with a geocentric distance $\Delta = 1.31$ AU (Yeomans, 1996). The equilibrium surface temperature for Hale–Bopp at perigee, assuming a rapidly rotating body with an albedo of 0.04, is ~300 K. However, as mentioned above, the temperature is more likely determined by the sublimation temperature of water-ice, which is ~195 K. If we assume a radius of 25 km and a temperature of 195 K, the flux density expected at a wavelength of 2.7 mm is 3.7 mJy, and at 3.6 cm it is 22 μJy. Hence, the thermal emission from the nucleus of Hale–Bopp may be detected by both BIMA and the VLA if the radius of the nucleus is larger than 25 km.

Halo

The geocentric distance of comet Hale–Bopp at perigee is 13 times larger than that of comet Hyakutake at closest approach. If we assume that the number of grains per square cm (along the line of sight) in a comet's halo scales linearly with the total gas production rate, i.e. with the surface area of a comet's nucleus ($\propto R^2$), and that the size distribution of particles in the halo follows a power law $S \propto v^q$ with $q \approx 2.8$, one could argue that if the radius of Hale–Bopp's nucleus is 13 times larger than that of Hyakutake, we would detect an equal flux density from the halos of the two comets.

In reality we have to consider the array configuration at the time of the observations, and compare the size of the coma with the angular resolution of the telescope. At the time of the BIMA Hyakutake observations, our synthesized beam of 5″ was much smaller than the expected size of a large-particle halo for Hyakutake at $\Delta = 0.1$ AU. The same synthesized beam of 5″ scales to ~ 5000 km for Hale–Bopp at $\Delta = 1.3$ AU, which should encompass most, if not all, of the halo in contrast to our Hyakutake observations. Thus, if we assume equal sensitivity in the Hyakutake and Hale–Bopp BIMA observations, we expect to detect Hale–Bopp's halo if the flux density is larger than three times the r.m.s. noise in the images, i.e. $\gtrsim 6.3$ mJy for a 5″ beam. If the radius of Hyakutake's nucleus is indeed 1 km (Harmon *et al.*, 1996), we expect that the halo of comet Hale–Bopp should be detectable with BIMA in the C-array if its radius is larger than 8 km.

At the time of Hale–Bopp's closest approach, the VLA will be in the B-array, with a synthesized beam of $\sim 1''$ at a wavelength of 3.6 cm. The 3σ upper limit of 23 μJy for Hyakutake (Fernandez *et al.*, 1997) was taken in the VLA C-array, i.e. for an angular resolution of 2.5″. If we degrade the resolution for both the Hyakutake and Hale–Bopp observations by a factor of 5, the r.m.s. noise will increase by a factor of ~ 2, increasing the 3σ upper limit from 23 up to $\sim 50\,\mu$Jy. This implies that comet Hale–Bopp should be at least ~ 50 km in diameter for thermal emission from the coma to be detectable at the VLA in observations of equal sensitivity to those made for Hyakutake.

Despite the many failures to detect thermal emission from comets at mm–cm wavelengths, we strongly encourage multi-wavelength studies of the continuum emission from comet Hale–Bopp. This comet may provide us with an opportunity to detect the halo's emission at mm–cm wavelengths. Such observations, combined with data at sub-mm wavelengths, are necessary to determine the size distribution and possible limits to the particle size of large ($\gtrsim$sub-mm sized) grains in cometary halos. Not much is known about such large grains, and data on all grain sizes are needed to further develop models of cometary nuclei, a key ingredient for theories on planetary formation.

Acknowledgements. We greatly appreciate the help of W. Hoffman, D. K. Yeomans and C. Acton for their help in preparing the comet ephemerides for the BIMA array. We further like to thank D. Jewitt and B. Butler for comments and communication of their own data. We acknowledge partial financial support from NASA Grant NAGW-1131 to the University of Illinois. The BIMA Array is supported by funds from the University of California at Berkeley, the University of Illinois at Urbana–Champaign, the University of Maryland at College Park, and the National Science Foundation through Grants Nos AST 93-20238, AST 93-20239, AST 93-14847.

References

Altenhoff, W. J., Bartla, W., Huchtmeier, W. K., Schmidt, J., Stumpff, P. and Walmsley, M. (1983) Radio observations of comet 1983d. *Astron. Astrophys.* **125**, L19–L22.

Altenhoff, W. J., Huchtmeier, W. K., Schmidt, J., Schraml, J. P. and Thum, C. (1986) Radio continuum observations of Comet Halley. *Astron. Astrophys.* **164**, 227–230.

Altenhoff, W. J., Huchtmeier, W. K., Kreysa, E., Schmidt, J., Schraml, J. P. and Thum, C. (1989) Radio continuum observations of Comet P/Halley at 250 GHz. *Astron. Astrophys.* **222**, 2323–2328.

Altenhoff, W. J., Bieging, J. H., Butler, B., Chini, R., Haslam, C. G. T., Kreysa, E., Martin, R. N., Mauersberger, R., McMullin, J. P., Sievers, A., Schmidt, J., Stumpff, P., Thum, C., von Kap-herr, A., Wiesemeyer, H., Wink, J. E. and Zylka, R. (1996) Simultaneous radio continuum observations of comet Hyakutake. *BAAS* **28**, 928–929.

Delsemme, A. H. (1982) Chemical composition of cometary nuclei. In *Comets*, ed. L. Wilkening, pp. 85–130. University of Arizona Press, Tucson, Arizona.

de Pater, I., Wade, C. M., Houpis, H. L. F. and Palmer, P. (1985) The non-detection of continuum radiation from comet IRAS–Araki–Alcock at 2- to 6-cm wavelengths and its implication on the icy grain halo theory. *Icarus* **62**, 349–359.

Fernández, Y. R., Kundu, A., Lisse, C. M. and A'Hearn, M. F. (1997) X-Band VLA observations of comet Hyakutake (C/1996 B2) and implications for nuclear properties. *Planet. Space Sci.* **45**, 735–739.

Goldstein, R. M., Jurgens, R. F. and Sekanina, Z. (1984) A radar study of comet Iras–Araki–Alcock 1983d. *Astron. J.* **89**, 1745–1754.

Harmon, W. K., Ostro, S. J., Rosema, K. D., Jurgens, R. F., Winkler, R., Yeomans, D. K., Choate, D., Benner, L. A. M., Cormier, R., Giorgini, J. D., Mitchell, D. L., Rose, R., Slade, M. A. and Thomas, M. L. (1996) Radar echoes from comet Hyakutake (C/1996 B2). *BAAS* **28**, 1195.

Hoban, S. and Baum, S. (1987) A VLA search for 2-cm continuum radiation from comet Halley. *Icarus* **70**, 264–268.

Jewitt, D. C. and Matthews, H. E. (1997) Submillimeter continuum observations of comet Hyakutake (1996 B2). *Astron. J.* **113**, 1145–1151.

Minter, A. H. and Langston, G. (1996) 8.35 and 14.35 GHz continuum observations of comet Hyakutake C/1996 B2. *Astrophys. J. Lett.* **467**, L37–L40.

Schenewerk, M., Palmer, P., Snyder, L. E. and de Pater, I. (1986) VLA limits for comets Austin (1982 VI) and p/Crommelin (1983n): evidence for a diffuse OH halo. *Astron. J.* **92**, 166–170.

Snyder, L. E., Palmer, P. and Wade, C. M. (1983) An upper limit to the microwave-continuum radiation from comet Austin (1982g). *Astrophys. J. Lett.* **269**, L21–L23.

Welch, W. J. (1996) The Berkeley–Illinois–Maryland-Association Millimeter Array. *PASP* **108**, 93–103.

Whipple, F. L. (1951) A comet model. II. Physical relations for comets and meteors. *Astrophys. J.* **113**, 464–474.

Yeomans, D. K. (1996) Ephemerides of comets Hyakutake and Hale-Bopp, Private commun.

Appendix B

Autocorrelation Data: Molecular Transitions, Acquisition, and Reduction

Below are the molecular transitions observed in autocorrelation mode, as well as one example each of an observe command file, a data reduction script, and a correlator setup. In this case, the end result is an autocorrelation spectrum of HCO^+ in the $J=1\rightarrow0$ transition. Autocorrelation observations employ frequency switching; this is the reason for two correlator setups, which are shown in Figure B.1.

B.1 Molecular Transitions

TABLE B.1: 89 GHz Autocorrelation Passband Molecular Transitions[a]

Species	Transition	Rest Freq.	Targeted
U		85.067	
C_6H	$^2\Pi_{1/2}$ J=61/2→59/2	85.1311	
OCS	J=7→6	85.139108	
C_3H_2	$J_{K_-,K_+}=2_{1,2}\rightarrow1_{0,1}$	85.338905	
HCS^+	J=2→1	85.3479	
HCN	J=1→0 F=1→1	88.630415	✓
HCN	J=1→0 F=2→1	88.631847	✓
HCN	J=1→0 F=0→1	88.633936	✓
C_5H	$^2\Pi_{3/2}$ J=37/2→35/2	88.91414	
U		88.916	
C_5H	$^2\Pi_{3/2}$ J=37/2→35/2	88.91619	
U		89.084	
HCN	J=1→0 ℓ=0 F=1→1 ν_2=2	89.08653	
HCN	J=1→0 ℓ=0 F=2→1 ν_2=2	89.08792	
HCN	J=1→0 ℓ=0 F=0→1 ν_2=2	89.09013	
^{29}SiS	J=5→4	89.10373	
HC_7N	J=79→78	89.1046	
HCO^+	J=1→0	89.188518	✓

[a] for observations in Table 2.1 indicated by [a]

TABLE B.2: 89 GHz Autocorrelation Passband Molecular Transitions[a]

Species	Transition	Rest Freq.	Targeted
HCN	J=1→0 F=1→1	88.630415	✓
HCN	J=1→0 F=2→1	88.631847	✓
HCN	J=1→0 F=0→1	88.633936	✓
$HCOOCH_3$	$J_{K_-,K_+}=7_{1,6}\rightarrow6_{1,5}$ A	88.8516	
U		88.861	
$H^{15}NC$	J=1→0	88.865692	
HCO^+	J=1→0	89.188518	✓
CH_2CHCN	$J_{K_-,K_+}=10_{1,10}\rightarrow9_{1,9}$	92.42626	
U		92.456	
C_3S	J=16→15	92.48849	
^{13}CS	J=2→1	92.494299	

[a] for observations in Table 2.1 indicated by [b]

TABLE B.3: 98 GHz Autocorrelation Passband Molecular Transitions[a]

Species	Transition	Rest Freq.	Targeted
U		93.844	
CH_3OCH_3	$J_{K_-,K_+}=4_{2,3}\rightarrow 4_{1,4}$ AE+EA	93.85444	
CH_3OCH_3	$J_{K_-,K_+}=4_{2,3}\rightarrow 4_{1,4}$ EE	93.85711	
CH_3OCH_3	$J_{K_-,K_+}=4_{2,3}\rightarrow 4_{1,4}$ AA	93.85964	
C_4H	$^2\Pi_{1/2}$ J=19/2→17/2	93.8633	
C_2S	J,N=8,7→7,6	93.870101	
NH_2CHO	$J_{K_-,K_+}=3_{2,2}\rightarrow 4_{1,3}$	93.8717	
U		94.175	
U		94.195	
U		97.569	
U		97.5747	
U		97.5779	
CH_3OH	$J_K=2_1\rightarrow 1_1$ A^-	97.58283	
U		97.5978	
SO_2	$J_{K_-,K_+}=7_{3,5}\rightarrow 8_{2,6}$	97.702359	
^{34}SO	$J_K=3_2\rightarrow 2_1$	97.715388	
U		97.7294	
CS	J=2→1	97.980968	✓
U		97.9911	
U		97.9938	
ℓ-C_3H	$^2\Pi_{1/2}$ J=9/2→7/2 F=5→4	97.995166	
ℓ-C_3H	$^2\Pi_{1/2}$ J=9/2→7/2 F=4→3	97.995213	
ℓ-C_3H	$^2\Pi_{1/2}$ J=9/2→7/2b	97.99545	

[a] for observations in Table 2.1 indicated by [c]

TABLE B.4: 98 GHz Autocorrelation Passband Molecular Transitions[a]

Species	Transition	Rest Freq.	Targeted
CH_3CH_2OH	$J_{K_-,K_+}=13_{7,7}\rightarrow14_{6,8}$?[b]	93.81263	
CH_3CH_2OH	$J_{K_-,K_+}=13_{7,6}\rightarrow14_{6,9}$?[b]	93.81315	
SO_2	$J_{K_-,K_+}=23_{6,18}\rightarrow24_{5,19}$	94.064779	
U		94.077	
U		94.195	
U		94.2	
U		94.473	
U		94.486	
U		94.499	
U		97.293	
$Si^{13}CC$	$J_{K_-,K_+}=4_{1,3}\rightarrow3_{1,2}$	97.29548	
OCS	$J=8\rightarrow7$	97.301208	√
U		97.569	
U		97.5747	
U		97.5779	
CH_3OH	$J_K=2_1\rightarrow1_1$ A^-	97.58283	
SO_2	$J_{K_-,K_+}=7_{3,5}\rightarrow8_{2,6}$	97.702359	
^{34}SO	$J_K=3_2\rightarrow2_1$	97.715388	
CS	$J=2\rightarrow1$	97.980968	√
U		97.9911	
U		97.9938	
ℓ-C_3H	$^2\Pi_{1/2}$ $J=9/2\rightarrow7/2$ $F=5\rightarrow4$	97.995166	
ℓ-C_3H	$^2\Pi_{1/2}$ $J=9/2\rightarrow7/2$ $F=4\rightarrow3$	97.995213	
ℓ-C_3H	$^2\Pi_{1/2}$ $J=9/2\rightarrow7/2b$	97.99545	

[a] for observations in Table 2.1 indicated by [d]

[b] ? indicates an uncertain identification

TABLE B.5: 85 GHz Autocorrelation Passband Molecular Transitions

Species	Transition	Rest Freq.	Targeted
HC_3N	$J=9\rightarrow8$	81.881468	
HC_3N	$J=9\rightarrow8$ $\nu_7=1$ $\ell=1e$	82.08273	
C_3H_2	$J_{K_-,K_+}=2_{0,2}\rightarrow1_{1,1}$	82.093559	√
CH_3CH_2OH	$J_{K_-,K_+}=3_{2,2}\rightarrow3_{1,3}$	82.11566	
$^{34}SO_2$	$J_{K_-,K_+}=10_{1,9}\rightarrow9_{2,8}$	82.124322	
U		82.472	
U		85.33	
C_3H_2	$J_{K_-,K_+}=2_{1,2}\rightarrow1_{0,1}$	85.338905	√
HCS^+	$J=2\rightarrow1$	85.3479	
$HCOOCH_3$	$J_{K_-,K_+}=4_{2,3}\rightarrow3_{1,2}$ E	85.63844	
SiO	$J=2\rightarrow1$ $\nu=2$	85.640456	
$HCOOCH_3$	$J_{K_-,K_+}=4_{2,3}\rightarrow3_{1.2}$ A	85.65563	
C_3H_2	$J_{K_-,K_+}=4_{3,2}\rightarrow4_{2,3}$	85.656422	√
C_4H	$N=9\rightarrow8$ $J=17/2$-$15/2$	85.67257	
U		85.943	

TABLE B.6: 87 GHz Autocorrelation Passband Molecular Transitions

Species	Transition	Rest Freq.	Targeted
MgNC	J=7→6 U	83.538	
$^{33}SO_2$	$J_{K_-,K_+}=18_{5,13}\rightarrow19_{4,16}$	83.54028	
C_5H	$^2\Pi_{1/2}$ J=35/2→33/2	83.5415	
C_5H	$^2\Pi_{1/2}$ J=35/2→33/2	83.5471	
CH_3CHO	$J_{K_-,K_+}=2_{1,2}\rightarrow1_{0,1}$ E	83.58426	
C_2H	N=1→0 J=3/2→1/2 F=1→1	87.284156	√
U		87.299	
CH_2CHCN	$J_{K_-,K_+}=9_{1,8}\rightarrow8_{1,7}$	87.312827	
C_2H	N=1→0 J=3/2→1/2 F=2→1	87.316925	√
U		87.323	
C_2H	N=1→0 J=3/2→1/2 F=1→0	87.328624	√
C_2H	N=1→0 J=1/2→1/2 F=1→1	87.402004	√
C_2H	N=1→0 J=1/2→1/2 F=0→1	87.407165	√
C_2H	N=1→0 J=1/2→1/2 F=1→0	87.446512	√
AlCl	J=6→5	87.458286	

TABLE B.7: 101 GHz Autocorrelation Passband Molecular Transitions

Species	Transition	Rest Freq.	Targeted
CH_3OH	$J_K=2_{-1}\rightarrow1_{-1}$ E	96.73939	√
CH_3OH	$J_K=2_0\rightarrow1_0$ A^+	96.74142	√
CH_3OH	$J_K=2_0\rightarrow1_0$ E	96.74458	√
CH_3OH	$J_K=2_1\rightarrow1_1$ E	96.75551	√
U		97.069	
U		97.263	
HC_3N	J=11→10 $\nu_6=1$ $\ell=1f$	100.31926	
HC_3N	J=11→10 $\nu_7=1$ $\ell=1e$	100.32235	
U		100.332	
$HCOOCH_3$	$J_{K_-,K_+}=8_{1,7}\rightarrow7_{1,6}$ E	100.48227	√
$HCOOCH_3$	$J_{K_-,K_+}=8_{1,7}\rightarrow7_{1,6}$ A	100.49067	√
U		100.4985	
$HCOOCH_3$	$J_{K_-,K_+}=9_{0,9}\rightarrow8_{0,8}$ E	100.68151	√
$HCOOCH_3$	$J_{K_-,K_+}=9_{0,9}\rightarrow8_{0,8}$ A	100.68336	√

TABLE B.8: 110 GHz Autocorrelation Passband Molecular Transitions

Species	Transition	Rest Freq.	Targeted
$HOCO^+$	$J_{K_-,K_+}=5_{0,5}\rightarrow4_{0,4}$	106.91352	
^{29}SiS	$J=6\rightarrow5$	106.92295	
U		106.942	
U		106.963	
U		106.981	
U		106.995	
CH_3OH	$J_K=3_1\rightarrow4_0$ A^+	107.01385	
U		110.24	
C_6H	$^2\Pi_{1/2}$ $J=79/2\rightarrow77/2$	110.2434	
$CH_3{}^{13}CN$	$J_K=6_3\rightarrow5_3$	110.30988	
$CH_3{}^{13}CN$	$J_K=6_1\rightarrow5_1$	110.32678	
$CH_3{}^{13}CN$	$J_K=6_0\rightarrow5_0$	110.32889	
CH_3CN	$J_K=6_5\rightarrow5_5$ $F=7\rightarrow6$	110.33063	√
CH_3CN	$J_K=6_5\rightarrow5_5$ $F=5\rightarrow4$	110.33087	√
CH_3CN	$J_K=6_4\rightarrow5_4$ $F=7\rightarrow6$	110.34966	√
CH_3CN	$J_K=6_4\rightarrow5_4$ $F=5\rightarrow4$	110.3498	√
CH_3CN	$J_K=6_3\rightarrow5_3$ $F=7\rightarrow6$	110.36447	√
CH_3CN	$J_K=6_3\rightarrow5_3$ $F=5\rightarrow4$	110.36452	√
HC_3N	$J=12\rightarrow11$ $\nu_7=3$ $\ell=1f$	110.36648	
CH_3CN	$J_K=6_2\rightarrow5_2$ $F=7\rightarrow6$	110.37505	√
CH_3CN	$J_K=6_1\rightarrow5_1$ $F=7\rightarrow6$	110.3814	√
CH_3CN	$J_K=6_0\rightarrow5_0$ $F=7\rightarrow6$	110.38352	

B.2 Sample Observe Command File

```
#! /bin/csh -f
#
#   Observing script for comet Hale-Bopp, _1000132,
#   for the autocorrelation.
#
#   HCN J=1-0 in USB.  Also in there are HCO+, HCS+, and OCS.
#
#   PI: Jeff Veal
#   Email: veal@astro.uiuc.edu
#   Telephone: (217) 244-5471 (office)
#
#   LST range for script:
#
#   Source      =  _1000132 (comet Hale-Bopp)
#   ra(J2000)   =
#   dec(J2000)  =
#   vlsr        =  0 km/s
#   rise time   =  1400        (5 feb 97)
#   set time    =  2600
#   elev limit  =  10 degrees
#
#
#----------------------------SETUPS--------------------------------
setup name=tunea freq=88.631847 source=_1000132 dopsrc=_1000132 \
   ants=2456789 obsline=HCN.J=1-0 iffreq=235 cormode=4 \
   coptions=auto,hanning,nocable \
   corf=251.24512,498.75488,732.25098,783.74634 corbw=25,25,25,25 \
   restfqs=88.631847,85.347900,85.139108,89.188518
#
setup name=tuneb freq=88.631847 source=_1000132 dopsrc=_1000132 \
   ants=2456789 obsline=HCN.J=1-0 iffreq=245 cormode=4 \
   coptions=auto,hanning,nocable \
   corf=255.00488,485.74829,719.25659,790.99731 corbw=25,25,25,25 \
   restfqs=88.631847,85.347900,85.139108,89.188518
#
setup name=observea task=xmint source=_1000132 vis=_1000132a itime=20 \
   stop=+60 'grid=dra(20.,0.),ddec(0.,0.),on(0,1)' ants=2456789 \
   setup=tunea
#
setup name=observeb task=xmint source=_1000132 vis=_1000132b itime=20 \
   stop=+60 'grid=dra(20.,0.),ddec(0.,0.),on(0,1)' ants=2456789 \
   setup=tuneb
```

```
#
setup name=quality s=_1000132 p=3c273.n email=veal@astro.uiuc.edu
#
#--------------------------OBSERVING------------------------------
#
# the iffreq is changed from
# one tune to another so as to eliminate any possible spectral line
# misidentifications
#
set var0=‘cat /obs/obs/files/project.info | grep project= | cut -d"=" -f2‘
if ((-e $var0/_1000132a) || (-e $var0/_1000132b)) then
   set var1=‘du -k $var0/_1000132* | sort -n | head -1 | cut -d _ -f2
       | cut -c8‘
   set var2=‘du -k $var0/_1000132* | sort -nr | head -1 | cut -d _ -f2
       | cut -c8‘
   if ($var1 == $var2) then
      if ($var1 == "a") then
         set var1=b
      else
         set var1=a
      endif
   endif
else
   set var1=a
   set var2=b
endif

set observe1=observe$var1
set observe2=observe$var2

loop calsetup=$observe1,$observe2

exit 0
```

B.3 Sample Data Reduction Script

```
#!/bin/csh -vf

#things to edit: junk weights, possible uvflag of channels,
#channels for histo, rms values for imcombine, and date for plot

goto start

start:
```

```
rm -r source*
cp -r _1000132a sourcea
cp -r _1000132b sourceb

uvflag vis=sourcea edge=6 flagval=flag
uvflag vis=sourceb edge=6 flagval=flag

# The next flags are done the second time through after
#    finding the birdies with imspec
#uvflag vis=sourcea select= line= flagval=flag
#uvflag vis=sourceb select= line= flagval=flag

sinbad vis=sourcea out=sourcea.sb
sinbad vis=sourceb out=sourceb.sb

sinpoly vis=sourcea.sb out=sourcea.sp options=window device=/null npoly=2 \
    badchan=2,120,250,1650,1750
sinpoly vis=sourceb.sb out=sourceb.sp options=window device=/null npoly=2 \
    badchan=2,250,380,1705,1805

# Here you can check for unorthodox data
#uvspec vis=sourcea.sp device=/xw

varmap out=sourcea.mp2 vis=sourcea.sp ’select=ant(2)’ imsize=1 \
    cell=180
varmap out=sourcea.mp4 vis=sourcea.sp ’select=ant(4)’ imsize=1 \
    cell=180
varmap out=sourcea.mp5 vis=sourcea.sp ’select=ant(5)’ imsize=1 \
    cell=180
varmap out=sourcea.mp6 vis=sourcea.sp ’select=ant(6)’ imsize=1 \
    cell=180
varmap out=sourcea.mp7 vis=sourcea.sp ’select=ant(7)’ imsize=1 \
    cell=180
varmap out=sourcea.mp8 vis=sourcea.sp ’select=ant(8)’ imsize=1 \
    cell=180
varmap out=sourcea.mp9 vis=sourcea.sp ’select=ant(9)’ imsize=1 \
    cell=180
varmap out=sourceb.mp2 vis=sourceb.sp ’select=ant(2)’ imsize=1 \
    cell=180
varmap out=sourceb.mp4 vis=sourceb.sp ’select=ant(4)’ imsize=1 \
    cell=180
varmap out=sourceb.mp5 vis=sourceb.sp ’select=ant(5)’ imsize=1 \
    cell=180
varmap out=sourceb.mp6 vis=sourceb.sp ’select=ant(6)’ imsize=1 \
```

```
    cell=180
varmap out=sourceb.mp7 vis=sourceb.sp 'select=ant(7)' imsize=1 \
    cell=180
varmap out=sourceb.mp8 vis=sourceb.sp 'select=ant(8)' imsize=1 \
    cell=180
varmap out=sourceb.mp9 vis=sourceb.sp 'select=ant(9)' imsize=1 \
    cell=180

# Watch for birdies and make note
imspec in=sourcea.mp2 plot=mean options=style,step device=/xw
imspec in=sourcea.mp4 plot=mean options=style,step device=/xw
imspec in=sourcea.mp5 plot=mean options=style,step device=/xw
imspec in=sourcea.mp6 plot=mean options=style,step device=/xw
imspec in=sourcea.mp7 plot=mean options=style,step device=/xw
imspec in=sourcea.mp8 plot=mean options=style,step device=/xw
imspec in=sourcea.mp9 plot=mean options=style,step device=/xw
imspec in=sourceb.mp2 plot=mean options=style,step device=/xw
imspec in=sourceb.mp4 plot=mean options=style,step device=/xw
imspec in=sourceb.mp5 plot=mean options=style,step device=/xw
imspec in=sourceb.mp6 plot=mean options=style,step device=/xw
imspec in=sourceb.mp7 plot=mean options=style,step device=/xw
imspec in=sourceb.mp8 plot=mean options=style,step device=/xw
imspec in=sourceb.mp9 plot=mean options=style,step device=/xw

goto end
#after finding birdies, pick a good region
histo in=sourcea.mp2 region=image'(1200,1600)' | grep Rms
histo in=sourcea.mp4 region=image'(1200,1600)' | grep Rms
histo in=sourcea.mp5 region=image'(1200,1600)' | grep Rms
histo in=sourcea.mp6 region=image'(1200,1600)' | grep Rms
histo in=sourcea.mp7 region=image'(1200,1600)' | grep Rms
histo in=sourcea.mp8 region=image'(1200,1600)' | grep Rms
histo in=sourcea.mp9 region=image'(1200,1600)' | grep Rms
histo in=sourceb.mp2 region=image'(1200,1600)' | grep Rms
histo in=sourceb.mp4 region=image'(1200,1600)' | grep Rms
histo in=sourceb.mp5 region=image'(1200,1600)' | grep Rms
histo in=sourceb.mp6 region=image'(1200,1600)' | grep Rms
histo in=sourceb.mp7 region=image'(1200,1600)' | grep Rms
histo in=sourceb.mp8 region=image'(1200,1600)' | grep Rms
histo in=sourceb.mp9 region=image'(1200,1600)' | grep Rms

# The imcombine's are for the third time through
imcombine in=sourcea.mp2,sourcea.mp4,sourcea.mp5,sourcea.mp6,sourcea.mp7,
sourcea.mp8,sourcea.mp9 out=mapa rms=1.03342E-01,6.47905E-02,6.19459E-02,
```

```
3.07475E-02,6.69377E-02,1.04309E-01,3.85215E-02
imcombine in=sourceb.mp2,sourceb.mp4,sourceb.mp5,sourceb.mp6,sourceb.mp7,
sourceb.mp8,sourceb.mp9 out=mapb rms=6.39620E-02,5.38175E-02,4.65929E-02,
2.29582E-02,4.48547E-02,7.90833E-02,2.62605E-02
imspec in=mapa plot=mean options=style,step device=/xw
imspec in=mapb plot=mean options=style,step device=/xw
maths exp='mapa*.4' out=junka
maths exp='mapb*.6' out=junkb
maths exp='junka+junkb' out=map
rm -r junk*
imspec in=map plot=mean options=style,step device=/xw

cp -r sourcea.sp sourcea.hco
cp -r sourceb.sp sourceb.hco
#puthd in=sourcea.hco/restfreq value=89.188518 type=d
#puthd in=sourceb.hco/restfreq value=89.188518 type=d

varmap out=hcoa.mp2 vis=sourcea.hco 'select=ant(2)' \
    line=channel,200,1598,1,1 imsize=1 cell=180
varmap out=hcoa.mp4 vis=sourcea.hco 'select=ant(4)' \
    line=channel,200,1598,1,1 imsize=1 cell=180
varmap out=hcoa.mp5 vis=sourcea.hco 'select=ant(5)' \
    line=channel,200,1598,1,1 imsize=1 cell=180
varmap out=hcoa.mp6 vis=sourcea.hco 'select=ant(6)' \
    line=channel,200,1598,1,1 imsize=1 cell=180
varmap out=hcoa.mp7 vis=sourcea.hco 'select=ant(7)' \
    line=channel,200,1598,1,1 imsize=1 cell=180
varmap out=hcoa.mp8 vis=sourcea.hco 'select=ant(8)' \
    line=channel,200,1598,1,1 imsize=1 cell=180
varmap out=hcoa.mp9 vis=sourcea.hco 'select=ant(9)' \
    line=channel,200,1598,1,1 imsize=1 cell=180
varmap out=hcob.mp2 vis=sourceb.hco 'select=ant(2)' \
    line=channel,200,1655,1,1 imsize=1 cell=180
varmap out=hcob.mp4 vis=sourceb.hco 'select=ant(4)' \
    line=channel,200,1655,1,1 imsize=1 cell=180
varmap out=hcob.mp5 vis=sourceb.hco 'select=ant(5)' \
    line=channel,200,1655,1,1 imsize=1 cell=180
varmap out=hcob.mp6 vis=sourceb.hco 'select=ant(6)' \
    line=channel,200,1655,1,1 imsize=1 cell=180
varmap out=hcob.mp7 vis=sourceb.hco 'select=ant(7)' \
    line=channel,200,1655,1,1 imsize=1 cell=180
varmap out=hcob.mp8 vis=sourceb.hco 'select=ant(8)' \
    line=channel,200,1655,1,1 imsize=1 cell=180
varmap out=hcob.mp9 vis=sourceb.hco 'select=ant(9)' \
```

```
    line=channel,200,1655,1,1 imsize=1 cell=180

imspec in=hcoa.mp2 plot=mean options=style,step device=/xw
imspec in=hcoa.mp4 plot=mean options=style,step device=/xw
imspec in=hcoa.mp5 plot=mean options=style,step device=/xw
imspec in=hcoa.mp6 plot=mean options=style,step device=/xw
imspec in=hcoa.mp7 plot=mean options=style,step device=/xw
imspec in=hcoa.mp8 plot=mean options=style,step device=/xw
imspec in=hcoa.mp9 plot=mean options=style,step device=/xw
imspec in=hcob.mp2 plot=mean options=style,step device=/xw
imspec in=hcob.mp4 plot=mean options=style,step device=/xw
imspec in=hcob.mp5 plot=mean options=style,step device=/xw
imspec in=hcob.mp6 plot=mean options=style,step device=/xw
imspec in=hcob.mp7 plot=mean options=style,step device=/xw
imspec in=hcob.mp8 plot=mean options=style,step device=/xw
imspec in=hcob.mp9 plot=mean options=style,step device=/xw

# The imcombine's are for the third time through
imcombine in=hcoa.mp2,hcoa.mp4,hcoa.mp5,hcoa.mp6,hcoa.mp7,hcoa.mp8,hcoa.mp9
out=hcoa.map rms=1.03342E-01,6.47905E-02,6.19459E-02,3.07475E-02,
6.69377E-02,1.04309E-01,3.85215E-02
imcombine in=hcob.mp2,hcob.mp4,hcob.mp5,hcob.mp6,hcob.mp7,hcob.mp8,hcob.mp9
out=hcob.map rms=6.39620E-02,5.38175E-02,4.65929E-02,2.29582E-02,
4.48547E-02,7.90833E-02,2.62605E-02
imspec in=hcoa.map plot=mean options=style,step device=/xw
imspec in=hcob.map plot=mean options=style,step device=/xw
maths exp='hcoa.map*.4' out=junka
maths exp='hcob.map*.6' out=junkb
maths exp='junka+junkb' out=hco+.map
rm -r junk*
imspec in=hco+.map plot=mean options=style,step device=/xw

cp -r hco+.map hco.map
maths exp='hco.map*1.2*1.850' out=hco+.spectrum
rm -r hco.map
puthd in=hco+.spectrum/bunit value=Kelvins
imspec in=hco+.spectrum plot=flux \
    options=style,step,ymin,-.12,ymax,.44,title,12-Mar-UT device=hco+.ps/ps

end:
```

B.4 Sample Correlator Setup

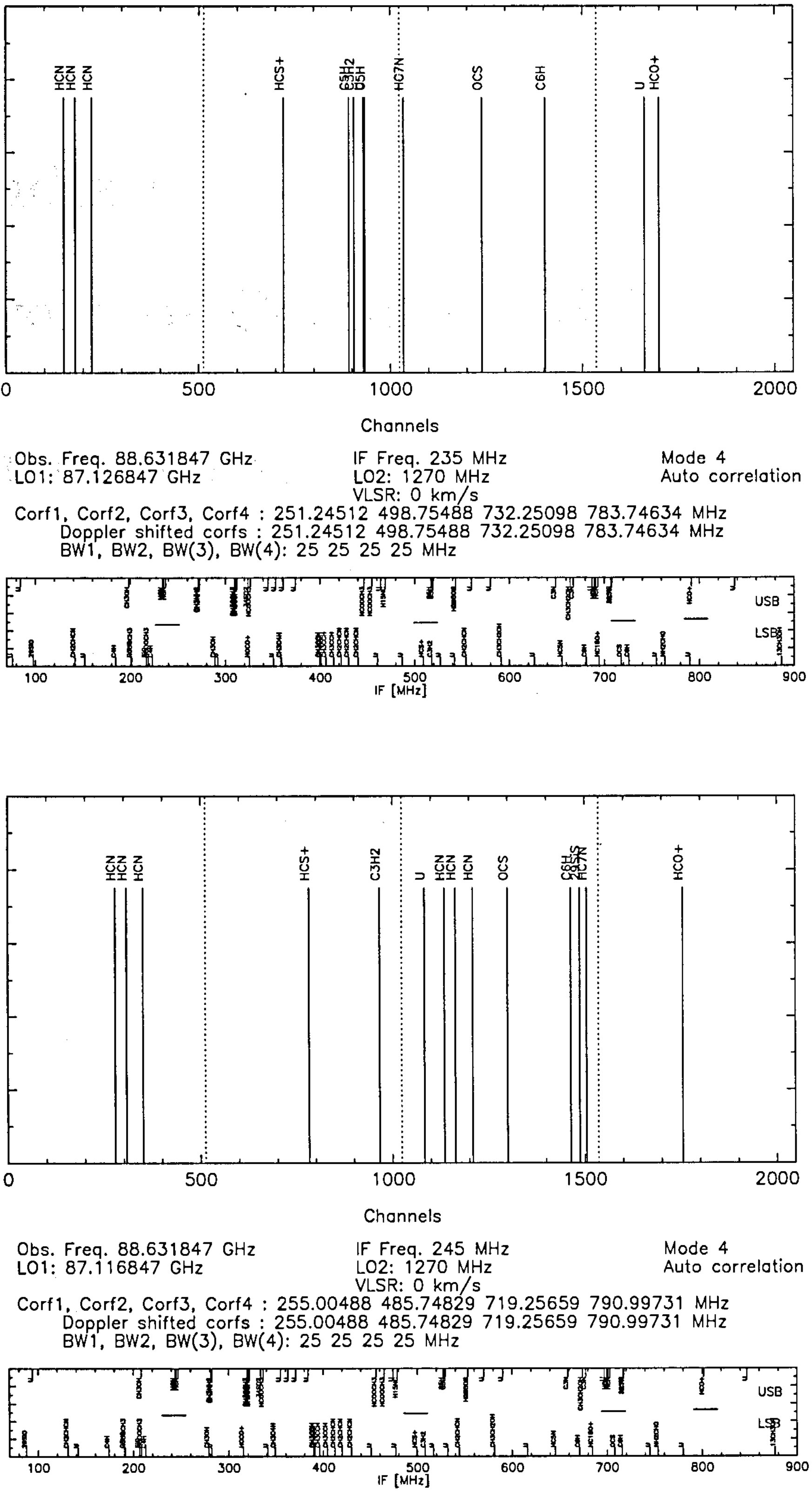

```
Obs. Freq. 88.631847 GHz          IF Freq. 235 MHz          Mode 4
LO1: 87.126847 GHz                LO2: 1270 MHz             Auto correlation
                                  VLSR: 0 km/s
Corf1, Corf2, Corf3, Corf4 : 251.24512 498.75488 732.25098 783.74634 MHz
     Doppler shifted corfs : 251.24512 498.75488 732.25098 783.74634 MHz
     BW1, BW2, BW(3), BW(4): 25 25 25 25 MHz
```

```
Obs. Freq. 88.631847 GHz          IF Freq. 245 MHz          Mode 4
LO1: 87.116847 GHz                LO2: 1270 MHz             Auto correlation
                                  VLSR: 0 km/s
Corf1, Corf2, Corf3, Corf4 : 255.00488 485.74829 719.25659 790.99731 MHz
     Doppler shifted corfs : 255.00488 485.74829 719.25659 790.99731 MHz
     BW1, BW2, BW(3), BW(4): 25 25 25 25 MHz
```

FIGURE B.1: Correlator setups used for autocorrelation observations

Appendix C

Discovery of Cometary HCO^+

C.1 IAU Circular No. 6575

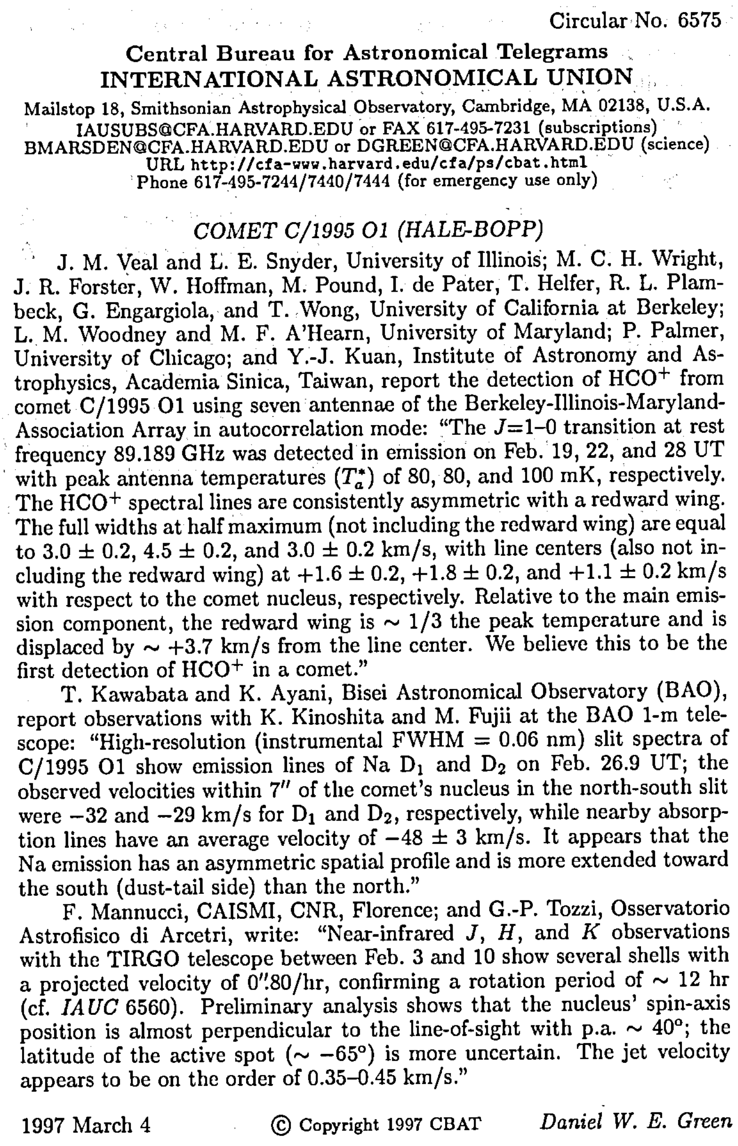

Circular No. 6575

Central Bureau for Astronomical Telegrams
INTERNATIONAL ASTRONOMICAL UNION
Mailstop 18, Smithsonian Astrophysical Observatory, Cambridge, MA 02138, U.S.A.
IAUSUBS@CFA.HARVARD.EDU or FAX 617-495-7231 (subscriptions)
BMARSDEN@CFA.HARVARD.EDU or DGREEN@CFA.HARVARD.EDU (science)
URL `http://cfa-www.harvard.edu/cfa/ps/cbat.html`
Phone 617-495-7244/7440/7444 (for emergency use only)

COMET C/1995 O1 (HALE-BOPP)

J. M. Veal and L. E. Snyder, University of Illinois; M. C. H. Wright, J. R. Forster, W. Hoffman, M. Pound, I. de Pater, T. Helfer, R. L. Plambeck, G. Engargiola, and T. Wong, University of California at Berkeley; L. M. Woodney and M. F. A'Hearn, University of Maryland; P. Palmer, University of Chicago; and Y.-J. Kuan, Institute of Astronomy and Astrophysics, Academia Sinica, Taiwan, report the detection of HCO$^+$ from comet C/1995 O1 using seven antennae of the Berkeley-Illinois-Maryland-Association Array in autocorrelation mode: "The J=1–0 transition at rest frequency 89.189 GHz was detected in emission on Feb. 19, 22, and 28 UT with peak antenna temperatures (T_a^*) of 80, 80, and 100 mK, respectively. The HCO$^+$ spectral lines are consistently asymmetric with a redward wing. The full widths at half maximum (not including the redward wing) are equal to 3.0 ± 0.2, 4.5 ± 0.2, and 3.0 ± 0.2 km/s, with line centers (also not including the redward wing) at +1.6 ± 0.2, +1.8 ± 0.2, and +1.1 ± 0.2 km/s with respect to the comet nucleus, respectively. Relative to the main emission component, the redward wing is ~ 1/3 the peak temperature and is displaced by ~ +3.7 km/s from the line center. We believe this to be the first detection of HCO$^+$ in a comet."

T. Kawabata and K. Ayani, Bisei Astronomical Observatory (BAO), report observations with K. Kinoshita and M. Fujii at the BAO 1-m telescope: "High-resolution (instrumental FWHM = 0.06 nm) slit spectra of C/1995 O1 show emission lines of Na D$_1$ and D$_2$ on Feb. 26.9 UT; the observed velocities within 7″ of the comet's nucleus in the north-south slit were −32 and −29 km/s for D$_1$ and D$_2$, respectively, while nearby absorption lines have an average velocity of −48 ± 3 km/s. It appears that the Na emission has an asymmetric spatial profile and is more extended toward the south (dust-tail side) than the north."

F. Mannucci, CAISMI, CNR, Florence; and G.-P. Tozzi, Osservatorio Astrofisico di Arcetri, write: "Near-infrared J, H, and K observations with the TIRGO telescope between Feb. 3 and 10 show several shells with a projected velocity of 0″.80/hr, confirming a rotation period of ~ 12 hr (cf. *IAUC* 6560). Preliminary analysis shows that the nucleus' spin-axis position is almost perpendicular to the line-of-sight with p.a. ~ 40°; the latitude of the active spot (~ −65°) is more uncertain. The jet velocity appears to be on the order of 0.35–0.45 km/s."

1997 March 4 © Copyright 1997 CBAT *Daniel W. E. Green*

FIGURE C.1: IAU Circular No. 6575

C.2 Ephemeris

TABLE C.1: Explanation of Symbols

α = Geocentric astrometric right ascension in hours, minutes and seconds, referred to the mean equator and equinox of J2000. Light time corrections have been applied.

δ = Geocentric astrometric declination in degrees, arcminutes and arcseconds, referred to the mean equator and equinox of J2000. Light time corrections have been applied.

Δ = Geocentric distance of comet in AU

$\dot{\Delta}$ = Geocentric radial velocity of comet in km/s

r = Heliocentric distance of comet in AU

$\dot{r}$ = Heliocentric radial velocity of comet in km/s

θ = Sun-Earth-Comet angle (elongation) in degrees

β = Sun-Comet-Earth angle (phase) in degrees

Moon = Comet-Earth-Moon angle in degrees

PsAng = Position angle of extended radius vector in degrees

PsAMV = Position angle of minus velocity vector in degrees

TMag = Total magnitude = $-1.0 + 5.00 \log \Delta + 10.00 \log r$

TABLE C.2: JPL Ref. Orbit 41 by D.K. Yeomans, Sept. 12, 1996: Part 1 of 2

Date (0^h UTC)	α	δ	Δ	$\dot{\Delta}$	r
1997 Feb 2	19 42 59.59	+15 57 45.0	1.985	-34.182	1.356
1997 Feb 7	19 56 07.43	+18 33 08.2	1.886	-34.147	1.297
1997 Feb 12	20 10 58.21	+21 25 59.6	1.788	-33.550	1.240
1997 Feb 17	20 28 00.23	+24 36 48.9	1.693	-32.263	1.186
1997 Feb 22	20 47 51.37	+28 04 41.5	1.602	-30.158	1.134
1997 Feb 27	21 11 20.59	+31 46 11.6	1.519	-27.113	1.086

Table C.3: JPL Ref. Orbit 41 by D.K. Yeomans, Sept. 12, 1996: Part 2 of 2

Date (0^h UTC)	θ	β	Moon	PsAng	PsAMV	TMag
1997 Feb 2	38.3	26.7	67	328.2	201.2	1.3
1997 Feb 7	40.1	29.3	35	326.4	206.2	1.0
1997 Feb 12	41.8	32.0	78	325.3	211.3	0.7
1997 Feb 17	43.3	34.8	123	325.2	216.7	0.5
1997 Feb 22	44.5	37.7	139	326.1	222.4	0.2
1997 Feb 27	45.5	40.6	112	328.3	228.6	-0.1

Table C.4: JPL Ref. Orbit 55 by D.K. Yeomans, Mar. 4, 1997: Part 1 of 2

Date (0^h UTC)	α	δ	Δ	$\dot{\Delta}$	r
1997 Mar 1	21 21 58.51	+33 17 10.4	1.489	-25.61	1.067
1997 Mar 2	21 27 35.30	+34 02 47.6	1.474	-24.79	1.059
1997 Mar 3	21 33 24.71	+34 48 23.2	1.460	-23.93	1.050
1997 Mar 4	21 39 27.23	+35 33 50.0	1.447	-23.03	1.042
1997 Mar 5	21 45 43.35	+36 19 00.2	1.434	-22.08	1.033
1997 Mar 6	21 52 13.52	+37 03 45.5	1.421	-21.09	1.025
1997 Mar 7	21 58 58.18	+37 47 56.4	1.409	-20.06	1.018
1997 Mar 8	22 05 57.67	+38 31 23.2	1.398	-18.99	1.010
1997 Mar 9	22 13 12.31	+39 13 55.2	1.387	-17.88	1.003
1997 Mar 10	22 20 42.32	+39 55 21.1	1.378	-16.73	0.996
1997 Mar 11	22 28 27.81	+40 35 29.3	1.368	-15.54	0.989
1997 Mar 12	22 36 28.80	+41 14 07.4	1.360	-14.31	0.982
1997 Mar 13	22 44 45.16	+41 51 03.0	1.352	-13.06	0.976
1997 Mar 14	22 53 16.60	+42 26 03.1	1.344	-11.77	0.970

Table C.5: JPL Ref. Orbit 55 by D.K. Yeomans, Mar. 4, 1997: Part 2 of 2

Date (0^h UTC)	θ	β	Moon	PsAng	PsAMV	TMag
1997 Mar 1	45.7	41.7	96	329.5	231.3	0.7
1997 Mar 2	45.9	42.2	88	330.3	232.7	0.6
1997 Mar 3	46.0	42.7	80	331.1	234.1	0.6
1997 Mar 4	46.0	43.3	72	331.9	235.6	0.5
1997 Mar 5	46.1	43.8	64	332.9	237.1	0.5
1997 Mar 6	46.2	44.3	57	333.9	238.7	0.4
1997 Mar 7	46.2	44.7	51	335.0	240.3	0.4
1997 Mar 8	46.2	45.2	47	336.2	241.9	0.4
1997 Mar 9	46.2	45.7	45	337.5	243.6	0.3
1997 Mar 10	46.2	46.1	46	338.8	245.4	0.3
1997 Mar 11	46.2	46.5	50	340.2	247.2	0.2
1997 Mar 12	46.2	46.9	55	341.8	249.1	0.2
1997 Mar 13	46.1	47.2	62	343.4	251.0	0.2
1997 Mar 14	46.0	47.6	69	345.1	253.0	0.1

TABLE C.6: JPL Ref. Orbit 59 by D.K. Yeomans, Apr. 10, 1997: Part 1 of 4

Date (0^h UTC)	α	δ	Δ	$\dot{\Delta}$	r	$\dot{r}$
1997 Mar 15	23 02 02.68	+42 58 56.4	1.338	-10.45	0.964	-9.74
1997 Mar 16	23 11 02.77	+43 29 27.8	1.332	-9.10	0.959	-9.24
1997 Mar 17	23 20 16.05	+43 57 26.3	1.328	-7.74	0.953	-8.73
1997 Mar 18	23 29 41.49	+44 22 40.5	1.323	-6.36	0.949	-8.21
1997 Mar 19	23 39 17.87	+44 44 59.5	1.320	-4.96	0.944	-7.68
1997 Mar 20	23 49 03.75	+45 04 13.8	1.318	-3.55	0.940	-7.14
1997 Mar 21	23 58 57.56	+45 20 15.1	1.316	-2.14	0.936	-6.59
1997 Mar 22	00 08 57.52	+45 32 56.7	1.315	-.72	0.932	-6.03
1997 Mar 23	00 19 01.76	+45 42 13.4	1.315	.70	0.929	-5.46
1997 Mar 24	00 29 08.29	+45 48 02.1	1.316	2.11	0.926	-4.89
1997 Mar 25	00 39 15.10	+45 50 21.3	1.318	3.50	0.923	-4.30
1997 Mar 26	00 49 20.14	+45 49 11.6	1.320	4.89	0.921	-3.71
1997 Mar 27	00 59 21.41	+45 44 35.4	1.323	6.26	0.919	-3.12
1997 Mar 28	01 09 16.97	+45 36 37.1	1.327	7.60	0.917	-2.52
1997 Mar 29	01 19 05.03	+45 25 22.6	1.332	8.92	0.916	-1.91
1997 Mar 30	01 28 43.91	+45 10 59.3	1.338	10.20	0.915	-1.31
1997 Mar 31	01 38 12.11	+44 53 36.2	1.344	11.46	0.914	-.70
1997 Apr 1	01 47 28.34	+44 33 23.0	1.351	12.68	0.914	-.09
1997 Apr 2	01 56 31.48	+44 10 30.5	1.359	13.86	0.914	.52
1997 Apr 3	02 05 20.63	+43 45 10.1	1.367	15.01	0.915	1.13
1997 Apr 4	02 13 55.09	+43 17 33.6	1.376	16.11	0.916	1.74
1997 Apr 5	02 22 14.33	+42 47 52.9	1.385	17.16	0.917	2.34
1997 Apr 6	02 30 18.03	+42 16 20.0	1.396	18.17	0.918	2.94
1997 Apr 7	02 38 06.00	+41 43 06.6	1.406	19.14	0.920	3.54
1997 Apr 8	02 45 38.20	+41 08 24.3	1.418	20.05	0.922	4.13
1997 Apr 9	02 52 54.73	+40 32 24.1	1.430	20.93	0.925	4.72
1997 Apr 10	02 59 55.78	+39 55 16.5	1.442	21.75	0.928	5.30
1997 Apr 11	03 06 41.64	+39 17 11.5	1.455	22.53	0.931	5.87
1997 Apr 12	03 13 12.67	+38 38 18.4	1.468	23.26	0.935	6.43
1997 Apr 13	03 19 29.29	+37 58 45.8	1.482	23.94	0.938	6.98
1997 Apr 14	03 25 31.96	+37 18 41.9	1.496	24.58	0.943	7.53
1997 Apr 15	03 31 21.17	+36 38 14.0	1.510	25.18	0.947	8.06
1997 Apr 16	03 36 57.44	+35 57 28.9	1.525	25.73	0.952	8.58
1997 Apr 17	03 42 21.29	+35 16 32.5	1.540	26.24	0.957	9.10
1997 Apr 18	03 47 33.26	+34 35 30.5	1.555	26.71	0.962	9.60
1997 Apr 19	03 52 33.88	+33 54 27.8	1.571	27.14	0.968	10.09

TABLE C.7: JPL Ref. Orbit 59 by D.K. Yeomans, Apr. 10, 1997: Part 2 of 4

Date (0^h UTC)	α	δ	Δ	$\dot{\Delta}$	r	$\dot{r}$
1997 Apr 20	03 57 23.67	+33 13 28.8	1.586	27.54	0.974	10.56
1997 Apr 21	04 02 03.16	+32 32 37.4	1.602	27.89	0.980	11.03
1997 Apr 22	04 06 32.84	+31 51 57.0	1.619	28.21	0.987	11.48
1997 Apr 23	04 10 53.20	+31 11 30.6	1.635	28.50	0.994	11.92
1997 Apr 24	04 15 04.71	+30 31 20.9	1.651	28.75	1.001	12.35
1997 Apr 25	04 19 07.83	+29 51 30.1	1.668	28.98	1.008	12.76
1997 Apr 26	04 23 02.99	+29 12 00.1	1.685	29.17	1.015	13.16
1997 Apr 27	04 26 50.61	+28 32 52.5	1.702	29.33	1.023	13.55
1997 Apr 28	04 30 31.08	+27 54 08.7	1.719	29.47	1.031	13.93
1997 Apr 29	04 34 04.77	+27 15 49.8	1.736	29.58	1.039	14.29
1997 Apr 30	04 37 32.05	+26 37 56.7	1.753	29.66	1.047	14.65
1997 May 1	04 40 53.25	+26 00 30.1	1.770	29.72	1.056	14.99
1997 May 2	04 44 08.70	+25 23 30.4	1.787	29.76	1.065	15.31
1997 May 3	04 47 18.68	+24 46 58.1	1.804	29.77	1.074	15.63
1997 May 4	04 50 23.50	+24 10 53.3	1.822	29.77	1.083	15.94
1997 May 5	04 53 23.42	+23 35 16.1	1.839	29.74	1.092	16.23
1997 May 6	04 56 18.68	+23 00 06.5	1.856	29.70	1.102	16.51
1997 May 7	04 59 09.52	+22 25 24.3	1.873	29.64	1.111	16.78
1997 May 8	05 01 56.18	+21 51 09.4	1.890	29.56	1.121	17.04
1997 May 9	05 04 38.86	+21 17 21.5	1.907	29.47	1.131	17.29
1997 May 10	05 07 17.75	+20 44 00.2	1.924	29.37	1.141	17.53
1997 May 11	05 09 53.05	+20 11 05.1	1.941	29.25	1.151	17.76
1997 May 12	05 12 24.93	+19 38 35.9	1.958	29.12	1.161	17.99
1997 May 13	05 14 53.56	+19 06 31.9	1.975	28.97	1.172	18.20
1997 May 14	05 17 19.09	+18 34 52.8	1.992	28.82	1.182	18.40
1997 May 15	05 19 41.68	+18 03 37.9	2.008	28.66	1.193	18.60
1997 May 16	05 22 01.46	+17 32 46.8	2.025	28.49	1.204	18.78
1997 May 17	05 24 18.57	+17 02 18.8	2.041	28.31	1.215	18.96
1997 May 18	05 26 33.13	+16 32 13.5	2.057	28.12	1.226	19.13
1997 May 19	05 28 45.26	+16 02 30.1	2.074	27.92	1.237	19.29
1997 May 20	05 30 55.08	+15 33 08.1	2.090	27.72	1.248	19.45
1997 May 21	05 33 02.68	+15 04 07.0	2.106	27.51	1.259	19.60
1997 May 22	05 35 08.18	+14 35 26.0	2.121	27.30	1.271	19.74
1997 May 23	05 37 11.66	+14 07 04.7	2.137	27.08	1.282	19.87
1997 May 24	05 39 13.21	+13 39 02.4	2.153	26.85	1.294	20.00
1997 May 25	05 41 12.93	+13 11 18.5	2.168	26.62	1.305	20.12
1997 May 26	05 43 10.88	+12 43 52.4	2.183	26.39	1.317	20.24
1997 May 27	05 45 07.16	+12 16 43.6	2.199	26.15	1.329	20.35
1997 May 28	05 47 01.83	+11 49 51.5	2.214	25.90	1.340	20.46
1997 May 29	05 48 54.95	+11 23 15.5	2.228	25.65	1.352	20.56
1997 May 30	05 50 46.60	+10 56 55.0	2.243	25.40	1.364	20.65
1997 May 31	05 52 36.83	+10 30 49.5	2.258	25.15	1.376	20.74

TABLE C.8: JPL Ref. Orbit 59 by D.K. Yeomans, Apr. 10, 1997: Part 3 of 4

Date (0^h UTC)	θ	β	Moon	PsAng	PsAMV	TMag
1997 Mar 15	46.0	47.9	76	346.8	255.1	-0.5
1997 Mar 16	45.9	48.1	83	348.7	257.1	-0.6
1997 Mar 17	45.7	48.4	90	350.6	259.3	-0.6
1997 Mar 18	45.6	48.6	97	352.6	261.5	-0.6
1997 Mar 19	45.5	48.8	104	354.7	263.7	-0.6
1997 Mar 20	45.3	48.9	110	356.8	266.0	-0.7
1997 Mar 21	45.2	49.0	117	359.0	268.3	-0.7
1997 Mar 22	45.0	49.1	123	1.3	270.6	-0.7
1997 Mar 23	44.8	49.1	129	3.6	273.0	-0.7
1997 Mar 24	44.6	49.1	134	5.9	275.4	-0.7
1997 Mar 25	44.4	49.1	138	8.2	277.7	-0.7
1997 Mar 26	44.1	49.0	140	10.6	280.1	-0.8
1997 Mar 27	43.9	48.9	141	13.0	282.5	-0.8
1997 Mar 28	43.7	48.7	138	15.3	284.8	-0.8
1997 Mar 29	43.4	48.5	134	17.7	287.1	-0.8
1997 Mar 30	43.1	48.3	128	20.0	289.4	-0.8
1997 Mar 31	42.9	48.0	120	22.3	291.7	-0.7
1997 Apr 1	42.6	47.7	111	24.6	293.9	-0.7
1997 Apr 2	42.3	47.4	101	26.9	296.1	-0.7
1997 Apr 3	42.0	47.0	91	29.1	298.2	-0.7
1997 Apr 4	41.7	46.6	80	31.3	300.3	-0.7
1997 Apr 5	41.4	46.2	69	33.4	302.3	-0.7
1997 Apr 6	41.1	45.7	57	35.5	304.2	-0.6
1997 Apr 7	40.7	45.2	46	37.6	306.1	-0.6
1997 Apr 8	40.4	44.7	37	39.5	308.0	-0.6
1997 Apr 9	40.1	44.2	29	41.5	309.8	-0.6
1997 Apr 10	39.7	43.6	26	43.4	311.5	-0.5
1997 Apr 11	39.4	43.1	29	45.3	313.2	-0.5
1997 Apr 12	39.0	42.5	35	47.1	314.8	-0.5
1997 Apr 13	38.7	41.9	43	48.9	316.4	-0.4
1997 Apr 14	38.3	41.3	52	50.6	317.9	-0.4
1997 Apr 15	37.9	40.6	62	52.3	319.3	-0.3
1997 Apr 16	37.6	40.0	72	53.9	320.8	-0.3
1997 Apr 17	37.2	39.4	82	55.6	322.1	-0.3
1997 Apr 18	36.8	38.7	92	57.2	323.5	-0.2
1997 Apr 19	36.4	38.0	102	58.7	324.8	-0.2

TABLE C.9: JPL Ref. Orbit 59 by D.K. Yeomans, Apr. 10, 1997: Part 4 of 4

Date (0^h UTC)	θ	β	Moon	PsAng	PsAMV	TMag
1997 Apr 20	36.1	37.4	113	60.3	326.0	-0.1
1997 Apr 21	35.7	36.7	124	61.8	327.2	-0.1
1997 Apr 22	35.3	36.0	135	63.3	328.4	0.0
1997 Apr 23	34.9	35.4	146	64.8	329.5	0.0
1997 Apr 24	34.5	34.7	156	66.2	330.6	0.1
1997 Apr 25	34.1	34.0	165	67.7	331.6	0.1
1997 Apr 26	33.7	33.4	167	69.1	332.6	0.2
1997 Apr 27	33.3	32.7	159	70.5	333.6	0.3
1997 Apr 28	32.9	32.1	148	71.9	334.6	0.3
1997 Apr 29	32.5	31.4	136	73.3	335.5	0.4
1997 Apr 30	32.1	30.8	123	74.7	336.4	0.4
1997 May 1	31.8	30.1	110	76.1	337.3	0.5
1997 May 2	31.4	29.5	96	77.5	338.2	0.5
1997 May 3	31.0	28.9	82	78.9	339.0	0.6
1997 May 4	30.6	28.3	69	80.3	339.8	0.6
1997 May 5	30.2	27.7	55	81.7	340.6	0.7
1997 May 6	29.8	27.1	41	83.1	341.3	0.8
1997 May 7	29.4	26.5	28	84.5	342.0	0.8
1997 May 8	29.1	25.9	15	85.9	342.8	0.9
1997 May 9	28.7	25.4	4	87.3	343.5	0.9
1997 May 10	28.3	24.8	12	88.8	344.1	1.0
1997 May 11	28.0	24.3	23	90.2	344.8	1.1
1997 May 12	27.6	23.8	35	91.7	345.4	1.1
1997 May 13	27.3	23.3	47	93.2	346.0	1.2
1997 May 14	26.9	22.8	58	94.6	346.6	1.2
1997 May 15	26.6	22.3	70	96.2	347.2	1.3
1997 May 16	26.3	21.8	81	97.7	347.8	1.3
1997 May 17	25.9	21.3	92	99.2	348.4	1.4
1997 May 18	25.6	20.9	104	100.8	348.9	1.5
1997 May 19	25.3	20.5	116	102.4	349.4	1.5
1997 May 20	25.0	20.0	128	104.0	350.0	1.6
1997 May 21	24.7	19.6	140	105.6	350.5	1.6
1997 May 22	24.4	19.2	152	107.2	350.9	1.7
1997 May 23	24.2	18.9	165	108.9	351.4	1.7
1997 May 24	23.9	18.5	175	110.6	351.9	1.8
1997 May 25	23.7	18.1	167	112.3	352.3	1.8
1997 May 26	23.4	17.8	154	114.0	352.8	1.9
1997 May 27	23.2	17.5	141	115.8	353.2	1.9
1997 May 28	23.0	17.2	127	117.5	353.6	2.0
1997 May 29	22.8	16.9	114	119.3	354.1	2.1
1997 May 30	22.6	16.6	100	121.1	354.5	2.1
1997 May 31	22.4	16.3	86	123.0	354.9	2.2

Appendix D

Interferometric Data: Molecular Transitions, Acquisition, and Reduction

Below are the molecular transitions observed in interferometric mode, as well as one example each of an observe command file, a data reduction script, and a correlator setup. In this case, the end result is a map of the sum of two hyperfine components of the $J=1\rightarrow0$ transition of HCN, a spectral cut through the window of the data cube containing the HCN emission, and a map of the 3 mm continuum from the comet. In this case, both HCN and continuum were observed simultaneously. Figure D.1 shows the correlator setup used.

D.1 Molecular Transitions

TABLE D.1: 89 GHz Interferometric Passband Molecular Transitions[a]

Species	Transition	Rest Freq.	Targeted
continuum			✓
$HC^{18}O^+$	$J=1\rightarrow0$	85.162256	
HC_5N	$J=32\rightarrow31$	85.201348	
U		85.2306	
CH_3CH_2OH	$J_{K_-,K_+}=6_{0,6}\rightarrow5_{1,5}$	85.26547	
CH_2CHCN	$J_{K_-,K_+}=9_{2,8}\rightarrow8_{2,7}$	85.302654	
U		85.33885	
CH_2CHCN	$J_{K_-,K_+}=9_{4,6}\rightarrow8_{4,5}$	85.416762	
CH_2CHCN	$J_{K_-,K_+}=9_{4,5}\rightarrow8_{4,4}$	85.416813	
CH_2CHCN	$J_{K_-,K_+}=9_{3,7}\rightarrow8_{3,6}$	85.426932	
U		85.435	
CH_3CCH	$J_K=5_3\rightarrow4_3$	85.442601	
CH_3CCH	$J_K=5_2\rightarrow4_2$	85.450766	
CH_3CCH	$J_K=5_1\rightarrow4_1$	85.455666	
CH_3CCH	$J_K=5_0\rightarrow4_0$	85.4573	
U		85.506	
$HOCO^+$	$J_{K_-,K_+}=4_{0,4}\rightarrow3_{0,3}$	85.53068	
U		85.565	
C_4H	$N=9\rightarrow8$ $J=17/2\text{-}15/2$	85.67257	
HCN	$J=1\rightarrow0$ $F=1\rightarrow1$	88.630415	✓
HCN	$J=1\rightarrow0$ $F=2\rightarrow1$	88.631847	✓
HCN	$J=1\rightarrow0$ $F=0\rightarrow1$	88.633936	✓
U		88.7418	
U		88.7498	
U		88.7708	
$HCOOCH_3$	$J_{K_-,K_+}=7_{1,6}\rightarrow6_{1,5}$ E	88.84324	
$HCOOCH_3$	$J_{K_-,K_+}=7_{1,6}\rightarrow6_{1,5}$ A	88.85161	
U		88.861	
$H^{15}NC$	$J=1\rightarrow0$	88.865692	
C_3N	$N=9\rightarrow8$ $J=19/2\rightarrow17/2$	89.04559	
C_3N	$N=9\rightarrow8$ $J=17/2\rightarrow15/2$	89.06436	
U		89.087	
^{29}SiS	$J=5\rightarrow4$	89.10373	
HCO^+	$J=1\rightarrow0$	89.188518	✓

[a] for observations in Table 2.2 indicated by [a] and [d]

TABLE D.2: 89 GHz Interferometric Passband Molecular Transitions[a]

Species	Transition	Rest Freq.	Targeted
CH_3CH_2OH	$J_{K_-,K_+}=6_{0,6}\rightarrow5_{1,5}$	85.26547	
CH_3CCH	$J_K=5_2\rightarrow4_2$	85.450766	
CH_3CCH	$J_K=5_1\rightarrow4_1$	85.455666	
CH_3CCH	$J_K=5_0\rightarrow4_0$	85.4573	
C_4H	N=9→8 J=17/2→15/2	85.67257	
HCN	J=1→0 F=1→1	88.630415	√
HCN	J=1→0 F=2→1	88.631847	√
HCN	J=1→0 F=0→1	88.633936	√
$HCOOCH_3$	$J_{K_-,K_+}=7_{1,6}\rightarrow6_{1,5}$ E	88.84324	
$HCOOCH_3$	$J_{K_-,K_+}=7_{1,6}\rightarrow6_{1,5}$ A	88.85161	
C_3N	N=9→8 J=19/2→17/2	89.04559	
HCO^+	J=1→0	89.188518	√

[a] for observations in Table 2.2 indicated by [b]

TABLE D.3: 89 GHz Interferometric Passband Molecular Transitions[a]

Species	Transition	Rest Freq.	Targeted
C_6H	$^2\Pi_{1/2}$ J=61/2→59/2	85.1311	
OCS	J=7→6	85.139108	
CH_3CCH	$J_K=5_2\rightarrow4_2$	85.450766	
CH_3CCH	$J_K=5_1\rightarrow4_1$	85.455666	
CH_3CCH	$J_K=5_0\rightarrow4_0$	85.4573	
C_4H	N=9→8 J=17/2→15/2	85.67257	
HCN	J=1→0 F=1→1	88.630415	√
HCN	J=1→0 F=2→1	88.631847	√
HCN	J=1→0 F=0→1	88.633936	√
$HCOOCH_3$	$J_{K_-,K_+}=7_{1,6}\rightarrow6_{1,5}$ E	88.84324	
$HCOOCH_3$	$J_{K_-,K_+}=7_{1,6}\rightarrow6_{1,5}$ A	88.85161	
HCO^+	J=1→0	89.188518	√

[a] for observations in Table 2.2 indicated by [c]

TABLE D.4: 98 GHz Interferometric Passband Molecular Transitions

Species	Transition	Rest Freq.	Targeted
CS	J=2→1	97.980968	√
U		97.9911	
U		97.9938	
ℓ-C_3H	$^2\Pi_{1/2}$ J=9/2→7/2b	97.99545	
U		98.2659	
C_3S	J=17→16	98.268516	
$HCOOCH_3$	$J_{K_-,K_+}=8_{6,2}\rightarrow7_{6,1}$ E	98.27041	
$HCOOCH_3$	$J_{K_-,K_+}=8_{6,3}\rightarrow7_{6,2}$ E	98.27902	
$HCOOCH_3$	$J_{K_-,K_+}=8_{6,3}\rightarrow7_{6,2}$ A	98.27974	
$HCOOCH_3$	$J_{K_-,K_+}=8_{6,2}\rightarrow7_{6,1}$ A	98.27974	
HC_5N	J=37→36	98.512522	
CH_3CH_2CN	$J_K=11_6\rightarrow10_6$	98.52388	
CH_3CH_2CN	$J_K=11_7\rightarrow10_7$	98.524661	
C_5H	$^2\Pi_{3/2}$ J=41/2→29/2	98.52494	
C_5H	$^2\Pi_{3/2}$ J=41/2→29/2	98.52744	
$HCOOCH_3$	$J_{K_-,K_+}=8_{4,5}\rightarrow7_{4,4}$ E	98.71228	
H_2CS	$J_{K_-,K_+}=3_{1,3}\rightarrow2_{1,2}$	101.47775	
$^{33}SO_2$	$J_{K_-,K_+}=12_{4,8}\rightarrow12_{3,11}$	101.6885	
NH_2CH_2COOH	$J_{K_-,K_+}=17_{0,17}\rightarrow16_{1,16}$	101.6887	
NH_2CH_2COOH	$J_{K_-,K_+}=17_{1,17}\rightarrow16_{1,16}$	101.69064	
NH_2CH_2COOH	$J_{K_-,K_+}=17_{0,17}\rightarrow16_{0,16}$	101.69245	
NH_2CH_2COOH	$J_{K_-,K_+}=17_{1,17}\rightarrow16_{0,16}$	101.69439	
C_6H	$^2\Pi_{1/2}$ J=73/2→71/2	101.9252	
NH_2CHO	$J_{K_-,K_+}=2_{1,2}\rightarrow1_{0,1}$	102.21758	

TABLE D.5: 97 GHz Interferometric Passband Molecular Transitions

Species	Transition	Rest Freq.	Targeted
CH_3OH	$J_K=2_{-1}\rightarrow1_{-1}$ E	96.73939	√
CH_3OH	$J_K=2_0\rightarrow1_0$ A+	96.74142	√
CH_3OH	$J_K=2_0\rightarrow1_0$ E	96.74458	√
CH_3OH	$J_K=2_1\rightarrow1_1$ E	96.75551	√
^{34}SO	$J_K=4_5\rightarrow4_4$	96.781849	
U		96.797	
$C^{33}S$	J=2→1	97.172086	
$HCOOCH_3$	$J_{K_-,K_+}=8_{1,7}\rightarrow7_{1,6}$ E	100.48227	
$HCOOCH_3$	$J_{K_-,K_+}=8_{1,7}\rightarrow7_{1,6}$ A	100.49066	
$HCOOCH_3$	$J_{K_-,K_+}=9_{0,9}\rightarrow8_{0,8}$ E	100.68158	
$HCOOCH_3$	$J_{K_-,K_+}=9_{0,9}\rightarrow8_{0,8}$ A	100.68333	
CH_3COOH	$J_{K_-,K_+}=9_{*,9}\rightarrow8_{*,8}$ E	100.85502	
CH_3COOH	$J_{K_-,K_+}=9_{*,9}\rightarrow8_{*,8}$ A	100.89783	

TABLE D.6: 115 GHz Interferometric Passband Molecular Transitions

Species	Transition	Rest Freq.	Targeted
continuum			✓
CH_3COOH	$J_{K_-,K_+}=10_{*,10}\rightarrow 9_{*,9}$ E	111.50682	
CH_3COOH	$J_{K_-,K_+}=10_{*,10}\rightarrow 9_{*,9}$ A	111.54895	
HCOOH?	$J_{K_-,K_+}=5_{0,5}\rightarrow 4_{0,4}$	111.74678	
CH_3OCH_3	$J_{K_-,K_+}=7_{0,7}\rightarrow 6_{1,6}$ EE	111.78326	
$(NH_2)_2CO$	$J_{K_-,K_+}=4_{2,2}\rightarrow 3_{1,3}$	112.01032	
$(NH_2)_2CO$	$J_{K_-,K_+}=5_{5,0}\rightarrow 4_{4,1}$	112.02419	
CH_3CHO	$J_{K_-,K_+}=6_{0,6}\rightarrow 5_{0,5}$ E	114.9399	
CH_3CHO	$J_{K_-,K_+}=6_{0,6}\rightarrow 5_{0,5}$ A	114.95965	
NS	$^2\Pi_{1/2}$ J=5/2→3/2 F=7/2 c	115.15384	
NS	$^2\Pi_{1/2}$ J=5/2→3/2 F=5/2 c	115.1568	
NS	J=5/2→3/2 F=3/2→3/2 c	115.18533	
CO	J=1→0	115.2712	✓
SiC_2	$J_{K_-,K_+}=5_{0,5}\rightarrow 4_{0,4}$	115.383	

TABLE D.7: 104 GHz Interferometric Passband Molecular Transitions

Species	Transition	Rest Freq.	Targeted
continuum			✓
C_3H	$^2\Pi_{3/2}$ J=9/2→7/2 b	103.37266	
$HCOOCH_3$	$J_{K_-,K_+}=8_{2,6}\rightarrow7_{2,5}$ E	103.4666	
$HCOOCH_3$	$J_{K_-,K_+}=8_{2,6}\rightarrow7_{2,5}$ A	103.47864	
U		103.549	
CH_2CHCN	$J_{K_-,K_+}=11_{0,11}\rightarrow10_{0,10}$	103.5754	
U		103.6418	
CH_3CH_2OH?	$J_{K_-,K_+}=9_{1,8}\rightarrow8_{2,7}$	103.70281	
HC_5N	J=39→38	103.83681	
U		103.915	
SO_2	$J_{K_-,K_+}=3_{1,3}\rightarrow2_{0,2}$	104.02942	✓
CH_3OH	$J_K=3_1\rightarrow4_0$ A+	107.01385	
$^{13}CH_3CN$	$J_K=6_3\rightarrow5_3$	107.17849	
$^{13}CH_3CN$	$J_K=6_2\rightarrow5_2$	107.18855	
$^{13}CH_3CN$	$J_K=6_1\rightarrow5_1$	107.19458	
$^{13}CH_3CN$	$J_K=6_0\rightarrow5_0$	107.19659	
CH_3SH	$J_K=3_{-1}\text{-}3_0$ A	107.31646	
CH_3CH_2CN	$J_{K_-,K_+}=12_{7,5}\rightarrow11_{7,4}$	107.48518	
CH_3CH_2CN	$J_{K_-,K_+}=12_{7,6}\rightarrow11_{7,5}$	107.48518	
CH_3CH_2CN	$J_{K_-,K_+}=12_{6,6}\rightarrow11_{6,5}$	107.48696	
CH_3CH_2CN	$J_{K_-,K_+}=12_{6,7}\rightarrow11_{6,6}$	107.48696	
CH_3CH_2CN	$J_{K_-,K_+}=12_{8,4}\rightarrow11_{8,3}$	107.49157	
CH_3CH_2CN	$J_{K_-,K_+}=12_{8,5}\rightarrow11_{8,4}$	107.49157	
CH_3CH_2CN	$J_{K_-,K_+}=12_{5,8}\rightarrow11_{5,7}$	107.50243	
CH_3CH_2CN	$J_{K_-,K_+}=12_{5,7}\rightarrow11_{5,6}$	107.50247	
NH_2CH_2COOH	$J_{K_-,K_+}=18_{0,18}\rightarrow17_{1,17}$	107.5126	
NH_2CH_2COOH	$J_{K_-,K_+}=18_{1,18}\rightarrow17_{1,17}$	107.51359	
NH_2CH_2COOH	$J_{K_-,K_+}=18_{0,18}\rightarrow17_{0,17}$	107.51454	
NH_2CH_2COOH	$J_{K_-,K_+}=18_{1,18}\rightarrow17_{0,17}$	107.51553	
CH_3CH_2CN?	$J_{K_-,K_+}=12_{10,2}\rightarrow11_{10,1}$	107.51993	
CH_3CH_2CN?	$J_{K_-,K_+}=12_{10,3}\rightarrow11_{10,2}$	107.51993	
$HCOOCH_3$	$J_{K_-,K_+}=9_{2,8}\rightarrow8_{2,7}$ E	107.53727	
$HCOOCH_3$	$J_{K_-,K_+}=9_{2,8}\rightarrow8_{2,7}$ A	107.54366	
CH_3CH_2CN	$J_{K_-,K_+}=12_{3,10}\rightarrow11_{3,9}$	107.59405	

TABLE D.8: 109 GHz Interferometric Passband Molecular Transitions

Species	Transition	Rest Freq.	Targeted
continuum			√
$HOCO^+$	$J_{K_-,K_+}=5_{0,5}\rightarrow4_{0,4}$	106.91352	
^{29}SiS	$J=6\rightarrow5$	106.92295	
U		106.942	
U		106.963	
U		106.981	
U		106.995	
CH_3OH	$J_K=3_1\rightarrow4_0$ A^+	107.01385	
U		110.24	
C_6H	$^2\Pi_{1/2}$ $J=79/2\rightarrow77/2$	110.2434	
$CH_3{}^{13}CN$	$J_K=6_3\rightarrow5_3$	110.30988	
$CH_3{}^{13}CN$	$J_K=6_1\rightarrow5_1$	110.32678	
$CH_3{}^{13}CN$	$J_K=6_0\rightarrow5_0$	110.32889	
CH_3CN	$J_K=6_5\rightarrow5_5$ $F=7\rightarrow6$	110.33063	√
CH_3CN	$J_K=6_5\rightarrow5_5$ $F=5\rightarrow4$	110.33087	√
CH_3CN	$J_K=6_4\rightarrow5_4$ $F=7\rightarrow6$	110.34966	√
CH_3CN	$J_K=6_4\rightarrow5_4$ $F=5\rightarrow4$	110.3498	√
CH_3CN	$J_K=6_3\rightarrow5_3$ $F=7\rightarrow6$	110.36447	√
CH_3CN	$J_K=6_3\rightarrow5_3$ $F=5\rightarrow4$	110.36452	√
HC_3N	$J=12\rightarrow11$ $\nu_7=3$ $\ell=1f$	110.36648	
CH_3CN	$J_K=6_2\rightarrow5_2$ $F=7\rightarrow6$	110.37505	√
CH_3CN	$J_K=6_1\rightarrow5_1$ $F=7\rightarrow6$	110.3814	√
CH_3CN	$J_K=6_0\rightarrow5_0$ $F=7\rightarrow6$	110.38352	√

TABLE D.9: 112 GHz Interferometric Passband Molecular Transitions

Species	Transition	Rest Freq.	Targeted
continuum			✓
^{13}CN	$J=1/2\rightarrow1/2\ F=2\rightarrow1,F_1=0,F_2=1\rightarrow0$	108.6513	
^{13}CN	$J=1/2\rightarrow1/2\ F=2\rightarrow2,F_1=1,F_2=1\rightarrow1$	108.65765	
^{13}CN	$J=1/2\rightarrow1/2\ F=1\rightarrow2,F_1=1,F_2=1\rightarrow1$	108.65895	
HC^{13}CCN	$J=12\rightarrow11$	108.71052	
HCC^{13}CN	$J=12\rightarrow11$	108.72101	
^{13}CN	$J=3/2\rightarrow1/2\ F=3\rightarrow2,F_1=1,F_2=2\rightarrow1$	108.7802	
^{13}CN	$J=3/2\rightarrow1/2\ F=2\rightarrow1,F_1=1,F_2=2\rightarrow1$	108.78237	
^{13}CN	$J=3/2\rightarrow1/2\ F=1\rightarrow0,F_1=1,F_2=2\rightarrow1$	108.78698	
C_3N	$N=11\rightarrow10\ J=23/2\rightarrow21/2$	108.83427	
C_3N	$N=11\rightarrow10\ J=21/2\rightarrow19/2$	108.85302	
O^{13}CS	$J=9\rightarrow8$	109.11084	
HC_3N	$J=12\rightarrow11\ \nu_5=1\ \ell=1f$	109.24434	
SO	$J_K=2_3\rightarrow1_2$	109.25218	✓
$(NH_2)_2CO$	$J_{K_-,K_+}=4_{2,2}\rightarrow3_{1,3}$	112.01032	
$(NH_2)_2CO$	$J_{K_-,K_+}=5_{5,0}\rightarrow4_{4,1}$	112.02419	
CH_3CHO	$J_{K_-,K_+}=6_{1,6}\rightarrow5_{1,5}$ A	112.24872	
CH_3CHO	$J_{K_-,K_+}=6_{1,6}\rightarrow5_{1,5}$ E	112.25448	
HCOOH	$J_{K_-,K_+}=5_{3,3}\rightarrow4_{3,2}$	112.45961	
HCOOH	$J_{K_-,K_+}=5_{3,2}\rightarrow4_{3,1}$	112.467	
CH_3CH_2CN	$J_{K_-,K_+}=13_{1,13}\rightarrow12_{1,12}$	112.64624	

TABLE D.10: 73 GHz Interferometric Passband Molecular Transitions

Species	Transition	Rest Freq.	Targeted
CH_3OCH_3	$J_{K_-,K_+}=10_{1,9}\rightarrow10_{0,10}$	72.2987	
U		72.403	
H_2CO	$J_{K_-,K_+}=5_{1,4}\rightarrow5_{1,5}$	72.409092	
DCN	$J=1\rightarrow0\ F'=1\rightarrow1\ F=1\rightarrow0,1,2$	72.413484	
DCN	$J=1\rightarrow0\ F''=1\rightarrow1\ F=2\rightarrow1,2$	72.413514	
DCN	$J=1\rightarrow0\ F''=1\rightarrow1\ F=0\rightarrow0,1$	72.413558	
DCN	$J=1\rightarrow0\ F''=2\rightarrow1\ F=1\rightarrow0,1,2$	72.414905	
DCN	$J=1\rightarrow0\ F''=2\rightarrow1\ F=2\rightarrow1,2$	72.414927	
DCN	$J=1\rightarrow0\ F''=2\rightarrow1\ F=3\rightarrow2$	72.414973	
DCN	$J=1\rightarrow0\ F''=0\rightarrow1\ F=1\rightarrow0,1,2$	72.417029	
U		72.42	
$HCOOCH_3$	$J_{K_-,K_+}=6_{2,5}\rightarrow5_{2,4}$ E	72.680848	
$HCOOCH_3$	$J_{K_-,K_+}=6_{2,5}\rightarrow5_{2,4}$ A	72.685581	
H_2CO	$J_{K_-,K_+}=1_{0,1}\rightarrow0_{0,0}$	72.83795	✓
CH_3OCH_3	$J_{K_-,K_+}=12_{2,10}\rightarrow12_{1,11}$ AE	75.90642	
CH_3OCH_3	$J_{K_-,K_+}=12_{2,10}\rightarrow12_{1,11}$ EE	75.90803	
CH_3OCH_3	$J_{K_-,K_+}=12_{2,10}\rightarrow12_{1,11}$ AA	75.90965	
DNC	$J=1\rightarrow0$	76.305727	

Table D.11: 87 GHz Interferometric Passband Molecular Transitions

Species	Transition	Rest Freq.	Targeted
C_2H	N=1→0 J=3/2→1/2 F=1→1	87.284156	√
U		87.299	
CH_2CHCN	$J_{K_-,K_+}=9_{1,8}\rightarrow 8_{1,7}$	87.312827	
C_2H	N=1→0 J=3/2→1/2 F=2→1	87.316925	√
U		87.323	
C_2H	N=1→0 J=3/2→1/2 F=1→0	87.328624	√
C_2H	N=1→0 J=1/2→1/2 F=1→1	87.402004	√
C_2H	N=1→0 J=1/2→1/2 F=0→1	87.407165	√
C_2H	N=1→0 J=1/2→1/2 F=1→0	87.446512	√
AlCl	J=6→5	87.458286	
U		90.809	
U		90.814	
U		90.82	
U		90.864	
CH_3OCH_3	$J_{K_-,K_+}=6_{0,6}\rightarrow 5_{1,5}$ AA	90.937539	
CH_3OCH_3	$J_{K_-,K_+}=6_{0,6}\rightarrow 5_{1,5}$ EE	90.938099	
CH_3OCH_3	$J_{K_-,K_+}=6_{0,6}\rightarrow 5_{1,5}$ AE+EA	90.938674	
HC_3N	J=10→9	90.978993	
HC_3N	J=10→9 $\nu_5=1$ $\ell=1e$	90.987005	

Table D.12: 91 GHz Interferometric Passband Molecular Transitions

Species	Transition	Rest Freq.	Targeted
HCOOH	$J_{K_-,K_+}=4_{1,4}\rightarrow 3_{1,3}$	86.54618	
U		86.98	
NH_2CH_2COOH	$J_{K_-,K_+}=15_{0,15}\rightarrow 14_{1,14}$	90.035997	
U		90.038	
NH_2CH_2COOH	$J_{K_-,K_+}=15_{1,15}\rightarrow 14_{1,14}$	90.043211	
NH_2CH_2COOH	$J_{K_-,K_+}=15_{0,15}\rightarrow 14_{0,14}$	90.049773	
U		90.051	
NH_2CH_2COOH	$J_{K_-,K_+}=15_{1,15}\rightarrow 14_{0,14}$	90.056987	
CH_3COOH	$J_{K_-,K_+}=8_{*,8}\rightarrow 7_{*,7}$ E	90.20335	
U		90.212	
CH_3COOH	$J_{K_-,K_+}=8_{*,8}\rightarrow 7_{*,7}$ A	90.24626	
HNC	J=1→0 F=0→1	90.66345	√
HNC	J=1→0	90.663543	√
HNC	J=1→0 F=2→1	90.663574	√
HNC	J=1→0 F=1→1	90.663656	√

D.2 Sample Observe Command File

```
#!/bin/csh -f
#
#    Observing script for comet Hale-Bopp, _1000132,
#    for the cross-correlation.
#
#    HCN J=1-0 and HCO+ J=1-0 in USB.
#    Also in there is continuum containing a lot of lines
#
#    PI: Jeff Veal
#    Email: veal@astro.uiuc.edu
#    Telephone: (217) 244-5471 (office)  (217) 367-4459 (home)
#
#    Source     =  _1000132 (comet Hale-Bopp)
#    vlsr       =  0 km/s
#    elev limit =  15 degrees
#
#    97mar18:00
#    Rises at LST = 16:02:35.874   sets at 30:56:29.741
#    J2000    RA: 23:29:32.794        DEC: 44:21:36.222
#    97mar25:00
#    Rises at LST = 17:04:10.707   sets at 08:14:00.088
#    J2000    RA: 00:39:05.382        DEC: 45:49:14.769
#    97apr01:00
#    Rises at LST = 18:19:23.786   sets at 09:15:11.561
#    J2000    RA: 01:47:17.654        DEC: 44:32:18.646
#    97apr08:00
#    Rises at LST = 19:34:44.595   sets at 09:56:09.279
#    J2000    RA: 02:45:26.920        DEC: 41:07:24.957
#
#---------------------------------SETUPS------------------------------------
#
setup name=tune freq=88.631847 iffreq=209 obsline=hcn dopsrc=_1000132
#
setup name=narrow cormode=6 corbw=12.5,100,12.5,100 \
      corf=215.002,416.254,772.504,637.500 \
      restfqs=85.672570,85.457300,85.265470,85.139108,0,0,88.631847,
88.843240,89.045590,89.188518,0,0 \
     elevlim=15,85 itime=50 nchan=-1
#
setup name=wide cormode=8 corbw=100,100,100,100 corf=205,400,600,800 \
     restfqs=0,0,0,0,0,0,0,0,0,0,0,0,0,0,0,0 elevlim=15,85 itime=50 nchan=-1
#
```

```
setup name=comet setup=narrow source=_1000132 vis=_1000132 stop=+25 nchan=+1
#
setup name=0102 setup=wide source=0102+584 vis=0102+584 stop=+5
#
setup name=3c273.w setup=wide source=3c273 vis=3c273.w stop=+5
setup name=3c273.n setup=narrow source=3c273 vis=3c273.n stop=+30
setup name=venus.w setup=wide source=venus vis=venus.w stop=+5
setup name=venus.n setup=narrow source=venus vis=venus.n stop=+18
setup name=3c111.w setup=wide source=3c111 vis=3c111.w stop=+5
setup name=3c111.n setup=narrow source=3c111 vis=3c111.n stop=+28
#
setup name=quality s=_1000132 c=0102+584,3c273.w,venus.w,3c111.w p=3c273.n,
 venus.n,3c111.n email=veal@astro.uiuc.edu
#
#------------------------------OBSERVING-----------------------------------
#
scan setup='tune'
#
loop srcsetup='3c273.n' calsetup='3c273.w' stop=1615
#
loop srcsetup='comet|(venus.w,venus.n,venus.w)' calsetup='0102'
#
exit 0
```

D.3 Sample Data Reduction Script

```
#! /bin/csh -vf

goto start

start:
cp -r bllac phasecal
cp -r _1000132 source
listobs in=phasecal,source log=listobs.log
uvplt vis=source axis=uc,vc inc=1 options=equal,nobase device=/xw

# Do the linelength calibration
linecal vis=phasecal
uvcat   vis=phasecal out=phasecal.ll
linecal vis=source
uvcat   vis=source out=source.ll

# Flag obvious bad data
uvflag vis=phasecal.ll select=shadow'(6.1)' flagval=flag
```

```
uvflag vis=source.ll select=shadow'(6.1)' flagval=flag
uvflag vis=phasecal.ll edge=2,2 flagval=flag
uvflag vis=source.ll edge=2,2 flagval=flag

# Find elusive bad data
uvplt vis=phasecal.ll axis=time,amp inc=1 line=wide,1,1 nxy=2,2 device=/xw
uvplt vis=phasecal.ll axis=time,amp inc=1 line=wide,1,2 nxy=2,2 device=/xw
uvplt vis=phasecal.ll axis=time,phase inc=1 line=wide,1,1 nxy=2,2 device=/xw
uvplt vis=phasecal.ll axis=time,phase inc=1 line=wide,1,2 nxy=2,2 device=/xw
uvplt vis=source.ll axis=time,amp inc=1 line=wide,1,1 nxy=2,2 device=/xw
uvplt vis=source.ll axis=time,amp inc=1 line=wide,1,2 nxy=2,2 device=/xw
uvplt vis=source.ll axis=time,phase inc=1 line=wide,1,1 nxy=2,2 device=/xw
uvplt vis=source.ll axis=time,phase inc=1 line=wide,1,2 nxy=2,2 device=/xw
uvplt vis=source.ll axis=time,amp inc=1 device=/xw options=nobase

# Hone in on and flag elusive bad data
uvspec vis=phasecal.ll device=/xw nxy=2,2
uvplt vis=source.ll axis=time,amp inc=1 device=/xw options=nobase \
      select=time'(97mar18:12,97mar18:13)'
uvspec vis=source.ll device=/xw nxy=2,2
uvflag vis=phasecal.ll select=-amp'(.1,20)' flagval=flag
uvflag vis=source.ll select=time'(97mar18:12,97mar18:13)' flagval=f
uvplt vis=source.ll axis=time,amp inc=1 device=/xw options=nobase
uvplt vis=source.ll axis=time,amp inc=1 line=wide,1,1 nxy=2,2 device=/xw
uvplt vis=source.ll axis=time,amp inc=1 line=wide,1,2 nxy=2,2 device=/xw

# Remake wideband after flagging and fit phases of phase calibrator
uvwide vis=phasecal.ll out=phasecal.nw
uvwide vis=source.ll out=source.nw
gmake vis=phasecal.nw interval=10 refant=6 options=phase out=phasecal.gm
gfiddle vis=phasecal.gm device=/xw out=phasecal.gf
gapply vis=phasecal.nw gvis=phasecal.gf options=phase out=phasecal.ga

# Inspect phase calibrator uv data
uvplt vis=phasecal.ga axis=time,amp inc=1 line=wide,1,1 nxy=2,2 device=/xw
uvplt vis=phasecal.ga axis=time,amp inc=1 line=wide,1,2 nxy=2,2 device=/xw
uvplt vis=phasecal.ga axis=time,phase inc=1 line=wide,1,1 nxy=2,2 device=/xw
uvplt vis=phasecal.ga axis=time,phase inc=1 line=wide,1,2 nxy=2,2 device=/xw

# Image phase calibrator and make sure it looks like a point source
invert vis=phasecal.ga map=phasecal.mp beam=phasecal.bm imsize=128 \
       cell=1.5 sup=0 line=wide,2,1 options=systemp
cgdisp in=phasecal.mp device=/xw nxy=2,1 options=fiddle
gapply vis=source.nw gvis=phasecal.gf options=phase out=source.ga
```

```
uvcat vis=source.ga out=source.done

# Inspect source uv data
uvplt vis=source.done axis=time,amp inc=1 line=wide,1,1 nxy=2,2 device=/xw
uvplt vis=source.done axis=time,amp inc=1 line=wide,1,2 nxy=2,2 device=/xw
uvplt vis=source.done axis=time,phase inc=1 line=wide,1,1 nxy=2,2 device=/xw
uvplt vis=source.done axis=time,phase inc=1 line=wide,1,2 nxy=2,2 device=/xw
uvplt vis=source.done axis=time,amp inc=1 device=/xw options=nobase

# Ftp data to "hat" computer at Hat Creek to run the ephemeris corrector and
# then ftp adjusted data back
ephmedit vis=source.done source=_1000132 apfile=fm18

# Image HCN window
uvcat vis=source.done_c select=window'(7)' out=hcn
uvlist vis=hcn options=spectra,full
invert vis=hcn map=hcn.mp beam=hcn.bm imsize=256 \
       cell=1 robust=0.5 line=channel,128,72,1,1 options=systemp
cgdisp in=hcn.bm device=/xw
cgdisp in=hcn.bm type=contour region=relpix,box'(-50,-50,50,50)' slev=p,1 \
       levs1=5,20,35,50,65,80,95 device=/xw options=full
cgdisp in=hcn.bm type=contour region=relpix,box'(-50,-50,50,50)' slev=p,1 \
       levs1=5,20,35,50,65,80,95 device=hcn.bm.ps/ps options=full

# Find clean cutoff and produced finished image
histo in=hcn.mp region=relpix,box'(-110,-110,-40,110)'
clean map=hcn.mp beam=hcn.bm cutoff=.176 niters=3000 out=hcn.cl
restor model=hcn.cl map=hcn.mp beam=hcn.bm out=hcn.cm
#moment in=hcn.cm out=hcn.mm mom=0
histo in=hcn.cm region=relpix,box'(-110,-110,-40,110)'
fits in=hcn.cm op=xyout out=hcn.cm.fits

# Find channels over which to sum for line image
cgdisp in=hcn.cm region=relpix,box'(-20,-20,20,20)(50,80)' device=/xw
cgdisp in=hcn.cm region=relpix,box'(-5,-5,5,5)(66)' device=/xw
imspec in=hcn.cm region=relpix,box'(1,-1,1,-1)' plot=mean \
       options=style,step device=/xw
imspec in=hcn.cm region=relpix,box'(1,-1,1,-1)(23,73)' plot=mean \
       options=style,step device=/xw
mv hcn.cm hcn.cm.2
imbin in=hcn.cm.2 bin=1,1,1,1,2,2 out=hcn.cm
histo in=hcn.cm region=relpix,box'(-110,-110,-40,110)'
imspec in=hcn.cm region=relpix,box'(1,-1,1,-1)' plot=mean \
       options=style,step device=/xw
```

```
# Create HCN image and spectrum
moment in=hcn.cm region=image'(29,35)' out=hcn5.cm mom=-1
moment in=hcn.cm region=image'(15,21)' out=hcn3.cm mom=-1
maths exp='(hcn5.cm+hcn3.cm)' out=hcn53.cm
rm -r hcn3.cm hcn5.cm
cgdisp in=hcn53.cm type=contour region=relpix,box'(-40,-40,40,40)' \
       slev=a,.062 levs1=-6,-3,3,6,9,12,15,18,21,24,27,30,33,36,39,42 \
       device=/xw labtyp=arcsec options=full,beambl csize=2,0,2,0 \
       olay=olay.in
cgdisp in=hcn53.cm type=contour region=relpix,box'(-10,-10,10,10)' \
       slev=a,.062 levs1=-6,-3,3,6,9,12,15,18,21,24,27,29.1 \
       device=/xw labtyp=arcsec options=full csize=2,0,2,0 olay=olay.in
cgdisp in=hcn53.cm type=contour region=relpix,box'(-40,-40,40,40)' \
       slev=a,.062 levs1=-6,-3,3,6,9,12,15,18,21,24,27 \
       device=/xw labtyp=arcsec options=beambl csize=2,0,2,0 olay=olay.in
cgdisp in=hcn53.cm type=contour region=relpix,box'(-40,-40,40,40)' \
       slev=a,.062 levs1=-6,-3,3,6,9,12,15,18,21,24,27 \
       device=hcn53.mar18.ps/ps \
       labtyp=arcsec options=beambl csize=2,0,2,0 olay=olay.in
imspec in=hcn.cm region=relpix,box'(1,2,1,2)' plot=mean \
       options=style,step,title,18-Mar-UT device=/xw
hanning in=hcn.cm out=spectrum region=relpix,box'(1,2,1,2)' width=1
fits in=spectrum out=spectrum.fits op=xyout
rm -r spectrum

# Proceed to image continuum
uvcat vis=source.done_c select=window'(2)' out=c2
uvcat vis=source.done_c select=window'(3)' out=c3
uvcat vis=source.done_c select=window'(5)' out=c5
uvcat vis=source.done_c select=window'(6)' out=c6
uvcat vis=source.done_c select=window'(8)' out=c8
uvcat vis=source.done_c select=window'(9)' out=c9
uvcat vis=source.done_c select=window'(11)' out=c11
uvcat vis=source.done_c select=window'(12)' out=c12
invert vis=c2,c3,c5,c6,c8,c9,c11,c12 map=cont.mp \
       beam=cont.bm imsize=256 cell=1 robust=0.5 line=channel,1,3,28 \
       options=systemp
cgdisp in=cont.bm device=/xw
cgdisp in=cont.bm type=contour region=relpix,box'(-50,-50,50,50)' slev=p,1 \
       levs1=5,20,35,50,65,80,95 device=/xw options=full
cgdisp in=cont.bm type=contour region=relpix,box'(-50,-50,50,50)' slev=p,1 \
       levs1=5,20,35,50,65,80,95 device=cont.bm.ps/ps options=full
histo in=cont.mp region=relpix,box'(-110,-110,-40,110)'
```

```
clean map=cont.mp beam=cont.bm cutoff=.00161 niters=3000 out=cont.cl
restor model=cont.cl map=cont.mp beam=cont.bm out=cont.cm
histo in=cont.cm region=relpix,box'(-110,-110,-40,110)'
cgdisp in=cont.cm type=contour region=relpix,box'(-40,-40,40,40)' \
       slev=a,.00153 levs1=-4,-2,2,4,6,7.5 device=/xw \
       labtyp=arcsec options=full,beambl csize=2,0,2,0 olay=olay.in
cgdisp in=cont.cm type=contour region=relpix,box'(-40,-40,40,40)' \
       slev=a,.00153 levs1=-4,-2,2,4,6 device=/xw \
       labtyp=arcsec options=beambl csize=2,0,2,0 olay=olay.in
cgdisp in=cont.cm type=contour region=relpix,box'(-40,-40,40,40)' \
       slev=a,.00153 levs1=-4,-2,2,4,6 device=cont.mar18.ps/ps \
       labtyp=arcsec options=beambl csize=2,0,2,0 olay=olay.in
end:

#rm -r source phasecal *.ll *.nw *.gm *.gf *.ga *.mp *.bm hcn *.cl *.fits
#rm -r c2 c3 c5 c6 c8 c9 c11 c12

#olay.in:
#line arcsec arcsec id no 0  0 -2.6 -20
#clear arcsec arcsec to_Sun yes -7 -25
#clear arcsec arcsec 18_Mar yes 25 35
##clear arcsec arcsec (g) yes -30 35
```

D.4 Sample Correlator Setup

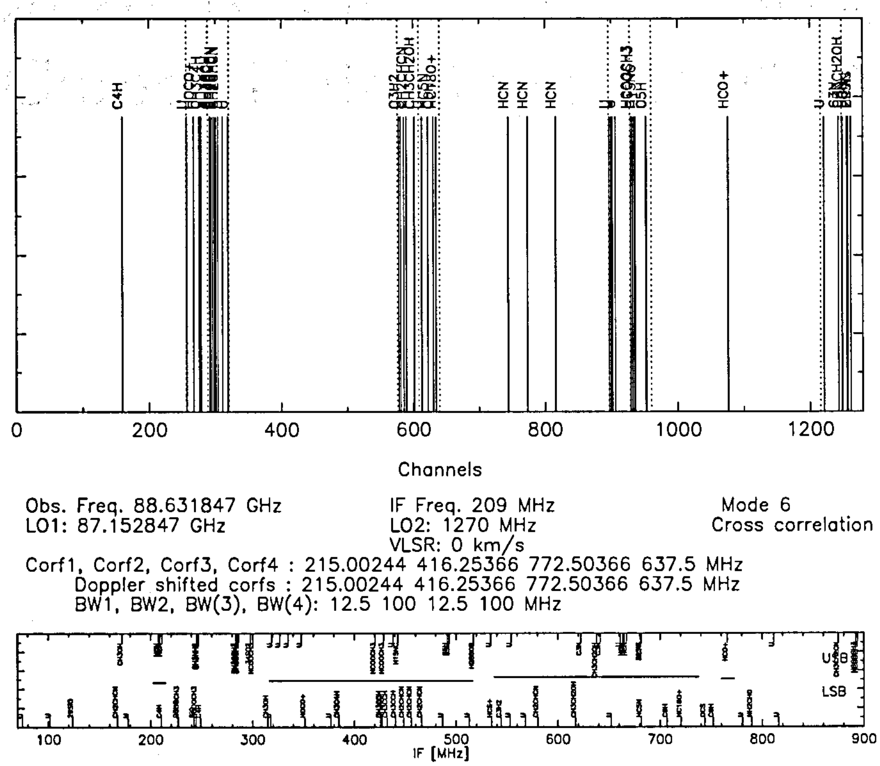

```
Obs. Freq. 88.631847 GHz          IF Freq. 209 MHz          Mode 6
LO1: 87.152847 GHz                LO2: 1270 MHz             Cross correlation
                                  VLSR: 0 km/s
Corf1, Corf2, Corf3, Corf4 : 215.00244 416.25366 772.50366 637.5 MHz
      Doppler shifted corfs : 215.00244 416.25366 772.50366 637.5 MHz
      BW1, BW2, BW(3), BW(4): 12.5 100 12.5 100 MHz
```

FIGURE D.1: Correlator setup used for interferometric observations

Appendix E

Mosaicked Images and Spectra of $J=1\rightarrow0$ HCN and HCO^+ emission from Comet Hale-Bopp (1995 O1)

THE ASTRONOMICAL JOURNAL, 116:3018–3028, 1998 December

MOSAICKED IMAGES AND SPECTRA OF $J = 1 \rightarrow 0$ HCN AND HCO^+ EMISSION FROM COMET HALE-BOPP (1995 O1)

M. C. H. WRIGHT,[1] I. DE PATER,[1] J. R. FORSTER,[1] PATRICK PALMER,[2] LEWIS E. SNYDER,[3] J. M. VEAL,[3]
MICHAEL F. A'HEARN,[4] L. M. WOODNEY,[4] WILLIAM M. JACKSON,[5] Y.-J. KUAN,[6] AND A. J. LOVELL[7]

Received 1998 June 26; revised 1998 August 26

ABSTRACT

We used the BIMA array to map comet Hale-Bopp (1995 O1) in HCN and HCO^+ emission at 89 GHz with 10″ angular resolution. The mosaicked images with seven pointing centers were combined with single-dish data to form completely sampled images of a region ~4′ in diameter. The HCN image is roughly compatible with a Haser model in which most of the HCN comes from the nucleus. However, clear deviations from circular symmetry are present, and roughly 20% of the HCN does not appear to come from the nuclear source. Frequently, the HCN has an asymmetric, double-peaked profile. The double peak is expected from the Haser model, and the asymmetry observed on April 3 could come from an increased gas production toward the Sun and facing the observer. The abundance of HCN relative to H_2O is ~0.3%. The HCO^+, in contrast, is smooth, almost completely resolved in the interferometer observations, and offset toward the ion tail by about 1′. This behavior is compatible with expectations from a simple scaling of previous work.

Key words: comets: individual (Hale-Bopp 1995 O1) — techniques: interferometric

1. INTRODUCTION

The size scales of comets range from a few kilometers for the nucleus, to a few times 10^4 km for the coma, and up to more than 10^6 km for the dust and ion tails; the corresponding angular sizes for Earth-based observations range from the subarcsecond scale to many degrees on the sky. Therefore, telescopes with many different fields of view must be used to obtain a complete picture of the behavior of a comet. Because comet Hale-Bopp (1995 O1) was extremely bright, it was probably the most widely observed comet in history.

The very high gas production rate of comet Hale-Bopp presented a unique opportunity to image emission at millimeter wavelengths from a variety of molecules. If the emission originates from molecules sublimed directly from the nucleus, the scale length is approximately equal to the product of the lifetime of the molecules against photodissociation and the average outflow velocity of the molecules. A typical molecular lifetime at Earth's orbit is ~0.1–1.0 day, which with a typical outflow velocity of ~1 km s^{-1} translates into a scale length of order ~10^4–10^5 km. For a comet at a geocentric distance of 1 AU, these distances correspond to angular scales of 10″–100″. Single-dish observations are sensitive to the large angular scales but lack the resolution to map emission structure close to the nucleus. Interferometric arrays provide higher resolution but are insensitive to emission with spatial scales greater than $\lambda/D_{\rm min}$, where $D_{\rm min}$ is the shortest interferometer baseline. Because larger scale structure is resolved out in the images, single-dish spectra can look quite different from spectra constructed from interferometric images. If the source region is very large and smooth, interferometer images may not show any emission despite strong signals in single-dish spectra. A combination of single-dish and interferometer observations at multiple pointing centers can effectively image structure larger than the primary beam and $\lambda/D_{\rm min}$ by using a mosaicking algorithm (Cornwell & Fomalont 1989; Sault, Staveley-Smith, & Brouw 1996).

In this paper we present autocorrelation spectra (single-dish observations) and mosaicked images of Hale-Bopp in HCN and HCO^+ emission obtained with the BIMA array.[8] The 10″ angular resolution corresponds to linear resolutions from 9900 to 13,500 km at the comet during the observations reported here. This paper concentrates on emission from relatively large angular scales, although our resolution is similar to that expected for the smallest angular scales for these molecules. Detailed analysis of a large number of single-field images in HCN during the apparition of Hale-Bopp will be presented in separate papers.

Optical CN lines from comets have been studied for many decades. The parent molecule of CN has been heavily debated, and HCN emerged early on as a likely possibility (see, for example, Whipple 1950). HCN was first directly identified through its $J = 1 \rightarrow 0$ transition at 3 mm wavelength in comet Kohoutek (Huebner, Snyder, & Buhl 1974) and seemed to solve the problem of the identification of the parent molecule of CN. Beginning with comet Halley in

---

[1] Department of Astronomy, University of California, Berkeley, CA 94720; mwright@astro.berkeley.edu, rforster@astro.berkeley.edu, imke@floris.berkeley.edu.

[2] Department of Astronomy and Astrophysics, University of Chicago; ppalmer@oskar.uchicago.edu.

[3] Department of Astronomy, University of Illinois, 1002 West Green Street, Urbana, IL 61801; snyder@astro.uiuc.edu, veal@astro.uiuc.edu.

[4] Department of Astronomy, University of Maryland, College Park, MD 20742-2421; ma@astro.umd.edu, woodney@astro.umd.edu.

[5] Department of Chemistry, University of California, Davis, CA 95616; jackson@indigo.ucdavis.edu.

[6] Department of Earth Sciences, National Taiwan Normal University; and Academia Sinica, Institute of Astronomy and Astrophysics, Taipei, Taiwan; kuan@biaa17.biaa.sinica.edu.tw.

[7] Department of Astronomy, Five College Radio Astronomy Observatory (FCRAO); lovell@fcraol.phast.umass.edu.

[8] The BIMA array is operated by the Berkeley-Illinois-Maryland Association under funding from the National Science Foundation.

1986, additional measurements of radio emission of HCN were made, and the CN parent issue was again raised (e.g., compare Schloerb et al. 1986 with Depois et al. 1986). An additional question about the relationship between optical CN and radio HCN lines was implicitly raised by the observation of a spiral-like component in the CN emission from comet Halley (A'Hearn et al. 1986). This component was at a distance beyond the HCN photodissociation scale length and was believed to be produced from dust. Therefore a careful study of the distribution of radio HCN emission in a bright comet is desired. Does a significant part of the observed CN come from HCN, and is HCN produced from the dust that is hypothesized to produce the CN in the spiral features? An early attempt to address these problems (Palmer et al. 1990) failed both because comet Austin (1989c1 = C/1989 X1) was too faint and because instrumentation and techniques were not sufficiently developed to permit the type of observations presented here.

In this paper, we discuss the first detection of HCO^+ in a comet (Veal et al. 1997). HCO^+ was first detected in the interstellar medium in 1970 in the form of the unidentified spectral line, X-ogen, at 89.189 GHz (Buhl & Snyder 1970; Snyder & Buhl 1971). Because it was the first unidentified interstellar microwave spectral line, its identification attracted a great deal of interest. Klemperer (1970) proposed that the carrier of the X-ogen line was the $J = 1 \rightarrow 0$ transition of HCO^+, but it took 6 more years to confirm the interstellar HCO^+ identification via the measurements of $H^{13}CO^+$ and DCO^+ in the interstellar medium (Snyder et al. 1976; Hollis et al. 1976) and in the laboratory by Woods et al. (1975). Starting with the seminal papers by Watson (1973) and by Herbst & Klemperer (1973), HCO^+ is now recognized as a keystone molecule for the ion-molecule reaction pathways for the formation of molecules in interstellar clouds. Although the probable formation of HCO^+ in cometary comae by ion-molecule reactions was discussed by Biermann & Diercksen (1974), it was labeled "invisible" at the time. The first detection of cometary HCO^+ was reported some 27 years after HCO^+ was detected in the interstellar medium. The focus of most previous radio molecular observations was on neutral species. Because of the lack of observational data, the chemical role of HCO^+ in comets is only rarely discussed in the literature. For example, although Huebner & Giguere (1980) included HCO^+ in their models, a decade later Huebner et al. (1991) noted that HCO^+ is included as an ion species in the proposed cometary chemical reaction network of Schmidt et al. (1988), but it is secondary to H_2O^+, H_3O^+, NH_4^+, and CH_2OH^+. In contrast to HCN, HCO^+ clearly is not a parent molecule. In order to understand the chemistry of HCO^+ it is essential to understand its spatial distribution with respect to cometary parent species like HCN. The chemistry of cometary HCO^+ is discussed by Lovell et al. (1998a, 1998b) and by Kuan et al. (1998).

2. OBSERVATIONS

Autocorrelation spectra and interferometer observations were obtained with the nine-antenna BIMA array (Welch et al. 1996). Autocorrelation observations were obtained using seven antennas simultaneously. We observed HCN $J = 1 \rightarrow 0$ at 88.63185 GHz and HCO^+ $J = 1 \rightarrow 0$ at 89.18852 GHz simultaneously with 0.16 km s^{-1} resolution. The amplitude scale was determined from planet observations, resulting in an absolute flux calibration to about 20% in both autocorrelation and interferometric observations.

2.1. *Autocorrelation Observations*

Autocorrelation spectra of comet Hale-Bopp were obtained between 1997 February 19 and May 6, spanning the period from approximately 1.5 months before perihelion passage until about 1 month after. A time sequence of the "single-dish" spectra is shown in Figures 1 (HCN) and 2 (HCO^+). All velocities in this paper are given in the cometocentric rest frame with the positive (redward) direction away from the observer. For HCN, the $F = 2 \rightarrow 1$ is used as the origin. On May 1 the comet was nearly directly in front of the large Heiles 2 molecular cloud complex, which itself shows HCN and HCO^+ line emission. A line at the typical velocity of peak emission for a number of molecules in this part of Heiles cloud 2 would be expected to show up in the range 0.9–1.9 km s^{-1} in the spectrum of the comet and is clearly seen in the HCO^+ spectra on this day. The half-power beamwidth of the 6 m antennas is 2′.2, which corresponds to a radius of 70,000–90,000 km at the comet, about the same as the HCN scale length during these observations (see § 4.1). Therefore, ~70% of the HCN emission

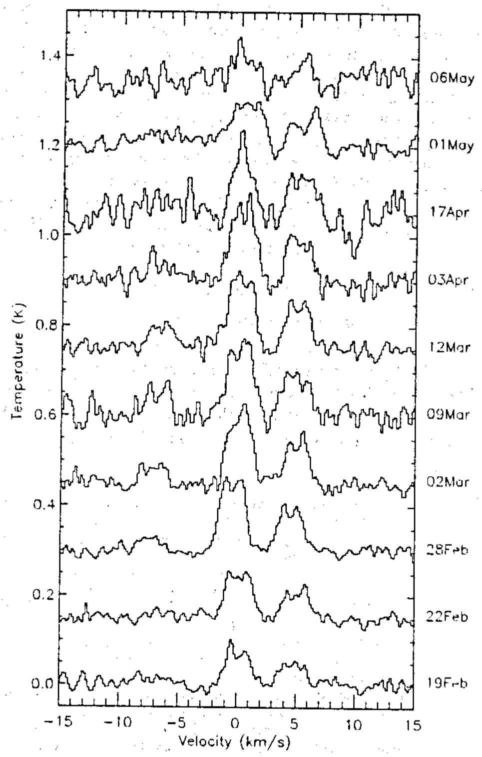

FIGURE E.1: HCN autocorrelation spectra.

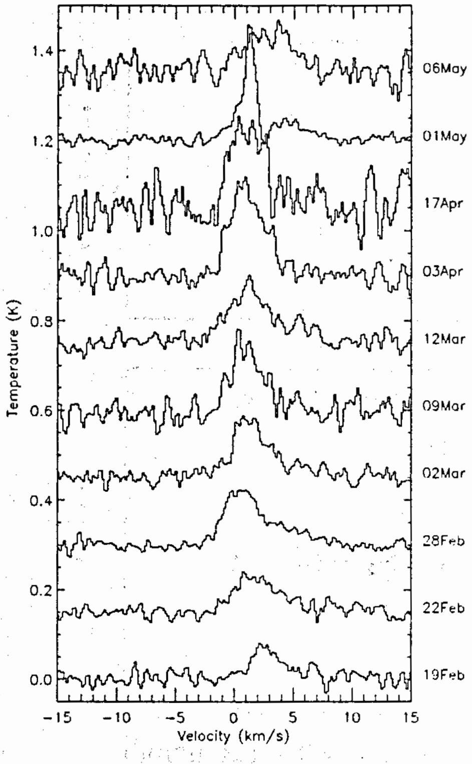

FIGURE E.2: HCO$^+$ autocorrelation spectra.

(assuming the source is purely nuclear; see § 4.1.1) is expected to be included in the autocorrelation spectra.

2.2. *Interferometer Observations*

The interferometer observations were obtained on 1997 April 3 and May 6. The times and ephemeris data used for these observations are given in Table 1. Hale-Bopp was observed using a compact configuration of the antennas providing 36 antenna separations from 6 to 69 m. We observed seven pointing positions on a hexagonal grid with 1′ spacing. The April 3 observations were centered on the nucleus using the JPL ephemeris reference orbit 55 (see Table 1). The May 6 observations were offset by 1′ in an antisolar direction, centered on the peak HCO$^+$ emission as estimated from preliminary images from FCRAO. Some of these images have been published in Lovell et al. (1998b). The quasar 0102+584 was observed as a phase calibrator at 25–30 minute intervals, after four complete cycles of the hexagonal pointing pattern with 50 s integrations at each pointing. Single-dish observations at the nuclear position were obtained using seven antennas on both days. On May 6 we also observed several offset positions to confirm the peak HCO$^+$ position.

Note that confusion with a background source, such as Heiles cloud 2 discussed above, will not be a problem for interferometric observations because we are tracking the comet, not the background source. In early May, the comet moved two synthesized beams in one 50 s integration period, very effectively suppressing any emission from the background. In addition to HCN and HCO$^+$, we observed with six 100 MHz wideband channels that we used to map the 3 mm continuum emission. These continuum observations are reported elsewhere (de Pater et al. 1998).

The interferometer data were corrected to the JPL ephemeris reference orbit 77 and combined using a maximum entropy mosaicking algorithm using the single-dish data as a default image (Cornwell & Fomalont 1989; Sault et al. 1996). The single-dish data were convolved onto the same grid as the interferometer image using the primary beamwidth of the BIMA antennas: 130″ (FWHM) at 89 GHz. Images were made with the MIRIAD software package (Sault, Teuben, & Wright 1995; Wright & Sault 1993). The synthesized beam was 11″ × 8″ for the April 3 data and 16″ × 8″ for the May 6 data.

3. RESULTS

3.1. *Autocorrelation Observations*

To quantify the evolution of the HCN and HCO$^+$ spectra shown in Figures 1 and 2, we made simple Gaussian fits to the data, where the peak intensity, line width (FWHM), and velocity offset of the peak are shown in

TABLE E.1: Ephemeris (with perturbations) for comet Hale-Bopp (C/1995 O1) at 1 day steps (0 hr UTC).

Date (UT) (1)	R.A. (J2000.0) (2)	Decl. (J2000.0) (3)	Δ (AU) (4)	$\dot{\Delta}$ (km s^{-1}) (5)	R (AU) (6)	Θ (deg) (7)	β (deg) (8)	P.A. (deg) (9)	P.A.($-V$) (deg) (10)
1997 Apr 3^a……	02 05 20.64	+43 45 08.5	1.367	15.01	0.915	42.0	47.0	29.1	298.2
1997 Apr 4^b……	02 13 55.10	+43 17 31.9	1.376	16.11	0.916	41.7	46.6	31.3	300.3
1997 May 6^c……	04 56 18.66	+23 00 03.9	1.856	29.70	1.102	29.8	27.1	83.1	341.3
1997 May 7^d……	04 59 09.50	+22 25 21.7	1.873	29.64	1.111	29.4	26.5	84.5	342.0

NOTE.—Data are for JPL reference orbit 55 by D. K. Yeomans (1997 March 4). Cols. (2) and (3): Geocentric astrometric right ascension and declination referred to the mean equator and equinox of J2000.0 (units of right ascension are hours, minutes, and seconds, and units of declination are degrees, arcminutes, and arcseconds). Light time corrections have been applied. Col. (4): Geocentric distance of object. Col. (5): Geocentric radial velocity of object. Col. (6): Heliocentric distance of object. Col. (7): Sun-Earth-object angle. Col. (8): Sun-object-Earth angle. Col. (9): Position angle of extended radius vector. Col. (10): Position angle of minus velocity vector.

[a] Starting date: 1997 April 3 14:13:29.9.

[b] Ending date: 1997 April 4 04:31:12.3.

[c] Starting date: 1997 May 6 16:29:39.6.

[d] Ending date: 1997 May 7 00:41:57.7.

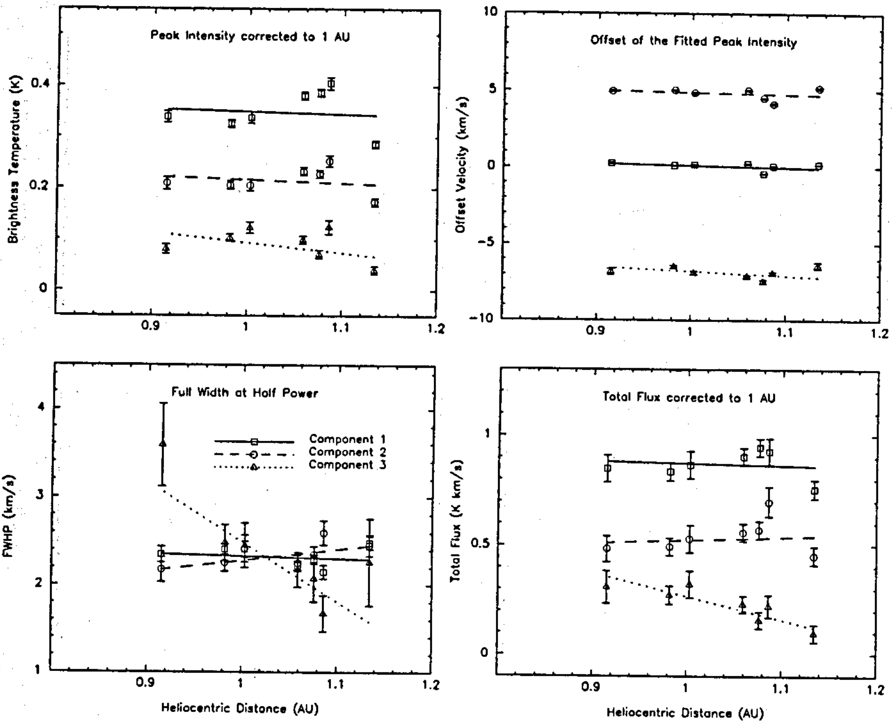

FIGURE E.3: HCN evolution determined from autocorrelation spectra.

Figures 3 and 4 for HCN and HCO$^+$, respectively. Data with low signal-to-noise ratio (April 17 and May 6) and the data contaminated by emission from Heiles cloud 2 (May 1) are not included in the fits. Therefore only the point at the smallest heliocentric distance (April 3) is after perihelion. For HCN we show fits for all three components separately (component 1, the $F = 2 \rightarrow 1$, is strongest; component 3, the $F = 0 \rightarrow 1$, is weakest). The lower right panel on both plots shows the integrated antenna temperature (K km s^{-1}). The integrated antenna temperatures were normalized to a geocentric distance of 1 AU assuming that they scale as $1/\Delta^2$. Although a Haser model predicts that the fraction of the HCN flux included in the single-dish beam varies from 66% to 71% over this period of time, this variation is small compared to other uncertainties and will be ignored. All graphs are plotted as a function of heliocentric distance. Our first data point, taken on February 19, is at a heliocentric distance of ~1.15 AU; the points are in chronological order, and we omit the last three spectra. The average of the HCN and HCO$^+$ autocorrelation spectra (February 19–April 3), scaled to 1 AU, are shown in Figure 5.

3.1.1. HCN

The ratio between the three hyperfine components does not change noticeably over time, or with heliocentric distance, which suggests that the gas remained optically thin throughout our observing period. (Note that the modest optical depths in the HCN $J = 4 \rightarrow 3$ line reported by Jewitt et al. 1997 correspond to $\tau < 0.1$ for the $J = 1 \rightarrow 0$ line.) The central velocity does not change and may be slightly (~0.1 km s^{-1}) offset toward the red part of the spectrum. When plotted as a function of time, the line width changes nearly linearly from ~2.8 to 2.5 km s^{-1}. However, all components are also consistent with a line width of ~2.7 km s^{-1}. Biver et al. (1998) show a strong correlation in the comet's production rate as a function of heliocentric distance, where (as expected) the rate increases with decreasing heliocentric distance. Our observations span only a small range in heliocentric distance, from ~0.91 AU up to 1.15 AU. If anything, we show the same trend, i.e., the measured intensity increases with decreasing R.

A simple Gaussian fit to the average single-dish HCN spectrum (Fig. 5) yields peak antenna temperatures for the three hyperfine lines of 0.29, 0.17, and 0.06 K, respectively, with an rms uncertainty of 0.01 K. The ratios between the peaks are consistent with the 5:3:1 ratios expected for optically thin emission, with a line width (FWHM) of 2.75 ± 0.02 km s^{-1} and offset velocity 0.09 ± 0.01 km s^{-1} in the cometocentric frame.

3.1.2. HCO$^+$

The offset in peak velocity is largest at the largest heliocentric distance. The line usually consists of two recog-

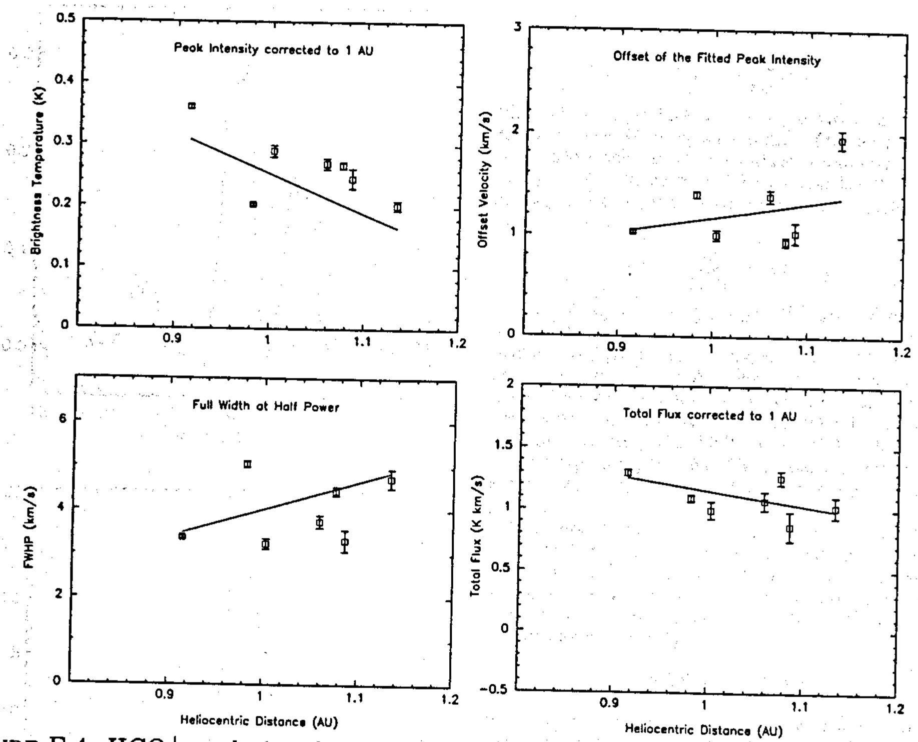

FIGURE E.4: HCO$^+$ evolution determined from autocorrelation spectra. The points are in chronological order from right to left. The solid lines indicate linear least-square fits.

nizable components: one relatively symmetric and peaked near the velocity of the comet, and the other a redward tail. The line width of the symmetric component varies quite a lot but is typically ~3–5 km s^{-1}, significantly larger than the HCN line widths. This is because the HCO+ line widths are governed by acceleration of ions due to their interaction with the solar wind (see, for example, Altwegg et al. 1993) and partially due to the tailward acceleration of the ions across the ~130,000 km projected diameter of the antenna beam. In the integrated antenna temperature we see a similar trend as for HCN.

A Gaussian fit to the average HCO$^+$ spectrum yields a peak antenna temperature of 0.24 ± 0.01 K and a line width of 4.6 ± 0.02 km s^{-1}. The center is offset toward the red by 1.3 ± 0.02 km s^{-1}. There is a tail toward the red, which extends out to ~8 km s^{-1}.

3.2. *Interferometer Observations*

Although HCN and HCO$^+$ have similar antenna temperatures in the single-dish data, the HCN and HCO$^+$ emission have quite different spatial distributions. The interferometer observations easily detected HCN on both April 3 and May 6 but detected only a small fraction of the HCO$^+$ emission on either day. These observations were carried out in a hexagonal mosaicking pattern with 1′ spacings. This observing mode results in rather modest losses in signal to noise at any point in the mosaic compared with a single-field observation in which all of the time was spent centered at that point; the sensitivity is 0.84 at the center, falling slowly to 0.7 at 1′ radius and 0.5 at 2′ radius. The observations on April 3 were centered on the nucleus and produced the best data set from which to analyze HCN; the observations on May 6 were offset from the nucleus and produced the best data set from which to analyze HCO$^+$.

3.2.1. HCN

The HCN extends over ~50″ and is centered close to the ephemeris position with a peak brightness of 4 K in a 0.25 km s^{-1} channel. The mosaicked image from April 3 is shown in Figure 6. The integrated flux density of HCN emission in the mosaicked image is consistent with the single-dish data, so that Figure 6 represents all the HCN emission within the ~4′ mosaicked region.

3.2.2. HCO$^+$

The HCO$^+$ image from April 3 shows two peaks displaced about 50″ east of the ephemeris position, consistent with the FCRAO single-dish data. The HCO$^+$ is better imaged in the offset mosaic from May 6 (Fig. 7). A patchy, large-scale structure extending over ~160″ can be seen with a peak brightness of 0.85 K averaged from −2 to 7 km s^{-1}. By May 6, the Heiles cloud was quite far away. Although there is probably some emission from dark clouds associated with Gould's belt in that general direction, any background emission would be strongly attenuated by the

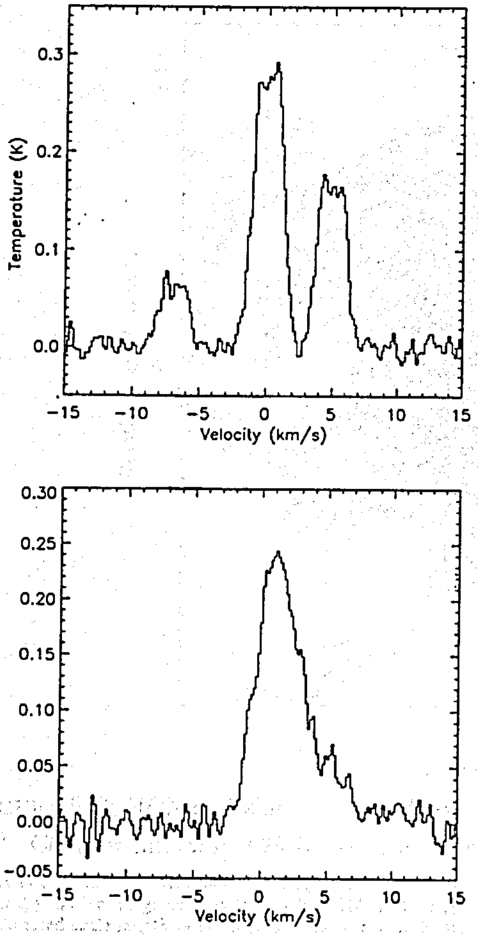

FIGURE E.5: Average autocorrelation spectra.

interferometer observations. The mapped structure is the poorly represented HCO$^+$ emission from Hale-Bopp.

4. DISCUSSION

4.1. HCN

In this paper we concentrate on the large-scale HCN distribution. Therefore, we treat the emission as circularly symmetric on the sky. (The deviations from circular symmetry are analyzed by Veal et al. 1998.) We make simple approximations to enable us to make quantitative estimates of the scale length, the outflow velocity, and the abundance of HCN relative to H_2O. We believe that this is the first time such estimates have been made from radio images.

4.1.1. *Haser Model*

As a first approximation, we assume that the HCN distribution is described by the Haser model, that is, we assume spherically symmetric, radial outflow at a constant velocity v_0. At the surface of the comet the density of parent molecules will be

$$n_p(r_0) = \frac{Q_p}{4\pi r_0^2 v} ,$$

where Q_p is the production rate of the parent molecule (here assumed to be HCN), r_0 is the radius of the nucleus, and v is the outflow velocity at the surface. Assuming a constant radial outflow velocity, v_0, for a scale length for photodissociation of λ_p, the actual density as a function of r will be

$$n_p(r) = \frac{Q_p}{4\pi r^2 v_0} \exp(-r/\lambda_p) .$$

For HCN, we use $\lambda_p = v_0/r_p^0 R^{1.5}$ km, where $r_p^0 = 1.3 \times 10^{-5}$ s^{-1} is the photodissociation rate in the solar UV field at 1 AU (Huebner, Keady, & Lyon 1992) and R is the heliocentric distance in AU. We have assumed $v_0 \propto R^{-0.5}$ (see Delsemme 1982), and we expect v_0 = 1–1.2 km s^{-1} (see comments by Cochran & Schleicher 1993). For $v_0 \sim 1.0$ km s^{-1}, the scale length for HCN on April 3 is then ~67,300 km, corresponding to ~68″. (We actually determine v_0 from a fit of the interferometric data to the Haser model; see § 4.1.2.)

In general, the populations of the energy levels, the temperature, the outflow velocity, etc., will change along the line of sight (see, for example, Crovisier 1987; Combi et al. 1998), but we will ignore these effects in our simple model. The observed lines are then proportional to the projected density (column density):

$$N_p(p) = \int_{-\infty}^{\infty} n_p(r) dz ,$$

where N_p is the column density, p is the radial distance from the nucleus in the plane of the sky, and z is measured along the line of sight.

Consider a point on the line of sight that passes a distance p from the nucleus. For a given value of z, this will correspond to a distance $r = (p^2 + z^2)^{1/2}$ from the nucleus. Therefore we obtain

$$N_p(p) = \frac{Q_p}{4\pi v} \int_{-\infty}^{\infty} \frac{\exp\{-[(p^2 + z^2)^{1/2}/\lambda_p]\}}{(p^2 + z^2)} dz . \quad (1)$$

The specific intensity is proportional to this integral. For a linear molecule in the Rayleigh-Jeans approximation, assuming that $T_{ex} \gg T_{bg}$ and that the optical depth is small, the brightness temperature averaged over the synthesized beam $\langle T_R \rangle$ is related to the projected density in the lower level averaged over the synthesized beam, $\langle N_l \rangle$, by

$$\int \langle T_R(v) \rangle dv = \frac{8\pi^3}{3} \frac{\nu_1}{k} \frac{\mu^2 J^2}{2J - 1} \langle N_l(p) \rangle ,$$

where μ is the permanent dipole moment, ν_1 is the rest frequency of the $J = 1 \rightarrow 0$ transition, and J is the rotational quantum number of the upper state. (Here it is assumed that one has summed over all hyperfine levels.) Assuming that the rotational energy levels are thermalized to a temperature T, $\int \langle T_R(v) \rangle dv$ is related to the total number of molecules summed over all states, $\langle N_T \rangle$, by

$$\int \langle T_R(v) \rangle dv = \frac{4\pi^3}{3} \frac{h}{k^2} \nu_1^2 \mu^2 J^2 e^{-h\nu_1 J(J-1)/2kT} \frac{\langle N_T \rangle}{T} . \quad (2)$$

Figure 8 shows the azimuthally averaged brightness of HCN as a function of radius. Model fits to a constant velocity radial expansion with exponential decay of the number

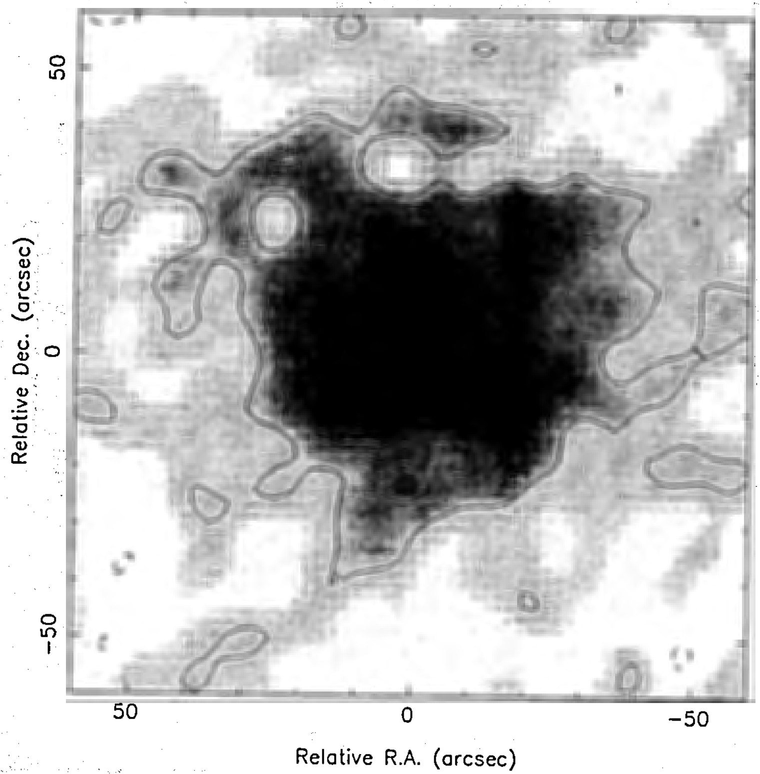

FIGURE E.6: HCN emission on April 3, averaged over the velocity interval -1.5 to 1.5 km s^{-1}. Contour interval: 0.23 K averaged over 3.5 km s^{-1}.

of HCN molecules are also plotted in Figure 8. Fitting both Q_p and scale length gives a scale length of 88″. Fitting Q_p with a fixed scale length of 60″ increases the error in the fit by 60%—the model falls off too fast. Fitting Q_p with fixed scale length of 6000″ increases the error in the fit by 110%—the model falls off too slow. Thus the data are consistent with a Haser model for the azimuthally averaged HCN distribution with a scale length of 88″, corresponding to a constant outflow velocity of 1.2 km s^{-1} with about a 10% rms error. We emphasize that our procedure fits for the scale length; the outflow velocity that corresponds to this scale length is also dependent on the (unknown) errors in the photodissociation lifetime of HCN. The outflow velocity has also been estimated to be $1.120 \pm 0.014\, R^{-0.41(\pm.01)}$ by Biver et al. (1998) by assuming that the blue wing of the lines indicates the outflow velocity. We note that if the direction of maximum outflow is displaced from the Earthward direction, this procedure will result in a systematic underestimate of the outflow velocity. Therefore we do not consider the results to be significantly different.

4.1.2. *Average Line Profile*

Figure 9 shows the HCN spectrum at the peak of the emission with 10″ resolution. Each hyperfine component has two velocity components separated by about 1.4 km s^{-1}. A very similar splitting was observed in the HCN $J = 4 \rightarrow 3$ line on 1997 February 16 (Jewitt et al. 1997). (While the latter observations used a 19.7″ beam, when the differing distances from the Earth and from the Sun are accounted for, Jewitt et al. probed a rather similar fraction of the inner coma as measured in HCN scale lengths.)

In Figure 9 we show a fit to the HCN spectrum. Because the hyperfine amplitudes are consistent with optically thin ratios, the line ratios, velocity separations, and line widths have been constrained in the fits. Table 2 shows a Gaussian fit to the two velocity components at the peak of the HCN distribution. The integrated emission is 14.2 K km s^{-1}. We adopt a temperature of 100 K, as found by Bird et al. (1997) for NH_3 for comet Hale-Bopp for the period around 1997 April 1. Equation (2) yields $\langle N_T \rangle = 1.4 \times 10^{14}$ cm^{-2}. Using the Haser model (eq. [1]) convolved over a Gaussian beam with an FWHM θ_b, we obtain the relationship

$$\langle N_T \rangle \sim 0.656 \frac{Q}{v \theta_b \Delta} .$$

Therefore, on April 3, with $\theta_b = 10''$ and $v = 1.2 \times 10^5$ cm s^{-1}, $Q_{\rm HCN} = 2.6 \times 10^{28}$ s^{-1}. We note that our value of $Q_{\rm HCN}$ is in good agreement with the value found by Biver et al.

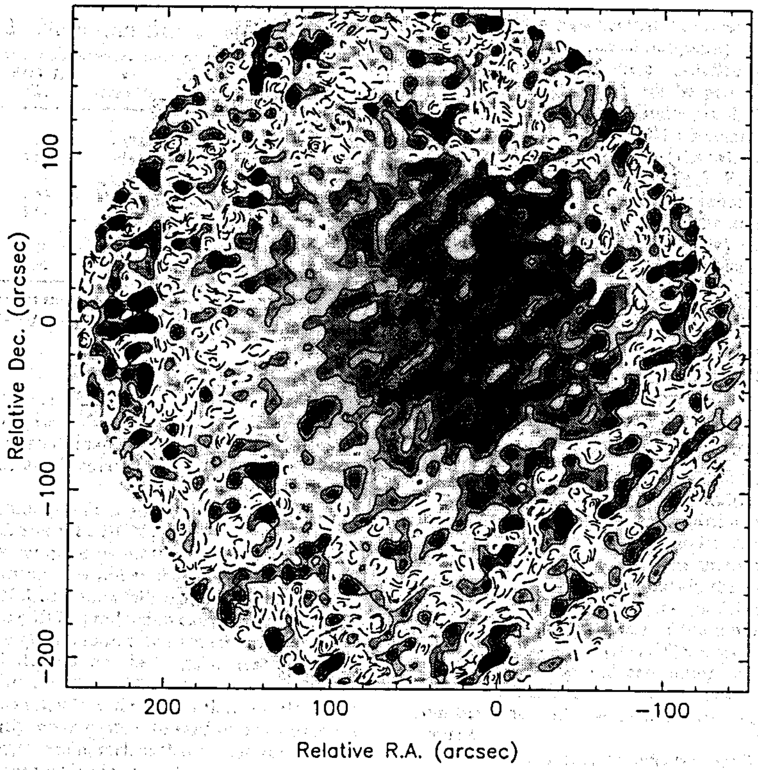

FIGURE E.7: HCO$^+$ emission on May 6, averaged over -2 to 7 km s^{-1}. Contour interval is 0.13 K averaged over 10 km s^{-1}; the gray scale runs from 0.01 (*white*) to 1 K (*black*).

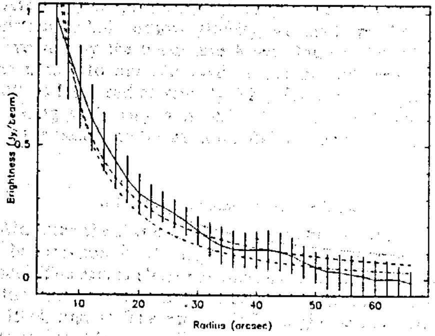

FIGURE E.8: Radial profile of HCN.

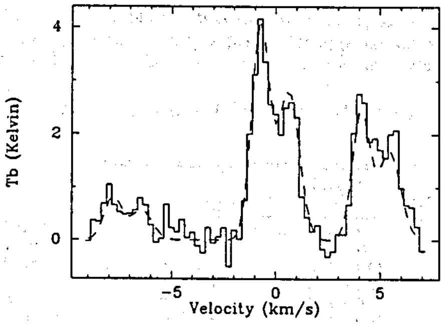

FIGURE E.9: HCN spectrum in an 11″ × 8″ beam.

TABLE E.2: Gaussian fits to HCN spectra

Line	Peak T_a (K)	v (km s^{-1})	ΔV (km s^{-1})	Area (K km s^{-1})
$F = 2 \rightarrow 1$:				
Blue......	4.07	−0.74	0.98	4.25
Red	2.82	0.62	1.21	3.63
$F = 1 \rightarrow 1$:				
Blue......	2.44	−0.76	0.98	2.55
Red	1.69	0.61	1.21	2.18
$F = 1 \rightarrow 0$:				
Blue......	0.81	−0.76	0.98	0.85
Red	0.56	0.61	1.21	0.73

NOTE.—Rms errors are about ±0.01 K, ±0.01 km s^{-1}, and ±0.01 K km s^{-1}, respectively.

(1998) at about the same time. Biver et al. also quote a value for the production rate of OH, Q_{OH}, of $\sim 10^{31}$ s^{-1} at near the time of our observations, which we take to be equal to Q_{H_2O}. This yields an abundance of HCN = 0.26% relative to H_2O.

The observed line profile is also entirely consistent with the Haser model. Since the HCN emission is optically thin, the two velocity components must come from the density and velocity distributions rather than from optical depth effects. The HCN distribution falls off with radius from the nucleus, suggesting HCN production close to the center and a decreasing density with radius. In such circumstances, the line profile will depend on the angular resolution (see Morris 1975). For a radial outflow with this density distribution, in a beam significantly smaller than a scale length, the gas is primarily moving either toward or away from the observer. (In a larger beam, such as that for the autocorrelation spectra, the gas moving in other directions tends to "fill in" the line profile; however, double peaks are sometimes visible in the spectra in Fig. 1.) The stronger blueshifted component in Figure 9 could be explained if the solar-heated surface, which has a higher gas production rate, is facing the observer.

Assuming a spherically symmetric Haser model with a constant radial outflow velocity, we made model images, convolved by the beam and fitted Gaussian profiles. The best match to our observed profile in both velocity and width is for a radial velocity 1.2 ± 0.1 km s^{-1}. The corresponding scale length is 68″ × 1.2 = 82″ ± 7″, consistent with the best fit to the azimuthally averaged HCN distribution.

4.1.3. *Comparison with Other Data*

Although the Haser model is a good fit, about 20% of the HCN emission is at larger radii than predicted by the model. The excess HCN emission has a similar distribution to the dust emission mapped at $\lambda = 3$ mm (see de Pater et al. 1998, Fig. 1). The excess HCN might be released from dust grains at larger radii.

The association of HCN with dust at larger radii could provide the parent molecule for the CN that also seems to be associated with dust. However, two other possibilities remain to be examined in future work: (1) failure of the simple model used here and (2) possible time variability. For example, the models of HCN excitation predict significant deviations from a constant value of T_{ex} (e.g., Crovisier 1987). Also, it is possible that the excess HCN at larger radii was the result of increased outgassing ~0.2 days before the observation reported here. Detailed analysis of HCN images and CN images will be presented in subsequent papers (Veal et al. 1998; Woodney et al. 1998).

Our estimate of the HCN abundance, ~0.3% that of H_2O, is comparable to most of the values reported for other comets as summarized in Table 3. For comet Kohoutek, we have taken Q_{H_2O} to be $\frac{1}{2}Q_H$ reported by Meier et al. (1976). We have made no attempt to adjust these values to state-of-the-art physical models—they are simply the values reported. However, model-dependent differences are expected to be less than a factor of 2–4. Therefore, this summary lends support to the argument of A'Hearn et al. (1995) that there are intrinsic differences in chemical composition among comets. Because the water production rate in comet Hale-Bopp was so much larger than in previous comets, a definitive comparison of model-dependent values must await a complete physical model of the coma.

4.1.4. *Position of Maximum Emission*

We convolved the Haser model with the same beam used in the HCN image and used the MIRIAD task IMDIFF to find optimum parameters (in a maximum likelihood sense) for making the convolved model consistent with the observed HCN distribution. The fitted parameters are an amplitude scale factor and shifts in the *x*- and *y*-directions. Both the HCN image and the model are primary-beam corrected. The central pixel of the model is masked. The residual image shows excess HCN emission mostly between 10″ and 30″ radius and amounting to 23% of the total. Therefore a significant part of the observed HCN deviates from the spherically symmetric Haser model, as evident in Figure 6.

The best-fitting Haser model is offset 0″.9 in R.A. and 1″.0 in declination. The resulting profiles are only weakly dependent on the central position used. However, when the difference between JPL reference orbit 77 (used in the data reductions) and JPL reference orbit 106 (1998 April) is taken into account, the net offset is 0″.6 in R.A. and −0″.6 in declination. Therefore, the peak position for HCN agrees with the position of the nucleus of the comet to within the estimated 1 σ errors in the data and in the ephemeris.

4.1.5. *Deviations from Circular Symmetry*

Finally, we emphasize that the above analysis assuming circular symmetry is only a first-order approximation. As seen in Figure 6, there is a rather narrow and relatively

TABLE E.3: Reported HCN production rates.

Comet	Date	Q_{HCN}/Q_{H_2O} (%)	Reference
Kohoutek.............	1973 Dec/1974 Jan	~4.0	1
P/Halley	1985 Nov–Dec	~0.05	2
P/Borosen-Metcalf....	1989 Sep	0.15 ± 0.05	3
Austin	1990 May	0.13 ± 0.03	3
Levy	1990 Aug	0.12 ± 0.02	3
P/Swift-Tuttle	1992 Dec	0.24 ± 0.02	3
Hyakutake............	1996 Mar	0.1	4
Hale-Bopp	1997 Apr 6	0.26	5

REFERENCES.—(1) Huebner, Snyder, & Buhl 1974; (2) Crovisier et al. 1990; (3) N. Biver 1998, private communication of values in 1997 Ph.D. thesis, Univ. Paris VII; (4) Lis et al. 1997; (5) this paper.

bright extension to the southwest in P.A. 250°. (On 1997 April 3 the radius vector to the Sun was in P.A. 210°.) These deviations are quantified by Veal et al. (1998). There is also a broad extension of the lowest contour toward the northwest in about P.A. 300°. This latter extension is along the path of the comet (in the trailing sense) at this time.

4.2. HCO^+

In order to investigate the effects of the spatial filtering imposed by the interferometer we made model *u-v* data using the same mosaicked pointing pattern and imaged the data using the same processing as for the actual data. We made model data for Gaussian brightness distributions with a range of angular sizes, $\Delta\theta$ (FWHM) from 0 (unresolved) to 120″, with the same *u-v* coverage and thermal noise as the observations. Gaussian models with $\Delta\theta$ up to 60″ are quite well reproduced in the model images. With $\Delta\theta = 75''$ the image is poorly reproduced, and with $\Delta\theta = 120''$ there is no detectable emission above the noise level. To quantify these results we fitted Gaussian components to the CLEAN and maximum entropy deconvolutions of the model images. The results are shown in Table 4. Maximum entropy deconvolution is more successful at recovering flux in the more extended distributions. Our HCO^+ image (Fig. 7) is consistent with structure on scales of 60″–120″.

The photodissociation lifetime of HCO^+ is estimated to be greater than 3.3×10^8 s based on cross sections of Koch, von Hemet, & van Dishoeck (1995) and the solar flux data of Huebner et al. (1992). Therefore, its scale length is much larger than the scale of the observations, so it can be assumed infinite for the purposes of this paper. This is consistent with the apparently very smooth HCO^+ distribution; some structure on a scale of 75″ is barely detected in our images. Note that the velocity shift is in the same sense as seen for other molecular ions in comets. For example, Spinrad, Brown, & Johns (1994) observed a tailward shift of about 2 km s^{-1} in the near tail of comet Swift-Tuttle for H_2O^+.

In the model of Huebner & Giguere (1980), the abundance of HCO^+ is approximately constant out to a radius of ~3000 km from a model comet which has a 1 km radius and $Q_{H_2O} \sim 2 \times 10^{29}$ s^{-1}. For Hale-Bopp at the time of our observations, $Q_{H_2O} \sim 10^{31}$ s^{-1}, i.e., 50 times greater than the Huebner & Giguere model. The size should scale approximately as Q_{H_2O}, so that the constant density region would be expected to have a radius of 150,000 km (~5′ angular diameter). This is in rough accord with of the observed size. For comet Swift-Tuttle, Spinrad et al. found that H_2O^+ peaked about 20,000 km down the ion tail, and they suggested that the peak occurred near the downstream end of the predicted teardrop-shaped ionopause. The size of the cavity outlined by the ionopause is expected to scale at $Q_{H_2O}^{3/4}$ (see, for example, Wu 1988). Scaling from the production rate of H_2O for Swift-Tuttle at the time of their observations to our comet Hale-Bopp observations, we expect that the end of the ionopause cavity for Hale-Bopp is about 10 times as far from the nucleus: 200,000 km, corresponding to ~200″. This is roughly consistent with the observed offset of the HCO^+ of ~60″. From these crude scalings, we conclude that the general picture of the distribution of HCO^+ that may be inferred from previous models is roughly consistent with the radio observations. Clearly, detailed chemical and physical models are needed.

TABLE E.4: Gaussian fits to model *uv* data.

	CLEAN		MAXEN	
GAUSSIAN FWHM	Fitted Flux (K km s^{-1})	FWHM (arcsec)	Fitted Flux (K km s^{-1})	FWHM (arcsec)
0	1.53	0 × 0	1.49	0 × 0
15	1.75	18 × 15	1.36	16 × 14
30	1.75	30 × 29	1.30	30 × 27
45	1.13	35 × 31	0.94	37 × 35
60	0.56	38 × 32	0.67	47 × 44
75	0.25	42 × 35	0.78	78 × 73
90	0.26	91 × 81	1.63	153 × 131
120	Fail	Fail	Fail	Fail

5. CONCLUSIONS

We used the BIMA array to map comet Hale-Bopp (1995 O1) in HCN and HCO^+ emission at 89 GHz with 10″ angular resolution over a field of view of ~4′.

1. The HCN image shows a compact distribution centered on the nucleus with a prominent extension at P.A. 250°.
2. The HCN emission maximum coincides with the position of the comet nucleus to ~0″.8.
3. To first order, the HCN radial distribution is consistent with a Haser model with a scale length 80″ ± 10″, which corresponds to an outflow velocity 1.2 ± 0.1 km s^{-1}.
4. The high-resolution HCN profile at the maximum is double peaked, as expected in the Haser model. The asymmetric profile could come from an increased gas production toward the Sun and facing the observer.
5. The production rate of HCN is ~0.26% that of water. Most of the reported values of the HCN/H_2O abundance in Table 3 agree to within a factor of 2, although they disagree significantly according to their formal errors. Much more detailed physical modeling is required to quantify the range of comet to comet variation of the HCN/H_2O abundance.
6. In contrast to the strongly peaked HCN, the HCO^+ is smooth, almost completely resolved in the interferometer observations, and offset toward the ion tail by about 1′ with structure on a scale of 75″.
7. The large size and the offset of HCO^+ are roughly in accord with expectations based on earlier theoretical work.

This work was partially supported by NSF grant AST 96-13998 to the University of California, Berkeley; NASA grant NAG 5-4292 to the University of Illinois and the University of Chicago; NSF grant AST 96-13999 to the University of Illinois; NSF grant AST 96-13716 to the University of Maryland; and NASA grant NAG 5-4711 to the University of California, Davis. We thank Carl Heiles for discussions regarding the Heiles cloud and Nicolas Biver for permission to quote several papers before publication. We also thank an anonymous referee for a careful reading of the manuscript.

REFERENCES

A'Hearn, M. F., Hoban, S., Birch, P. V., Bowers, C., Martin, R., & Klinglesmith, D. A. III. 1986, Nature, 324, 649
A'Hearn, M. F., Millis, R. L., Schleicher, D. G., Osip, D. J., & Birch, P. V. 1995, Icarus, 118, 223
Altwegg, K., et al. 1993, A&A, 279, 260
Biermann, L., & Diercksen, G. 1974, Origins of Life, 5, 297
Bird, M. K., Huchtmeier, W. K., Gensheimer, P., Wilson, T. L., Janardhan, P., & Lemme, C. 1997, A&A, 325, L5
Biver, N., et al. 1998, Earth Moon Planets, in press
Buhl, D., & Snyder, L. E. 1970, Nature, 228, 267
Cochran, A. L., & Schleicher, D. G. 1993, Icarus, 105, 235
Combi, M. R., Brown, M. E., Feldman, P. D., Keller, H. U., Meier, R. R., & Smyth, W. H. 1998, ApJ, 494, 816
Cornwell, T. J., & Fomalont, E. B. 1989, in ASP Conf. Ser. 6, Synthesis Imaging in Radio Astronomy, ed. R. A. Perley, F. R. Schwab, & A. H. Bridle (San Francisco: ASP), 185
Crovisier, J. 1987, A&AS, 68, 223
Crovisier, J., et al. 1990, A&A, 234, 535
Delsemme, A. 1982, in Comets, ed. L. L. Wilkening (Tucson: Univ. Arizona Press), 85
de Pater, I., Forster, J. R., Wright, M. C. H., Butler, B. J., Palmer, P., Veal, J. M., A'Hearn, M. F., & Snyder, L. E. 1998, AJ, 116, 987
Depois, D., Crovisier, J., Bockelée-Morvan, D., Schraml, J., Forveille, T., & Gérard, E. 1986, A&A, 160, L11
Herbst, E., & Klemperer, W. 1973, ApJ, 185, 505
Hollis, J. M., Snyder, L. E., Lovas, F. J., & Buhl, D. 1976, ApJ, 209, L83
Huebner, W. F., Boice, D. C., Schmidt, H. U., & Wegmann, R. 1991, in Comets in the Post-Halley Era, ed. R. L. Newburn et al. (Dordrecht: Kluwer), 907
Huebner, W. F., & Giguere, P. T. 1980, ApJ, 238, 753
Huebner, W. F., Keady, J. J., & Lyon, S. P. 1992, Ap&SS, 195, 1
Huebner, W., Snyder, L. E., & Buhl, D. 1974, Icarus, 23, 580
Jewitt, D. C., Matthews, H. E., Owen, T., & Meier, R. 1997, Science, 278, 90
Klemperer, W. 1970, Nature, 227, 1230
Koch, A., van Hemet, M. C., & van Dishoeck, E. F. 1995, J. Chem. Phys., 103, 7006
Kuan, Y.-J., et al. 1998, AGU, 79, W63
Lis, D. C., et al. 1997, Icarus, 130, 355
Lovell, A. J., Bergin, E. A., Dickens, J. E., Devries, C. H., Senay, M. C., & Irvine, W. M. 1998a, Earth Moon Planets, in press
Lovell, A. J., Schloerb, F. P., Dickens, J. E., Devries, C. H., Senay, M. C., & Irvine, W. M. 1998b, ApJ, 497, L117
Meier, R. R., Opal, C. B., Keller, H. U., Page, T. L., & Carruthers, G. R. 1976, A&A, 52, 283
Morris, M. 1975, ApJ, 197, 603
Palmer, P., A'Hearn, M. A., de Pater, I., Klavetter, J. J., Mehringer, D., Schloerb, F. P., Snyder, L. E., & Wilner, D. 1990, in Workshop on Observations of Recent Comets (1990), ed. W. F. Huebner, P. A. Webinger, J. Rahe, & I. Konno (San Antonio: Southwest Research Inst.), 40
Sault, R. J., Staveley-Smith, L., & Brouw, W. N. 1996, A&AS, 120, 375
Sault, R. J., Teuben, P. J., & Wright, M. C. H. 1995, in ASP Conf. Ser. 77, Astronomical Data Analysis Software and Systems IV, ed. R. A. Shaw, H. E. Payne, & J. J. E. Hayes (San Francisco: ASP), 433
Schloerb, F. P., Kinzel, W. M., Swade, D. A., & Irvine, W. M. 1986, ApJ, 310, L55
Schmidt, H. U., Wegmann, R., Huebner, W. F., & Boice, D. C. 1988, Comput. Phys. Comm., 49, 17
Snyder, L. E., & Buhl, D. 1971, in Highlights of Astronomy, Vol. 2, ed. C. de Jager (Dordrecht: Reidel), 407
Snyder, L. E., Hollis, J. M., Lovas, F. J., & Ulich, B. L. 1976, ApJ, 209, 67
Spinrad, H., Brown, M. E., & Johns, C. M. 1994, AJ, 108, 1462
Veal, J. M., et al. 1997, IAU Circ. 6575
———. 1998, BAAS, 30, 826
Watson, W. D. 1973, ApJ, 183, L17
Welch, W. J., et al. 1996, PASP, 108, 93
Whipple, F. L. 1950, ApJ, 111, 375
Woodney, L. M., et al. 1998, 30th meeting AAS Div. Planet. Sci., No. 31.03
Woods, R. C., Dixon, T. A., Saykally, R. J., & Szanto, P. G. 1975, Phys. Rev. Lett., 35, 1269
Wright, M. C. H., & Sault, R. J. 1993, ApJ, 402, 546
Wu, Z.-J. 1988, Ann. Geophys., 6, 355

Appendix F

BIMA Array Spectral Line Observations of Comet Hale-Bopp (C/1995 O1)

resubmitted to ApJ, 20 Jan. 1999

BIMA Array Spectral Line Observations of Comet Hale-Bopp (C/1995 O1)

L. E. Snyder[1], J. M. Veal[1], L. M. Woodney[2], M. F. A'Hearn[2], Y.-J. Kuan[3], J. R. Forster[4], M. C. H. Wright[4], R. L. Plambeck[4], I. de Pater[4], M. W. Pound[2,4], G. Engargiola[4], and Patrick Palmer[5]

ABSTRACT

We present sample images and spectra of HCN, CH_3OH, and CS from comet Hale-Bopp (C/1995 O1) observed with the BIMA Array. Prior to the 1997 apparition of Hale-Bopp, there were no published measurements of cometary spectral lines observed with a millimeter-wavelength interferometric array. These observations illustrate the value of array measurements in order to determine the origins, spatial distributions, production rates, and photodissociation scale lengths of cometary species. In particular, Haser modeling of our interferometric measurements of CS gives a scale length which is $\sim$ 10 times smaller than the commonly accepted value. Consequently, the CS fraction in comets is increased with respect to some earlier determinations.

Subject headings: comets: individual (Hale-Bopp (C/1995 O1)) — molecular processes — techniques: interferometric — radio lines: solar system

1. Introduction

Comets differ chemically (A'Hearn et al. 1995), so understanding the distribution of coma gases is essential for accurate production rate measurements and modeling. For practical reasons, cometary models are primarily spherically symmetric-despite obvious asymmetric features. It is essential to test how well such models fit. A second problem is to test fundamental parameters of modeling such as the scale lengths and photodissociation rates. A third problem is to measure whether molecular production rates determined from low spatial resolution data are comparable with the rates derived from higher resolution data. If not, intervening chemical processes change the rates as the gas flows from the inner to the outer coma. Millimeter-wavelength arrays can be used to study all three of these problems because interferometric mode observations can provide velocity resolved two-dimensional images in which the data points are all measured simultaneously, while single-element mode observations can supply low resolution measurements of the

---

[1] Department of Astronomy, 1002 W. Green St., University of Illinois, Urbana IL 61801 e-mail: snyder@astro.uiuc.edu

[2] Department of Astronomy, University of Maryland, College Park MD 20742-2421

[3] Department of Earth Sciences, National Taiwan Normal University, and Academia Sinica, Institute of Astronomy and Astrophysics, Taipei, Taiwan

[4] Department of Astronomy, University of California, Berkeley, CA 94720

[5] Department of Astronomy and Astrophysics, University of Chicago

total coma emission. Comet Hale-Bopp (C/1995 O1) was the first comet detected by the BIMA Array[6]. In this Letter, we use a sample of our 1997 preperihelion molecular line measurements to demonstrate their potential for addressing the above questions.

2. Observations

We used the BIMA Array to observe the comet both in interferometric (cross-correlation) mode with 9 antennas and in autocorrelation (single-element) mode with 7 antennas. Channel widths were 0.098 MHz for the former and 0.049 MHz for the latter observations. Typical system temperatures ranged from ~200K at high to ~400K at lower elevations. HCN, CH_3OH, and CS were the primary target molecules. Figure 1 shows representative images (corrected to JPL Reference Orbit 77) and spectra. Table 1 lists: quantum numbers; frequency (Lovas 1992); E_u, upper energy; $S\mu^2$, line strength times square of the dipole moment (in Debye^2); I_ν, peak flux density per beam in Jy beam^{-1} for cross-correlation spectra; and T_A^*, peak antenna temperature corrected for atmospheric loss for autocorrelation spectra. For each observation, Table 2 lists: r_{hel}, Sun-comet distance; Δ, Earth-comet distance; and beam size.

3. Discussion

In order to calculate the beam-averaged molecular column densities, $< N_T >$, required to determine production rates, we assumed low optical depths to obtain

$$< N_T >= \frac{2.04\ W_{\rm I}\ Z\ e^{E_{\rm u}/T_{\rm rot}}}{\theta_{\rm a}\theta_{\rm b} S\mu^2\nu^3} \times\ 10^{20}\ {\rm cm}^{-2} = \frac{1.67 W_{\rm T}\ Z\ e^{E_{\rm u}/T_{\rm rot}}}{S\mu^2\nu} \times 10^{14}\ {\rm cm}^{-2}. \tag{1}$$

The first expression is used for cross-correlation observations where $W_{\rm I} = \int I_\nu dv$ in Jy beam^{-1} km s^{-1}, and I_ν is the flux density per beam; the second is used for autocorrelation observations where $W_{\rm T} = \int T_{\rm mb} dv$ in K km s^{-1}, and $T_{\rm mb}$ is the spectral line brightness temperature. Z is the rotational partition function, $\theta_{\rm a}$ and $\theta_{\rm b}$ are the FWHM synthesized beam dimensions in arcsec, and ν is the frequency in GHz. The resulting column densities are discussed below.

HCN. HCN was observed in interferometric mode on several days, but the March 29 data set had the highest signal-to-noise ratio. Figure 1(a) shows the brightness distribution on March 29 averaged over 7 channels (~ 2 km s^{-1}) in the F=2-1 and F=1-1 hyperfine lines. Figure 1(b) shows the peak HCN cross-correlation spectrum. Figure 1(c) shows an excellent HCN autocorrelation spectrum which was observed on March 12. The $T_{\rm A}^*$ of the F=2-1 line gives an integrated[7] flux density of 76 ± 8 Jy km s^{-1}. The integrated flux density obtained from the cross-correlation data is 33 ± 4 Jy km s^{-1}, which is ~ 43% of the flux in the autocorrelation data. The cross-correlation spectrum yields $< N_T > = 1.39\times 10^{14}$ cm^{-2} for a coma gas temperature of 104 K (Bird et al. 1997), but the autocorrelation spectrum gives 6.07×10^{12} cm^{-2}, or ~ 23 times less. A higher column density from interferometric data is a consequence of the high concentration of HCN inside the smaller synthesized beam. Haser modeling of the interferometer and autocorrelation data gave comparable gas production rates, Q(HCN) = $1.5 \pm 0.3 \times 10^{28}$ s^{-1}, and $1.7 \pm 0.3 \times 10^{28}$ s^{-1} respectively. This is consistent with no significant production or destruction of HCN in the

---

[6] Operated by the Berkeley-Illinois-Maryland Association with support from the NSF.

[7] In this paper, "integrated" always refers to integration over velocity, not space.

coma region bounded by the synthesized and single-element beams. For $Q(\mathrm{H_2O}) \sim 10^{31}\ \mathrm{s^{-1}}$ on 1997 March 29 (Biver et al. 1998), we estimate that the production of HCN relative to H_2O is ~ 0.002, in general agreement with 0.0026 found by Wright et al. for April 3 and with ~ 0.0025 for March 29 interpolated from Figure 3 of Biver el al.

The March 29 HCN image deviates from circular symmetry with small spurs to the north, southeast, and southwest. The dust emission shows similar spurs (de Pater et al. 1998). We convolved a Haser model with the image beam and subtracted the best fitting model. A Haser model with scale length $80'' \pm 8''$ ($7.5 \pm 0.8 \times 10^4$ km) fits the HCN distribution with 3 σ (0.05 Jy $\mathrm{beam^{-1}}$) deviations corresponding to the spurs. Our scale length is in excellent agreement with the $82 \pm 7''$ found from the mosaiced HCN data on April 3 (Wright et al.). For an outflow velocity of 1.2 km $\mathrm{s^{-1}}$ (Biver et al.; Wright et al.), both of these results are in excellent agreement with expectations based on the 1 AU HCN photodissociation lifetime given by Huebner, Keady, & Lyon (1992).

CH_3OH. CH_3OH was observed only in interferometric mode. Figure 1(d) shows the map of the CH_3OH brightness distribution on March 27. Because the emission was weak, this is a map of the sum of all 4 CH_3OH lines in Table 1. The position offset of $\sim 5''$ cannot be regarded as significant because of the signal-to-noise ratio and ephemeris error with respect to JPL Reference Orbit 106 (which accounts for $\sim 2''$). Figure 1(e) shows the weighted average of the CH_3OH cross-correlation spectra from March 27, March 31, and April 8. The J(K)=2(-1)-1(-1)E can be seen at 6.5 km $\mathrm{s^{-1}}$; 2(0)-1(0)A^+ at 0 km $\mathrm{s^{-1}}$; 2(0)-1(0)E at -9.5 km $\mathrm{s^{-1}}$; and 2(1)-1(1)E at -44 km $\mathrm{s^{-1}}$. All lines fall at ~ 0 km $\mathrm{s^{-1}}$ in the cometocentric frame. The narrow unidentified 2 σ features at -18 and -29 km $\mathrm{s^{-1}}$ appear to be artifacts, but because our spectra have the best signal-to-noise ratios ever reported for these particular CH_3OH lines, there are no other published spectra to check against. However, the data quality was not quite high enough for determination of the CH_3OH scale length. The average from all 4 lines yields $< N_T > = 2.06 \times 10^{15}\mathrm{cm^{-2}}$ for 104 K. We used a Haser model with an outflow velocity of 1.2 km $\mathrm{s^{-1}}$ and a photodissociation lifetime at 1 AU of 1.3×10^{-5} $\mathrm{s^{-1}}$ (Huebner et al.) to find $Q(\mathrm{CH_3OH}) = 2.2 \pm 0.4 \times 10^{29}\ \mathrm{s^{-1}}$, in good agreement with CH_3OH values found by Biver et al. The abundance relative to H_2O is ~ 0.02.

CS. As with HCN, strong CS emission was observed in interferometric mode on several different days, but the March 25 data set had the highest signal-to-noise ratio. Figure 1(f) shows the CS image from March 25. Figure 1(g) shows the CS cross-correlation spectrum from that image. The CS image resembles the HCN image (Figure 1(a)), but it is more compact. Like HCN, CS also deviates from circular symmetry with spurs to the north, southeast, and southwest. Figure 1(h) is a high-quality CS autocorrelation spectrum taken on February 28.

Numerous ultraviolet measurements imply that CS has a parent, such as CS_2, with a very short lifetime of $\sim 10^3$ s or less. Hence, at the resolution of our observations, CS can be fit as though it were a parent species. The CS lifetime is poorly known, but $\sim 10^5$ s is customarily assumed (Jackson et al. 1982). Figure 2 (solid line) shows the CS radial profile averaged over 360° around the fitted centroid of Figure 1(f). A Haser model was fit (dashed line) to obtain a scale length of $10 \pm 2''$, or $9.6 \pm 1.9 \times 10^3$ km at a Sun-comet distance of 0.923 AU. For an outflow velocity of 1.2 km $\mathrm{s^{-1}}$, this corresponds to a CS lifetime of 0.9×10^4 s at 1 AU, which is ~ 10 times smaller than the customary value. Scale lengths resulting from 1 AU lifetimes of either 3×10^4 s or 10^5 s would yield grossly different radial profiles, as shown in Figure 2.

We convolved a CS Haser model with the image beam and subtracted the best fitting model from the CS image (Figure 3). The obvious residuals from the two southern spurs are also seen in Figure 2 but their interpretation is ambiguous. The widths of the spurs are sufficiently large that one can not argue strongly for a grain source from these data. The spurs coincide with optical features in, e.g., CN images at about the same time. If they represent the edges of a cone formed by a rotating jet, the radial separation implies a projected motion of 3000 km during half a rotation of the nucleus. With an 11.3-hour period (Schleicher, private communication), this yields $\sim$ 0.1 km s^{-1} projected on the sky, which is lower than expected from the 0.3 - 0.5 km s^{-1} projected velocities deduced from optical images for both gas and dust. Nevertheless, if the temporal variation interpretation is valid, a more extensive set of CS images with subsets of the data from different days, but corresponding to the same rotational phase of the comet, should show very different intensity ratios between the two spurs.

The March 25 CS cross-correlation data give $< N_T > = 1.93 \times 10^{14}$ cm^{-2}. This yields Q(CS) = 3.6 $\pm$ 0.7 $\times 10^{28}$ s^{-1} for a CS lifetime of 0.9 $\times$ 10^4 s. The February 28 autocorrelation data give $< N_T >=$ 2.79$\times$ 10^{12} cm^{-2}, which yields Q(CS)= 5.4 $\pm$ 1.1 $\times 10^{28}$ s^{-1}. For $Q(H_2O) \sim 8 \times 10^{30}$ s^{-1} on March 25 and $\sim 3 \times 10^{30}$ s^{-1} on February 28 (Biver et al.), the respective production rates of CS relative to H_2O were $\sim$ 0.005 and $\sim$ 0.018. Our values are larger than the values of 0.001 -0.002 reported by earlier workers (Biver et al.; Feldman 1991) because of the difference in assumed lifetime. Our new scale length would increase by $\sim$ 50 % the cometary CS production rates derived from ultraviolet observations by Meier & A'Hearn (1997). Even so, the increased values are still within the error bars of their estimates. Therefore, unless there was a very dramatic and fortuitous variation in CS production during our observations, our CS image makes our conclusion about the shorter CS lifetime unavoidable.

4. Summary

We have presented sample molecular images and spectra of HCN, CH_3OH, and CS from comet Hale-Bopp. These species all have spatially resolved distributions. We have used a Haser model to show that the HCN and CH_3OH production rates are in reasonable agreement with other measurements of the comet. The CS image from March 25 strongly resembles the HCN image on March 29, but on a smaller scale. At the resolution of the array, both appear to originate on or near the nucleus. Both can be fit to determine a scale length or lifetime. Our derived HCN scale length is in excellent agreement with other values, but our derived CS lifetime is $\sim$ 10 times smaller than the commonly used CS lifetime. Consequently, the CS fraction in comets is increased with respect to some earlier determinations. Both images have small spurs which deviate from circular symmetry. These could be due to either grain or gas jets, but a more extensive set of CS images should reveal whether the southern spurs are due to a rotating gas jet.

We thank D. K. Yeomans for ephemerides assistance, T. T. Helfer, W. Hoffman, and an anonymous referee. This work was partially funded by: NASA NAG5-4292, NAG5-4080, and NGT5-0083; NSF AST 96-13998, AST96-13999, AST96-13716, and AST96-15608; Taiwanese grants NSC 86-2112-M-003-T and 87-2112-M-003-007; and the Universities of Illinois, Maryland, and California, Berkeley.

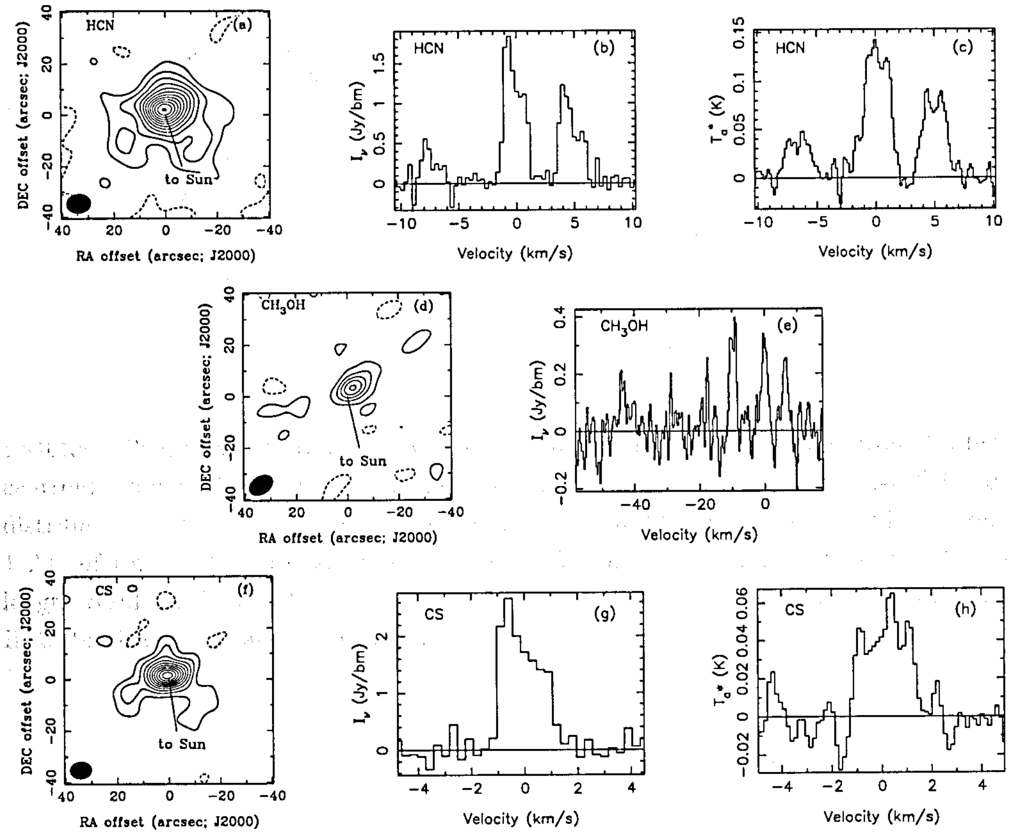

FIGURE F.1: Comet Hale-Bopp images and spectra observed with the BIMA array. Image coordinates are arcsec offsets ($1'' \sim 10^3$ km) relative to the predicted position of the nucleus Synthesized beams are in the lower left and line segments show solar directions. Spectra abscissae are radial velocity relative to the nucleus. Ordinates are flux density per beam, I_ν, in Jy beam^{-1} for cross-correlation and beam-averaged antenna temperature, T_A^*, in K for autocorrelation spectra. (a) HCN image on March 29 showing the intensities of the F=2-1 plus 1-1 hyperfine lines. The peak is 2.71 Jy beam^{-1}, contours are 3σ, and $\sigma = 0.06$ Jy beam^{-1}. (b) HCN cross-correlation spectrum on March 29 with $\sigma = 0.11$ Jy beam^{-1}. (c) HCN autocorrelation spectrum on March 12 with $\sigma = 0.011$ K. (d) CH_3OH image on March 27 constructed from intensity sum of all 4 lines. The peak is 1.45 Jy beam^{-1}, contours are 2σ, and $\sigma = 0.14$ Jy beam^{-1}. (e) Weighted average of CH_3OH cross-correlation spectra from March 27, March 31, and April 8 with $\sigma = 0.11$ Jy beam^{-1}. (f) CS image on March 25. The peak is 1.84 Jy beam^{-1}, contours are 3σ, and $\sigma = 0.06$ Jy beam^{-1}. (g) CS cross-correlation spectrum on March 25 with $\sigma = 0.15$ Jy beam^{-1}. (h) CS autocorrelation spectrum on February 28 with $\sigma = 0.01$ K.

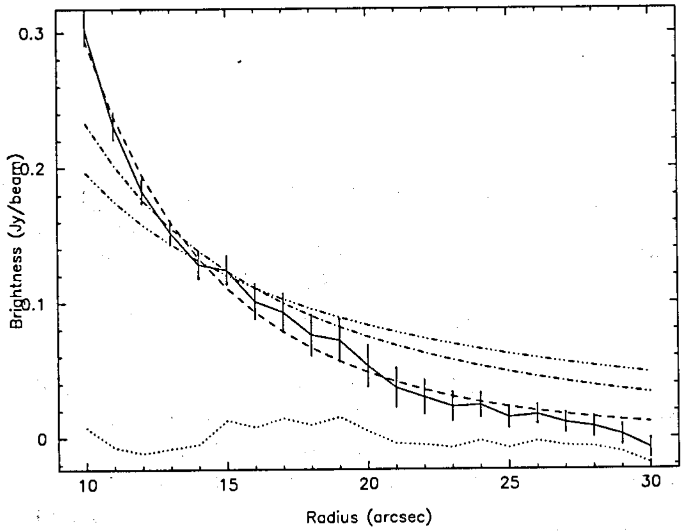

FIGURE F.2: CS radial profile for March 25 which is averaged in annuli around a fitted centroid. *Solid Line* : CS distribution. *Dashed Line* : Haser fit to average CS radial distribution. *Dot – Dashed Line* : Haser model for a 33″ scale length resulting from a 1 AU lifetime of 3 × 10^4 s. *Triple Dot – Dashed Line* : Haser model for a 113″ scale length resulting from a 1 AU lifetime of 10^5 s. *Dotted Line* : residuals. *Vertical Bars* : RMS brightness variations within each annulus.

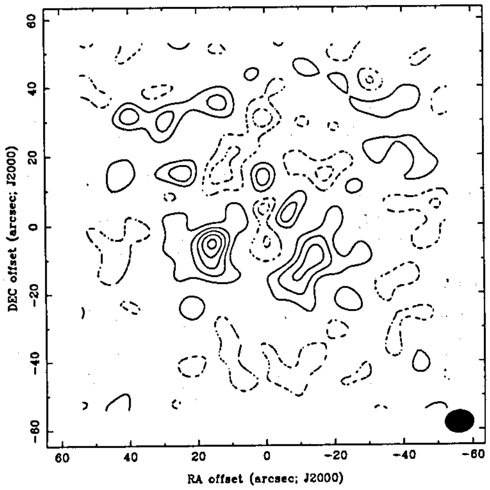

FIGURE F.3: Map of the difference between the CS image on March 25 (Figure 1(f)) and the best fitting CS Haser model convolved with the CS image beam.

TABLE F.1: Parameters of the Observed Cometary Molecules

Molecule	Quantum Numbers	Frequency (MHz)	E_u (K)	$S\mu^2$ (D^2)	I_ν (Jy bm^{-1})	T_A^* (K)
HCN	J=1-0, F=1-1	88,630.42				
	F=2-1	88,631.85	4.3	8.9	1.8	0.14
	F=0-1	88,633.94				
CH_3OH	J(K)=2(-1)-1(-1)E	96,739.39	12.5	1.2	0.26	
	2(0)-1(0)A^+	96,741.42	7.0	1.6	0.34	
	2(0)-1(0)E	96,744.58	20.0	1.6	0.38	
	2(1)-1(1)E	96,755.51	28.0	1.2	0.21	
CS	J=2-1	97,980.97	7.1	7.7	2.7	0.07

TABLE F.2: Distances and Beam Sizes

Molecule	Date (1997)	r_{hel} (AU)	Δ (AU)	Beam ($''$)
CS	February 28	1.1	1.5	118
HCN	March 12	1.0	1.4	130
CS	March 25	0.9	1.3	8.5 x 6.7
CH_3OH	March 27	0.9	1.3	10.2 x 7.0
HCN	March 29	0.9	1.3	9.5 x 7.7

REFERENCES

A'Hearn, M. F., Millis, R. L., Schleicher, D. G., Osip, D. J., & Birch, P. V. 1995, Icarus, 118, 223

Bird, M. K., Huchtmeier, W. K., Gensheimer, P., Wilson, T. L., Janardhan, P., & Lemme, C. 1997, A&A, 325, L5

Biver, N., et al. 1998, Earth, Moon, and Planets, in press

de Pater, I., et al. 1998, AJ, 116, 987

Feldman, P. D. 1991, in Comets in the Post-Halley Era, Vol. 1, ed. R. L. Newburn, Jr., M. Neugebauer, & J. Rahe (Dordrecht: Kluwer), 139

Huebner, W. F., Keady, J. J., & Lyon, S. P. 1992, A&SS, 195, 1

Jackson, W. M., Halpern, J. B., Feldman, P. D., & Rahe, J. 1982, A&A, 107, 385

Lovas, F. J. 1992, J. Phys. Chem. Ref. Data, 21, 181

Meier, R., & A'Hearn, M. F. 1997, Icarus, 125, 164

Wright, M. C. H., et al. 1998, AJ, 116,3018

This preprint was prepared with the AAS LATEX macros v4.0.

Appendix G

Model Image Code

```
      PROGRAM modelimage
c
c     Here is a program that uses qsimp from numerical recipes (which uses
c     trapzd) to evaluate the integral in Equation 3.1 of my thesis for
c     enough values of "a" to fill in a 256 by 256 model image of a comet
c     with density dropoff of parent molecules due to spherical expansion
c     and photodestruction.
c
c     Written and/or put together on Monday 20 October 1997 by J. M. Veal.
c
c     Imax is the maximum intensity in the map; rn is the radius of the
c     comet's nucleus; scale is the number of centimeters per pixel; dim is
c     equal to the size in pixels of the square image; xoff is the r.a.
c     offset in pixels of the emission peak in the map; yoff is the dec
c     offset in the same fashion (these offsets are adjusted to jive with
c     fitsio software); p is the impact parameter; intrn is the value of the
c     integral for p=rn; a is the lower limit of integration; m is the power
c     of 2 that defines the increasing limits of integration; b is the
c     upper limit of integration; s is the value of each integral returned
c     from the recipes; losfun is the function being integrated along the
c     line of sight; intp is the value of the integral for any given value
c     of p; Ip is the intensity in the image as a function of p (it is
c     multiplied by a large constant so it will jive with the fitsio that
c     writes integer arrays -- then the image is divided by the same later);
c     Ip0 is the intensity in the image as a function of p but without the
c     exponential dropoff due to photodestruction; diff is Ip0 minus Ip.
c     Units of distance are cm and units of intensity are Jy/bm.  The first
c     part finds the value of the integral for p = rn. The limits are varied
c     so as to make things more efficient and accurate (that is, a simple
c     approach to variable step size).  For example, the function is
c     integrated from 0 to 2, 2 to 4, 4 to 8, 8 to 16, 16 to 32, and so on
```

```
c     up in powers of 2 until the distance of about .1 AU is reached.  Each
c     bin is integrated to a fractional accuracy of 10**-5 and the bins are
c     added up as the program goes.
c
      IMPLICIT none
      DOUBLE PRECISION Imax,rn,scale,dim,xoff,yoff,tempo
      DOUBLE PRECISION p,intrn,a,m,b,s,losfun
      DOUBLE PRECISION g,h,intp,Ip,Ip0,diff
      EXTERNAL losfun
c
      Imax = 0.2280
      rn = 2.d06
      scale = .25*1.332*dtan(2.*3.14159265/(360.*3600.))*1.496d13
      dim = 240.
      xoff = 1.
      yoff = 11.
c
      open(unit=1,file='modelimage.out')
      p = rn
      intrn = 0.
      a = 0.
      do m = 1.,41.
        b = 2.**m
        CALL qsimp(losfun,a,b,s,p)
        intrn = intrn + s
        a = b
      enddo
c
c     The next part varies "p" as well so as to find all the values
c     necessary to fill in the image.  Ip = Imax * intp / intrn
c
      do h = -dim/2.+1.,dim/2.
        do g = -dim/2.+1.,dim/2.
          p = scale * dsqrt( (g-xoff)**2. + (h-yoff)**2. )
          if (p.eq.0) then
            intp = intrn
            Ip = Imax
            Ip0 = Imax
          else
            intp = 0.
            a = 0.
            do m = 1.,41.
              b = 2.**m
              CALL qsimp(losfun,a,b,s,p)
```

```
              intp = intp + s
              a = b
            enddo
            Ip = Imax * intp / intrn
            Ip0 = Imax * rn / p
          endif
          diff = Ip0 - Ip
          Ip = Ip * 1.d08
          write (1,101) Ip
c          write (1,101) p,intp,Ip,Ip0,diff
        enddo
      enddo
      close(1)

  101 format (1pe11.4)
c  101 format (3x,1pe9.2,3x,1pe10.3,3x,1pe10.3,3x,1pe10.3,3x,1pe10.3)

      END
c
c     The next part is the subroutine qsimp to perform the numerical
c     integration.  "EPS" is the desired fractional error in the value
c     of the integral, and 2^("JMAX"-1) is the maximum number of allowed
c     steps.  See figure 4.2.1 (pg 130) of Numerical Recipes.
c
      SUBROUTINE qsimp(losfun,a,b,s,p)
      INTEGER JMAX
      DOUBLE PRECISION a,b,losfun,s,EPS
      EXTERNAL losfun
      PARAMETER (EPS=1.d-5, JMAX=20)
CU    USES trapzd
      INTEGER j
      DOUBLE PRECISION os,ost,st,p
      ost=-1.d30
      os= -1.d30
      do 11 j=1,JMAX
        call trapzd(losfun,a,b,st,j,p)
        s=(4.d0*st-ost)/3.d0
        if (abs(s-os).lt.EPS*abs(os)) return
        os=s
        ost=st
11    continue
      pause 'too many steps in qsimp'
      END
C  (C) Copr. 1986-92 Numerical Recipes Software R2A24"o1j.
```

```
c
c     The next part is the workhorse subroutine, trapzd, that qsimp uses.
c
      SUBROUTINE trapzd(losfun,a,b,s,n,p)
      INTEGER n
      DOUBLE PRECISION a,b,s,losfun
      EXTERNAL losfun
      INTEGER it,j
      DOUBLE PRECISION del,sum,tnm,x,p
      if (n.eq.1) then
        s=0.5d0*(b-a)*(losfun(p,a)+losfun(p,b))
      else
        it=2**(n-2)
        tnm=it
        del=(b-a)/tnm
        x=a+0.5d0*del
        sum=0.d0
        do 11 j=1,it
          sum=sum+losfun(p,x)
          x=x+del
11      continue
        s=0.5d0*(s+(b-a)*sum/tnm)
      endif
      return
      END
C  (C) Copr. 1986-92 Numerical Recipes Software R2A24"o1j.
c
c     The next part is the function to be integrated.  L is the scale length
c     for photodestruction of molecules; rsq is r squared; r is the distance
c     from the nucleus; x is along the line of sight.  L is just expansion
c     velocity times the Sun-comet distance (AU) squared divided by the
c     number from Huebner's paper.
c
      FUNCTION losfun(p,x)
c
      IMPLICIT none
      DOUBLE PRECISION L,rsq,r,p,x,losfun
c
      L = 1.2d05*(.916)**2./1.3d-05
c
      rsq = p**2. + x**2.
      r = dsqrt(rsq)
      losfun = (rsq*dexp(r/L))**(-1.)
      return
```

```
END
```

Appendix H

Sample Model Image Script

```
#! /bin/csh -vf
goto start

cgdisp in=hcn53.cm,hcn53.cm type=contour,grey \
       region=relpix,box'(-10,-10,10,10)' \
       slev=a,.058 levs1=-6,-3,3,6,9,12,15,18,21,24,27,30,33,36,36.31 \
       device=/xw options=full,beambl

# Find beam dimensions and coordinates
prthd in=hcn53.cm

# Create and check regridded HCN image
imgen out=fake object=gaussian spar=1,0,0,9.52,7.74,-82.8 imsize=240 \
      cell=.25 radec=1:24:26,45:16:32
imsub in=hcn53.cm out=hcn53.60 region=relpix,box'(-30,-30,29,29)'
regrid in=hcn53.60 out=hcn53 axes=1,2 tin=fake options=offset tol=.06
prthd in=hcn53
histo in=hcn53
maxfit in=hcn53
cgdisp in=hcn53 type=contour device=/xw options=full,beambl  \
       slev=a,.058 levs1=-6,-3,3,6,9,12,15,18,21,24,27,30,33,36,36.41
cgdisp in=hcn53 type=contour device=/xw options=full,beambl labtyp=abspix \
       slev=a,.058 levs1=-6,-3,3,6,9,12,15,18,21,24,27,30,33,36,36.41
cgdisp in=hcn53 type=contour device=/xw options=full labtyp=abspix \
       slev=a,.058 levs1=-6,-3,3,6,9,12,15,18,21,24,27,30,33,36,36.41 \
       region=box'(120,125,130,135)'
goto end

# Create model image from code output; writefits is an executable that
# I created using fitsio libraries; inspect model image -- make sure
# position is correct
```

```
writefits
fits in=modelimage.fits op=xyin out=modelimage.temp
maths exp='(modelimage.temp/100000000.0)' out=modelimage
puthd in=modelimage/cdelt1 value=1.212e-06
puthd in=modelimage/cdelt2 value=1.212e-06
prthd in=modelimage
histo in=modelimage
maxfit in=modelimage
cgdisp in=modelimage type=contour device=/xw options=full
cgdisp in=modelimage type=contour device=/xw options=full labtyp=abspix
cgdisp in=modelimage type=contour device=/xw options=full labtyp=abspix \
       region=box'(120,125,130,135)'

# Convolve model image with appropriate beam and inspect; find image max;
# After first code run, take desired Imax from HCN image, divide it by Imax
# found here, and multiply by Imax in code to get new Imax for second run of
# code.  The resulting Imax found here in the second time through should
# then match desired Imax from HCN image.  Then ready to proceed.
imgen out=beam.cm object=gaussian spar=1,0,0,9.52,7.74,-82.8 \
     imsize=240 cell=.25
convol map=modelimage beam=beam.cm out=modelimage.cnv options=asymmetric
prthd in=modelimage.cnv
histo in=modelimage.cnv
maxfit in=modelimage.cnv
cgdisp in=modelimage.cnv type=contour \
       slev=a,.058 levs1=-6,-3,3,6,9,12,15,18,21,24,27,30,33,36,36.41 \
       device=/xw options=full labtyp=abspix
cgdisp in=modelimage.cnv type=contour region=box'(120,125,130,135)' \
       slev=a,.058 levs1=-6,-3,3,6,9,12,15,18,21,24,27,30,33,36,36.41 \
       device=/xw options=full labtyp=abspix

# Create difference map
maths exp='(hcn53-modelimage.cnv)' out=excess.cm
prthd in=excess.cm
histo in=excess.cm
maxfit in=excess.cm
fits in=excess.cm out=excess.fits op=xyout

# Here, to make display coordinates better, change crpix1 and crpix2 to the
# pixel location of the max in the HCN and model images.
# Eg: -7.54600000E+03 changes to 1.21000000E+02.  emacs because vi says
# line too long to edit
emacs excess.fits
fits in=excess.fits out=excess op=xyin
```

```
cgdisp in=excess,excess type=contour,grey range=-.36,.42,lin,1 \
       slev=a,.058 levs1=-8,-6,-4,-2,2,4,6,8 device=/xw \
       options=beambl labtyp=arcsec olay=olay.in csize=2,0,2,0
cgdisp in=excess,excess type=contour,grey range=-.66,.42,lin,-1 \
       slev=a,.058 levs1=-8,-6,-4,-2,2,4,6,8 device=excess.ps/ps \
       options=beambl labtyp=arcsec olay=olay.in csize=2,0,2,0
cgdisp in=excess,excess type=contour,grey range=-.36,.42,lin,1 \
       slev=a,.058 levs1=-8,-6,-4,-2,2,4,6,8 device=/xw \
       options=beambl labtyp=arcsec olay=olay2.in csize=2,0,2,0
start:
cgdisp in=excess,excess type=contour,grey range=-.66,.42,lin,-1 \
       slev=a,.058 levs1=-8,-6,-4,-2,2,4,6,8 device=excess2.ps/ps \
       options=beambl labtyp=arcsec olay=olay2.in csize=2,0,2,0

goto end
rm -r fake hcn53.60 hcn53 modelimage.temp beam.cm hcn53.cm excess.fits~
rm -r modelimage.fits modelimage modelimage.cnv excess.cm excess.fits
end:
```

Appendix I

BIMA and VLA Observations of Comet Hale-Bopp at 22 – 115 GHz

THE ASTRONOMICAL JOURNAL, 116:987–996, 1998 August

BIMA AND VLA OBSERVATIONS OF COMET HALE-BOPP AT 22–115 GHz

IMKE DE PATER,[1] J. R. FORSTER,[1] MELVYN WRIGHT,[1] BRYAN J. BUTLER,[2] PATRICK PALMER,[3] JEFFREY M. VEAL,[4]
MICHAEL F. A'HEARN,[5] AND LEWIS E. SNYDER[4]

Received 1998 March 24; revised 1998 April 21

ABSTRACT

We observed comet Hale-Bopp with the Berkeley-Illinois-Maryland Association (BIMA) array at frequencies between 85 and 115 GHz and with the VLA at 43 and 22.5 GHz during 1997 March and April. The continuum radiation of the comet was "easily" detected in the 3 mm wavelength band, where a peak flux density of 12.8 ± 0.65 mJy beam^{-1} was obtained for all the data averaged together (scaled to a geocentric distance of 1.322 AU). The beam size for this observation was $11''.9 \times 8''.8$. The total flux density was 47 ± 4 mJy. We believe that only about 2 mJy can be attributed to thermal emission from the nucleus itself; the remaining emission is thermal emission from large (roughly millimeter-sized or greater) grains in the comet's coma. Roughly 25% of the emission comes from an unresolved source at the center (i.e., an area with a radius of $\lesssim 4500$ km), which is surrounded by a much larger area of low-level emission, visible in the BIMA images up to distances of at least ~25,000 km. Most of this emission can be reconciled with thermal emission from dust flowing away from the nucleus, although there is also clear evidence of distinct emission features ~25,000 km to the southeast and southwest of the nucleus, suggesting former outbursts and/or dust jets. The spectral index of the millimeter emission is consistent with a thermal blackbody spectrum, while a comparison with data at submillimeter wavelengths suggests a steepening in spectral index at shorter wavelengths. The total mass of the dust in the coma is at least a few times 10^{11} kg, and the dust production rate is of the order $\sim 10^6$ kg s^{-1}.

Key words: comets: individual (Hale-Bopp 1995 O1) — techniques: interferometric

1. INTRODUCTION

In 1996 we searched for, but did not detect, the thermal radio emission from comet Hyakutake (C/1996 B2) with the Berkeley-Illinois-Maryland Association (BIMA) array at a wavelength of 2.7 mm (de Pater et al. 1997), whereas the comet was detected at submillimeter wavelengths by Jewitt & Matthews (1997) and Altenhoff et al. (1996). Jewitt & Matthews fitted a power law $S \propto \nu^q$ (S is the flux density and ν the frequency) with $q = 2.8$ to the data. Our 3 σ upper limit of 20 mJy in a 16″ beam fell exactly along this line. For thermal blackbody emission from a large object the index q should be equal to 2 (Planck radiation law in the Rayleigh Jeans limit), while for emission from particles with sizes $\ll \lambda$, $q = 4$. Jewitt & Matthews noted that their power-law index of 2.8 is very similar to that observed in circumstellar disks, and they concluded that the submillimeter emission from comet Hyakutake is dominated by emission from large (roughly submillimeter-sized or greater) grains.

Although there have been many attempts to detect radio emission from comets, very few experiments have been successful (see, e.g., de Pater et al. 1997): apart from comet Hyakutake, continuum radio emission has only been detected from comet IRAS-Araki-Alcock (1.3 cm; Altenhoff et al. 1983), comet Halley (3.58, 1.33, and 1.20 mm; Altenhoff et al. 1986, 1989), and comet Swift-Tuttle (at 0.85 mm; Jewitt 1996). Measurements of the thermal emission from a comet's coma at radio frequencies contain information on the size distribution of relatively large cometary grains. Though centimeter-sized material is expected to be present based upon both the theory of dust being dragged off comets (Whipple 1951; de Pater et al. 1985) and radar observations (e.g., Harmon et al. 1997; Goldstein et al. 1984), it is not known if the size distribution of large grains follows the same power law as that of the smaller grains. Such constraints contain information on the ejection mechanisms of dust and larger sized material.

In order to better constrain the size distribution of large-sized grains, we observed comet Hale-Bopp at BIMA (3 mm) and the VLA[6] (0.7–1.3 cm). We observed the 3 mm continuum emission from the comet on eight different days during 1997 March and April and the 0.7 and 1.3 cm emission on 1997 April 14 and 24. In this paper we report these data and compare the results with predictions made by de Pater et al. (1997).

2. OBSERVATIONS

We observed comet Hale-Bopp (1995 O1) at wavelengths of 0.3, 0.7, and 1.3 cm in 1997 March and April with the BIMA array and the VLA. The ephemerides for all observations, as well as the integration times and total bandwidths for all the BIMA observations, are summarized in Table 1. The geocentric distance varied from 1.3 to 1.66 AU

---

[1] Department of Astronomy, University of California at Berkeley, 601 Campbell Hall, Berkeley, CA 94720; imke@astron.berkeley.edu, rforster@astro.berkeley.edu, mwright@astro.berkeley.edu.

[2] National Radio Astronomy Observatory, P.O. Box O, 1003 Lopezville Road, Socorro, NM 87801; bbutler@nrao.edu.

[3] Department of Astronomy and Astrophysics, University of Chicago, 5640 South Ellis Avenue, Chicago IL 60637; ppalmer@oskar.uchicago.edu

[4] Department of Astronomy, University of Illinois at Urbana-Champaign, 1002 West Green Street, Urbana IL 61801; veal@astro.uiuc.edu; snyder@astro.uiuc.edu.

[5] Department of Astronomy, University of Maryland, College Park, MD 20742-2421; ma@astro.umd.edu.

[6] The VLA is operated by the National Radio Astronomy Observatory, which is a facility of the National Science Foundation, operated under cooperative agreement by Associated Universities, Inc.

TABLE I.1: Ephemeris for comet Hale-Bopp based on JPL ref. orbit 106.

Date (UT)	Start/End (UT)	α(app)[a]	δ(app)[a]	r (AU)	Δ (AU)	SEC[b] (deg)	SCE[b] (deg)	P.A.[c] (deg)	Int. Time (hr)	Bandwidth (MHz)
1997 Mar 18......	12:30–01:00	23 34 31	+44 33 42	0.946	1.322	46	49	354	7.5	2 × 400
1997 Mar 26......	13:30–15:30	00 54 48	+45 46 04	0.920	1.322	44	49	12	1.8	2 × 600
1997 Apr 02	14:00–19:30	02 01 31	+43 55 10	0.915	1.363	42	47	28	3.2	2 × 600
1997 Apr 03	02:30–04:30	02 06 03	+43 41 33	0.915	1.367	42	47	29	1.3	2 × 600
1997 Apr 04	14:00–04:30	02 18 37	+42 59 40	0.916	1.381	42	46	33	8.5	2 × 400
1997 Apr 07	14:30–21:00	02 42 29	+41 21 33	0.921	1.413	41	45	39	4.2	2 × 600
1997 Apr 07	22:30–05:00	02 44 59	+41 09 52	0.922	1.417	40	45	39	4.4	2 × 600
1997 Apr 14	15:30–17:30	03 29 07	+36 45 14	0.945	1.505	38	41	52	2.0	180
1997 Apr 24	18:00–04:30	04 18 15	+30 00 58	1.006	1.664	34	34	67	7.3	2 × 600

NOTE.—Units of right ascension are hours, minutes, and seconds, and units of declination are degrees, arcminutes, and arcseconds.

[a] All coordinates are apparent geocentric coordinates at the approximate starting times of each observing session.

[b] SEC and SCE are the angles between the Sun, Earth, and comet and the Sun, comet and Earth, respectively.

[c] Position angle of the extended Sun-comet radius vector as seen in the observer's plane of sky, measured CCW from reference frame's north celestial pole.

and the heliocentric distance from 0.915 to 1.0 AU. At perigee (1.3 AU) a 1″ beam corresponds to a distance of ~1000 km at the comet.

2.1. *BIMA*

At the time of the observations, the BIMA array consisted of nine 6 m dishes on a *T*-track. The array is located at the Hat Creek Radio Observatory in northern California. The instrument is described in detail by Welch et al. (1996). The observations were carried out at frequencies between 85 and 115 GHz. The comet was observed in both the upper and lower sidebands, which are separated by 3.5 GHz. The data from the two sidebands were combined to increase the signal-to-noise ratio in the final images (in part by doubling the data, but also by improving the UV coverage). The data were calibrated and edited in the usual way using MIRIAD (Sault, Teuben, & Wright 1995). Absolute calibration is assumed to be accurate to within 20% (based upon regular observations of planets and quasars), while the relative calibration across the frequency band is probably accurate to 10%. Before making maps, we adjusted the visibility phases to shift the position of the comet to the "final" Hale-Bopp position (from JPL reference orbit solution 55 to JPL reference orbit solution 77).

Interferometric arrays such as the BIMA array image structure in the radio emission on spatial scales between $\sim\lambda/D_{\min}$ and $\sim\lambda/D_{\max}$, where $D_{\max}$ and $D_{\min}$ are the longest and shortest interferometer baselines. The BIMA observations were carried out while the array was in its C configuration, where the longest and shortest spacings between antennas are 73 and 8.3 m, respectively (note, however, that the actual spatial scales are set by the baselines projected onto the sky so are slightly larger due to foreshortening). The array is thus insensitive to spatial scales $\gtrsim 1'$, or 6×10^4 km at the comet, while the resolution is of order $\sim 10''$.

2.2 *VLA*

The VLA consists of 27 25 m antennas spread out in a *Y* shape on the plains of San Augustin, New Mexico. We used it to observe Hale-Bopp on 1997 April 14 and 24. The April 24 data are of questionable quality and hence will not be discussed here. On April 14, we observed the comet for 3.5 hours, about 2 hours of which were usable (poor atmospheric phase stability ruined the remainder). We observed in two frequency bands: *Q* band (near 7 mm) and *K* band (near 1.3 cm). Only 13 of the VLA antennas were equipped with *Q*-band receivers, so the other 14 were tuned to the *K*-band frequencies. The VLA electronics system allows two independent frequency ranges to be received within each frequency band; these frequencies were 42.9649 and 43.0351 GHz for *Q* band and 22.4851 and 22.4351 GHz for *K* band. Therefore, the total bandwidth was 100 MHz for each band. Stokes LL and RR were measured independently, then combined into total intensity (Stokes *I*).

On April 14, Hale-Bopp was very near 3C 84 (5° plane-of-sky separation), so it was used as the calibrator with which to fix the time varying amplitude and phase of the antennas. Note that since 3C 84 was so near Hale-Bopp, elevation variations are handled by this as well. 3C 84 was also used to fix the absolute flux density scale of the observations, with assumed flux densities of 9.0 Jy at 43.0 GHz and 14.0 Jy at 22.46 GHz. These flux densities were determined by comparing the flux density of 3C 84 to that of 3C 286 during times encompassing April 14. The flux density of 3C 286 has been determined at these two frequencies by comparing it to Mars and basing the expected Mars flux density on the model of Rudy et al. (1987). This scale should be good to between 5% and 10% at *K* band and 10% and 20% at *Q* band. Every hour, a special observation of 3C 84 at *X* band (3.5 cm) was used to adjust the pointing of the individual antennas of the interferometer. A TIP scan was used to determine the opacity of the atmosphere and the system temperatures of the antennas at both frequencies. At *Q* band, the measured zenith opacity was 6.5%, and the mean zenith system temperature was 90 K. At *K* band, the measured zenith opacity was 5.2% and the mean zenith system temperature was 140 K. The comet was tracked as a function of time using the JPL reference orbit 59 solution. Visibilities were recorded every 5 s to reduce atmospheric decorrelation.

Data reduction was performed in the AIPS processing package. After initial data inspection and flagging, calibration solutions for 3C 84 were transferred to the comet data, and these data were then used to make maps of the sky brightness distribution.

3. RESULTS

All data were edited and calibrated, and images were made using natural weighting for maximum sensitivity. The comet was readily detected in the BIMA data but not in the VLA data.

3.1. *BIMA*

To ensure that the data were of the best quality possible, images of the individual sidebands were always made and inspected. The comet was detected in each individual image. The best signal-to-noise ratio is obtained by adding all the data together, while adjusting the UV coordinates and amplitude to the geocentric distance of the comet on 1997 March 18. The result for all data combined is shown in Figure 1*a*, where the lowest contour is equal to twice the rms noise in the image. The peak flux density is 12.8 ± 0.65 mJy beam^{-1}, within a beam size of $11\farcs9 \times 8\farcs8$. Although at first glance the source seems unresolved, it is clearly surrounded by an extended region of low-level flux density. The total flux density is 47 ± 4 mJy. Figure 1*b* shows an image after subtraction of a point source with peak flux density of 12.8 mJy, convolved with the proper beam. This image clearly shows the extended structure of the emission. Roughly 25% of the emission comes from an unresolved source at the center, i.e., from within an area with a radius of $\lesssim 4\farcs5$, or 4500 km, but emission is seen up to distances of $\gtrsim$25,000 km.

When dust is dragged off the nucleus, it will move radially away at basically the terminal velocity. Hence the dust

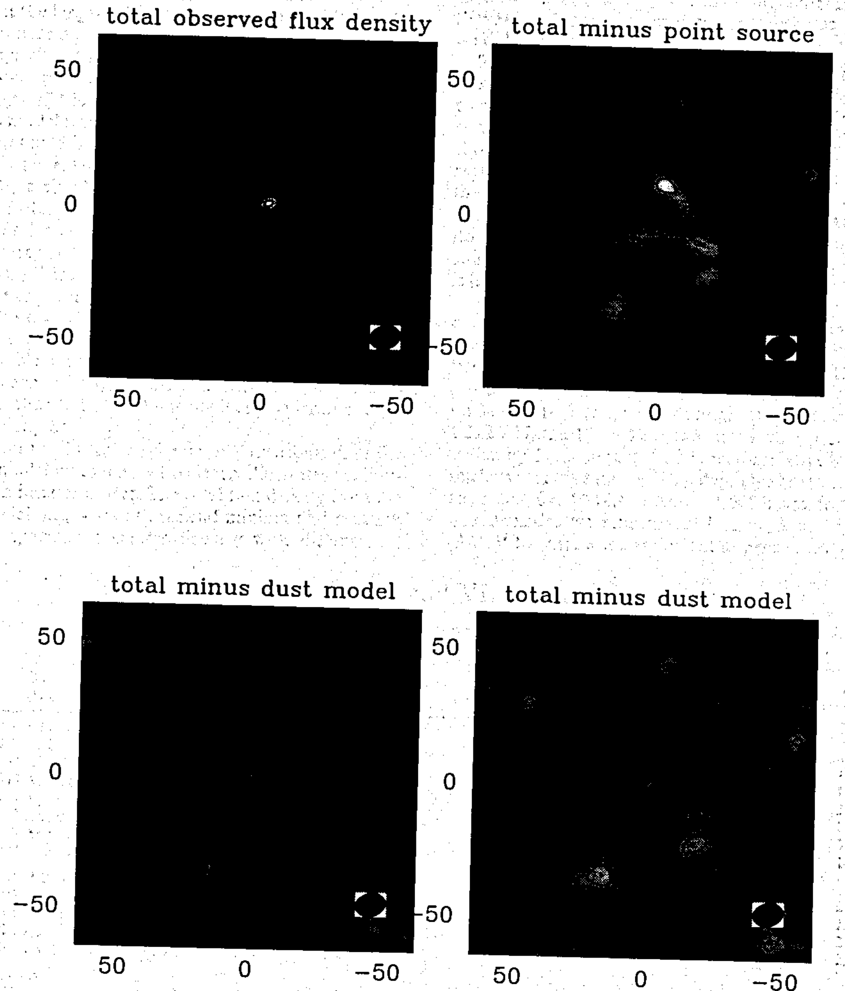

FIGURE I.1: (a) Image of 3 mm continuum emission from comet Hale-Bopp. The peak flux density is 12.8 mJy beam^{-1}. (b) The residual image after a point source with peak flux density of 12.8 mJy was subtracted. (c) The residual image after a dust model, convolved with a Gaussian beam equal to the restoring beam in the clean image (a) was subtracted. (d) Residual image after a dust model, suitably modeled by the BIMA response to such a model, was subtracted from the data.

density in the coma will decrease with distance, r_c, roughly as r_c^{-2} for a constant, spherically symmetric, outflow velocity. We calculated the thermal emission from the coma, assuming an r_c^{-2} density distribution for the emitting dust particles. The resulting model was convolved with the same Gaussian beam as used to restore the cleaned image in Figure 1*a* ($11''.9 \times 8''.8$). After scaling the modeled peak flux density to 11 mJy beam^{-1} (the "observed" peak flux density in the coma, if 1.8 mJy can be attributed to the nucleus [§ 4.1]), we subtracted the model from the data. This difference map is shown in Figure 1*c*. The thermal emission from the nucleus is surrounded by negative contours; thus, we subtracted too much emission at a radial distance of $\sim 25''$. Is this realistic, or would the interferometer filter out the large-scale structure of such a dusty coma? A simulation using appropriate minimum and maximum UV spacings shows that the BIMA array would "see" an emission source much more confined to the center than indicated by a r_c^{-2} law for the spatial dust density. Subtraction of this model from the data is shown in Figure 1*d*. Such a model does match the data very well. Thus most, though not all, of the extended emission in Figure 1*b* can be explained by a simple r_c^{-2} law in the spatial density of the dust. Two features show up bright and clear: one to the southwest and one to the southeast of the nucleus, which may form part of a larger ring of enhanced emission around the nucleus. These features must be produced by local and/or temporal variations in the dust ejection mechanism. We note, however, that the image is an average of data taken over a period of about six weeks; these features are likely not stable over this long a time period and may not be present in each individual data set. The features could be related to outbursts and dust jets, such as frequently seen at visible wavelengths.

In addition to illustrating the density distribution in the coma, this modeling exercise also clearly illustrates the limitations of an interferometer. The total flux density from the original model, i.e., without artificial minima and maxima in the UV spacings, increases linearly with distance, r_c, while the surface brightness decreases with r_c^{-1}. One would expect the signal to drop below the instrument's sensitivity level at a distance $r_c \approx 25''$–$30''$. Simulating the interferometer response to such a model with proper UV minima and maxima showed that BIMA is not sensitive to structures $\gtrsim 1'$ in size. We measure a total flux density of 40 mJy from an area confined to $r_c \approx 35''$, both in the model and the data. While the total flux density in the original model continues to increase with distance, BIMA cannot detect emissions from larger distances (unless they are from compact separate components, as observed and discussed above). In comparison with most single-dish observations, we assume that we measured all the flux density; however, if one were to observe with a very sensitive telescope $\lesssim 8$ m in size (FWHP $> 1'$), one might detect a larger flux density than we did.

Figure 2 shows images from individual days, where the flux density on each day was scaled by $(\Delta/\Delta_0)^2$, with Δ, the comet's geocentric distance, and $\Delta_0 = 1.322$ AU, the comet's geocentric distance on March 18. The images are shown at their full resolution (see Table 2). The source region is (slightly) extended in all of the images. Based upon the low signal-to-noise ratio in these images and on differences between images made of each sideband separately, we do not trust variations in the detailed morphology of the source region. However, the emission is clearly detected and is (slightly) extended in each image.

To evaluate the time evolution and the variation in flux density with frequency, we restored the clean components of each image with the same beam but scaled in proportion to the size of the comet. We chose a beam size of $15'' \times 12''$ at a position angle of $\sim 95°$ (measured from north through east) on March 18. Using a standard geocentric distance of $\Delta_0 =$ 1.322 AU, the $15'' \times 12''$ beam size on individual days was scaled by Δ_0/Δ, so that the beam size relative to the comet's nucleus was the same on each day. This beam size is referred to as the "fixed" 14,400 km × 11,500 km beam. In addition, the flux densities were normalized through multiplication by $(\Delta/\Delta_0)^2$ to correct for variations in geocentric distance. The

TABLE I.2: BIMA and VLA observations.

			OBSERVED[a]		FIXED BEAM[b]		NORMALIZED[c]		OFFSET	
DATE (UT)	ν (GHz)	BEAM (arcsec)	Peak (mJy)	rms (mJy)	Peak (mJy)	rms (mJy)	Peak (mJy)	rms (mJy)	α (arcsec)	δ (arcsec)
BIMA data:										
1997 Mar 18......	87.2	10.8 × 8.2	12.5	1.5	14.4	1.6	14.4	1.6	−0.7	2.4
1997 Mar 26......	105.6	19.7 × 6.2	19.0	5.9	18.9	5.8	18.9	5.8	−1.1	4.7
1997 Apr 02	105.6	11.2 × 6.3	14.3	1.6	16.5	1.6	17.6	1.6	−1.2	1.1
1997 Apr 04	87.2	11.0 × 7.7	11.2	2.8	12.2	2.9	13.3	2.9	−5.2	2.3
1997 Apr 07	110.9	14.0 × 11.2	13.9	2.8	13.9	2.9	16.6	3.3	−4.2	2.8
1997 Apr 07	113.5	14.0 × 11.2	17.6	3.1	17.6	3.1	20.2	3.6	−0.3	3.6
1997 Apr 24	87.2	11.2 × 8.0	6.7	0.8	7.2	0.75	11.3	1.2	0.5	1.8
Averaged BIMA data:										
1997 Apr 07	112.2	9.0 × 6.2	13.0	2.1	14.5	2.0	16.6	2.3	−2.8	2.8
All days:	87.2						13.8	0.95	−1.1	2.3
All days:	109						17.6	1.6	−2.2	2.6
All days:	98	11.9 × 8.8	12.8	0.65			15.3	0.70	−1.5	2.1
VLA data:										
1997 Apr 14	43.0	0.49 × 0.42	<0.50							
	22.5	0.98 × 0.58	<0.52							

[a] Absolute calibration errors have not been included in the uncertainties reported. Upper limits are at the 3 σ level.

[b] "Fixed" 14,400 × 11,500 km beam (see text).

[c] Flux densities in col. (6) multiplied by $(\Delta/\Delta_0)^2$.

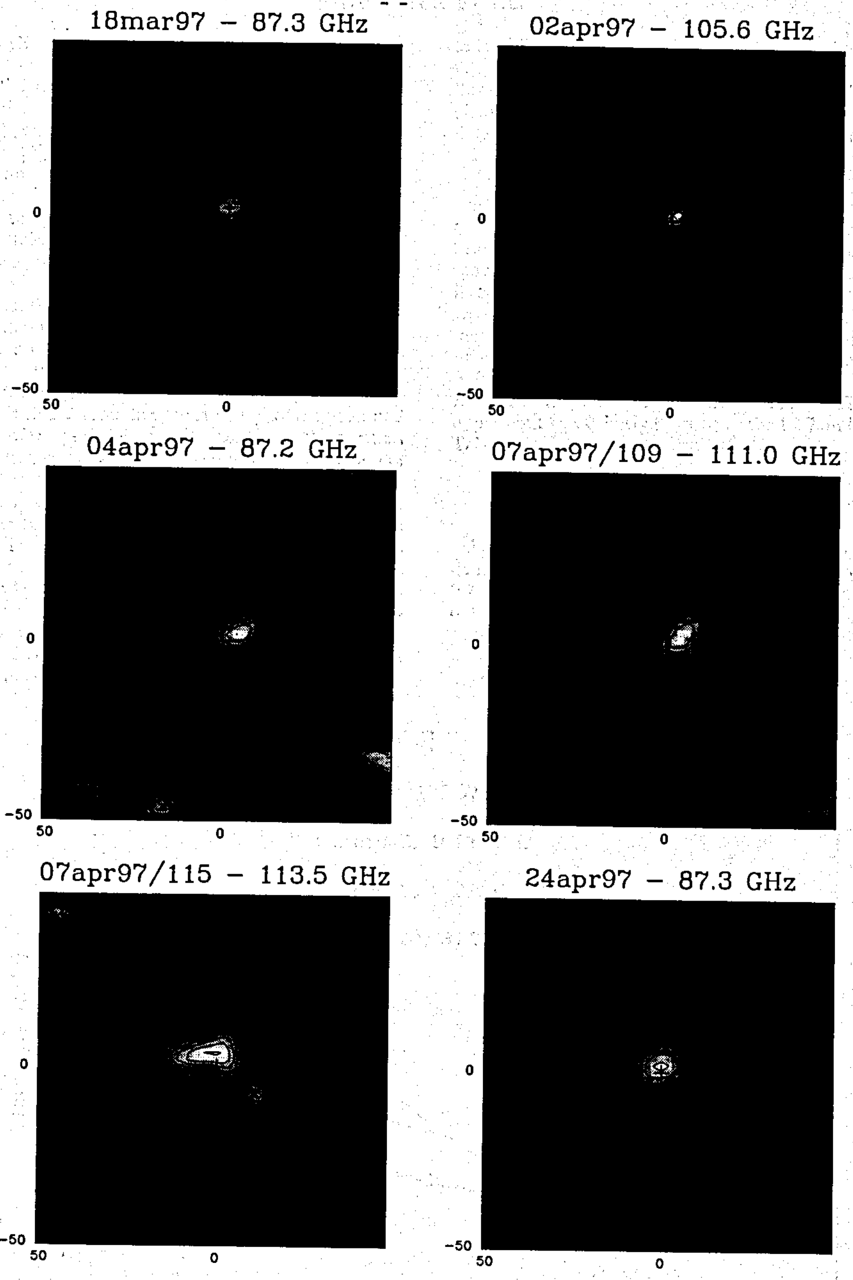

18mar97 – 87.3 GHz

02apr97 – 105.6 GHz

04apr97 – 87.2 GHz

07apr97/109 – 111.0 GHz

07apr97/115 – 113.5 GHz

24apr97 – 87.3 GHz

FIGURE I.2: Images of the continuum emission from comet Hale-Bopp on individual days, and at different frequencies, as indicated at the top of each image. All intensities are scaled by $(\Delta/\Delta_0)^2$, with $\Delta_0 = 1.322$ AU. Flux densities are at 4, 6, 8, ..., 18 mJy beam^{-1} (in steps of 2 mJy beam^{-1}). The peak flux densities and beam sizes are indicated in Table I.2.

results are shown in Table 2. In this table we show the high-resolution peak flux densities in individual images (col. [4], with the rms uncertainty in col. [5]), the peak flux density in the "fixed" 14,400 km × 11,500 km beam (cols. [6] and [7]), and the normalized flux density in the "fixed" beam (cols. [8] and [9]). The beam size for the high-resolution images is given in column (3) (this is also the beam size used in Fig. 2). The data for April 2 were combined with those taken on April 3. The middle section in Table 2 contains average values: the first row for the two sessions on April 7, and the remaining rows for all data at frequencies $\nu < 100$ GHz (indicated by 87.2 GHz), $\nu > 100$ GHz (109 GHz), and at all frequencies (effectively, 98 GHz). Average values in the table were obtained from images constructed from the relevant UV data; so the rms noise and peak flux density may be different than one would obtain by averaging the numbers in Table 2. The rightmost two columns in Table 2 show the offset in right ascension and declination of the peak flux density, i.e., this is the position of the cometary emission relative to the adopted position of the cometary nucleus.

We note that for a point source the peak flux density is equal to the total flux density, and should not vary with beam size. The peak flux density in the images of comet Hale-Bopp increases with increasing beam size, suggestive of an extended source, such as is seen in Figure 1*a*. To further prove that the source region is extended, we measured the flux density on four different days directly from the UV data, as a function of UV distance (not scaled with Δ_0/Δ). The results are shown in Figure 3. At each UV distance *X*, the total vector-averaged flux density in the UV range between zero and *X* is measured. We normalized the flux density to a geocentric distance of 1.322 AU [i.e., multiplied by $(\Delta/\Delta_0)^2$]. The flux density clearly increases toward the shorter spacings, as expected for a resolved source.

3.2. *VLA*

Maps were made at two resolutions for each of the frequencies: the full resolution of the array and relatively heavily tapered (30% UV taper distance = $\frac{1}{3}$ of maximum spacing). At the time of the observations, the VLA was in its B configuration, with minimum and maximum physical separation between antennas of about 0.2 and 11.4 km. For the sky positions covered by the comet during the observation, this resulted in resolutions of 0″.291 × 0″.205 (0″.493 × 0″.421) at *Q* band and 0″.718 × 0″.332 (0″.982 × 0″.582) at *K* band in the full resolution (tapered) maps. The 3 σ VLA upper limit was 0.5 mJy beam^{-1} both at 0.7 and 1.3 cm (see Table 2).

4. DISCUSSION

4.1. *Nucleus*

De Pater et al. (1997) predicted that, near perigee, the flux density from comet Hale-Bopp's nucleus at a wavelength of 2.7 mm (109 GHz) would be $S_{109} \approx 3.7$ mJy and at 3.6 cm (8.5 GHz) $S_{8.5} \approx 22\mu$Jy, if its diameter is 50 km and temperature ~195 K, i.e., the sublimation temperature of water ice at $r \approx 1$ AU. If substantial areas on the comet's surface are dark rock rather than ice, the average temperature may

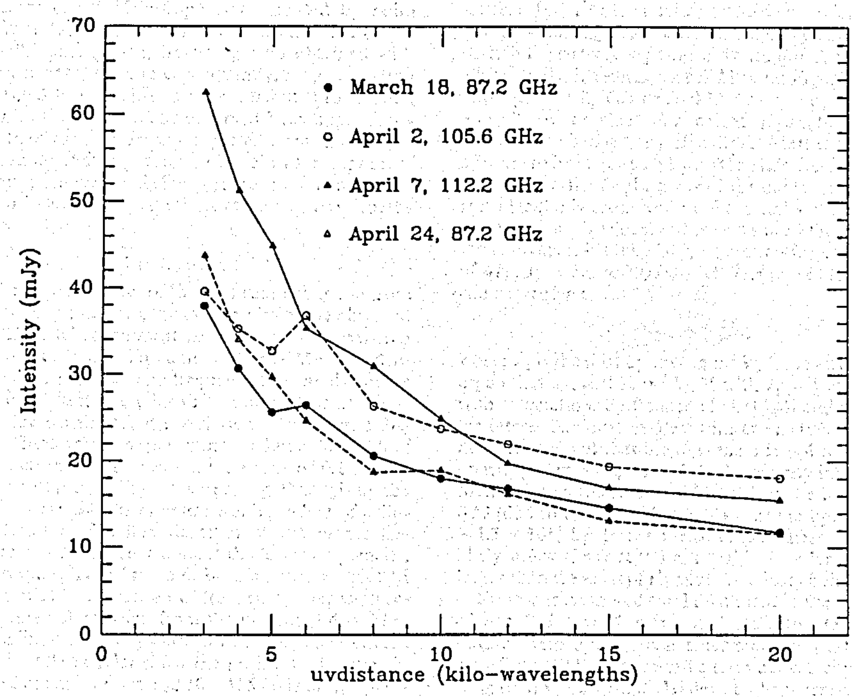

FIGURE I.3: Flux density as a function of UV distance on four different days. The flux densities have been scaled by $(\Delta/\Delta_0)^2$, with $\Delta_0 = 1.322$ AU.

be higher, i.e., somewhere between 195 and 280 K, the blackbody temperature of a dark body at $r \approx 1$ AU. We ignore this effect in this paper, but it would increase all flux densities approximately linearly with temperature. We further note that the above predictions were based upon a unit emissivity, i.e., giving maximum flux densities for the assumed size and temperature. The emissivities could be substantially less than unity, such as those measured at centimeter wavelengths for the icy surfaces of Europa and Ganymede (Pauliny-Toth et al. 1974, 1977; de Pater, Brown, & Dickel 1984; Muhleman et al. 1986) and possibly for comet IRAS-Araki-Alcock (de Pater et al. 1985). Both Europa and Ganymede had more "normal" emissivities at millimeter wavelengths, though (e.g., Ulich et al. 1984; de Pater et al. 1989; Muhleman & Berge 1991). *HST* and infrared observations suggest the nuclear diameter to be between 40 km (Weaver 1998) and 70 km (Sekanina 1998). In this paper we adopt a diameter of 40 km, which best agrees with size estimates based upon radio observations by Fernandez et al. (1998), as detailed below. A diameter of 40 km rather than 50 km would lower de Pater et al.'s (1997) estimates somewhat. With the assumptions given above, at a geocentric distance of 1.322 AU, the flux densities from the nucleus are expected to be $S_{87} = 1.4$ mJy, $S_{109} = 2.2$ mJy, $S_{43} = 0.35$ mJy, and $S_{8.5} \approx 14$ μJy. As stated in § 3, the emission detected at millimeter wavelengths is much larger than expected from the nucleus alone; a value of 15.3 mJy at 98 GHz would correspond to a nucleus (spherical blackbody of temperature 195 K) with a diameter of ~ 115 km. This is inconsistent with the value derived from *HST* and infrared observations. We, therefore, conclude that the millimeter emission from comet Hale-Bopp is dominated by radio emission from dust or grains in its coma. The VLA observations at 0.7 and 1.3 cm, however, were obtained with small beam sizes ($\lesssim 1''$), and consequently, a large fraction of the expected flux densities can be attributed to thermal emission from the nucleus. The observed VLA upper limits are larger than the flux density expected from the nucleus alone. We note that separation of the two components requires an iterative modeling procedure for both the nucleus and halo, and observations at several wavelengths are required.

4.2. *Coma*

Given the expected level of thermal radio emission from comet Hale-Bopp's nucleus, the radio emission we observed with the BIMA telescope must be dominated by emission from the comet's coma. To compare the BIMA flux densities at the different times and frequencies, we made images with the same beam size relative to the nucleus and corrected the flux density for the variation in geocentric distance (§ 2). These values were summarized in column (8) of Table 2. Since the data span only a range of 0.1 AU in heliocentric distance, it is not surprising that, given the error bars, the emission is essentially independent of heliocentric distance r. The flux densities at the higher frequencies are generally larger than at the lower frequencies, as shown graphically in Figure 4. In this figure we plotted the flux densities as a function of frequency, after subtraction of the thermal emission from the nucleus (§ 4.1). Flux densities for individual days are shown with open circles, while the two filled circles show the peak flux densities in maps made from all 87 GHz and 105–115 GHz data separately. A power law $S \propto \nu^q$ with $q = 1.26$ gives a best fit to the data but seems physically implausible. Since the thermal emission from the nucleus was subtracted from the data, this fit is not influenced by the blackbody curve of the nucleus. Ignoring the nuclear emission completely results in $q = 1.34$; raising the nuclear flux density tends to lower q (flatten the curves). A power law with $q = 2$, as expected for a blackbody, is shown as a solid line on Figure 4 and fits the data quite well. The dashed line shows a power law with $q = 2.8$, as obtained for comet Hyakutake from submillimeter observations (Jewitt & Matthews 1997); this appears to be inconsistent with the Hale-Bopp data.

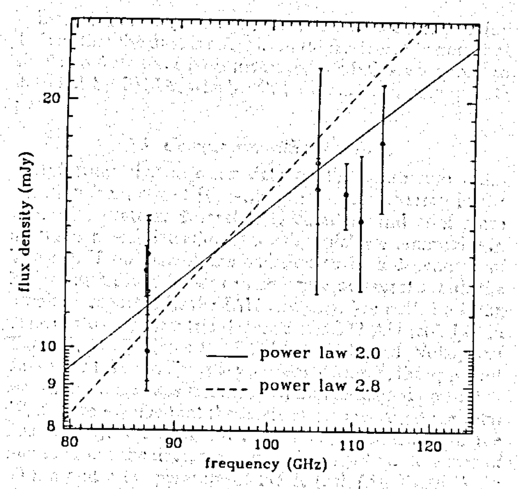

FIGURE I.4: Spectrum of the radio emission.

We can estimate the mass of the coma from the equivalent blackbody cross section of the emission. Assuming the temperature of the dust in the coma is 300 K (at $r \approx 1$ AU), the equivalent blackbody cross section for a total emission of 47 mJy is $\pi r_c^2 \approx 20{,}000$ km^2. The mass of the halo, M_h, can be written as

$$M_h = \pi r_c^2 / \kappa_\lambda \,, \qquad (1)$$

where κ_λ is the dust opacity in m^2 kg^{-1}. Jewitt & Matthews argue that $\kappa_{\lambda_0} = 0.05$ m^2 kg^{-1} with $\lambda_0 = 1$ mm, consistent with calculations by Pollack et al. (1994) and with numbers for interstellar dust by Beckwith et al. (1990). Using these numbers we find that the dust mass is $\sim 4 \times 10^{11}$ kg if the opacity index $\beta = q - 2 = 0$. If the opacity index $\beta \approx 1$, the total mass in the halo would be decreased by $(\lambda/\lambda_0)^{-\beta} \approx 0.33$ (due to the dependence of κ_λ on the opacity index) to $\sim 1.3 \times 10^{11}$ kg. Hence the total dust mass in the coma is likely a few times 10^{11} kg, roughly 1 order of magnitude larger than the mass of Hyakutake's dusty halo.

From our measured total dust mass in the coma, the size of our "observed" coma and an estimate of the dust outflow velocity, one can determine the dust production rate. Crifo (1991) determined a terminal velocity for the dust of $\gtrsim 10$ m s^{-1} for comet Halley at a heliocentric distance of ~ 1 AU. The terminal velocity varies with particle size by over an order of magnitude, roughly between ~ 10 and ~ 400 m s^{-1} for sizes ranging from a few centimeter down to 0.1 mm. The velocity further depends strongly on the gas production rate (Grün & Jessberger 1990; Combi et al. 1998). We further note that the total dust mass detected by BIMA is likely a lower limit, since BIMA cannot detect the comet's large-scale structure (§ 3.1), nor is BIMA sensitive to grains roughly submillimeter-sized or smaller. If we assume that all the dust detected by BIMA is confined to a sphere with a radius of 20,000 km and that the terminal velocity is 100 m s^{-1}, the dust production rate is $dM_N/dt = M_N/t_e = 3 \times 10^{11}/2 \times 10^5 \approx 10^6$ kg s^{-1}. Similar numbers are obtained if we use the peak flux density of 12.8 mJy within a sphere of radius $6'' \approx 6000$ km, corresponding to a beam size with a FWHM of $\sim 12''$.

Jewitt & Matthews determined a dust production rate for comet Hyakutake of $\sim 3 \times 10^4$ kg s^{-1}, assuming a terminal velocity of 10 m s^{-1}. Given the size of comet Hale-Bopp (40 km diameter) compared to Hyakutake (3 km diameter), one would expect the production rates for the two comets to differ by about 2 orders of magnitude, more or less in agreement with the "observed" values. We stress, however, that these numbers have large error bars associated with them, due to the uncertainties in the adopted parameters. Detailed physical models are needed to improve these estimates.

The average radio emission is offset from the adopted ephemeris position of the nucleus, $\sim 1''.5$ to the west in right ascension and $2''$ to the north in declination. A comparison between JPL orbits 77 and 106 shows that the former ephemeris (orbit 77, used to map the data) is about $-1''.5$ to $-2''$ off in declination and $\lesssim -0''.5$ in right ascension; i.e., the comet in our maps should appear $\sim 1''.5$–$2''$ to the north and $\lesssim 0''.5$ to the east. So the offset in declination is consistent with the "known" ephemeris error (orbit 77 to orbit 106), whereas the offset in right ascencion is in the opposite direction, i.e., would be increased from $-1''.5$ to $-2''$ compared with JPL reference orbit 106. As shown in Table 2 and Figure 2, the offset positions for the individual days vary by a few arcseconds. This suggests either that the ephemeris is not quite right (JPL reference orbit solution 106) or that the dust is offset from the nucleus. We note that similar offsets have been measured for HCN emissions as detected by BIMA, which will be discussed in a separate paper.

4.3. *Comparison with Other Data*

Unfortunately, no other data on the continuum radio emission from comet Hale-Bopp have yet appeared in the refereed literature. Several IAU circulars and conference abstracts report detections, though, which we summarize in Table 3. If we assume the emission to be independent of heliocentric distance, we can compare our results with the numbers reported in the IAU circulars. We scaled all flux densities to a geocentric distance of 1.322 AU (col. [4] in Table 3; § 4.1). Since the IRAM, JCMT, and Nobeyama data were taken in February and early March, the apparent size of the comet was smaller than that measured on March 18, and we assume that these telescopes measured the total flux density. We subtracted the thermal emission of the nucleus from the data, assuming a body with a diameter of 40 km and a temperature of 195 K (col. [5], Table 3). As shown in Table 3, the assumed nuclear contribution is usually a small fraction of the total flux density, unless the beam size of the telescope is small ($\lesssim 1''$). In Figure 5 we compare these numbers with the total flux densities received with BIMA, after subtraction of the assumed nuclear contribution. Note that BIMA peak and total fluxes are tabulated separately. The synthesized beam sizes of the VLA, IRAM Plateau de Bure Interferometer, and Owens Valley Radio Observatory (OVRO) were $\lesssim 3''$. Since our observations show that the source is clearly extended, these values are lower limits to the total flux densities, and we indicated these numbers, as well as the BIMA peak flux densities, as open symbols.

In Figure 5 we superposed the same power law as in Figure 4. At first sight, the $\nu^{2.8}$ power law, as found for comet Hyakutake by Jewitt & Matthews (1997), seems to fit most data in Figure 5*a*. However, the open symbols are

TABLE I.3: Comet Hale-Bopp: all available flux density measurements.

Date (UT)	ν (GHz)	S_ν (mJy)	S_ν Normalized[a] (mJy)	Nucleus (mJy)	Halo (mJy)	Beam Size (arcsec)	Telescope
1997 Feb 9–16........	344	440	800	21.5	780	14.5	JCMT[b]
1997 Feb 2............	250	100	225	11.5	214	~10	30 m IRAM[c]
1997 Mar 9–11	229	24 ± 1	26 ± 1	9.7	16	1.5	Plateau de Bure[d]
1997 Apr 1............	223	33	34	9.2	24.8	1.0 × 0.9	OVRO[e]
1997 Mar 3–6	150	55 ± 7	65 ± 8	4.2	61	~10	45 m Nobeyama[f]
1997 Mar 18..........	109	17.6 ± 1.6	17.6 ± 1.6	2.22	15.4	12 × 15	BIMA[g]
1997 Mar 18..........	109	39 ± 4	39 ± 4	2.22	37	~40	BIMA[g]
1997 Mar 6	100	29 ± 4	34 ± 5	1.9	32	~15	45 m Nobeyama[f]
1997 Apr 1............	86–100	13.5 ± 1	14.0	1.65	12.3	3	OVRO[e]
1997 Mar 18..........	87	13.8 ± 1	13.8 ± 1	1.42	12.4	12 × 15	BIMA[g]
1997 Mar 18..........	87	48 ± 5	48 ± 5	1.42	47	~40	BIMA[g]
1997 Apr 14	43	<0.5	<0.6	0.35	<0.25	~0.5	VLA[g]
1997 Apr 14	22.5	<0.5	<0.6	0.10	<0.5	~1	VLA[g]
1997 Mar 20–30......	8.5	0.020 ± 3	0.020 ± 3	0.014	0.006	1	VLA[h]

[a] All flux densities were multiplied by $(\Delta/\Delta_0)^2$, where Δ_0 is the geocentric distance of the comet on March 18.

[b] Matthews & Jewitt 1997.

[c] Kreysa et al. 1997.

[d] Wink et al. 1997.

[e] Blake et al. 1998.

[f] Matsuo et al. 1997.

[g] This paper.

[h] Fernandez et al. 1998.

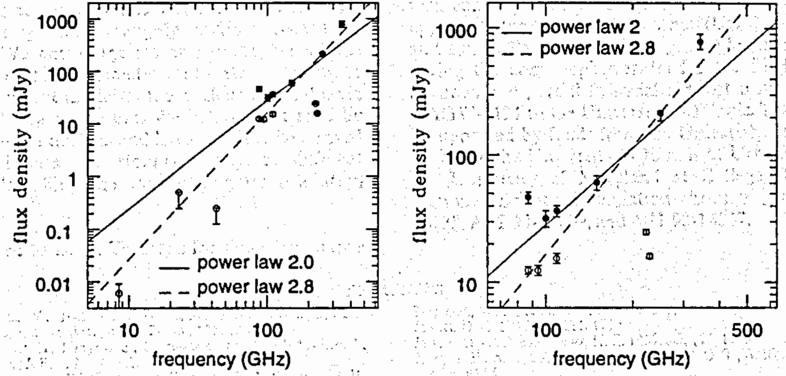

FIGURE I.5: (a) A comparison of all available data (Table I.3). The open circles are lower limits to the total flux density, because of a much smaller beam size used (see text). (b) An expanded view of the high-frequency spectrum from (a).

lower limits to the total flux density, and we believe that, although the higher frequency data (greater than 150 GHz) are matched fairly well with a power-law index $q = 2.8$, this power law may be too steep at frequencies below 150 GHz, where a thermal profile (ν^2) matches the data better. If true, this suggests that the emission at higher frequencies is dominated by a combination of thermal emission from particles both greater than and $\ll \lambda$, whereas at the lower frequencies the flux density is probably dominated by thermal emission from large (roughly millimeter-sized or greater) grains in the comet's coma. It must be kept in mind, though, that most observers detected lower limits to the actual total flux density. If the numbers at submillimeter wavelengths are higher than quoted here, a power law with $2 < q < 3$ may well fit all the data. In addition, the flux density may vary over time, so ideally power-law spectra should be measured on the same day, within the same relative beam size. A new power-law fit should be obtained once all the measurements are public and adjusted to the same angular resolution.

Bieging et al. (1997) reported on observations between 32 and 860 GHz. Their results are quite similar to ours: (1) They suggest that any emission from the nucleus is confined to a body with a diameter less than 50 km. If we attribute the total flux density measured by the VLA at 3.6 cm, as reported by Fernandez et al. (1998), to thermal emission from the nucleus, then the maximum size of the nucleus, using de Pater et al.'s (1997) assumptions, would be 47 km (see § 4.1). (2) Bieging et al. suggest that the half-power full width of the emission region is 11" or 11,000 km. This is roughly consistent with the numbers reported in this paper. (3) They fit a power law ν^q to the spectrum between 32 and 860 GHz, and found $q = 3$. Such a power law does seem to fit the higher frequency data, but we find that the lower frequency data (3 mm) are better matched by a blackbody curve. (4) They report a mass of the halo of 3×10^9 kg, nearly 2 orders of magnitude less than the number we report (and note that our number is likely a lower limit). From observations at 1.4 mm, Senay et al. (1997) determined a total dust mass of 1.7×10^{12} kg in the coma, with a dust production rate of 3.2×10^5 kg s^{-1}, numbers that agree better with the values reported in this paper.

5. CONCLUSIONS AND FUTURE

We have been able, for the first time, to detect and image the continuum radio emission from a comet at frequencies between 85 and 115 GHz. The emission is clearly extended, suggesting that the radiation originates from dust in the comet's coma. Roughly 25% of the emission comes from a region within a radius of $\lesssim 4500$ km, centered presumably around the nucleus. Low-level emission was seen up to distances of $\gtrsim 25{,}000$ km. Most of this emission is consistent with thermal radiation from dust in a sphere around the nucleus, with a spatial density $\rho \propto r_c^{-2}$. Several distinct emission features at ~ 25000 km suggest local and/or temporal variations in the dust outflow velocity, such as outbursts and/or dust jets. The thermal emission from the nucleus itself is probably not much more than 2 mJy (40 km diameter body with a temperature of 195 K), while the total flux density observed over 85–115 GHz was 47 ± 4 mJy. The spectral index of the emission is consistent with a thermal blackbody spectrum. We derive a lower limit of a few times 10^{11} kg for the total mass in the dust in the coma of comet Hale-Bopp, with a dust production rate $\sim 10^6$ kg s^{-1}.

We further report 3 σ upper limits of ~ 0.5 mJy at 0.7 and 1.3 cm, obtained with the VLA. Since the angular resolution for these observations was $\lesssim 1''$, these data were mainly sensitive to the thermal emission from the comet's nucleus. The measured upper limits are slightly larger than the flux densities expected from thermal emission from the nucleus alone. Data at different frequencies and at small angular resolution can be used in an iterative modeling process to separate the contributions of the nucleus and halo. Unfortunately, our VLA data are not of high enough quality (i.e., too little observing time) to undertake this task.

A comparison with data at higher frequencies, as reported in several IAU circulars and conference abstracts, suggests a steepening of the spectral index toward higher frequencies, from a power law $q \approx 2$ at $\nu \lesssim 150$ GHz, to $q \approx 3$ at $\nu \gtrsim 150$ GHz. We believe this change in the spectrum suggests that emission by small particles becomes important at submillimeter wavelengths, whereas the millimeter-centimeter emission is dominated by thermal emission from large-sized (roughly millimeter-sized or greater) grains. We encourage researchers to use all the radio observations at submillimeter-centimeter wavelengths to develop a consistent model of the nucleus and halo, via an iterative modeling procedure. We believe that realistic models of the comet's nucleus and halo can only be derived by analyzing all data sets simultaneously, at different resolutions, while taking the varying angular resolution into account.

We are indebted to D. K. Yeomans for timely assistance with ephemerides for all of these observations. We greatly appreciate the help of W. Hoffman (UCB) and of C. Acton and Bill L. Taber (JPL NAIF group) for their help in preparing the comet ephemerides for the BIMA array. We acknowledge partial financial support from NASA Grant NAGW-1131 to the University of Illinois. The BIMA array is supported by funds from the University of California at Berkeley, the University of Illinois at Urbana-Champaign, the University of Maryland at College Park, and the National Science Foundation through grants AST 93-20238, AST 93-20239, and AST 93-14847.

REFERENCES

Altenhoff, W. J., Bartla, W., Huchtmeier, W. K., Schmidt, J., Stumpff, P., & Walmsley, M. 1983, Astron. Astrophys. Trans., 125, L19
Altenhoff, W. J., Butler, B., Kreysa, E., Mauersberger, R., McMullin, J., Stumpff, P., & Wink, J. E. 1996, BAAS, 28, 928
Altenhoff, W. J., Huchtmeier, W. K., Kreysa, E., Schmidt, J., Schraml, J. P., & Thum, C. 1989, Astron. Astrophys. Trans., 222, 2323
Altenhoff, W. J., Huchtmeier, W. K., Schmidt, J., Schraml, J. P., & Thum, C. 1986, Astron. Astrophys. Trans., 164, 227
Beckwith, S. V. W., Sargent, A. J., Chini, R. S., & Güsten, R. 1990, AJ, 99, 924
Bieging, J. H., et al. 1997, BAAS, 191, 72.02
Blake, G. A., Qi, Q. C., Gurwell, M. A., & Muhleman, D. O. 1998, in preparation
Combi, M. R., Kabin, K., DeZeeuw, D. L., Gombosi, T. I., & Powell, K. G., 1998, in Earth Moon Planets, submitted
Crifo, J. F. 1991, in Comets in the Post–Halley Era, ed. R. L. Newburn, M. Neugebauer, & J. Rahe (Dordrecht: Kluwer), 937
de Pater, I., Brown, R. A., & Dickel, J. R. 1984, Icarus, 57, 93
de Pater, I., Snyder, L. E., Mehringer, D. M., Wright, M., Veal, J. M., Fernández, Y. R., Palmer, P., & A'Hearn, M. F. 1997. Planet. Space Sci., 45, No. 6, 731
de Pater, I., Ulich, B. L., Kreysa, E., & Chini, R. 1989. Icarus, 79, 190
de Pater, I., Wade, C. M., Houpis, H. L. F., & Palmer, P. 1985, Icarus, 62, 349
Fernandez, Y. R., et al. 1998. Earth Moon Planets, in press
Goldstein, R. M., Jurgens, R. F., & Sekanina, Z. 1984, AJ, 89, 1745
Grün, E., & Jessberger, E. 1990, in Physics and Chemistry of Comets, ed. W. F. Huebner (New York: Verlag), 113
Harmon, W. K., et al. 1997, Science, 278, 1921
Jewitt, D. C. 1996, AJ, 111, 1713,
Jewitt, D. C., & Matthews, H. E. 1997, AJ, 113, 1145
Kreysa, E., Altenhoff, W. A. J., Haslam, C. G. T., & Sievers, A. 1997, IAU Circ. 6555
Matthews, H., & Jewitt, D. 1997. IAU Circ. 6566
Matsuo, H., Sakamoto, A., Kuno, N., & Ukita, N. 1997, IAU Circ. 6585
Muhleman, D. O., & Berge, G. L. 1991, Icarus, 92, 263
Muhleman, D. O., Berge, G. L., Rudy, D., & Niell, A. E. 1986, AJ, 92, 1428
Pauliny-Toth, I. I. K., Witzel, A., & Gorgolewski, S. 1974, A&A, 34, 129
———. 1977, A&A, 58, L27
Pollack, J. B., Hollenbach, D., Beckwith, S., Simonelli, D. P., Roush, T., & Fong, W. 1994, AJ, 421, 615.
Rudy, D. J., Muhleman, D. O., Berge, G. L., Jakosky, B. M., & Christensen, P. R. 1987, Icarus, 71, 159
Sault, R. J., Teuben, P. J., & Wright, M. C. H. 1995, in ASP Conf. Ser. 77, Astronomical Data Analysis Software and Systems, ed. R. A. Shaw, H. E. Payne, & J. J. E. Hayes (San Francisco: ASP), 433
Sekanina, Z. 1998. Earth Moon Planets, submitted
Senay, M., et al. 1997, BAAS, 29, 1034
Ulich, B. L., Dickel, J. R., & de Pater, I. 1984, Icarus, 60, 590
Weaver H. A., 1998, First International Conference on Comet Hale-Bopp, Tenerife, Spain, Feb. 2-5, 1998
Welch, W. J., et al. 1996, PASP, 108, 93
Whipple, F. L. 1951, AJ, 113, 464
Wink, J. E., et al., 1997. IAU Circ. 6587

Appendix J

Monte Carlo Code

```
      PROGRAM comet
c
c     This program is the Monte Carlo code described in Chapter 3 Section
c     3.4 of my thesis.  It does what the thesis says it does, except for
c     the fact that the code is entirely in units of cgs.
c
!$pragma C ( erand48 )

      IMPLICIT none
      INTEGER*2 iseed(3)
      INTEGER*4 timeseed,time,ldim,hdim,alphai,deltai
      REAL*8 pi,k,N
      REAL*8 erand48,Omega,ts,tf,td,taup,rdo
      REAL*8 phi,theta,xf,yf,zf,v,rn
      REAL*8 m,m1,m2,m3,rd1,rd2,phisym,thetasym
      REAL*8 rd1,rd2,c,c1,c2,c3,mu,mu1,mu2,mu3,ca,ca1,ca2,ca3
      REAL*8 cb,cb1,cb2,cb3,cc,cc1,cc2,cc3,sc,sc1,sc2,sc3
      REAL*8 rs,grs,rmax,rmax1,rmax2,rmax3,rr,rr1,rr2,rr3,frs,Omegagrs
      REAL*8 cp,sp,ct,st,cd,ce,cf,factor
      REAL*8 eta,zeta,cg,ch,ci,factor2,cpsi,v6,ve,vgrain
      REAL*8 beta,sbeta,cbeta,xi,yi,PsAng,omeg,comeg,someg,alpha,delta
      REAL*8 image,beam,checker,F,counter,Nobs,S,Q,factor3
      PARAMETER (ldim=-119,hdim=120)
      DIMENSION image(ldim:hdim,ldim:hdim)

c     Here are the parameters to change frequently
      N = 1.d08
      rdo = .147
      m1 = 60.
      c1 = 160.
      mu1 = 90.
```

```
      m2 = 30.
      c2 = 110.
      mu2 = -40.
      m3 = 5.
      c3 = 30.
      mu3 = -30.
      beta = 48.5
      PsAng = 17.7

c     Here are some constants
      pi = 3.14159 26535 89793 23846
      taup = 1./1.3d-05
      tf = 7. * taup
      v = 1.2d05
      rn = 2.d06
      rmax1 = 8.346d08
      rr1 = rmax1/8.
      m1 = 2.*pi*m1/360.
      c1 = 2.*pi*c1/360.
      mu1 = 2.*pi*mu1/360.
      cc1 = dcos(c1)
      sc1 = dsin(c1)
      ca1 = dcos(mu1) * sc1
      cb1 = dsin(mu1) * sc1
      rd1 = .5254
      rmax2 = 2.067d09
      rr2 = rmax2/15.
      m2 = 2.*pi*m2/360.
      c2 = 2.*pi*c2/360.
      mu2 = 2.*pi*mu2/360.
      cc2 = dcos(c2)
      sc2 = dsin(c2)
      ca2 = dcos(mu2) * sc2
      cb2 = dsin(mu2) * sc2
      rd2 = .7026 + .05
      rmax3 = 2.031d09
      rr3 = rmax3/15.
      m3 = 2.*pi*m3/360.
      c3 = 2.*pi*c3/360.
      mu3 = 2.*pi*mu3/360.
      cc3 = dcos(c3)
      sc3 = dsin(c3)
      ca3 = dcos(mu3) * sc3
      cb3 = dsin(mu3) * sc3
```

```
      ve = dsqrt(8.*1.3807d-16*190./(pi*1.6605d-24*27.))
      vgrain = v/10.
      beta = 2.*pi*beta/360.
      sbeta = dsin(beta)
      cbeta = dcos(beta)
      PsAng = 2.*pi*PsAng/360.
      omeg = pi/2. + PsAng
      comeg = dcos(omeg)
      someg = dsin(omeg)
      beam = 18.
      Nobs = 1.35d14
      S = 1.332*dtan(.25*2.*pi/(360.*3600.))*1.496d13

c     start with the seed for the random number generator
      timeseed = time()
      iseed(1) = timeseed
      iseed(2) = 456
      iseed(3) = 789

      do k = 1,N

c        step 1: generate the time at which the molecule sublimates into
c        the gas phase
         Omega = erand48 (iseed)
         ts = Omega * tf

c        step 2: generate the time at which the molecule is destroyed by
c        photodissociation
         Omega = erand48 (iseed)
         td = ts - taup * dlog(Omega)
         if (td .lt. tf) then
            goto 19
         endif

c        step 3: decide if we have nuclear sublimation or coma sublimation
         Omega = erand48 (iseed)
         if ( Omega .gt. rdo ) then

c           step 4: nuclear sublimation:
c           find the comet frame sublimation location: (theta,phi)
            Omega = erand48 (iseed)
            phi = 2. * pi * Omega
            Omega = erand48 (iseed)
            theta = dacos(1 - 2.*Omega)
```

```
c       determine the comet frame coordinates of the molecule at tf
        xf = (v*(tf - ts)+rn) * dsin(theta) * dcos(phi)
        yf = (v*(tf - ts)+rn) * dsin(theta) * dsin(phi)
        zf = (v*(tf - ts)+rn) * dcos(theta)
        goto 17
      else

c       step 5: coma sublimation:
c       decide in which of the three excess blobs the
c       sublimation occurs
        Omega = erand48 (iseed)
        if (Omega.lt.rd1) then
          m = m1
          c = c1
          mu = mu1
          rmax = rmax1
          rr = rr1
          cc = cc1
          sc = sc1
          ca = ca1
          cb = cb1
        elseif (Omega.gt.rd2) then
          m = m2
          c = c2
          mu = mu2
          rmax = rmax2
          rr = rr2
          cc = cc2
          sc = sc2
          ca = ca2
          cb = cb2
        else
          m = m3
          c = c3
          mu = mu3
          rmax = rmax3
          rr = rr3
          cc = cc3
          sc = sc3
          ca = ca3
          cb = cb3
        endif
c       find the symmetry frame sublimation location: (thetasym,phisym)
        Omega = erand48 (iseed)
```

```
      phisym = 2. * pi * Omega
      Omega = erand48 (iseed)
      thetasym = m * Omega
c     more of finding the symmetry frame sublimation location: (rs)
 12   continue
      Omega = erand48 (iseed)
      rs = (2.*Omega-1.) * rr
      grs = 1. / rr
      frs = 1. - dabs(rs)/rr
      Omega = erand48 (iseed)
      Omegagrs = Omega * grs
      if ( Omegagrs .gt. frs ) then
        goto 12
      endif
      rs = rs + rmax

c     find the comet frame direction cosines of the sublimation
c     location: (cosd,cose,cosf)
      cp = dcos(phisym)
      sp = dsin(phisym)
      ct = dcos(thetasym)
      st = dsin(thetasym)
      cd = (st/sc) * (-1.*cb*sp + ca*cc*cp) + (ca*ct)
      ce = (st/sc) * (ca*sp + cb*cc*cp) + (cb*ct)
      cf = (-1.*sc*st*cp) + (cc*ct)
      factor = dsqrt(cd**2. + ce**2. + cf**2.)
      cd = cd / factor
      ce = ce / factor
      cf = cf / factor

c     step 6: molecular trajectory from coma sublimation
      Omega = erand48 (iseed)
      eta = 2. * pi * Omega
      Omega = erand48 (iseed)
      zeta = dacos(1 - 2.*Omega)
      cg = dsin(zeta) * dcos(eta)
      ch = dsin(zeta) * dsin(eta)
      ci = dcos(zeta)
      factor2 = dsqrt(cg**2. + ch**2. + ci**2.)
      cg = cg / factor2
      ch = ch / factor2
      ci = ci / factor2
      cpsi = cd*cg + ce*ch + cf*ci
      v6 = ve + vgrain*cpsi
```

```
          xf = rs*cd + v6*(tf-ts)*cg
          yf = rs*ce + v6*(tf-ts)*ch
          zf = rs*cf + v6*(tf-ts)*ci
        endif

c       extracting column densities and production rates
  17    continue
        xi = -1.*xf*sbeta + yf*cbeta
        yi = zf
        alpha = dnint( (xi*comeg - yi*someg)/S )
        alphai = idint(alpha)
        delta = dnint( (xi*someg + yi*comeg)/S )
        deltai = idint(delta)
        if ((alphai.lt.(ldim)).or.(alphai.gt.(hdim))) then
           goto 19
        elseif ((deltai.lt.(ldim)).or.(deltai.gt.(hdim))) then
           goto 19
        else
           image(alphai,deltai) = image(alphai,deltai) + 1.
        endif
  19 continue
     enddo

c    calculate the production rate
     do delta = -beam,beam
        do alpha = -beam,beam
           checker = dsqrt(alpha**2. + delta**2.)
           if (checker.lt.beam) then
              F = F + image( idint(alpha),idint(delta) )
              counter = counter + 1.
           endif
        enddo
     enddo
     F = F / counter
     F = Nobs * S**2. / F
     Q = N*F/tf
     write (*,101) Q

c    next, 2.11 is the observed image peak in Jy/bm, and 31 is
c    arbitrary
     factor3 = 2.11 / image(0,0) / 31.
     do deltai = ldim,hdim
        do alphai = ldim,hdim
           image(alphai,deltai) = image(alphai,deltai)*factor3
```

```
            enddo
         enddo
c        read out data
         open(unit=1,file='comet.out')
         do deltai = ldim,hdim
            do alphai = ldim,hdim
               write(1,101) image(alphai,deltai)
            enddo
         enddo
         close(1)

  101    format(1pe11.4)

         END
```

Appendix K

An Interferometric Study of HCN in Comet Hale-Bopp (C/1995 O1)

accepted for AJ

An Interferometric Study of HCN in Comet Hale-Bopp (C/1995 O1)

J. M. Veal[1], L. E. Snyder[1], Melvyn Wright[2], L. M. Woodney[3], Patrick Palmer[4],
J. R. Forster[2], Imke de Pater[2], M. F. A'Hearn[3], and Y.-J. Kuan[5]

ABSTRACT

We observed comet Hale-Bopp in HCN emission at 88.63 GHz using the BIMA array. We present images of the HCN emission with 9″ angular and 0.33 km s^{-1} spectral resolution for 12 days between 1997 March and April. These images show changes in the HCN distribution on short-term, daily, and weekly scales. There is a general trend of increasing brightness as the comet approaches the Sun. We investigate the evidence for jets through the characteristics of distinct emission spurs that appear in images created from 2 hour segments of the data. Within many 2 hour time spans, there is more than one active spot on the surface of the nucleus, although it may be active only for a short period. We explore deviations from spherical outflow by subtracting a Haser model parent distribution from the observed images. The excess emission in these "difference maps" is attributed to gas jets, or dust jets that produce an extended source of gas such as icy grains. The excess emission contains up to 15% of the total flux density, but these deviations are not enough to undermine the utility of spherical models of this comet. We calculated the HCN gas production rate for each of the 12 days and find $1.2 \times 10^{28} \leq Q \leq 1.8 \times 10^{28}$ s^{-1}. Quantitative investigation of the extent to which production rate calculations are affected by deviations from sphericity – via a non-spherically symmetric Monte Carlo model – shows that gas productions rates derived from a spherical model of comet Hale-Bopp should be accurate as a first approximation for determining global parameters. Finally, through comparison of continuum observations with our HCN observations, we determined a dust-to-gas ratio of 2.3 in the inner coma.

Subject headings: comets: individual (Hale-Bopp (C/1995 O1))

1. Introduction

Understanding the distribution and temporal behavior of molecular gases in cometary comae is essential for accurate production rate calculations and correct modeling of the comae. Several questions about the

---

[1] Department of Astronomy, University of Illinois 1002 W. Green St., Urbana, IL 61801, email: veal@astro.uiuc.edu

[2] Astronomy Department, University of California, Berkeley, CA 94720

[3] Astronomy Department, University of Maryland, College Park, MD, 20742

[4] Department of Astronomy and Astrophysics, University of Chicago, Chicago IL 60637

[5] Department of Earth Sciences, National Taiwan Normal University, and Academia Sinica, Institute of Astronomy and Astrophysics, Taipei, Taiwan

origin and time variability of coma gas have not been answered by low spatial resolution radio observations. Does the gas come directly from the nucleus or does it come from a distributed source within the coma? For example, optical CN jets have been observed in several comets (Klavetter & A'Hearn 1993). How much time variability is there in the flux density of cometary emission lines and is the variability significant enough to affect line detectability? We note that strong time variability on a 2 hour scale was reported for OCS emission in comet Hale-Bopp (Blake, Qi, & Muhleman 1998). How well does a spherical Haser model represent the actual cometary gas distribution and how do deviations from spherical symmetry affect the calculated gas production rate? The existence of time variability and distributed coma sources for smaller molecules makes it difficult to choose between photodissociation of larger molecules and sublimation from icy dust grains.

Standard models of cometary HCN (Bockelée-Morvan et al. 1984), H_2O (Bockelée-Morvan 1987), linear parent molecules (Crovisier 1987), and H_2CO (Bockelée-Morvan & Crovisier 1992) assume that the coma gas originates directly from the nucleus and flows outward through a collision-dominated emission regime into a fluorescent regime and then photodissociates. (We note that the collision dominated region extends much further from the nucleus in comet Hale-Bopp than in any other comet studied to date, and the assumptions of the standard models may be incorrect for this comet.) Ground-based and *in situ* measurements of P/Halley by the Giotto NMS showed that both the CO and the H_2CO were produced from an extended source such as icy dust grains or parent molecules (Snyder et al. 1989; Eberhardt et al. 1987; Meier et al. 1993). In order to study the temporal behavior of the coma with high spatial resolution, we made interferometric observations of HCN emission from comet Hale-Bopp (C/1995 O1) with the BIMA array[6] during the 1997 March and April period around perihelion passage. The comet Hale-Bopp continuum measurements were reported by de Pater et al. (1998), mosaic images and spectra of HCN and HCO^+ were reported by Wright et al. (1998), and a spectral line summary by Snyder et al. (1999a).

In this paper, we present images of the cometary HCN $J=1\rightarrow0$ emission with 9″ angular resolution, and spectra with 0.33 km s^{-1} spectral resolution for 12 days between 1997 March and April. For a comet at a geocentric distance of 1 AU, these observations map the inner coma region over a $\sim10^5$ km region with $\sim10^4$ km resolution in order to search for time-dependent variations in intensity, hyperfine anomalies, and deviations from spherical symmetry. Day-to-day flux density variability and significant hyperfine anomalies in the HCN $J=1\rightarrow0$ emission lines were first observed with single-element telescopes in comet P/Halley (Bockelée-Morvan et al. 1987; Schloerb et al. 1987; Winnberg, Ekelund, & Ekelund 1987). No interpretation of the variability was given. In the inner coma, collisions promote LTE ratios. Thus hyperfine anomalies would most likely be present in the transition region of the intermediate coma, where collisions compete with radiative processes. Our observations of comet Hale-Bopp were made with spatial resolution 3-6 times higher than the comet Halley observations, which would lessen the ratio of flux density from the transition region to that of the inner coma. As a result, the contribution of hyperfine anomalies to the overall HCN spectra would be minimized in our data.

2. Observations

Observations of spectral line emission from the HCN $J=1\rightarrow0$ transition in comet Hale-Bopp were obtained with the BIMA array (Welch et al. 1996), which at the time consisted of nine antennas. The

---

[6] Operated by the Berkeley-Illinois-Maryland Association with support from the National Science Foundation.

dates and times are listed in Table 1. BIMA mosaic images of HCN made on 1997 April 03 were reported by Wright et al. (1998). The rest frequencies for the HCN J=1→0 hyperfine transitions (F=1→1 at 88,630.42 MHz, F=2→1 at 88,631.85 MHz, and F=0→1 at 88,633.94 MHz) were taken from Maki (1974). The data were calibrated, edited, imaged and deconvolved in the usual way, using MIRIAD (Multichannel Image Reconstruction, Image Analysis, and Display) (Sault, Teuben, & Wright 1995). The absolute flux calibration, based on planet observations, is accurate to within 20%. Most of the spectral line observations were obtained with 8 spectral windows, using 256 channels over 25 MHz (0.33 km s^{-1} resolution) for the HCN data. The exception is the data from April 24, which have 128 channels over 25 MHz (0.66 km s^{-1} resolution) for the window containing HCN. The typical synthesized beam size was approximately 8″ by 10″. The data have all been corrected to the JPL Reference Orbit 106.

Fig. 1 shows images of the HCN emission on 12 days. The coordinates are in arcseconds; the conversion to physical size at the nucleus is given in Table 1. (See Table 2 for more complete ephemeris information.) The maps in Fig. 1 show the distribution of HCN intensity averaged over the 2.33 km s^{-1} linewidth in the F=2→1 and F=1→1 hyperfine components of the J=1→0 transition. That is, the two lines were individually averaged and then added together. We omit the F=0→1 hyperfine transition due to the low signal-to-noise ratio. Consequently, the peak intensity quoted in the figure caption represents 8/9 of the J=1→0 emission, given the observed LTE hyperfine ratio of 1:5:3 (Wright et al. 1998). The line segment in each image shows the projection of the direction toward the sun. The top end of the line segment is always anchored at the predicted position of the comet nucleus. After correcting to the JPL Reference Orbit 106, the small residual offset in the HCN peak intensity is within the combined ephemeris and fitting error. The contour interval is 3 times the rms noise, which varies from one map to the next due to the different integration times shown in Table 1.

Fig. 2 shows the HCN spectra toward the image maximum for the 12 days; the velocity resolution is 0.33 km s^{-1} per channel in Figs. 2a - 2k and 0.66 km s^{-1} per channel in Fig. 2l. The line profiles typically display a blueward peak. The line flux density decreases as the projected cometocentric distance increases, but the line shape is relatively constant over the emission region. The hyperfine components are consistently close enough to their LTE ratio of 1:5:3 that we cannot argue for significant hyperfine anomalies in the inner coma region. The trend in daily and weekly variability of peak intensity is shown in Fig. 3. Here the data are plotted as a function of R, the distance between the comet and the Sun in AU. The circles and their error bars represent the peak flux densities per beam and the rms values for the 12 maps in Fig. 1, with one important modification in order to make the variability meaningful; the data in Fig. 3 have been restored with circular Gaussian synthesized beams such that the beam subtends 12,000 km at the comet nucleus for all days.

3. Analysis

3.1. Short-term Variability of Flux Densities

The 1997 March 29 data set (Fig. 1i) has the highest signal to noise ratio. Short-term variability on this date is shown in two formats in Fig. 4, one per column. Each of the four maps in the left column represents roughly 2 hours of data. As in Fig. 1, the maps are sums of averaged F=2→1 and F=1→1 transitions. The time in the upper left corner of each is the approximate center of the time interval over which the data for each map were collected. In the 8-hour timespan shown, the peak intensity varies by more than 4 times the rms. Detailed modeling shows that the changes in structure apparent in Figure 4 are not due to the different *uv* sampling for each time interval. The right column shows the same data set restored with a circular beam of constant size determined by the longest of the beam axes shown in the left column. That is, we have sacrificed some resolution in order to see if the asymmetries in the images are results of the beam shape. Fig. 4 also shows that the outer structure (farther from the nucleus) does not depend significantly on whether the data are restored with the usual elliptical Gaussian synthesized beam or a circular Gaussian synthesized beam; the general features remain the same. Consequently, restoration of our data with a circular Gaussian synthesized beam is limited in display to the right hand column of Fig. 4. However, to make short-term variability in the peak flux densities per beam more meaningful in Figs. 4 - 6, for each figure caption we quote values from the data restored with a circular Gaussian synthesized beam of constant size determined by the longest of the beam axes shown in the figure. Short-term variability on March 13 and 18 – data sets with slightly lower signal to noise ratio – is shown in Figs. 5 & 6, respectively. We note that in Figs. 4 - 6 the inner structures of adjacent images are independent because the gas moves a significant fraction of the beam in 2 hours. (The gas with projected motion smaller than the beam doesn't provide structure.) For each date in Figs. 4 - 6, the HCN peak flux density per beam is slightly stronger at some times than at others, and these strengths are quantified in the captions. The residual offset in the peak intensity does not drift, and we do not address short-term effects of non-gravitational forces. The ~25% fluctuation in peak intensity seen in each of Figs. 4 - 6 is not necessarily the maximum possible fluctuation in comets, indicating the possibility that short-term variability of flux density could be responsible for the nondetection of a weak cometary emission line if the observations were made in the wrong time interval.

3.2. Evidence for Jets

Figs. 4, 5, & 6 show several HCN emission spurs, or concentrations. In general, these concentrations tend to slowly disappear over a period of ~2 hours, while new concentrations appear elsewhere. Similar concentrations were observed in the March 25 CS emission (Snyder et al. 1999a,b). The locations of these spurs do not seem to be correlated with any directional phenomena such as sunward and tailward directions, non-gravitational forces, or orientation of the rotation axis, which is offset to the NNE by 15° ± 10° (Schleicher & Farnham 1999).

These spurs may originate either from "gas jets" – gas sublimating from an active spot on the nucleus – or from more tightly collimated "dust jets" which carry icy dust grains away from the nucleus before HCN is released from them. We consider the possibility that the spurs represent concentrations of gas resulting from a gas jet. Several spurs are fairly strong, 7 to 12% of the total flux density in the image. If these spurs are the result of gas jets, they should be preluded by similar features in preceding adjacent images. The prelude should have a higher intensity since the number density in a parcel of gas decreases with time as it flows out from the nucleus. In addition, we expect the position of the prelude in the preceding adjacent image to be no more than 9″ (9 pixels) away from the position of the spur in the image of interest, given a ~2 hour time increment between adjacent images, a gas outflow velocity of ~1.2 km s^{-1}, a rotation period of 11.3 hours (Schleicher et al. (1998), Licandro et al. (1998)), and a rotation axis offset from the line of sight by 15° ± 10° (Schleicher & Farhnam 1999). In most cases, we cannot expect to see such features because of the signal-to-noise ratio of our data (and this is the reason we don't see the spiral patterns like those visible in optical CN images). Indeed, the expected features are absent even in the most likely cases. For example, since exceptionally strong spurs are found in Fig. 4g ($\Delta\alpha = 20'', \Delta\delta = -10''$) and Fig. 6b ($\Delta\alpha = -25'', \Delta\delta = 0''$), we would expect to see preludes in Figs. 4e & 6a if the signal-to-noise ratio of our data were higher. Yet absence of features in low signal-to-noise images is clearly not conclusive evidence that the preludes don't physically exist. Hence, we do not have enough evidence to rule out gas jets. In any case, it is possible that another phenomenon is occurring that explains the asymmetries we observe, and we explore options to the gas jet explanation. One alternative to gas jets is dust jets, whose tighter collimation could explain the appreciable distance from the nucleus of the identifiable spurs. For example, active spots on the surface of the nucleus may be releasing, in a collimated fashion, an extended source of HCN gas such as icy dust grains.[7] There can be more than one active spot at any given time, and these spots can be active for a period of < 2 hours. Here we draw attention to six "repeating spurs" that seem to show up in more than one panel. Their locations are summarized in Table 3. The angular displacement of the repeating spurs is consistent with a near pole-on axis exhibiting clockwise rotation, and the projected distance from the comet nucleus of the repeating spurs is consistent with the dust being an extended, non-nuclear source of gas. Lastly, we address the "fixed" spurs that seem to show up in the same location over a period of weeks. We draw attention to the existence of a lower right spur in Figs. 1g, 1h, 1i, & 1j, a lower left spur in Figs. 1a, 1d, 1g, 1i, & 1l, and lower left and right spurs in Fig. 8. Such a phenomenon is possible if θ, β (see Table 2) and the orientation of the rotation axis do not change significantly during this period, and they do not in the present case.

3.3. The Haser Model and Evidence for Deviations from Spherical Outflow

In order to explore the deviation of the detected emission from that expected for a spherically symmetric nuclear source, images based on the Haser model were subtracted from several HCN images. The Haser model describes the number density, $n(r)$, and the column density, $N(a)$, as cometary molecules flow spherically away from the nucleus and are dissociated by ultraviolet radiation (Haser 1957). The number density of parent molecules can then be written as

$$n(r) = \frac{Q}{4\pi r^2 v}\, e^{-(r-r_n)/\Lambda}, \tag{1}$$

where r is the distance from the nucleus, Q is the gas production rate, v is the gas outflow velocity, r_n is the nuclear radius, and Λ is the parent photodestruction scale length. Assuming a constant v, integration of $n(r)$ along the line of sight, z, gives the column density

$$N(a) = \frac{Q}{2\pi v}\, e^{r_n/\Lambda} \int_0^\infty \frac{e^{-\sqrt{a^2+z^2}/\Lambda}}{a^2+z^2}\, dz, \tag{2}$$

where a is the projected distance from the nucleus and the relation $r^2 = a^2 + z^2$ has been used. Fig. 7 shows a plot of amplitude vs. uv-distance for the 1997 March 29 HCN data as well as a model uv data set that shows what would be measured if the HCN distribution of flux density obeyed the Haser model for parent molecules. Clearly, the HCN source is resolved. The real HCN data drop more rapidly to zero than does the model, which indicates that the HCN flux density is less narrowly peaked at the nucleus than the Haser model. Fig. 8 shows a weighted average of HCN data from March 08, 10, 12, 13, 14, 17, 28, & 29 UT and April 01 & 15 UT, where all flux densities and uv-distances have been scaled to the first day. The distribution of intensity and the spectral line profiles are similar to Figs. 1 & 2, but with an improved signal to noise ratio. The intensity distribution shows small, but pronounced spurs, which deviate from

---

[7] The idea of icy dust grains in cometary comae is not new. For recent examples of work regarding this phenomenon, see Blake et al. (1999), de Pater et al. (1998), Greenberg & Li (1998), Jewitt & Matthews (1997), Sarmecanic et al. (1997), de Pater et al. (1997), and Williams et al. (1997).

spherical outflow and therefore are not described by a standard Haser model. These spurs have a similar appearance to those noted in Section 3.2, as well as those seen in Figs. 1, 4, 5, & 6, and in the work of Wright et al. (1998). However, given the large period of time over which these data are averaged, it is not possible to make any statements about time variability of jets as discussed in Section 3.2.

Images based on the Haser model were subtracted from several HCN images (Figs. 1d, 1g, 1h, 1i, & 1j). We assume the coma is optically thin (in agreement with Veal (2000), Blake et al. (1999), Wright et al. (1998), Irvine et al. (1998), and Crovisier (1987)) and the intensity is directly proportional to the column density. This may be stated as $I(a)/I(r_n) = N(a)/N(r_n)$. With substitution from the Haser model, the intensity in the model image as a function of projected distance from the nucleus can be written as

$$I(a) = I_{max} \frac{\int\limits_0^\infty \frac{e^{-\sqrt{a^2+z^2}/\Lambda}}{a^2+z^2} dz}{\int\limits_0^\infty \frac{e^{-\sqrt{r_n^2+z^2}/\Lambda}}{r_n^2+z^2} dz}, \tag{3}$$

where $I_{max} = I(r_n)$, the value of the peak intensity in the map. Equation 3 was solved for all values of a corresponding to the center of a pixel in the model image, with integration over z from 0 to 0.1 AU (excepting $a = 0$, where $a = r_n$ was used). The model image was then convolved with the Gaussian synthesized beam from the appropriate day. The result was regridded with a factor of 16 higher pixel resolution to better fit the actual convolution of a Haser model with a Gaussian. The model was then scaled so the peak matched that of the observations. This final model image was then subtracted from the regridded observed image.

Fig. 9 shows the resulting difference maps, where $r_n = 20$ km (after de Pater et al. (1998), Weaver & Lamy (1999), and Fernandez (1999)), $v = 1.2$ km s^{-1} (Wright et al. 1998[8]), and $\Lambda = vR^2\tau$, where the photodestruction rate, $1/\tau$, is equal to 1.3×10^{-5} s^{-1} (after Huebner, Keady, & Lyon 1992). The axes, noise level, and synthesized beam are the same, by date, as for Fig. 1. The cross at the middle denotes the location of the HCN peak of the corresponding map in Fig. 1. Fig. 10 shows the manner in which the distribution of the excess flux density depends on parameters such as r_n and Λ, and we have varied these parameters in each panel as shown in the figure: low $\Lambda = 4.7 \times 10^9$ cm, mid $\Lambda = 7.7 \times 10^9$ cm, and high $\Lambda = 9.5 \times 10^9$ cm. These values of Λ correspond to a Sun-comet distance of R=0.916 AU and an outflow velocity range of v=0.8, 1.2, and 1.6 km s^{-1}. The range in Λ could alternately represent a range in photodestruction rates of 2.0×10^{-5}, 1.3×10^{-5}, and 1.0×10^{-5} s^{-1}, respectively. The excess flux density in Fig. 10 changes very little from one panel to the next, and we conclude that our results do not depend on the adopted values of r_n and Λ.

Does the excess flux density come from gas jets? Any jet that is active during the observation would show a peak intensity at the nucleus because the number density of a parcel of gas decreases as it flows away from the nucleus. However, our model images were scaled to match the observed peak intensities. As a result Fig. 9 cannot provide strong evidence contrary to the gas jet explanation. We note that while Fig. 9e shows a peak significantly more than one beamwidth away from the nucleus, Figs. 9a - 9d do not.

Though gas jets are a viable explanation for the observed deviations from sphericity, they are not the only possibility. We again consider the alternative introduced in Sect. 3.2. As the icy dust grains slowly flow out from the nucleus, they heat up as they are insolated, subsequently acting as an extended source of

---

[8] Their analysis assumes $\Lambda = vR^{1.5}\tau$ where we assume $\Lambda = vR^2\tau$, yet the range in R is small and little disagreement is expected.

gas. This could also explain the peak flux densities per beam that are located away from the position of the nucleus in Fig. 9. (The excess flux density peaks in Figs. 9a - 9d have an average projected distance from the nucleus of ~7800 km; the values range from 7100 km to 8400 km.) The small radial extent (~8000 km; about 2 hours time in gas outflow velocity) of the excess flux density regions in Fig. 9 may indicate a rapid sublimation phase from the grain surfaces or even disintegration of grains due to sublimation of the volatile component gluing dust grains together (Oberc 1996). In any case, a cloud of HCN could appear away from the nucleus with a local (spatial and temporal) maximum in the excess flux density. From this point, the gas would flow away from the local maximum, decrease in intensity, be photodestroyed as time progresses, and still manifest itself in an image averaged over 6 to 15 hours, e.g. Fig. 9.

We note that Fig. 9d contains ~15% of the flux density in Fig. 1i (in qualitative agreement with the results of Blake et al. (1999), who find ~15% of the total HCN J=1→0 emission within 5″ of the nucleus arises in jet-like structures). This ~15% excess implies that the flux density in comet Hale-Bopp significantly deviates from sphericity. The Haser model remains a good approximation with 15% errors in either the distribution or flux density calibration.

3.4. Production Rates

HCN production rate calculations, using the Haser model in the manner outlined by Snyder et al. (1999a,b), show $1.2 \times 10^{28} \leq Q \leq 1.8 \times 10^{28}$ s^{-1} between 1997 March 08 and 1997 April 24 UT. Individual values are given in Table 1 and are comparable to several recent estimates: $Q = 2.08 \times 10^{28}$ s^{-1} on March 24 and $Q = 2.38 \times 10^{28}$ s^{-1} on March 30 (Lovell 1999), $Q = 2.6 \times 10^{28}$ s^{-1} on April 03 (Wright et al. 1998), $Q = 1.3 \times 10^{28}$ s^{-1} on March 29 and $Q = 2.0 \times 10^{28}$ s^{-1} on March 31 (Blake et al. 1999). We note that our values are lower limits due to flux lost as a result of the interferometer not measuring the zero *uv*-distance. We consider the extent to which this missing flux affects the production rate calculations by comparing interferometric data to autocorrelation data. The integrated intensity obtained from interferometric data is ~40% of that obtained from autocorrelation data. (See Wright et al. 1998, Snyder et al. 1999a, and 1999b for reports of autocorrelation data.) However, the production rate obtained from interferometric data is >85% of that obtained from autocorrelation data as a result of the high concentration of HCN inside the smaller synthesized beam. That is, the lost flux is spread out over an angular diameter much larger than the synthesized beam. Hence, the Haser model can be a good first approximation to the interferometric data points within the synthesized beam.

In order to quantitatively investigate how deviations from sphericity affect production rate calculations, we developed a Monte Carlo code to model the anisotropic, three-dimensional distribution of the HCN molecules in comet Hale-Bopp. Our first task was to use this model to evaluate the production rate of a spherical comet. We found $Q = 1.5 \times 10^{28}$ s^{-1} on March 29 for $N = 10^8$, where N is the number of particles in the simulation. This is analogous to the Haser model for a parent distribution (no excess flux density) and agrees with its counterpart value given in Table 1. We then modeled the intensity distribution and gas production rate of a non-spherical comet. For this purpose, we used the ~15% ratio of flux density in Fig. 9d to the flux density in Fig. 1i (both from March 29) in the code to correctly set the ratio of excess flux density to spherically symmetric flux density in the model. A model distribution of HCN molecules on March 29 was produced; the corresponding HCN production rate[9] was $Q = 1.6 \times 10^{28}$ s^{-1} for $N = 10^8$.

---

[9] The cause of the difference of <10% between Q calculated from the spherical Monte Carlo model and Q calculated with the aspherical Monte Carlo model should not be confused with the physics responsible for the ~15% that we are modeling. The

After convolving the Monte Carlo HCN distribution with the synthesized beam, we derived a difference map in order to model the data set shown in Fig. 9d. The result is shown in Fig. 11, labeled as "Monte Carlo HCN Excess."

This increase from the spherically symmetric $Q = 1.5 \times 10^{28}$ s^{-1} to the non-spherical $Q = 1.6 \times 10^{28}$ s^{-1} may indicate that gas production rate calculations that are based on interferometric observations and the Haser model may be too low by a factor on the order of 10% as a result of the excess flux density of the type shown in the difference maps in Fig. 9.

3.5. Comparison with Continuum Observations

De Pater et al. (1998) find excess continuum flux density (flux density left over after subtraction of a dust model from a continuum image) around comet Hale-Bopp in an image averaged over several dates (1997 March 18 & 26, and April 02, 04, 07, & 24 UT). The excess flux density in their Fig. 1d is similar in appearance to our Fig. 9, both in displacement from the nucleus and in signal strength relative to maximum before subtraction. They attribute their figure to outbursts and/or dust jets. Our discussion in Sections 3.2 & 3.3 are consistent with this.

Their observations also allow them to calculate a dust production rate of $\sim 10^6$ kg/s. We compare this to our average HCN production rate of ~700 kg/s for a dust-to-HCN ratio of ~1400 in the coma. Snyder et al. (1999a,b) find the production of HCN relative to H_2O is ~0.2%. If comet Hale-Bopp is 80% H_2O, this leads us to estimate a dust-to-gas ratio of ~2.3 (with a factor of ~2 uncertainty). We note that Wright et al.'s (1998) estimate of 0.26% HCN abundance results in a similar dust-to-gas ratio and that Jewitt & Matthews (1999) finds a dust-to-gas ratio of ~5.

4. Summary

- We observed HCN emission from comet Hale-Bopp with the BIMA array for 12 days near perihelion passage between 1997 March 08 and April 24.
- We found no evidence of HCN hyperfine anomalies.
- Daily and weekly variability showed a general trend for the flux density to increase as the comet approached the Sun and decrease as the comet receded, as expected.
- There was a ~25% fluctuation in peak intensity on a 2 hour time scale on 3 separate days. Larger fluctuations may make a weak emission line undetectable.
- Emission spurs seen in the 2 hour time segment images can be explained by the existence of jets. These may have been active spots on the surface of the nucleus which produced a collimated outflow of HCN gas, or an extended source of HCN gas such as icy dust grains.

---

one is a smaller effect than the other for the following reason. The model calculates Q, in part, by scaling the peak column density to match the observed peak column density (see Eq. A5). When the extended sources are included in the model at a ~15% level, the peak column density is a result of the nuclear source plus the extended sources. Hence the scaling needed to match the observed column density is less than 15%.

- For jets, a correlation between several molecular species produced by sublimation from icy dust grains and continuum emission from the dust jets themselves is expected in observations with sufficient angular resolution and synchronization.
- There can be more than one active spot at any given time, and these spots can be active for a period of < 2 hours.
- Deviations from a Haser parent model can be explained by the existence of jets releasing HCN gas, or an extended source of HCN gas such as icy dust grains. These deviations are ~15% or less of the total flux density.
- We used a spherical model to calculate the HCN gas production rate and found $1.2 \times 10^{28} \leq Q \leq 1.8 \times 10^{28}\ \mathrm{s}^{-1}$ between 1997 March 08 and 1997 April 24 UT.
- Production rates derived from a spherical model of comet Hale-Bopp differ from those of the Monte Carlo model by less than the error in our absolute flux calibration. Hence, spherical models of this comet are a good approximation for determining global parameters.
- A comparison of the HCN and 3mm continuum images yields a dust-to-gas ratio of ~ 2.3 in comet Hale-Bopp.

We are indebted to D. K. Yeomans for assistance with ephemerides. We would like to sincerely thank E. C. Sutton for several helpful discussions. This work was partially funded by: NASA NAG5-4292, NSF AST 96-13998, 96-13999, and 96-13716; Taiwanese grants NSC 86-2112-M-003-T and 87-2112-M-003-007; and by the Universities of Illinois, Maryland, and California, Berkeley.

A. The Monte Carlo Model

The deviations from spherical outflow in the comet, as a result of gas jets or dust jets producing an extended source of gas such as icy grains, can be difficult to model because of the lack of symmetry in three dimensions. The code in this investigation is aimed at modeling these asymmetries by injecting gas via excess sublimation at specific locations in the space around the nucleus and calculating $n(r)$, $N(a)$, and Q of HCN under asymmetric conditions such as those displayed in Fig. 9. The model addresses the following seven questions. 1) When does the molecule enter the gas phase? 2) When is the molecule destroyed? 3) Does the molecule sublimate from the nucleus or from the extended source? 4) If the molecule sublimates from the nucleus, what is its subsequent trajectory? 5) If the molecule sublimates from the extended source, where in the coma does it appear? 6) If the molecule sublimates in the coma, what is its subsequent trajectory? 7) How will this distribution of HCN molecules appear when observed from the Earth? We answer questions 1, 2, and 4 by following the approach of Combi & Delsemme (1980), the pioneers in Monte Carlo modeling of comet particle distributions. We answer question 3 by using the ratio of flux density in a distinct location in the difference map, Fig. 9d, to the flux density in the observed map, Fig. 1i. We address the nuclear distribution and questions 5 - 7 in some detail below.

We define the comet frame as the xyz coordinate system in which the xy-plane includes the comet, Sun, and Earth, with $\hat{\mathbf{x}}$ pointing from the comet toward the Sun. The quantity ϕ measures angle from the

x direction in the xy-plane and θ measures angle from the z direction. Given ϕ, θ, and the outflow velocity, v, the position, (x_f, y_f, z_f), of the molecule at t_f is readily determined:

$$\begin{aligned} x_f &= [v(t_f - t_s) + r_n] \sin\theta \cos\phi \\ y_f &= [v(t_f - t_s) + r_n] \sin\theta \sin\phi \\ z_f &= [v(t_f - t_s) + r_n] \cos\theta. \end{aligned} \tag{A1}$$

Here, the time at which the molecule sublimates into the gas phase, t_s, is bounded by $0 \leq t_s \leq t_f$, where t_f, the time at which $n(r)$ and $N(a)$ are tabulated, should be long enough so that a good approximation to a steady state situation is achieved.

If the molecule sublimates from the extended source, its initial comet frame position in the halo is determined by three coordinates, (r_s, θ_s, ϕ_s). We assume axial symmetry of each distinct extended source with the axis pointing from the nucleus to the excess flux density. Under this assumption it is simplest to perform a coordinate transformation so that a new Z-axis is directed along the axis of symmetry. Before we actually rotate our z-axis to the axis of symmetry, we first generate the angles designating the symmetry frame position of the location in the halo at which the molecule sublimates into the gas phase, $(r_{sym}, \theta_{sym}, \phi_{sym})$. As expected, $\phi_{sym} = 2\pi\Omega$, where Ω denotes a random number between 0 and 1. The method by which θ_{sym} is generated depends on the function used to represent the probability distribution. It should be noted that there is no conclusive evidence leading us to choose an exact probability distribution, and the present probability distribution function has been chosen on a semi-empirical basis. We assume $\theta_{sym} = m\Omega$, where m is the half angle of a right cylindrical cone.

Equation A2 gives the semi-empirically determined, normalized probability distribution function, $f(r_s)$, along with the second function, $g(r_s)$, needed for the standard rejection method.

$$f(r_s) = \begin{cases} \frac{r_r - |r_s - r_{max}|}{r_r{}^2}, & (r_{max} - r_r) < r_s < (r_{max} + r_r) \\ 0, & r_s \leq (r_{max} - r_r), (r_{max} + r_r) \leq r_s \end{cases} \quad \text{and} \quad g(r_s) = \frac{1}{r_r} \tag{A2}$$

The quantity r_{max} is the distance from the nucleus at which the excess emission peaks and r_r is the range of radial distance from r_{max} over which coma sublimation takes place. We note that $r_s = r_{sym}$, since the transformations to determine sublimation location are strictly rotations and involve no translations. The curves $f(r_s)$ and $g(r_s)$ are shown in Fig. 12. For simplicity, we shift $f(r_s)$ to the origin and find $r_s = (2\Omega - 1)r_r$ (which is rejected only if $\Omega g(r_s) > f(r_s)$), and then shift back with $r_s = r_s + r_{max}$.

Now that we have $(r_{sym}, \theta_{sym}, \phi_{sym})$, we can find the comet frame direction cosines of the sublimation location. With some calculation, we find the comet frame direction cosines, $\cos d$, $\cos e$, & $\cos f$, to be (prior to normalization by $\sqrt{\cos^2 d + \cos^2 e + \cos^2 f}$)

$$\begin{aligned} \cos d &= \frac{\sin\theta_{sym}}{\sin c}(-\cos b \sin\phi_{sym} + \cos a \cos c \cos\phi_{sym}) + \cos a \cos\theta_{sym} \\ \cos e &= \frac{\sin\theta_{sym}}{\sin c}(\cos a \sin\phi_{sym} + \cos b \cos c \cos\phi_{sym}) + \cos b \cos\theta_{sym} \\ \cos f &= -\sin c \sin\theta_{sym} \cos\phi_{sym} + \cos c \cos\theta_{sym}, \end{aligned} \tag{A3}$$

where $\cos a$, $\cos b$, & $\cos c$ are the comet frame direction cosines of the symmetry axis.

The direction, (ζ, η), of the trajectory of the molecule that sublimates from the extended source is found from $\zeta = \arccos(1 - 2\Omega)$ and $\eta = 2\pi\Omega$. We assume that the molecule sublimates from a particle moving away from the nucleus in a radial direction, such as an icy dust grain. The molecule's subsequent trajectory is then assumed to be isotropic in the moving frame of the dust grain, allowing the direction of the trajectory (which doesn't include the magnitude) to be isotropic even in the comet frame. The comet frame direction cosines of the trajectory are given by $\cos g = \sin\zeta\cos\eta$, $\cos h = \sin\zeta\sin\eta$, and $\cos i = \cos\zeta$. The magnitude of the velocity along this trajectory, v_6, is given by $v_6 = v_e + v_{grain}\cos\psi$, where $\cos\psi = \hat{\mathbf{r}}_s \cdot \hat{\mathbf{v}}_6 = \cos d\cos g + \cos e\cos h + \cos f\cos i$, as long as both sets of direction cosines are normalized. Here, we assume that the extended source is a halo of dust grains in the coma and each grain moves away from the nucleus at approximately $v/10$ (Grün & Jessberger 1990). The quantity v_e is the magnitude of the velocity of the HCN molecule with respect to the grain from which it sublimates and is approximately equal to 3.86×10^4 cm/s.[10] Therefore, the xyz comet frame coordinates of the molecule at time t_f are given by

$$\begin{aligned} x_f &= r_s\cos d + v_6(t_f - t_s)\cos g \\ y_f &= r_s\cos e + v_6(t_f - t_s)\cos h \\ z_f &= r_s\cos f + v_6(t_f - t_s)\cos i. \end{aligned} \tag{A4}$$

In order to calculate column densities, we start by tallying up the numbers of molecules in each bin corresponding to a pixel in one of the observed images. We rotate the comet frame coordinate system around $\hat{\mathbf{z}}$ by β (given in Table 2) so that $\hat{\mathbf{x}}$ points toward the Earth. The image coordinates on the plane of the sky are then just $x_i = y_f\cos\beta - x_f\sin\beta$ and $y_i = z_f$. We then rotate by an angle $-\omega$, where ω is just $\pi/2$+PsAng (from Table 2), to give right ascension, $\alpha = x_i\cos\omega - y_i\sin\omega$, and declination, $\delta = x_i\sin\omega + y_i\cos\omega$. Each molecule's image coordinates take on integral values of the number of km/pixel in the observed images. We digitize (α, δ) into (α_i, δ_i) and the array fills up with numbers and arrives at a form appropriate for viewing as an image.

The transition from the image to column densities and production rates is straightforward. The model parameters are adjusted to make the model image look like the observed image and then the model image is multiplied by a scale factor, F, so the column densities per beam match the observed column densities per beam. From here, we find

$$Q = NF/t_f, \tag{A5}$$

where N is the total number of molecules generated by the code.

---

[10] We assume that the vapor sublimating from the surface of the grain is in equilibrium with the surface and initially has the same temperature. We also assume the sublimation is controlled by H_2O, causing this temperature to be approximately 190 K (Houpis & Mendis 1981). We then set v_e equal to the average Maxwellian velocity of a gas at this temperature.

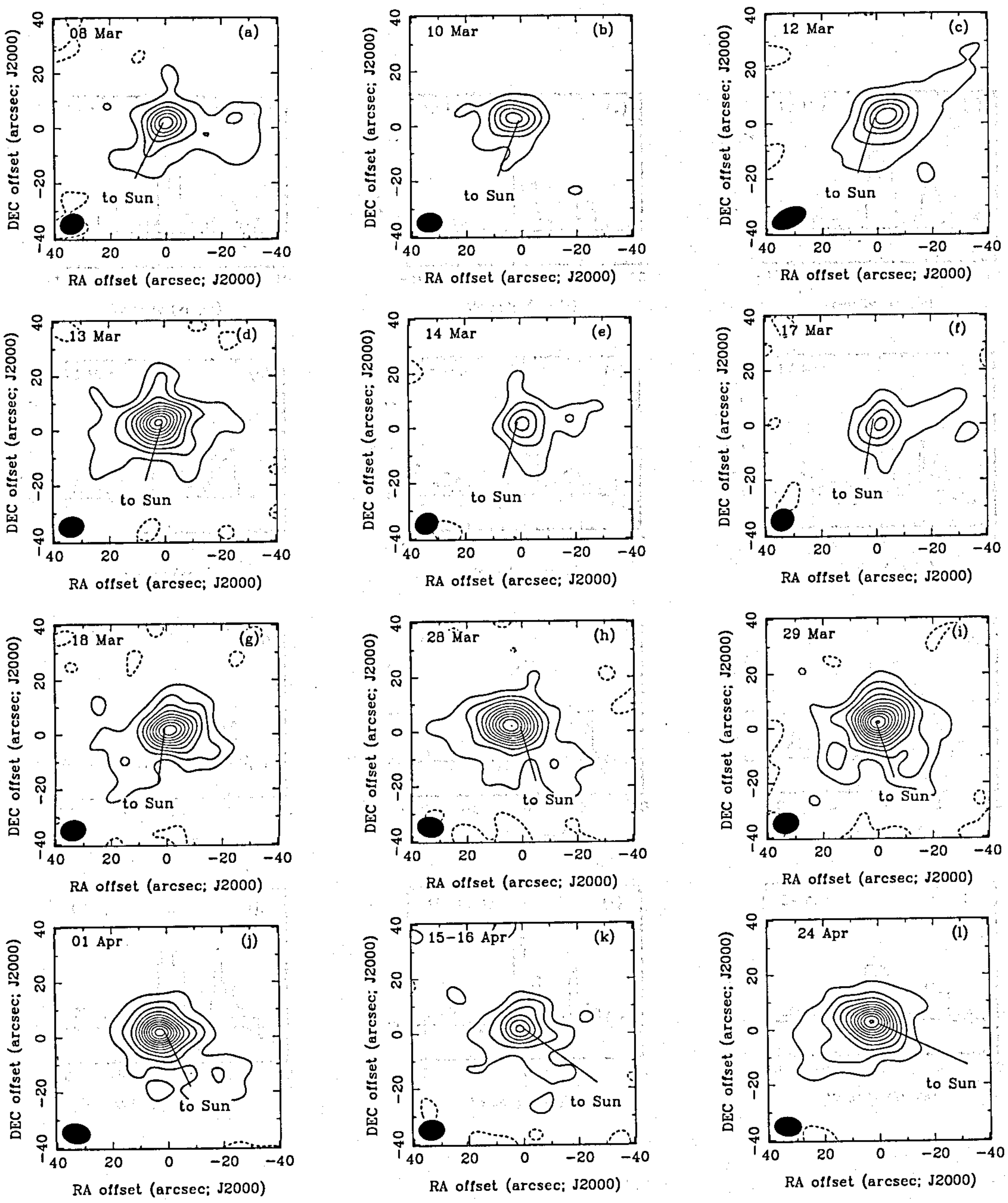

FIGURE K.1: HCN J=1→0 emission from comet Hale-Bopp observed with the BIMA array. The solid contours are successive multiples of 3σ, and dashed contours are negative. In the lower left corner of each map is given the size of the synthesized beam at full width half power. The peak intensity and rms values are, in Jy beam^{-1}: (a) 1.98 and 0.10, (b) 1.70 and 0.10, (c) 2.11 and 0.12, (d) 1.95 and 0.06, (e) 1.67 and 0.13, (f) 1.64 and 0.13, (g) 1.80 and 0.06, (h) 2.11 and 0.06, (i) 2.11 and 0.06, (j) 2.61 and 0.08, (k) 1.82 and 0.10, and (l) 1.32 and 0.05.

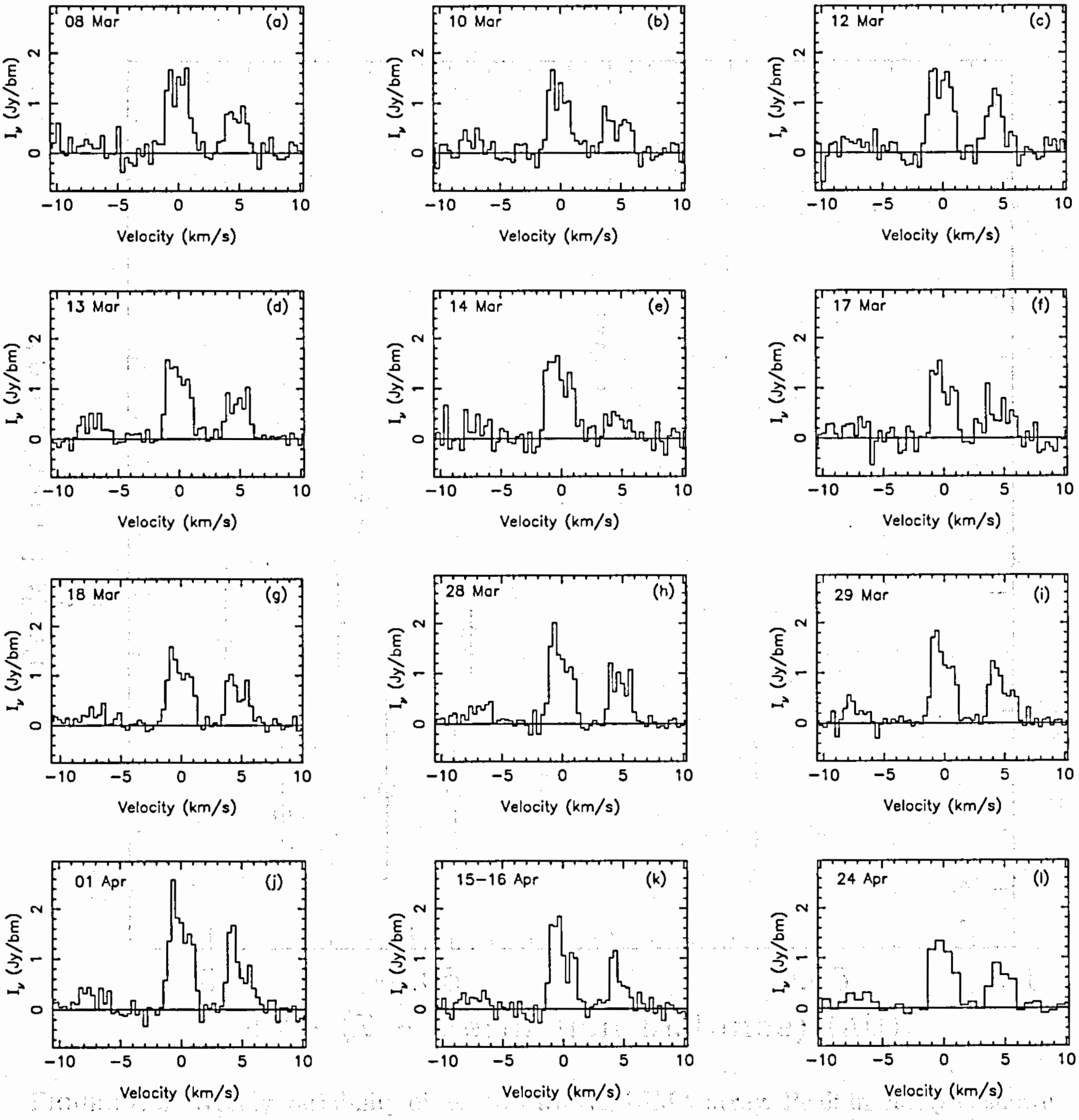

FIGURE K.2: HCN J=1→0 emission from comet Hale-Bopp observed with the BIMA array. Peak intensity is shown with velocity resolution of ~0.33 km s^{-1} per channel (except panel 2l, with ~0.66 km s^{-1} per channel). The three hyperfine transitions and their approximate velocities, from left to right, are F=0→1 at -7 km s^{-1}, F=2→1 at 0 km s^{-1}, and F=1→1 at 5 km s^{-1}, respectively. (All lines fall at ~0 km s^{-1} in the cometocentric frame.) The rms values for each date are, in Jy beam^{-1}: (a) 0.19, (b) 0.19, (c) 0.22, (d) 0.11, (e) 0.24, (f) 0.24, (g) 0.11, (h) 0.11, (i) 0.12, (j) 0.15, (k) 0.19, and (l) 0.08.

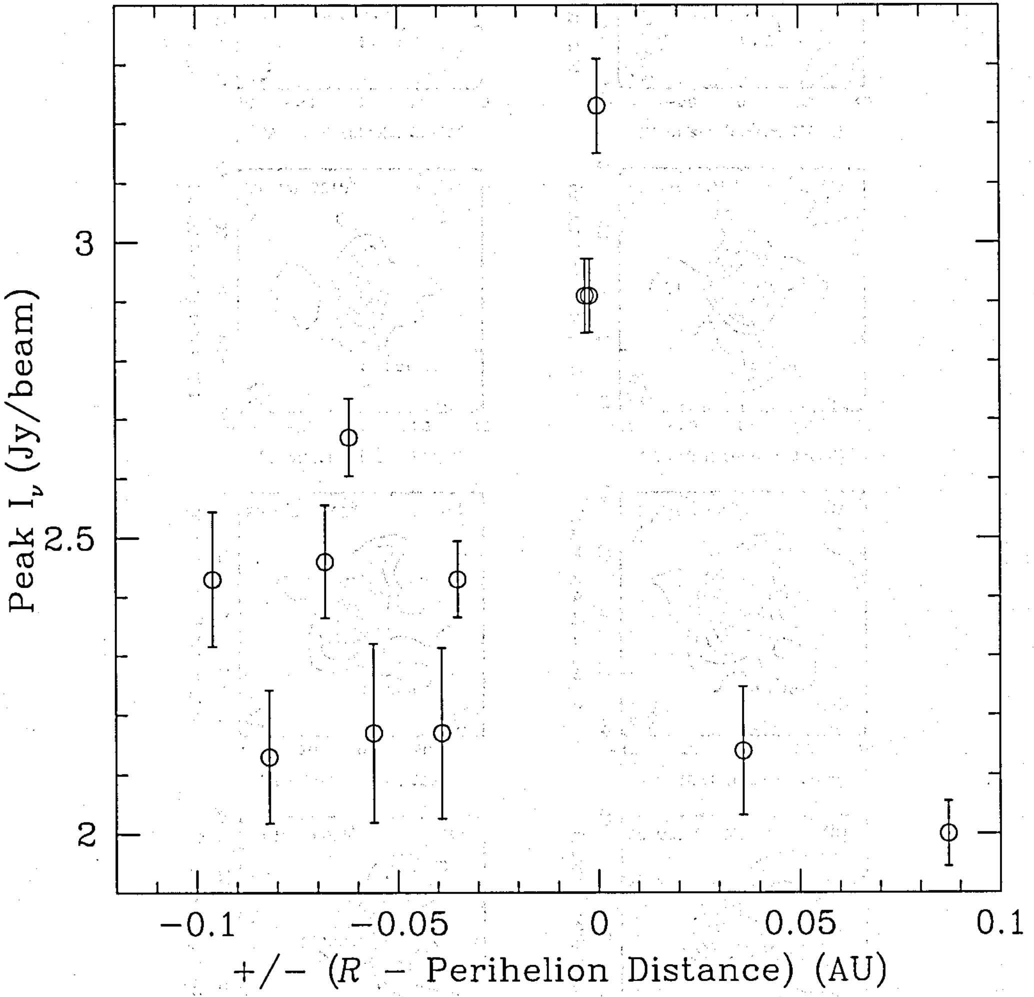

FIGURE K.3: Weekly variability observed with the BIMA array. Peak intensity is shown as a function of R, the distance between the comet and the Sun. In order to make the variability meaningful, this figure has been created by restoring the data used for Fig. 1 with specific circular Gaussian synthesized beams such that the physical beam size located at the comet nucleus is the same for all days. The abscissa is shifted so that perihelion (0.914 AU) is at 0, with negative pre-perihelion values and positive post-perihelion values.

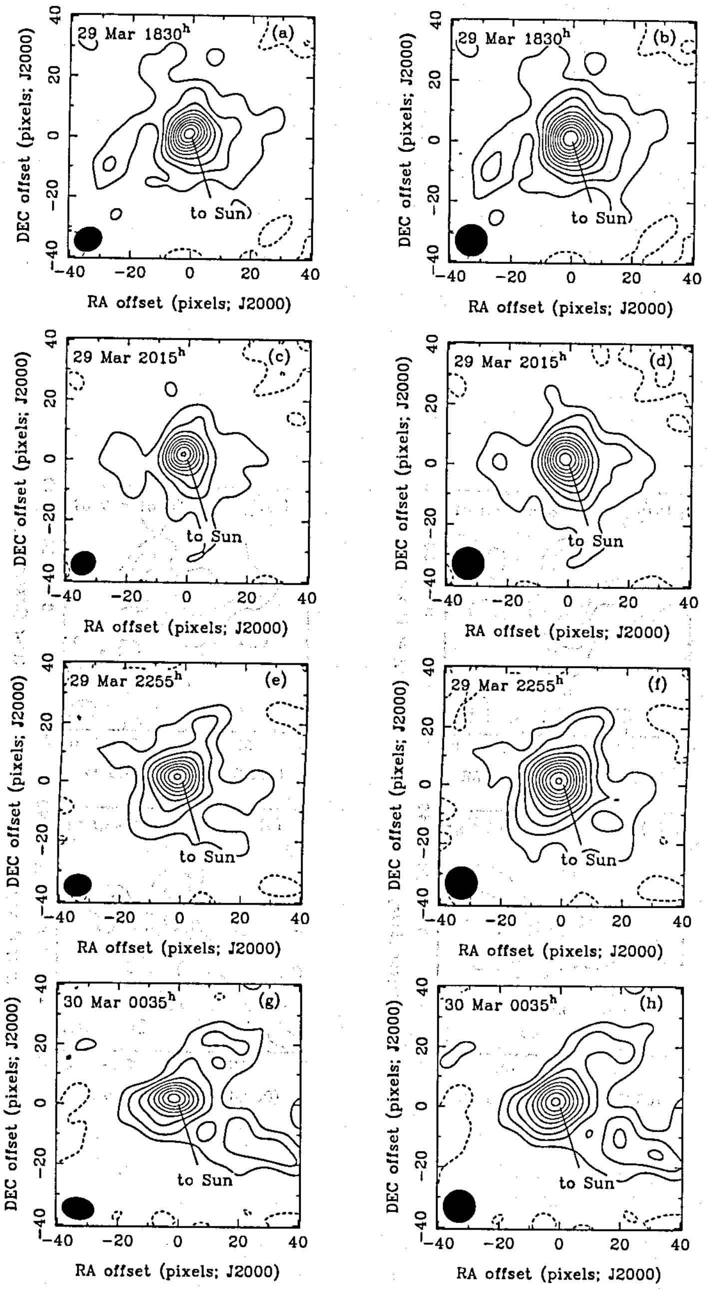

FIGURE K.4: HCN J=1→0 emission from comet Hale-Bopp observed with the BIMA array on 1997 March 29. The solid contours are successive multiples of 0.23 Jy beam^{-1}, which is $\sim 2\sigma$ in each of the maps. Dashed contours are negative. The observing intervals in hours (UT) are 17:43 - 19:11, 19:24 - 21:05, 22:05 - 23:39, and 23:50 - 01:20. The peak intensities in the right column are, in Jy beam^{-1}, 2.75, 2.45, 2.56, and 2.13, chronologically. The right column differs from the left in its synthesized beam; the 4 maps in the right column have been restored with a circular Gaussian synthesized beam of dimension equal to the largest beam dimension in the left column.

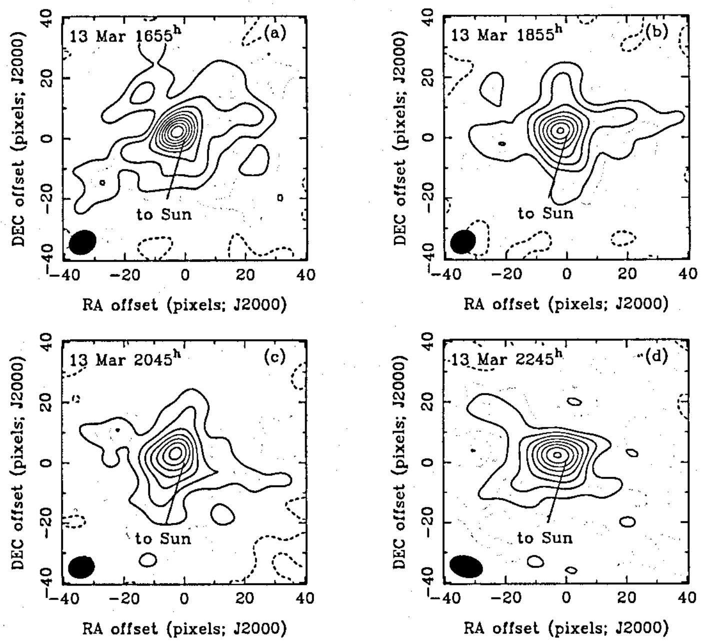

FIGURE K.5: HCN J=1→0 emission from comet Hale-Bopp observed with the BIMA array on 1997 March 13. The solid contours are successive multiples of 0.23 Jy beam^{-1}, which is $\sim 2\sigma$ in each of the maps. Dashed contours are negative. The observing intervals in hours (UT) are 15:52 - 17:59, 18:10 - 19:33, 20:03 - 21:33, and 21:43 - 23:46. The peak intensities for these data restored with a circular Gaussian synthesized beam, in Jy beam^{-1}, are 2.51, 2.29, 2.21, and 2.19, chronologically.

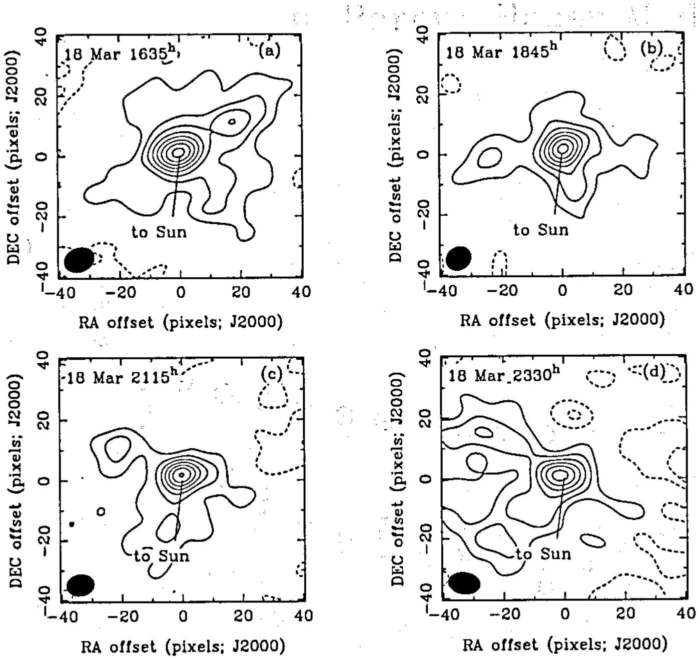

FIGURE K.6: HCN J=1→0 emission from comet Hale-Bopp observed with the BIMA array on 1997 March 18. The solid contours are successive multiples of 0.23 Jy beam^{-1}, which is $\sim 2\sigma$ in each of the maps. Dashed contours are negative. The observing intervals in hours (UT) are 15:51 - 17:23, 17:34 - 19:52, 20:54 - 22:26, and 22:38 - 00:17. The peak intensities for these data restored with a circular Gaussian synthesized beam, in Jy beam^{-1}, are 2.10, 1.98, 1.81, and 1.61, chronologically.

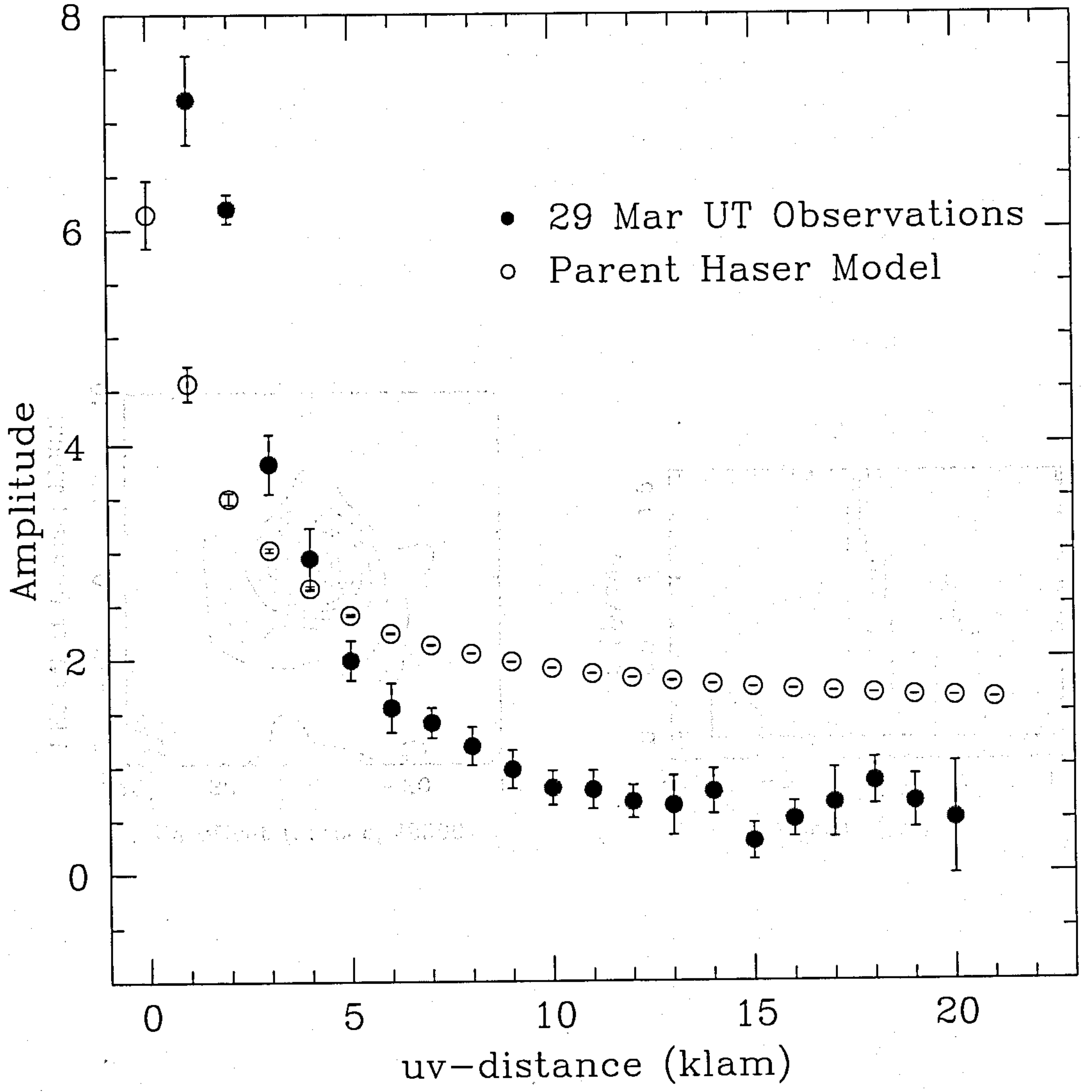

FIGURE K.7: Comparison of real and model *uv* data sets. The HCN source is resolved. Calculated statistical error bars for both data sets are included.

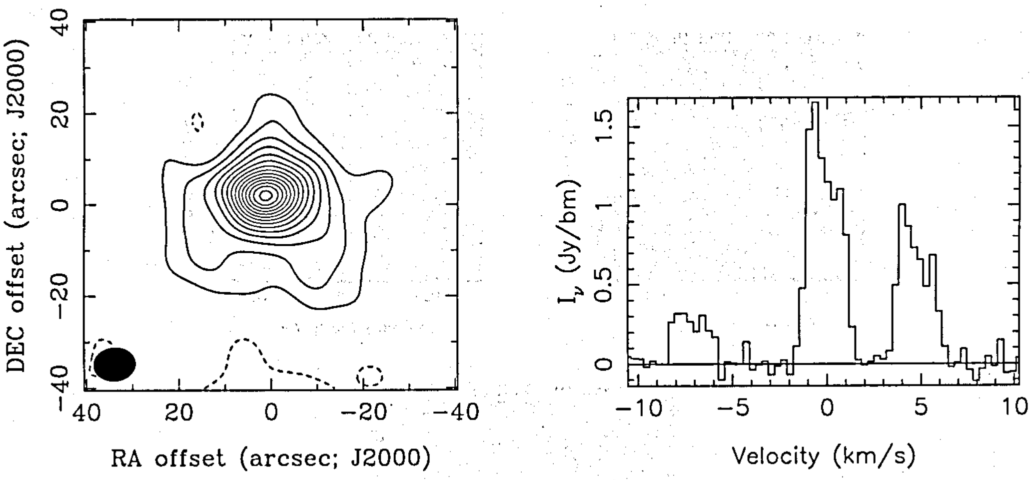

FIGURE K.8: An average over several days in 1997 March (08, 10, 12, 13, 14, 17, 28, and 29 UT) and April (01 and 15 UT). The HCN map and spectrum were created under the same guidelines as were Figs. 1 and 2, except the solid contours in the map are successive multiples of 5σ. The peak intensity and rms value in the map are, in Jy beam^{-1}, 2.01 and 0.03, respectively. The rms value in the spectrum is 0.05 Jy beam^{-1}.

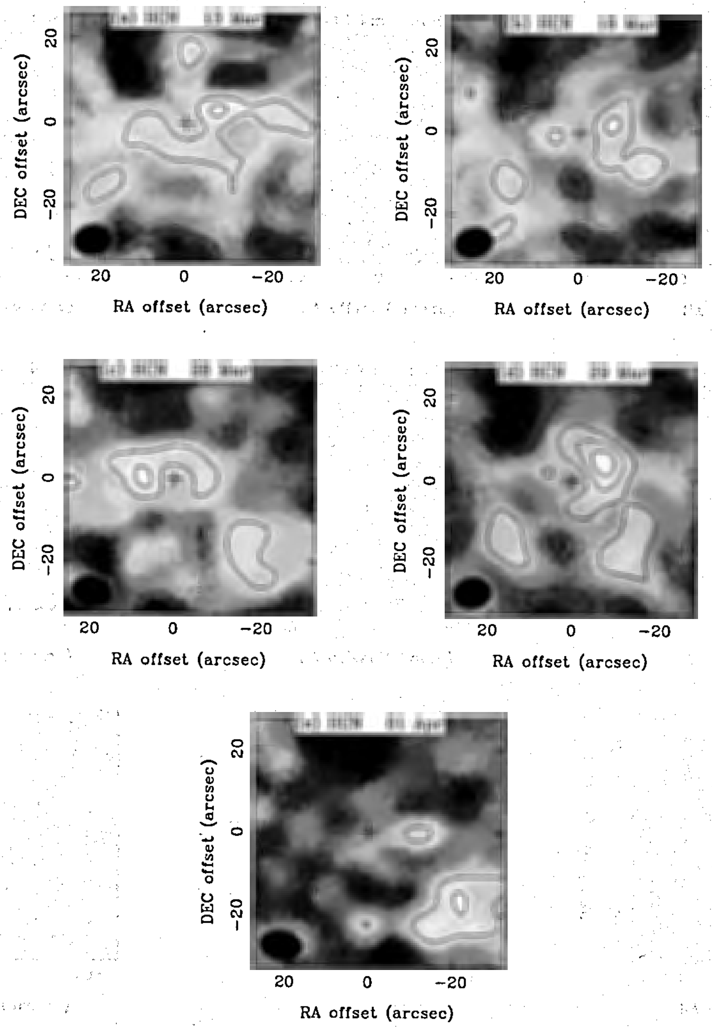

FIGURE K.9: Difference maps of HCN J=1→0 emission from C/1995 O1 observed with the BIMA array. The solid contours are successive multiples of 2σ. The percentage of flux density in (d) due to the excess flux density relative to the observed image is ~15%.

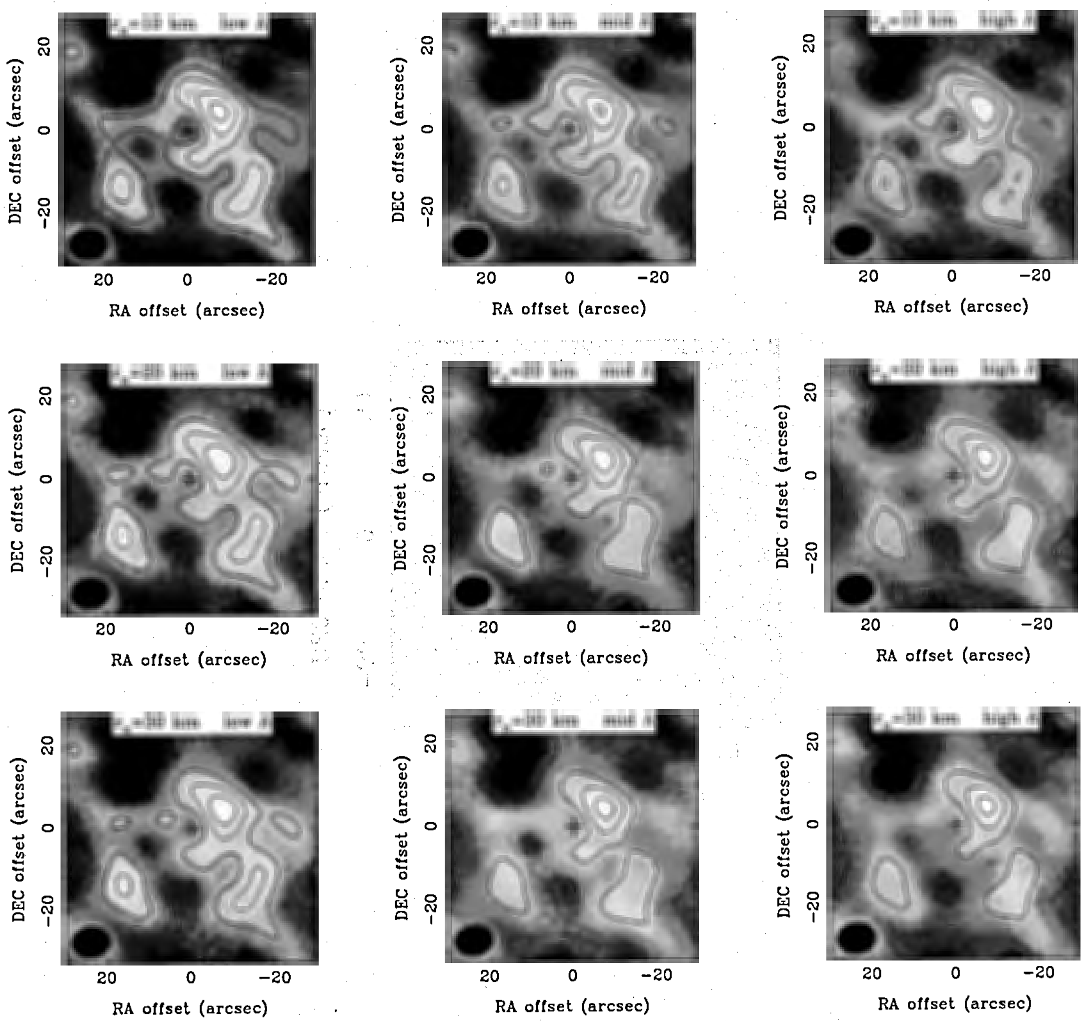

FIGURE K.10: A set of HCN difference maps for 1997 March 29 showing variations due to model adjustments of the nucleus size and photodestruction scale length. See text for values of Λ and their interpretation. Solid contours are successive multiples of 2σ.

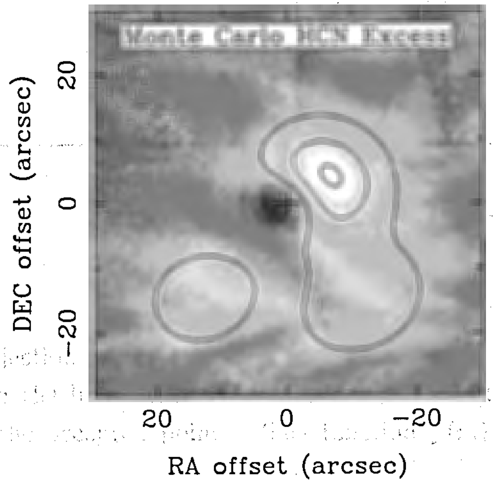

FIGURE K.11: The Monte Carlo method was used to model the distribution of HCN molecules in comet Hale-Bopp on 1997 March 29 UT. After the distribution was convolved with the synthesized beam, a model image based on the Haser distribution was subtracted. The difference map is shown. Essentially, this is a model of Fig. 9d, and the solid contours are the same as for Fig. 9d.

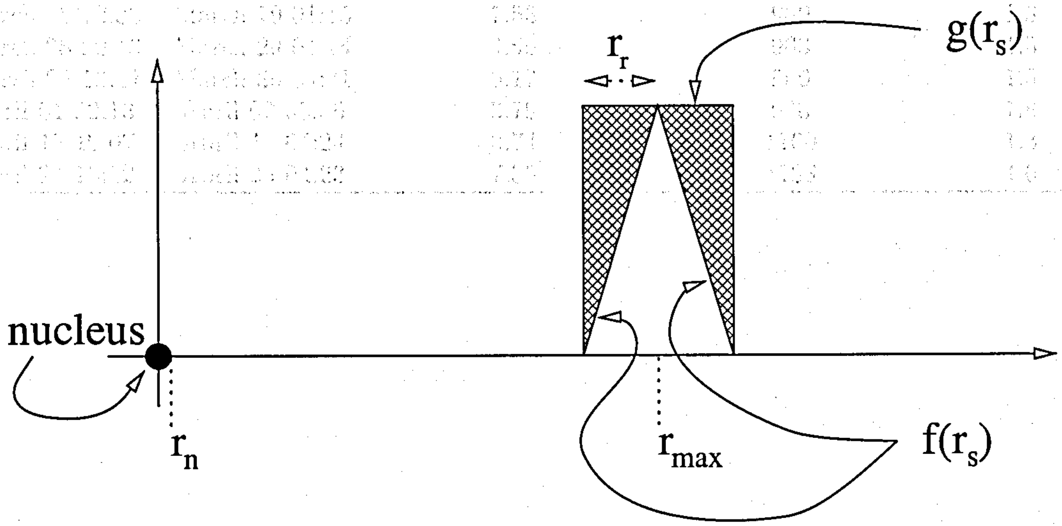

FIGURE K.12: The rejection method is used for determining the r coordinate of the sublimation location in the halo. The shaded area represents the rejected points and the inner white area the accepted points. The function $f(r_s)$ shows the probability distribution function.

TABLE K.1: 1997 Observations and HCN Gas Production Rates

UT Start	UT End	Total Obs. Time (hrs)	Image Scale (km/$''$)	Q ($\times 10^{28}$ s^{-1})
March 08 17:48	March 08 20:57	1.30	1014	1.4
March 10 20:11	March 10 22:27	1.34	999	1.3
March 12 13:14	March 12 16:28	1.95	986	1.4
March 13 13:15	March 14 01:27	6.63	981	1.4
March 14 17:59	March 14 19:17	1.17	975	1.4
March 17 17:44	March 17 19:41	0.93	963	1.2
March 18 12:33	March 19 01:15	7.53	960	1.3
March 28 20:13	March 29 04:14	4.69	963	1.5
March 29 13:41	March 30 04:31	9.17	966	1.5
April 01 22:13	April 02 03:56	3.79	980	1.8
April 15 19:07	April 16 04:24	3.74	1100	1.3
April 24 18:12	April 25 04:23	7.33	1198	1.6

TABLE K.2: Ephemeris Information

Date (0^h UTC)	α (J2000)	δ (J2000)	Δ (AU)	r (AU)	θ[a] (°)	β[b] (°)	PsAng[c] (°)
March 08	22 05 57.67	+38 31 23.2	1.398	1.010	46.2	45.2	336.2
March 10	22 20 42.32	+39 55 21.1	1.378	.996	46.2	46.1	338.8
March 12	22 36 28.80	+41 14 07.4	1.360	.982	46.2	46.9	341.8
March 13	22 44 45.16	+41 51 03.0	1.352	.976	46.1	47.2	343.4
March 14	22 53 16.60	+42 26 03.1	1.344	.970	46.0	47.6	345.1
March 17	23 20 16.05	+43 57 26.3	1.328	.953	45.7	48.4	350.6
March 18	23 29 31.91	+44 21 41.8	1.324	.949	45.6	48.6	352.6
March 28	01 09 05.78	+45 35 41.8	1.327	.917	43.7	48.7	15.3
March 29	01 18 53.71	+45 24 28.2	1.332	.916	43.4	48.5	17.7
April 01	01 47 16.71	+44 32 31.8	1.351	.914	42.6	47.7	24.6
April 15	03 31 09.26	+36 37 39.1	1.510	.947	37.9	40.6	52.3
April 24	04 14 53.13	+30 30 54.3	1.652	1.001	34.5	34.7	66.2

[a] The comet's elongation (Sun-Earth-Comet angle).

[b] The comet's phase (Sun-Comet-Earth angle).

[c] The position angle of the extended radius vector.

TABLE K.3: Repeating Spurs in Figs. 4, 5, and 6.

Designation	Figure	$\Delta\alpha('')$	$\Delta\delta('')$
1st	4e	5	20
	4g	15	20
2nd	5b	-20	0
	5c	-20	10
3rd	5b	-5	15
	5c	5	15
4th	5b	20	5
	5c	20	-5
5th	6b	5	-15
	6c	-5	-15
6th	6b	-25	0
	6c	-25	10

REFERENCES

Blake, G. A., Qi, C., Hogerheijde, M. R., Gurwell, M. A., & Muhleman, D. O. 1999, Nature, 398, 213

Blake, G. A., Qi, C., & Muhleman, D. O. 1998, Eos Supplement, Trans. WPAGU, 79, W63

Bockelée-Morvan, D., Crovisier, J., Despois, D., Forveille, T., Gérard, E., Schraml, J., & Thum, C. 1987, A&A, 180, 253

Bockelée-Morvan, D. & Crovisier, J. 1992, A&A, 264, 282

Bockelée-Morvan, D., et al. 1984, A&A, 141, 411

Combi, M. R., & Delsemme, A. H. 1980, ApJ, 237, 633

Crovisier, J. 1987, A&AS, 68, 223

de Pater, I., Forster, J. R., Wright, M. C. H., Butler, B. J., Palmer, P., Veal, J. M., A'Hearn, M. F., & Snyder, L. E. 1998, AJ, 116, 987

de Pater, I., Snyder, L. E., Mehringer, D. M., Wright, M. C. H., Veal, J. M., Fernández, Y. R., Palmer, P., & A'Hearn, M. F. 1997, P&SS, 45, 6, 731

Eberhardt, P., Krankowsky, D., Schulte, W., Dolder, U., Lammerzahl, P., Berthelier, J. J., Woweries, J., Stubbemann, U., Hodges, R. R., Hoffman, J. H., & Illiano, J. M. 1987, A&A, 187, 481

Fernández, Y. R. 1999, Ph. D. thesis, Univ. Maryland

Greenberg, J. M., & Li, A. 1998, A&A, 332, 374

Grün, E., & Jessberger, E. K. 1990, in *Physics and Chemistry of Comets*, ed W. F. Huebner (Berlin: Springer-Verlag), 113

Haser, L. 1957, Academie royale de Belgique, Bulletin de la classe des Sciences, Ser 5, 43, 740

Houpis, H. L. F., & Mendis, D. A. 1981, Moon & Planets, 25, 95

Huebner, W. F., Keady, J. J., & Lyon, S. P. 1992, Ap&SS, 195, 1

Irvine, W. M., Dickens, J. E., Lovell, A. J., Schloerb, F. P., Senay, M., Bergin, E. A., Jewitt, D. C., & Matthews, H. E. 1998, Faraday Discuss., 109

Jewitt, D. C., & Matthews, H. E. 1999, AJ, 117, 1056

Jewitt, D. C., & Matthews, H. E. 1997, AJ, 113, 1145

Klavetter, J. J. & A'Hearn, M. F. 1993, Icarus, 107, 322

Licandro, J., et al. 1998, ApJL, 501, 221

Lovell, A. J. 1999, Ph. D. thesis, University of Massachusetts, Amherst

Maki, A. G. 1974, J. Phys. Chem. Ref. Data, 3, 221

Meier, R., Eberhardt, P., Krankowsky, D., & Hodges, R. R. 1993, A&A, 277, 677

Oberc, P. 1996, Icarus, 124, 195

Sarmecanic, J., Fomenkova, M., Jones, B., & Lavezzi, T. 1997, ApJ, 483, L69

Sault, R. J., Teuben, P. J, & Wright, M. C. H. 1995, in *Astronomical Data Analysis Software and Systems IV*, ed. R. A. Shaw, H. E. Payne, & J. J. E. Hayes. PASP Conf Ser 77, 433

Schleicher, D. G. & Farnham, T. L. 1999, private communication

Schleicher, D. G., Farnham, T. L., Smith, B. R., Blount, E. A., Nielsen, E., Lederer, S. M. 1998, BAAS, 30, 1063

Schloerb, F. P., Kinzel, W. M., Swade, D. A., & Irvine, W. M. 1987, A&A, 187, 475

Snyder, L. E., Veal, J. M., Woodney, L. M., A'Hearn, M. F., Kuan, Y.-J., Forster, J. R., Wright, M. C. H., Plambeck, R. L., de Pater, I., Pound, M. W., Engargiola, G., & Palmer, P. 1999a, BAAS, 31, 848

Snyder, L. E., Veal, J. M., Woodney, L. M., Wright, M. C. H., Palmer, P., A'Hearn, M. F., Kuan, Y.-J., de Pater, I., & Forster, J. R. 1999b, in preparation

Snyder, L. E., Palmer, P., & de Pater, I. 1989, AJ, 97, 246

Veal, J. M. 2000, Ph. D. thesis, University of Illinois, Urbana

Weaver, H. A. & Lamy, P. L. 1999, Earth, Moon, and Planets, 79, in press

Welch, W. J., et. al. 1996, PASP, 108, 93

Williams, D. M., Mason, C. G., Gehrz, R. D., Jones, T. J., Woodward, C. E., Harker, D. E., Hanner, M. S., Wooden, D. H., Witteborn, F. C., & Butner, H. M. 1997, ApJ, 489, L91

Winnberg, A., Ekelund, L., & Ekelund, A. 1987, A&A, 172, 335

Wright, M. C. H., de Pater, I., Forster, J. R., Palmer, P., Snyder, L. E., Veal, J. M., A'Hearn, M. F., Woodney, L. M., Jackson, W. F., Kuan, Y.-J., & Lovell, A. J. 1998, AJ, 116, 3018

This preprint was prepared with the AAS LaTeX macros v4.0.

References

1997, *Comets and the Origin and Evolution of Life*, ed. P. J. Thomas, C. F. Chyba, & C. P. McKay (New York, Springer-Verlag)

A'Hearn, M. F. 1998, private communication

A'Hearn, M. F., & Festou, M. C. 1990, The Neutral Coma, in *Physics and Chemistry of Comets*, ed W. F. Huebner (Berlin: Springer-Verlag), 69

A'Hearn, M. F., Hoban, S., Birch, P. V., Bowers, C., Martin, R., & Klinglesmith, D. A. 1986, Cyanogen jets in comet Halley, Nature, 324, 649

Apponi, A. J., Pesch, T. C., Ziurys, L. M., Wehinger, P., & Wyckoff, S. 1997, Comet C/1995 O1 (Hale-Bopp), IAU Circ 6586

Biraud, F., Bourgois, G., Crovisier, J., Filit, R., Gérard, E., & Kazès, I. 1974, OH Observation of Comet Kohoutek (1973f) at 18 cm Wavelength, A&A, 34, 163

Bird, M. K., Huchtmeier, W. K., Gensheimer, P., Wilson, T. L., Janardhan, P., & Lemme, C. 1997, Radio detection of ammonia in comet Hale-Bopp, A&A, 325, L5

Blake, G. A., Qi, C., & Muhleman, D. O. 1998, Interferometric Imaging of Comet Hale-Bopp with the Owens Valley Millimeter Array, Eos Supplement, Trans. WPAGU, 79, W63

Bockelée-Morvan, D., Crovisier, J., Baudry, A., Despois, D., Perault, M., Irvine, W. M., Schloerb, F. P., & Swade, D. 1984, Hydrogen cyanide in comets: Excitation conditions and radio observations of comet IRAS-Araki-Alcock 1983d, A&A, 141, 411

Bockelée-Morvan, D., Crovisier, J., & Gérard, E. 1990, Retrieving the coma gas expansion velocity in P/Halley, Wilson (1987 VII), and several other comets from the 18-cm OH line shapes, A&A, 238, 382

Bockelée-Morvan, D., Colom, P., Crovisier, J., Despois, D., & Paubert, G. 1991, Microwave detection of hydrogen sulphide and methanol in comet Austin (1989c1), Nature, 350, 318

Colom, P., Despois, D., Germain, B., Moreno, R., Paubert, G., Biver, N., Bockelée-Morvan, D., Crovisier, J., Gérard, E., Lellouch, E., Rauer, H., Davies, J. K., & Dent, W. R. F. 1997, Comet C/1995 O1 (Hale-Bopp), IAU Circ 6645

Combi, M. R., & Delsemme, A. H. 1980, Neutral Cometary Atmospheres. I. An Average Random Walk Model for Photodissociation in Comets, ApJ, 237, 633

Cremonese, G., Boehnhardt, H., Crovisier, J., Rauer, H., Fitzsimmons, A., Fulle, M., Licandro, J., Pollacco, D., Tozzi, G. P., & West, R. M. 1997, Neutral Sodium from Comet

Hale-Bopp: A Third Type of Tail, ApJ, 490, L199

Crovisier, J. 1987, Rotational and vibrational synthetic spectra of linear parent molecules in comets, A&AS, 68, 223

Crovisier, J. 1998, Physics and chemistry of comets: recent results from comets Hyakutake and Hale-Bopp   Answers to old questions and new enigmas, Faraday Discuss., 108

de Pater, I., Forster, J. R., Wright, M. C. H., Butler, B. J., Palmer, P., Veal, J. M., A'Hearn, M. F., & Snyder, L. E. 1998, BIMA and VLA Observations of Comet Hale-Bopp at 22 – 115 GHz, AJ, 116, 987

de Pater, I., Palmer, P., & Snyder, L. E. 1986, The Brightness Distribution of OH Around Comet Halley, ApJ, 304, L33

de Pater, I., Snyder, L. E., Mehringer, D. M., Wright, M. C. H., Veal, J. M., Fernández, Y. R., Palmer, P., & A'Hearn, M. F. 1997, BIMA array observations of comet Hyakutake: upper limit to the 2.7 mm continuum emission, P&SS, 45, 6, 731

Depois, D., Crovisier, J., Bockelée-Morvan, D., Schraml, J., Forveille, T., & Gérard, E. 1986, Observations of hydrogen cyanide in comet Halley, A&A, 160, L11

Eberhardt, P., Krankowsky, D., Schulte, W., Dolder, U., Lammerzahl, P., Berthelier, J. J., Woweries, J., Stubbemann, U., Hodges, R. R., Hoffman, J. H., & Illiano, J. M. 1987, The CO and N_2 abundance in comet P/Halley, A&A, 187, 481

Elitzur, M. 1981, On Pumping of the OH Ground State in Comets, ApJ, 246, 354

Fernández, Y. R., A'Hearn, M. F., Lisse, C. M., Kundu, A., Weaver, H. A., Hoffman, W. F., Kauffl, U., Hora, J. L., Ressler, M. E., Hanner, M. S., Dayal, A., Deatsch, L. K., & Fazio, G. G. 1998, First International Conference on Comet Hale-Bopp, Physical properties of the nucleus of comet Hale-Bopp, Tenerife, Spain, 2-5 Feb 1998

Festou, M. 1978 Ph. D. thesis, Université Pierre et Marie Curie, Paris

Flammer, K. R., Mendis, D. A., & Houpis, H. L. F. 1998, On the Outgassing Profile of Comet Hale-Bopp, ApJ, 494, 822

Green, S., & Thaddeus, P. 1974, Rotational Excitation of HCN by Collisions, ApJ, 191, 653

Greenberg, J. M. 1982, What are Comets Made Of? A Model Based on Interstellar Dust, in *Comets*, ed. L. L. Wilkening (Tuscon: University of Arizona Press), 131

Greenberg, J. M., & Li, A. 1998, From interstellar dust to comets: the extended CO source in comet Halley, A&A, 332, 374

Grün, E., & Jessberger, E. K. 1990, Dust, in *Physics and Chemistry of Comets*, ed W. F. Huebner (Berlin: Springer-Verlag), 113

Haser, L. 1957, Distribution d'intensité dans la tête d'une comète, Academie royale de Belgique, Bulletin de la classe des Sciences, Ser 5, 43, 740

Houpis, H. L. F., & Mendis, D. A. 1981, The nature of the solar wind interaction with CO_2/CO-dominated comets, Moon & Planets, 25, 95

Huebner, W. F., Keady, J. J., & Lyon, S. P. 1992, Solar photorates for planetary atmospheres and atmospheric pollutants, Ap&SS, 195, 1

Huebner, W. F., Snyder, L. E., & Buhl, D. 1974, HCN Radio Emission from Comet Kohoutek (1973f), Icarus, 23, 580

Irvine, W. M., et al. 1996, Spectroscopic evidence for interstellar ices in comet Hyakutake, Nature, 383, 418

Irvine, W. M., Dickens, J. E., Lovell, A. J., Schleorb, F. P., Senay, M., Bergin, E. A., Jewitt, D. C., & Matthews, H. E. 1998, Chemistry in cometary comae, Faraday Discuss., 109

Jewitt, D. C., Matthews, H. E., Owen, T., & Meier, R. 1997, Measurements of ^{12}C/^{13}C, ^{14}N/^{15}N, and ^{32}S/^{34}S Ratios in Comet Hale-Bopp (C/1995 O1), Science, 278, 90

Jewitt, D. C., & Matthews, H. E. 1997, Submillimeter Continuum Observations of Comet Hyakutake (1996 B2), AJ, 113, 1145

Lis, D. C., Keene, J., Young, K., Phillips, T. G., Bockelée-Morvan, D., Crovisier, J., Schilke, P., Goldsmith, P. F., & Bergin, E. A. 1998, Spectroscopic Observation of Comet C/1996 B2 (Hyakutake) with the Caltech Submillimeter Observatory, Icarus, 130, 355

Lis, D. C., Mehringer, D. M., Benford, D., Gardner, M., Phillips, T. G., Bockelée-Morvan, D., Biver, N., Colom, P., Crovisier, J., Despois, D., & Rauer, H. 1998, New Molecular Species in Comet C/1995 O1 (Hale-Bopp) Observed with the Caltech Submillimeter Observatory, Earth, Moon, & Planets, in press

Lisse, C. M., Dennerl, K., Englhauser, J., Harden, M., Marshall, F. E., Mumma, M. J., Petre, R., Pye, J. P., Ricketts, M. J., Schmitt, J., Trümper, J., & West, R. G. 1996, Discovery of X-ray and Extreme Ultraviolet Emission from Comet C/Hyakutake 1996 B2, Science, 274, 205

Lovell, A., Schloerb, P., DeVries, C., Dickens, J., Irvine, W., & Senay, M. 1997, Comet C/1995 O1 (Hale-Bopp), IAU Circ 6590

Lovell, A. J., Schloerb, F. P., Dickens, J. E., DeVries, C. H., Senay, M. C., & Irvine, W. M. 1998, HCO^+ Imaging of Comet Hale-Bopp (C/1995 O1), ApJ, 497, L117

Meier, R., Owen, T. C., Jewitt, D. C., Matthews, H. E., Senay, M., Biver, N., Bockelée-Morvan, D., Crovisier, J., & Gautier, D. 1998, Deuterium in Comet C/1995 O1 (Hale-Bopp): Detection of DCN, Science, 279, 1707

Meier, R., Owen, T. C., Matthews, H. E., Jewitt, D. C., Bockelée-Morvan, D., Biver, N., Crovisier, J., & Gautier, D. 1998, A Determination of the HDO/H_2O Ratio in Comet C/1995 O1 (Hale-Bopp), Science, 279, 842

Miao, Y., Mehringer, D. M., Kuan, Y.-J., & Snyder, L. E. 1995, Complex Molecules in Sagittarius B2(N): The Importance of Grain Chemistry, ApJL, 445, L59

Mies, F. H. 1974, Ultraviolet Fluorescent Pumping of OH 18-Centimeter Radiation in Comets, ApJL, 191, L145

Mumma, M. J., Disanti, M. A., Russo, N. D., Fomenkova, M., Magee-Sauer, K., Kaminski,

C. D., & Xie, D. X. 1996, Detection of Abundant Ethane and Methane, along with Carbon Monoxide and Water, in Comet C/1996 B2 (Hyakutake): Evidence for Processed Interstellar Ice, Science, 272, 1310

Narayanan, G., Butner, H. M., McMullin, J., & Muders, D. 1997, Comet C/1995 O1 (Hale-Bopp), IAU Circ 6591

Palmer, P., de Pater, I., & Snyder, L. E. 1999, OH Imaging of Comet Shoemaker-Levy (C/1991 T2), AJ, submitted

Pound, M., & Helfer, T. 1997, Autocorrelation Observations with the BIMA Array, BIMA Memoranda Series, No. 57

Sarmecanic, J., Fomenkova, M., Jones, B., & Lavezzi, T. 1997, Constraints on the Nucleus and Dust Properties from the Mid-Infrared Imaging of Comet Hyakutake, ApJ, 483, L69

Sault, R. J., Teuben, P. J, & Wright, M. C. H. 1995, A Retrospective View of Miriad, in *Astronomical Data Analysis Software and Systems IV*, ed. R. A. Shaw, H. E. Payne, & J. J. E. Hayes. PASP Conf Ser 77, 433

Schloerb, F. P., Kinzel, W. M., Swade, D. A., & Irvine, W. M. 1986, HCN Production from Comet Halley, ApJ, 310, L55

Snyder, L. E., Palmer, P., & de Pater, I. 1989, Radio Detection of Formaldehyde Emission from Comet Halley, AJ, 97, 246

Snyder, L. E., Veal, J. M., Woodney, L. M., A'Hearn, M. F., Kuan, Y.-J., Forster, J. R., Wright, M. C. H., Plambeck, R. L., de Pater, I., Pound, M. W., Engargiola, G., & Palmer, P. 1999, BIMA Array Spectral Line Observations of Comet Hale-Bopp (C/1995 O1), BAAS, 31, 848

Snyder, L. E., Veal, J. M., Woodney, L. M., A'Hearn, M. F., Kuan, Y.-J., Forster, J. R., Wright, M. C. H., Plambeck, R. L., de Pater, I., Pound, M. W., Engargiola, G., & Palmer, P. 1999, BIMA Array Spectral Line Observations of Comet Hale-Bopp (C/1995 O1), unpublished reprint

Snyder, L. E., Webber, J. C., Crutcher, R. M., & Swenson, G. W., Jr. 1976, Radio Observations of OH in comet West 1975n, ApJ, 209, L49

Turner, B. E. 1974, Detection of OH at 18-centimeter Wavelength in Comet Kohoutek (1973f), ApJ, 189, L137

Veal, J. M., Snyder, L. E., de Pater, I., Wright, M. C. H., Forster, J. R., Palmer, P., Woodney, L. M., A'Hearn, M. F., & Kuan, Y.-J. 1998, BIMA Array Observations of Comet Hale-Bopp: Evidence of Deviations from Spherical Outflow, BAAS, 192, #08.03

Veal, J. M., Snyder, L. E., Wright, M. C. H., Forster, J. R., Hoffman, W., Pound, M., de Pater, I., Helfer, T., Plambeck, R. L., Engargiola, G., Wong, T., Woodney, L. M., A'Hearn, M. F., Palmer, P., & Kuan, Y.-J. 1997, Comet C/1995 O1 (Hale-Bopp), IAU Circ 6575

Weaver, H. A. 1998, Estimating the size of Hale-Bopp's nucleus, First International Conference on Comet Hale-Bopp, Tenerife, Spain, 2-5 Feb 1998

Webber, J. C., & Snyder, L. E. 1977, Detection of Radio OH in Periodic Comet D'Arrest, ApJ, 214, L45

Welch, W. J., et. al. 1996, The Berkeley-Illinois-Maryland-Association Millimeter Array PASP, 108, 93

Williams, D. M., Mason, C. G., Gehrz, R. D., Jones, T. J., Woodward, C. E., Harker, D. E., Hanner, M. S., Wooden, D. H., Witteborn, F. C., & Butner, H. M. 1997, Measurement of Submicron Grains in the Coma of Comet Hale-Bopp C/1995 O1 During 1997 February 15-20 UT, ApJ, 489, L91

Wink, J. E., Bockelée-Morvan, D., Biver, N., Colom, P., Crovisier, J., Gérard, E., Rauer, H., Despois, D., Moreno, R., Paubert, G., Davies, J. K., & Dent, W. R. F. 1997, Comet C/1995 O1 (Hale-Bopp), IAU Circ 6591

Wink, J. E., Bockelée-Morvan, D., Biver, N., Colom, P., Crovisier, J., Gérard, E., Rauer, H., Despois, D., Moreno, R., Paubert, G., Davies, J. K., & Dent, W. R. F. 1997, Comet C/1995 O1 (Hale-Bopp), IAU Circ 6599

Wright, M. C. H., de Pater, I., Forster, J. R., Palmer, P., Snyder, L. E., Veal, J. M., A'Hearn, M. F., Woodney, L. M., Jackson, W. F., Kuan, Y.-J., & Lovell, A. J. 1998, Mosaicked Images and Spectra of J=1$\rightarrow$0 HCN and HCO$^+$ emission from Comet Hale-Bopp (1995 O1), AJ, 116, 3018

Vita

Jeffrey Matthew Veal

Born:

1970 August 22, Newport Beach, California, U.S.A.

Education:

B. S. in Astronomy, Magna Cum Laude, with Distinction
San Diego State University, 1994

Experience:

Research Assistant, University of Illinois, Astronomy Department,
Spring 1995 to Summer 1998

Teaching Assistant, University of Illinois, Astronomy Department,
Fall 1994 to Spring 1996

Scholastic Honors and Scholarships:

Dean's List, 8 semesters, San Diego State University

Lucas Award, Fall 1991, San Diego State University, Astronomy Department

Honorary and Professional Organizations:

Society of Phi Beta Kappa

Society of Phi Kappa Phi

American Astronomical Society

Publications:

- Acord, J., **Veal, J. M.**, & Snyder, L. E. 1999, Measuring the Temperature of Sgr B2(N) with Multi-Transition HC_3N Observations, in preparation
- **Veal, J. M.**, Snyder, L. E., Woodney, L. M., Palmer, P., Forster, J. R., de Pater, I., A'Hearn, M. F., & Kuan, Y. -J. 2000, An Interferometric Study of HCN in Comet Hale-Bopp (C/1995 O1), AJ, in press
- Snyder, L. E., **Veal, J. M.**, Woodney, L. M., A'Hearn, M. F., Kuan, Y.-J., Forster, J. R., Wright, M. C. H., Plambeck, R. L., de Pater, I., Pound, M. W., Engargiola, G., & Palmer, P. 1999, BIMA Array Spectral Line Observations of Comet Hale-Bopp (C/1995 O1), BAAS, 31, 848
- Wright, M. C. H., de Pater, I., Forster, J. R., Palmer, P., Snyder, L. E., **Veal, J. M.**, A'Hearn, M. F., Woodney, L. M., Jackson, W. F., Kuan, Y.-J., & Lovell, A. J. 1998, Mosaicked Images and Spectra of $J=1\rightarrow0$ HCN and HCO^+ emission from Comet Hale-Bopp (1995 O1), AJ, 116, 3018
- Woodney, L. M., A'Hearn, M. F., Wellnitz, D. D., Schleicher, D. G., Farnham, T. L., Cheung, T. C., McMullin, J. P., **Veal, J. M.**, Snyder, L. E., de Pater, I., Forster, J. R., Wright, M. C. H., Palmer, P., Kuan, Y. -J., & Samarasinha, N. 1998, Morphology of HCN and CN in Comet Hale-Bopp, BAAS, DPS meeting 30, 31.03
- de Pater, I., Forster, J. R., Wright, M. C. H., Butler, B. J., Palmer, P., **Veal, J. M.**, A'Hearn, M. F., & Snyder, L. E. 1998, BIMA and VLA Observations of Comet Hale-Bopp at 22 – 115 GHz, AJ, 116, 987
- **Veal, J. M.**, Snyder, L. E., de Pater, I., Wright, M. C. H., Forster, J. R., Palmer, P., Woodney, L. M., A'Hearn, M. F., & Kuan, Y.-J. 1998, BIMA Array Observations of Comet Hale-Bopp: Evidence of Deviations from Spherical Outflow, BAAS, 192, #08.03

- Woodney, L. M., A'Hearn, M. F., Fernández, Y. R., Sherwin, A. K., Wellnitz, D. D., McMullin, J. P., Samarasinha, N., Farnham, T. L., Schleicher, D. G., **Veal, J. M.**, Snyder, L. E., Wright, M. C. H., Forster, J. R., Pound, M., de Pater, I., Helfer, T., Plambeck, R. L., Engargiola, G., Palmer, P., Kuan, Y. -J. 1997, Temporal and Spatial Variability of Parent Molecules in Comet Hale-Bopp, BAAS, DPS meeting 29, 37.01

- de Pater, I., Snyder, L. E., Mehringer, D. M., Wright, M. C. H., **Veal, J. M.**, Fernández, Y. R., Palmer, P., & A'Hearn, M. F. 1997, BIMA array observations of comet Hyakutake: upper limit to the 2.7 mm continuum emission, P&SS, 45, 6, 731

- **Veal, J. M.**, Snyder, L. E., Wright, M. C. H., Forster, J. R., Hoffman, W., Pound, M., de Pater, I., Helfer, T., Plambeck, R. L., Engargiola, G., Wong, T., Woodney, L. M., A'Hearn, M. F., Palmer, P., & Kuan, Y.-J. 1997, Comet C/1995 O1 (Hale-Bopp), IAU Circ 6575

- Shafter, A. W., **Veal, J. M.**, and Robinson, E. L. 1994, A Radial Velocity Study of the Dwarf Nova AR Andromedae: Comparison of the Quiescent and Outburst States, ApJ, 440, 853.

- Shafter, A. W., Misselt, K. A., and **Veal, J. M.** 1994, Two New Eclipsing Classical Novae: DO Aquilae and V849 Ophiuchi, in Interacting Binary Stars (ASP Conf. Ser., vol. 56), ed. A. W. Shafter (San Francisco: A. S. P. Conf. Ser.), 302.

- Shafter, A. W., Misselt, K. A., and **Veal, J. M.** 1993, The discovery of Unusual Eclipses in the Light Curves of the Classical Novae DO Aquilae and V849 Ophiuchi, PASP, 105, 853.